2019

Using Frequency Based Substructuring to Optimize Multi-Axis Resonant Plate Shock Tests

Erica M. Jacobson
Michigan Technological University, ejacobso@mtu.edu

USING FREQUENCY BASED SUBSTRUCTURING TO OPTIMIZE MULTI-AXIS RESONANT PLATE SHOCK TESTS

By

Erica M. Jacobson

A THESIS

Submitted in partial fulfillment of the requirements for the degree of

MASTER OF SCIENCE

In Mechanical Engineering

MICHIGAN TECHNOLOGICAL UNIVERSITY

2019

This thesis has been approved in partial fulfillment of the requirements for the Degree of MASTER OF SCIENCE in Mechanical Engineering.

Department of Mechanical Engineering-Engineering Mechanics

Thesis Advisor:	*Dr. Jason R. Blough*
Committee Member:	*Dr. James P. DeClerck*
Committee Member:	*Charles D. Van Karsen*
Department Chair:	*Dr. William W. Predebon*

Table of Contents

List of figures

List of tables

Preface

This work was funded by Honeywell Federal Manufacturing & Technologies under Contract No. DE-NA0002839 with the U.S. Department of Energy. The United States Government retains and the publisher, by accepting the article for publication, acknowledges that the United States Government retains a nonexclusive, paid up, irrevocable, world-wide license to publish or reproduce the published form of this manuscript, or allow others to do so, for the United States Government purposes.

Acknowledgements

I have encountered many people that have had a profound impact on my personal, academic, and professional development, and I'd like to take the time to address them individually.

First, I'd like to thank my advisor, Dr. Jason Blough, for … allowing me to have free reign on this project, providing me with the resources to satisfy my urges to answer ALL of the questions, and reminding me to "take a deep breath".

I would like to thank Chuck Van Karsen for sharing his infinite wisdom, stories, and witty comments with me, and evidently convincing me to stay in school. You reminded me, early on in my undergraduate career, that engineering is fun, and that I have much more to look forward to after completing the core courses. And that, as always, *thinking is not optional.*

Also, I want to thank Dr. Jim DeClerck, for his practical insight, bringing up questions that I didn't even know I had, and to question everything with such simple, yet powerful words, such as "why?" and "so?".

I want to thank my project sponsor, David Soine, for his interest in this project, help in understanding shock testing, and for always giving an encouraging "right on".

Thank you, students, of the Dynamic Systems Laboratory, for all of your academic and emotional support, the endless supply of resources, and memorable outdoor activities that took place outside of the windowless sub-basement.

I want to thank my parents, Jon and Karen, for always believing in me and keeping me grounded when times were tough. Thank you for your emotional and financial support, occasional (and very appreciated) photos of the cats, and care packages filled with nutritional food.

Lastly, I want to thank all the friends I've made over the years – you are all part of what made Houghton my home, opened my eyes to the future, and gave me hope.

Definitions

Accelerance: Frequency response function that is acceleration per unit force.

Assembly: The fully assembled impact pad, circular plate, and payload either physically or with frequency-based substructuring.

Circular plate: Shock waves travel through the circular plate and create a desired shock response on the payload (component).

Circular plate assembly: Circular plate and impact pad assembly, considered to be subsystem A in this thesis.

Condition number: The ratio of the largest singular value to the smallest singular value of a matrix, increases at system resonances when the small singular values approach zero.

Configuration: A combination of resonant plate assemblies, each with specific payload mounting location, mounting angle, and response node.

Component: The device under test, usually part of a larger assembly, is considered the payload in this thesis.

Coordinate compatibility: A mathematical expression in substructuring that assigns equal displacement to interface node pairs.

Dual assembly: A method of substructuring that keeps redundant degrees of freedom but creates additional equations using LaGrange Multipliers to satisfy the force equilibrium condition.

Fixture: The base that a component is mounted to in a laboratory test and is often created to mimic the service environment dynamics exerted on the component.

Force equilibrium: A mathematical expression in substructuring that assigns equal displacement to interface node pairs, based upon Newton's third law.

Impact pad: A small block bolted to the impact side of the circular plate, used to impact the resonant plate assembly with an impact hammer for laboratory shock tests without damaging the plate.

In-axis: The same direction as the shock impulse on the impact pad and normal to the plate surface, is considered to be +Z in this thesis.

Interface: The nodes and/or degrees of freedom that are constrained together in substructuring, must have mirrored geometry on each subsystem.

Kernel: The main calculation in frequency based substructuring that is the inversion of the sum of the interface drive point measurements, the kernel anti-resonances determine the substructured assembly resonances.

Knee frequency: Dominant frequency in a shock test where the peak of the shock response spectrum occurs, and where the tolerance band slope becomes flat.

LaGrange Multiplier: can be thought of as another variable introduced into a system of equations, to simplify calculations, without explicitly being solved for.

Maximax: A form of the shock response spectrum that calculates the absolute maximum response of an acceleration-based shock.

Off-axis: The two orthogonal directions normal to the in-axis direction, parallel to the surface of the plate, are considered +X (vertical) and +Y (horizontal) in this thesis.

Overtest: When a laboratory test of a component exceeds the dynamics of the service environment, possibly causing a false failure.

Payload: Is used in this thesis in place of a component, is a block mounted to the response side of the circular plate.

Primal assembly: A method of substructuring that maps all subsystem degrees of freedom to a unique set for the substructured assembly, eliminating redundant degrees of freedom.

Pyroshock: A short-duration impulse event that contains significant frequency content beyond 10,000 Hz with amplitudes exceeding 10,000 Gs.

Resonant plate: A method of laboratory component shock testing, in this thesis, is considered the assembly of the impact pad, circular plate, and payload (or test object).

Service environment: The dynamics a component experiences during its intended use, whether it is alone or part of a larger assembly.

Shock response spectrum: A calculation that uses time-based acceleration data and computes the response of mass-spring-damper sets with logarithmically-spaced natural frequencies, is useful for comparing different shock events.

Slinches: Engineering slang for a slug but in inches (lbf s^2/in) representing English base units in inches, seconds, and pound-force.

Subsystem: The pieces that are to be constrained together in substructuring, in this thesis are considered to be the impact pad + circular plate (subsystem A), and the payload (subsystem B).

Test environment: Dynamics created in a laboratory on the component and fixture assembly, often meant to mimic the service environment dynamics of the component.

Underdamped: When system damping is less than the critical damping, or the damping ratio is less than 100%, as most real-life systems are.

Undertest: When a laboratory test of a component does not meet the dynamics of the service environment, possibly causing a false pass.

List of abbreviations

ADC: Analog to digital converter

CMS: Component mode synthesis

CS: Contact surface

DAQ/DAS: Data acquisition system

DOF(s): Degree(s) of freedom

EOM: Equation of motion

FBS: Frequency based substructuring

FEA: Finite element analysis

FEM: Finite element model

FFT: Fast Fourier transform

FLV: Force-limited vibration

FRF(s): Frequency response function(s)

IFFT: Inverse fast Fourier transform

IMMAT: Impedance-match multi-axis testing

LDV: Laser Doppler vibrometer

LM-FBS: LaGrange multiplier frequency based substructuring

LPF: Low pass filter

MDOF: Multiple degree of freedom

MIPS: Mechanical impulse pyroshock

MTU: Michigan Technological University

RBE: Rigid bar element

RMS: Root mean square

SDOF: Single degree of freedom

SNR: Signal to noise ratio

SRS: Shock response spectrum

SVD: Singular value decomposition

TS: Transmission simulator

List of notation

Letters:

A/a: Residues

B: Signed Boolean matrix

Δf: Frequency resolution, Hz

Δt: Time resolution, s

f: External force

Fs: Sampling frequency

F_{max}: Maximum frequency without aliasing

g: Internal/interface force

G: Autopower, crosspower, or linear spectrum

γ^2: Coherence

H(jω)/h(jω): Frequency response function (motion/force)

H(s)/h(s): Transfer function

I: Identity matrix

j: Imaginary unit

L: Unsigned Boolean matrix

m: Total number of modes

M, C, K / m, c, k: Mass, damping, and stiffness

n: Total number of DOFs

N: Block size of data (spectral lines)

p: Modal domain independent variable

Q: Amplification factor using in SRS calculations

$\bar{Q}/\bar{q}$: Modal scale factor

q: Set of unique interface DOFs in primal assembly

s: LaPlace domain independent variable

t: Time domain independent variable, seconds

T: Data acquisition time

u: General motion variable (displacement, velocity, acceleration)

x: Displacement

z: Independent variable from the Z-transform

Z: Inverse of H (force/motion)

α: Digital filter denominator coefficients for SRS implementation

β: Digital filter numerator coefficients for SRS implementation

ζ: Damping ratio

Λ/λ: Roots of the characteristic equation, poles

λ: LaGrange multiplier

σ: Damping factor

Φ: Mode shape matrix

φ: Mode shape vectors, the columns of the mode shape matrix

ω: Frequency domain independent variable, rad/s

ω_d: Damped natural frequency

ω_n: Natural frequency

Operators

M^*: Complex conjugate

M^T: Transpose

M^{-1}: Inverse

Accents

Bar ($\overline{M}$): Modal mass, stiffness, or damping

Tilde ($\widetilde{M}$): Primal-assembly reduced equations of motion

Hat ($\widehat{M}$): Substructured assembly

Dot ($\dot{M}$): Single time derivative, dx/dt

Double dot ($\ddot{M}$): Double time derivative, d^2x/dt^2

Brackets

[M]: Matrix

{M}: Vector

Sub/superscripts

M_u: Uncoupled system (for modal substructuring)

M_c: Coupled system (for modal substructuring)

M_{uc}: Mapping between coupled and uncoupled system

M_{ABI}: Component A, B, or interface (I)

M^{ab}: DOF set a or b

M_k: Mode number from 1 to m

$M_{a,b}$: Input (a) and response (b) DOFs from 1 to n

Other

CAPITAL: Matrix or equivalent (3D for MDOF problems)

Lower case: Scalar or equivalent (2D for SDOF problems)

Abstract

Resonant plate pyroshock tests only offer to test one component axis at a time, while the qualification pyroshock tests often have three single-axis specifications to meet. There is an interest in creating a multi-axis test environment from the single-axis resonant plate parts to save testing time, create a more realistic test environment, and monitor the possibility of an overtest. To investigate this, LaGrange-multiplier frequency based substructuring was implemented to virtually arrange the single-axis resonant plate subsystems into different assembly configurations and mathematically calculate the new assembly dynamics. A shock response spectrum was calculated from the new assembly dynamics through an inverse Fourier transform and convolved with a simple shock pulse. Three objective functions were designated to minimize the difference between the in-axis and off-axis response magnitudes of the shock response spectrum over three frequency ranges. These objective functions included the root mean square, the sum of the square of the residuals, and absolute difference. This process of frequency based substructuring, to shock response spectrum, and to objective function calculation was repeated iteratively for 22 possible new assembly configurations, each with five possible response locations. The resulting assembly of the minimized objective function satisfied the requirements of in-axis and off-axis responses close in magnitude and within the shock test tolerance bands of +/- 6 dB. The iterative optimization process was performed on finite element model data, and three configurations were verified experimentally through full assembly modal tests and through experimental frequency based substructuring.

1 Introduction

Pyroshock is a high-amplitude, high-frequency event that often damages electronic components found in satellites and rockets. Therefore, these components must be tested and assessed for their ability to withstand pyroshock events before assembly. Traditionally, a resonant plate is used to perform these tests over a single axis, even if the qualification pyroshock tests have multiple single-axis specifications to be met. These single-axis tests have an off-axis response, which is not accounted for in three separate single-axis tests. There is an interest in creating a multi-axis test environment with the resonant plate parts to save time and create a more realistic test environment.

Frequency based substructuring is a method of calculating the dynamics of a whole assembly using the dynamics of each individual part. These dynamics are in the form of frequency response functions and can be gathered from modal test data or a finite element model. Frequency based substructuring couples the frequency response functions between individual parts through boundary condition equations. LaGrange-multiplier frequency based substructuring is a method of coupling frequency response functions using a signed Boolean matrix to organize interface degrees of freedom, and LaGrange multipliers to represent the interface internal forces. These attributes also make this method ideal for iterative optimization.

Assembly and subsystem dynamics, in the form of accelerance frequency response functions, are gathered from a finite element model. LaGrange-multiplier frequency based substructuring is implemented on the subsystems and compared to the assembly. A subset of possible assembly configurations is identified, and the assembly frequency response functions are calculated. Shock response spectrums are calculated from the substructured assembly frequency response functions by first applying an inverse Fourier transform and convolving the time domain response with a time domain shock pulse. Three objective functions are used to quantify how close the off-axis response is to the in-axis response of the shock response spectrum. The optimal configuration minimizes the objective functions and offers a potential configuration for a multi-axis resonant plate shock test. The original

configuration, the optimal configuration, and a third (arbitrary) configuration are all verified with modal tests of the assembly and compared to experimental frequency based substructuring results. Figure 1.1 shows a schematic of the resonant plate subsystems used in this thesis.

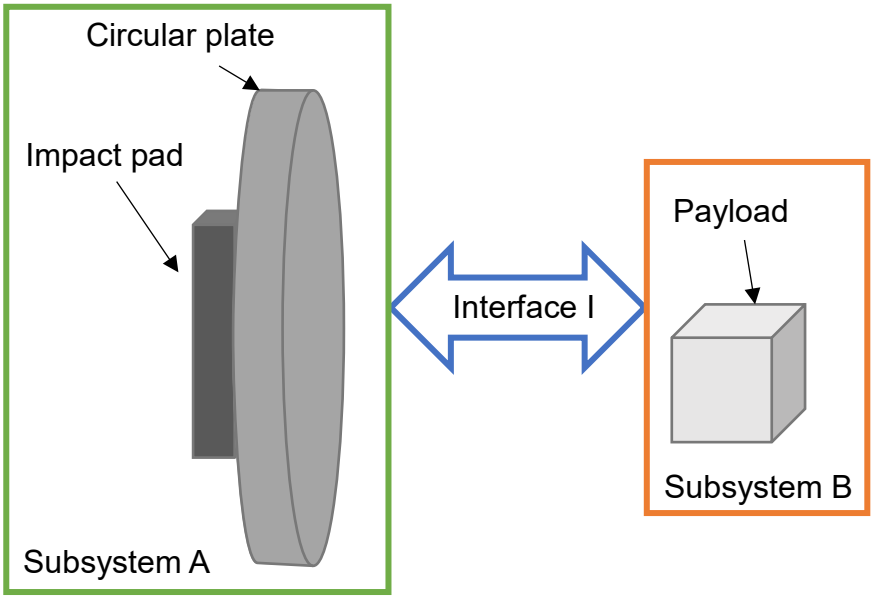

Figure 1.1 Resonant plate subsystems used in LaGrange multiplier frequency based substructuring to optimize the multi-axis shock response spectrum of the payload.

Applicably, a test engineer only has to collect the resonant plate FRFs once. Dynamics of a new payload or response locations can be gathered to fit different components for individual multi-axis test. After iterating through LM-FBS and least-squares optimization, the test engineer can use the optimized plate assembly to test all three single-axis qualification pyroshock tests with a single projectile impact. *The aim of this research is to use LaGrange-multiplier frequency based substructuring of resonant plate components to find an assembly for an equal-magnitude multi-axis qualification shock test.*

2 Theory

This chapter covers the basic single degree of freedom theory in the time, LaPlace, and frequency domains. These concepts are introduced for multiple degrees of freedom systems, including modal analysis and the modal domain. Then, substructuring in the physical, frequency, and modal domains are covered. Basic data acquisition, testing, and frequency response function theory follow. The shock response spectrum derivation and implementation conclude the chapter.

2.1 Single degree of freedom theory

Mathematical equations used in vibration theory and analysis begin with a simple, single degree of freedom (SDOF) mass-spring-damper model (Figure 2.1 A). The motion of this system, due to an external force *f*, is expressed as a linear, time-invariant, second-order differential equation. This equation of motion can be expressed in different domains (Figure 2.1 B), providing a variety of insight into the system's behavior. The equation of motion (EOM) is derived from Newton's second law.

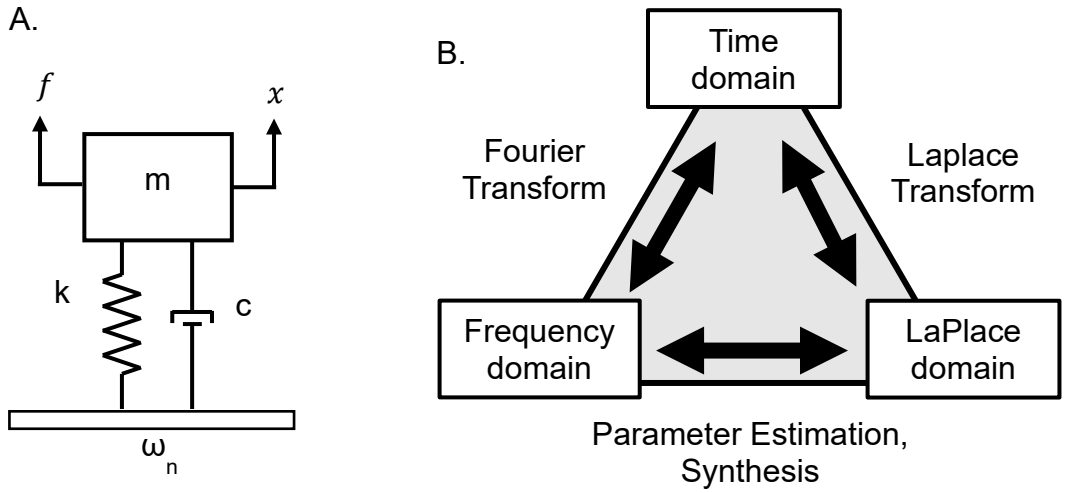

Figure 2.1 A, Single degree of freedom mass-spring-damper model which is used to develop equations that describe basic vibration problems, and B, the relationship between time domain, LaPlace Domain, and frequency domain representation.

Mass (m), stiffness (k), and damping (c) parameters can be used to describe a system's motion:

Natural frequency: $\omega_n = \sqrt{\frac{k}{m}}$

Damping ratio: $\zeta = \frac{c}{2m\omega_n} = \frac{c}{c_{critical}}$

Damped natural frequency: $\omega_d = \omega_n\sqrt{1-\zeta^2}$

Damping factor: $\sigma = \zeta\omega_n$

2.1.1 Time domain

The linear time-invariant, second-order differential equation derived from Newton's second law is as follows:

$$m\ddot{x}(t) + c\dot{x}(t) + kx(t) = f(t)$$

Where *x* is the dependent displacement variable, and *t* is the independent time variable. The time domain response can be broken down into a steady state (acting external force) and transient (no external force, free vibration).

The non-trivial roots of this equation are the system poles (λ) and can be reconstructed in the time domain as a decaying sinusoid with initial conditions (X):

$$x(t)_{transient} = X_1 e^{\lambda_1 t} + X_2 e^{\lambda_2 t}$$

Where…

$$\lambda_{1,2} = \frac{-c}{2m} \pm \sqrt{\frac{c}{2m}^2 - \frac{k}{m}} = -\zeta\omega_n \pm \sqrt{(\zeta\omega_n)^2 - {\omega_n}^2} = -\sigma \pm j\omega_d$$

Where * denotes the complex conjugate. For underdamped systems, the two poles are complex conjugates of each other ($\lambda_2 = \lambda_1^*$) [1]. An underdamped system meets the following criteria:

$$c < c_{critical}$$

Most real-world systems are underdamped. If this damping criterion is met, $\lambda_2 = \lambda_1^*$. All equations following assume an underdamped system. Expressing the above equations in terms of external force and time response, an impulse response function can be determined:

$$x(t) = h(t) \otimes f(t)$$

$$h(t) = a_1 e^{\lambda_1 t} + a_1{}^* e^{\lambda_1^* t}$$

Where a_1 is the system residue, the underdamped solution to X_1. Like the system poles, the system residues are complex conjugates of each other if the system is underdamped. The residues can be expressed as:

$$a_1 = \frac{1}{2jm\omega_d} \;\&\; a_1^* = -\frac{1}{2jm\omega_d}$$

The time domain impulse response function can also be expressed as decaying sinusoids using Euler's identity:

$$h(t) = \frac{e^{-\sigma t}}{m\omega_d} \sin(\omega_d t)$$

2.1.2 LaPlace domain

The equation of motion can also be expressed in the LaPlace Domain. It is often simpler to use the LaPlace domain to solve differential equations, like the SDOF equations above.

$$[ms^2 + cs + k]x(s) = f(s) + (ms + c)x(0) + m\dot{x}(0)$$

Assuming zero initial conditions:

$$[ms^2 + cs + k]x(s) = f(s)$$

Which can be simplified to the LaPlace transfer function h(s):

$$z(s)x(s) = f(s)$$

$$h(s) = \frac{1}{z(s)} = \frac{x(s)}{f(s)}$$

Where the LaPlace transfer function can be expressed in different forms:

polynomial: $h(s) = \frac{1}{ms^2+cs+k}$

pole-zero: $h(s) = \frac{1/m}{(s-\lambda_1)(s-\lambda_1^*)}$

partial fraction: $h(s) = \frac{a_1}{(s-\lambda_1)} + \frac{a_1^*}{(s-\lambda_1^*)}$

2.1.3 Frequency domain

The LaPlace independent variable *s* can be expressed as ($s = \sigma + j\omega$), which is a two-dimensional space consisting of complex frequency and damping factor. Setting the damping factor (σ) to zero essentially takes a two-dimensional slice along the complex frequency axis, resulting in $s = j\omega$. The transfer function is now referred to as a frequency response function:

$$z(j\omega)x(j\omega) = f(j\omega)$$

$$h(j\omega) = \frac{1}{z(j\omega)} = \frac{x(j\omega)}{f(j\omega)}$$

The frequency response functions can be expressed in polynomial, pole-zero, or partial fraction form.

polynomial: $h(j\omega) = \frac{1}{-m\omega^2+cj\omega+k}$

pole-zero: $h(j\omega) = \frac{1/m}{(j\omega-\lambda_1)(j\omega-\lambda_1^*)}$

partial fraction: $h(j\omega) = \frac{a_1}{j\omega-\lambda_1} + \frac{a_1{}^*}{j\omega-\lambda_1^*}$

There are different forms of frequency response functions, depending on the dependent variable (displacement (X), velocity (V), or acceleration (A)) and whether it is expressed as force (F) over response, or response over force.

Receptance (or dynamic compliance):	X/F	Dynamic stiffness:	F/X
Mobility:	V/F	Impedance:	F/V
Accelerance (or inertance):	A/F	Dynamic mass:	F/A

To take a derivative in the frequency domain, multiply by $j\omega$. So, mobility (V/F) is receptance (X/F) multiplied by $j\omega$, and accelerance (A/F) is receptance multiplied by $-\omega^2$.

2.2 Multiple degree of freedom theory

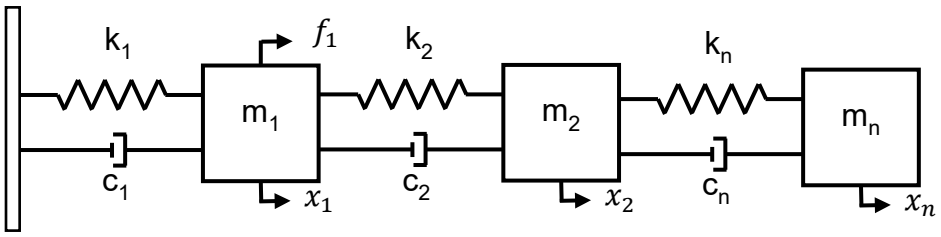

Figure 2.2 Multiple degree of freedom spring-mass-damper model that is used to develop the equations of motion for simple vibration problems.

The same equations for SDOF systems are used to express multiple degrees of freedom systems (MDOF) (Figure 2.2), where mass, stiffness, and damping are represented as block-diagonal matrices with *n* DOFs:

$$M = \begin{bmatrix} m_1 & 0 & 0 \\ 0 & \ddots & 0 \\ 0 & 0 & m_n \end{bmatrix}$$

$$K = \begin{bmatrix} [k_1] & 0 & 0 \\ 0 & \ddots & 0 \\ 0 & 0 & [k_n] \end{bmatrix} \qquad \text{where } [k_1] = \begin{bmatrix} k_1 & -k_1 \\ -k_1 & k_1 \end{bmatrix}$$

And the responses and input forces are represented as column vectors:

$$f = \begin{Bmatrix} f_1 \\ \vdots \\ f_n \end{Bmatrix} \text{ and } x = \begin{Bmatrix} x_1 \\ \vdots \\ x_n \end{Bmatrix}$$

Damping is often estimated as proportional to the stiffness (C = n*K) or eliminated from the problem.

2.2.1 Time domain

Below is the characteristic equation of motion and impulse response function for multiple degrees of freedom system in the time domain:

$$M\{\ddot{x}(t)\} + C\{\dot{x}(t)\} + K\{x(t)\} = \{f(t)\}$$

$$h_{ab}(t) = \sum_{k=1}^{m} A_{ab_k} e^{\lambda_k t} + A^*_{ab_k} e^{\lambda^*_k t}$$

Applying Euler's identity shows that any time domain response is the sum of exponentially decaying sinusoids.

2.2.2 Frequency domain

Below are frequency response functions written for a multiple degrees of freedom system, where *H* represents a full 3D matrix *n x n x ω*, and *h* represents the a^{th} row and b^{th} column of matrix *H* that is length *ω*:

polynomial: $H(j\omega) = \frac{1}{-M\omega^2+Cj\omega+K}$ $h_{ab}(j\omega) = \frac{1}{-M\omega^2+Cj\omega+K}$

pole-zero: $H(j\omega) = \frac{1/M}{(j\omega-\Lambda)(j\omega-\Lambda^*)}$ $h_{ab}(j\omega) = \frac{1/m_{ab}}{(j\omega-\Lambda)(j\omega-\Lambda^*)}$

partial fraction: $H(j\omega) = \sum_{k=1}^{m} \frac{A_k}{j\omega-\lambda_k} + \frac{A_k^*}{j\omega-\lambda_k^*}$ $h_{ab}(j\omega) = \sum_{k=1}^{m} \frac{a_{abk}}{j\omega-\lambda_k} + \frac{a_{abk}^*}{j\omega-\lambda_k^*}$

where *a* and *b* correspond to input and output locations, respectively, and *k* represents the summation of modes 1 through *m*. The contribution of individual modes within the frequency response function matrix will be discussed in the next section. The basis of frequency based substructuring uses MDOF frequency domain information.

Curve fitting frequency response functions in modal parameter estimation software (such as Siemens Test.Lab PolyMax Plus algorithm) solves for the poles and residues of the partial fraction representation within a selected band [2]. When curve fitting a frequency band, the upper and lower residuals can be calculated, compensating for the inherent modal truncation within the data and improving frequency response function correlation.

2.3 Modal analysis and the eigensolution

It is possible to uncouple the relationship between mass, stiffness, and damping through the eigenvalue problem. It is often assumed that damping is zero or proportional to the stiffness matrix. Some excellent references that explain modal analysis and the modal domain are [2], [1], and [3].

$$[K - \lambda M]\{x\} = 0$$

The eigensolution of the characteristic equation gives the natural frequencies and mode shapes for as many degrees of freedom that are expressed in the matrices. The eigensolution produces a diagonal matrix [λ], which is the square of the natural frequencies [ω_n^2], and a matrix of the mode shape vectors [Φ].

$$[K][\Phi] = [M][\Phi][{\omega_n}^2]$$

$$\lambda = \begin{bmatrix} {\omega_1}^2 & 0 & 0 \\ 0 & \ddots & 0 \\ 0 & 0 & {\omega_n}^2 \end{bmatrix} \qquad \text{and } [\Phi] = [\{\varphi_1\} \quad \dots \quad \{\varphi_n\}$$

2.3.1 Modal domain

Using the eigensolution of the characteristic equation, the mode shape vectors can be used to transform the mass, stiffness, and damping matrices. Once transformed, these matrices are now uncoupled from each other and transformed into the modal domain. In the modal domain, modal mass ($\bar{M}$) and modal stiffness ($\bar{K}$) are described in terms of natural frequencies and shapes. If the proof orthogonality holds true, the block matrices in the modal domain only have values on the diagonal.

Proof of orthogonality of eigenvectors: $\{\phi_a\}^T[M]\{\phi_b\} = 0$ for a =/= b

Modal mass: $\{\varphi_a\}^T[M]\{\varphi_a\} = \bar{m}_{aa}$

Modal stiffness: $\{\varphi_a\}^T[K]\{\varphi_a\} = \bar{k}_{aa}$

Now the mass and stiffness matrices are uncoupled in the modal domain. Damping is included in the following equations. Once this modal transformation is complete, the modal matrices can be expressed as:

$$[\bar{M}]\{\ddot{p}\} + [\bar{C}]\{\dot{p}\} + [\bar{K}]\{p\} = [\Phi]^T\{F\}$$

Where p is the modal coordinate. The mode shape vectors can be scaled so that the mass matrix M is equal to the identity matrix. This is known as unit modal mass scaling. Most FEM software and MATLAB automatically scale the mode shape vectors to unity modal mass. If this criterion is met, the modal stiffness is a diagonal of the squared natural frequencies (λ) and the modal damping matrix is a diagonal of twice the damping factor (σ).

$$[\Phi]^T[M][\Phi] = [I]$$

$$[I]\{\ddot{p}\} + [2\zeta\omega_n]\{\dot{p}\} + [{\omega_n}^2]\{p\} = [\Phi]^T\{F\}$$

The coordinate transformation between the modal domain and the time domain is dependent on the mode shape and modal coordinate *p*. Often, fewer modes (*m*) are solved for than total degrees of freedom (*n*).

$$\{x\} = [\Phi]\{p\} = \ [\{\varphi_1\} \quad \dots \quad \{\varphi_m\}]\begin{Bmatrix} p_1 \\ \vdots \\ p_m \end{Bmatrix}$$

The modal domain is useful for looking at modal participation. Each time domain response *x* consists of a summation of different modes (*1* to *m*) across all degrees of freedom (*1* to *n*) [2].

2.3.2 Modal participation

The poles and residues can also be expressed as a summation of modal participation. The residue corresponding to mode shape *k* is the vector of mode shape *k* multiplied by a modal participation scale factor, $\bar{Q}_k$. Residues are a system characteristic that is the product of mode shapes and modal participation scale factors:

$$A_k = \bar{Q}_k \varphi_k \varphi_k^T$$

For unit modal mass scaling: $Q_k = \frac{1}{2j\omega_k}$

$$h_{ab}(j\omega) = \sum_{k=1}^{m} \frac{\bar{Q}_k \varphi_{ak} \varphi_{bk}}{j\omega - \lambda_k} + \frac{\bar{Q}_k \varphi_{ak} {\varphi_{bk}}^*}{j\omega - {\lambda_k}^*}$$

$$h_{ab}(t) = \sum_{k=1}^{m} \bar{q}_k \varphi_{ak} \varphi_{bk} e^{\lambda_k t} + \bar{q}_k \varphi_{ak} {\varphi_{bk}}^* e^{\lambda_k^* t}$$

Any system response is a sum of mode shapes and scale factors across all calculated mode shapes.

2.4 Substructuring domains

Substructuring is the mathematical assembly of different component dynamics into a full structure (Figure 2.3). This can be done with the MDOF characteristic equation in any domain. Substructuring is commonly performed in the physical, modal, or frequency domain. There also exist methods the time domain (using impulse response functions) and state space domain but will not be discussed in this thesis.

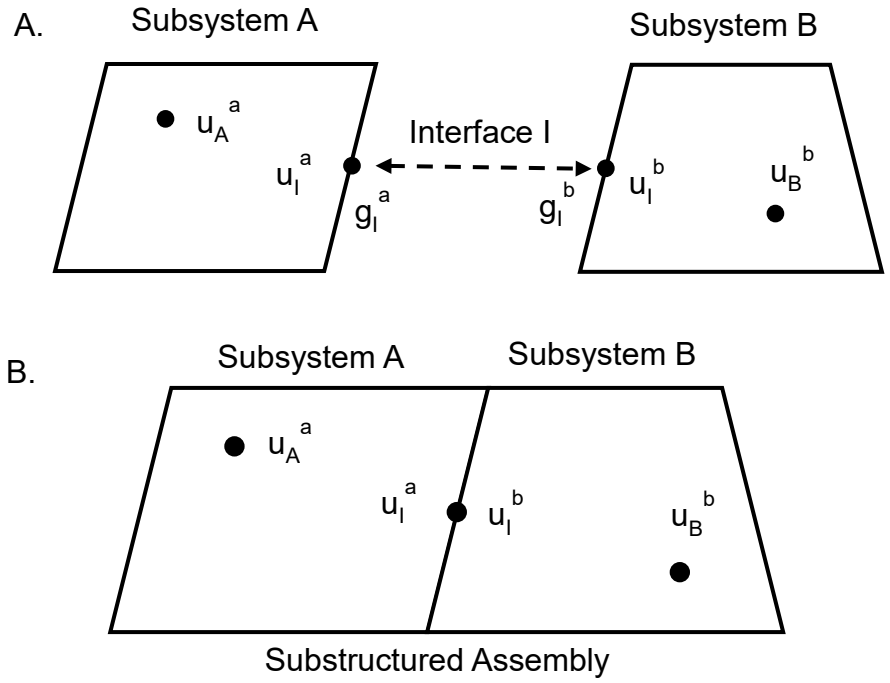

Figure 2.3 *A*, diagram of two subsystems before substructuring with internal and interface degrees of freedom (u) and interface forces (g), and *B*, the substructured assembly from the two subsystems with internal and interface degrees of freedom (u).

For this section, external forces are denoted as f and internal forces are denoted as g. B is a signed Boolean matrix to fulfill the compatibility constraint, and L is an unsigned Boolean matrix to fulfill the interface equilibrium condition. u is displacement in these derivations

but can also be velocity or acceleration in frequency-based substructuring. A subscript on u indicates the subsystem (A, B, or interface (I)) and a superscript indicates the DOFs. This notation is used for physical and frequency domain substructuring. Different notation is used in modal substructuring. Two excellent references on substructuring are [4] and [5].

There are two constraints that must be met in substructuring:

1. Compatibility condition: the interface DOFs to be connected have the same displacement and infinite stiffness (solid connection)
    a. $u_I^a = u_I^b$
    b. $Bu = 0$
2. Force equilibrium: the internal forces must be equal and opposite
    a. $g_I^a + g_I^b = 0$
    b. $L^T g = 0$

There are two methods of meeting these constraints:

1. Primal assembly: eliminates the internal DOFs from the problem. The problem is solved with a new set of DOFs [q] and a single Boolean matrix.
2. Dual assembly: all DOFs are retained in the problem, so some in the substructured assembly are redundant. The internal forces are represented by LaGrange multipliers and are not directly solved for.

To add spring to the interface (and make the coupling less stiff), the K matrix of the physical domain can be directly altered or the spring can be treated as an extra subsystem.

2.4.1 Physical domain

This method directly couples and modifies the M, C, and K matrices. The motion of the model is denoted as u, and can be displacement, velocity, or acceleration. $\underline{f}$ is the external force on the substructured assembly, and g is the interface internal force. M, C, and K are block-diagonal matrices, and u, f, and g are vectors.

$$M\ddot{u}(t) + C\dot{u}(t) + Ku(t) = f(t) + g(t)$$

The use of a signed Boolean matrix is used to constrain component DOFs together. This **first condition** states that the motion of DOF pairs is equivalent, and is expressed as the following:

$$Bu = 0$$

A **second condition** must be met, where the internal forces of the interface DOFs must be equal and opposite. L is an unsigned Boolean matrix indicating the interface DOFS. This is expressed as the following:

$$L^T g = 0$$

This substructured assembly EOM and two assembly conditions are used as the basis of physical domain substructuring. These equations are applied in two different ways: primal assembly and dual assembly.

Primal assembly eliminates interface internal forces from the problem. This method is often used with information obtained from finite element models. In primal assembly, a new set of DOFS (q) is used. Only one Boolean matrix is needed for this method.

$$u = Lq$$

The substructured assembly can be expressed as a function of q instead of u:

$$ML\ddot{q} + CL\dot{q} + KLq = f + g$$

$$L^T g = 0$$

$$\tilde{M}\ddot{q} + \tilde{C}\dot{q} + \tilde{K}q = \tilde{f}$$

Dual assembly retains all DOFs throughout the problem. The interface forces are expressed as a function of LaGrange Multipliers:

$$g = -B^T\lambda$$

The negative sign in front of the Boolean matrix indicates the interface forces act in the opposite direction as the degree of freedom. L^T is always the nullspace of B^T, therefore the compatibility and equilibrium conditions are always simultaneously met. Dual assembly is expressed in the block-diagonal format as:

$$\begin{bmatrix} M & 0 \\ 0 & 0 \end{bmatrix}\begin{bmatrix} \ddot{u} \\ \lambda \end{bmatrix} + \begin{bmatrix} C & 0 \\ 0 & 0 \end{bmatrix}\begin{bmatrix} \dot{u} \\ \lambda \end{bmatrix} + \begin{bmatrix} K & B \\ B^T & 0 \end{bmatrix}\begin{bmatrix} u \\ \lambda \end{bmatrix} = \begin{bmatrix} f \\ 0 \end{bmatrix}$$

2.4.2 Frequency domain

The same equations that describe the physical domain can also be expressed in the frequency domain by applying the Fourier transform to the time-dependent substructured assembly EOM:

$$Z(\omega)u(\omega) = f(\omega) + g(\omega) = F(\omega)$$

Where Z is the dynamic stiffness (or equivalent) matrix (F/U)

$$Z(\omega) = -\omega^2 M + j\omega C + K$$

Primal assembly is expressed as:

$$\tilde{Z}q = \tilde{F}$$

And **dual assembly** is expressed as:

$$\begin{bmatrix} Z & B^T \\ B & 0 \end{bmatrix}\begin{bmatrix} u \\ \lambda \end{bmatrix} = \begin{bmatrix} F \\ 0 \end{bmatrix}$$

And can be reformulated to a direct expression that uses frequency response functions from measured data:

$$u = HF - HB^T(BHB^T)^{-1}BHF$$

$$\widehat{H} = H - HB^T(BHB^T)^{-1}BH$$

Where $H = \frac{1}{Z}$

Practically, measured frequency response functions from accelerometers are used, making H an *accelerance* frequency response function - acceleration over force (A/F). This method is commonly known as **LaGrange-Multiplier Frequency Based Substructuring (LM-FBS)** and is implemented, both experimentally and analytically, in this thesis. A full derivation can be found in Appendix A.

Another frequency domain method is commonly referred to as Impedance-Based FBS. The equations are the same as LM-FBS but do not use Boolean mapping matrices. This was the first frequency based substructuring method proposed by Jetmundsen [6]. The notation explicitly connects components A and B through interface DOFs I.

$$[H]^{ab} = \begin{bmatrix} {H_{AA}}^a & {H_{AI}}^a & 0 \\ {H_{IA}}^a & {H_{II}}^a & 0 \\ 0 & 0 & {H_{BB}}^b \end{bmatrix} - \begin{bmatrix} {H_{AI}}^a \\ {H_{II}}^a \\ -{H_{BI}}^b \end{bmatrix} ({H_{II}}^a + {H_{II}}^b)^{-1} [{H_{AI}}^a \quad {H_{II}}^a \quad -{H_{BI}}^b]$$

This method produces the same results as LM-FBS, but the bookkeeping is much more difficult. LM-FBS was selected for its use of Boolean mapping matrices, which are simple to implement in an iterative optimization scheme.

There is another formulation of FBS that stems from the theory of transfer path analysis (TPA). The substructuring equations are developed for each path, but the global response DOF does not require an FRF formulation [7]. This method allows FBS to interfaces where measuring an input force or displacement/velocity/acceleration (u) is not possible.

$$\hat{u}_A^a = H_{AI}^a (H_{II}^a + H_{II}^b)^{-1} u_I^b$$

Part of the FBS formulation is referred to as the kernel. This part of the calculation determines the dynamics of the substructured assembly; where the mass and stiffness lines cross in the kernel sum become the substructured assembly resonances after inversion. The

conditioning of the kernel is important to keep track of to ensure accurate and stable calculations of assembly FRFs. Both FBS methods reduce to the same kernel.

LM-FBS Kernel: (BHB^T)

Impedance-Based and TPA-Based FBS Kernel: $({H_{II}}^a + {H_{II}}^b)$

2.4.3 Modal domain

Another common substructuring method uses the modal domain and coupled mode shapes. The component mass and stiffness matrices are brought into the modal domain, arranged in block diagonal form, and physically coupled by adding stiffness to the interface DOFs. The eigenvalue problem is solved for the new coupled system and provides the new substructured assembly natural frequencies (λ_c) and mapping mode shapes (U_{uc}). The mapping mode shapes are used to transform the uncoupled system mode shapes (U_u) to the substructured assembly mode shapes (U_c).

$$[I]\{q\} + \left[[{\omega_n}^2] + [\Phi^T][\Delta K][\Phi]\right]\{q\} = \{0\}$$

$$[\Phi_C] = [\Phi_u][\Phi_{uc}]$$

A common issue with modal substructuring is being able to obtain enough modes to successfully describe the coupled system. Errors are introduced with modal truncation: the out-of-band modes may be critical for the substructured assembly results but are not accounted for. Often, this method is paired with multiple methods of model reduction to account for the out-of-band modes [7].

Component mode synthesis (CMS) is a substructuring technique performed in the modal domain, following both primal and dual assembly formulation as previously mentioned. The dual assembly formulation of CMS is more commonly known as the Craig-Bampton method [4], which implements some allowance within the compatibility constraint. CMS is often used as a finite element model reduction technique.

2.5 Testing

Frequency response functions are collected experimentally by applying a force and measuring the system response. If the input force is an impulse from an impact hammer, the system free-vibration response is measured. The impact hammer is outfitted with a load cell to measure the input force. Most often, accelerometers are used to measure the system response. Therefore, the test frequency response functions are *accelerance*, or acceleration over force (A/F).

2.5.1 Sampling theory

When performing a test, sampling parameters must be set. These parameters include frequency resolution (Δf), time resolution (Δt), the maximum frequency of interest (f_{max}), block size (N), and length of acquisition (T). By picking two of these parameters, the rest is solved for using the list of equations below [2]:

$$\Delta t = \frac{1}{2f_{max}} = \frac{T}{N} \qquad f_{max} = \frac{1}{2\Delta t} = \frac{N\Delta f}{2}$$

$$\Delta f = \frac{1}{T} = \frac{1}{N\Delta t} \qquad \mathrm{T} = \frac{1}{\Delta f} = N\Delta t$$

The sample rate (Fs) is related to the maximum frequency of interest through Shannon's sampling theorem:

$$Fs > 2f_{max}$$

However, most acquisition systems use a scale factor greater than 2.

2.5.2 Frequency response calculations

There are different methods of calculating frequency response functions from a test (Figure 2.4). Each estimation method requires an assumption about noise in the system and whether it's assumed to be in the input, output, or both [8].

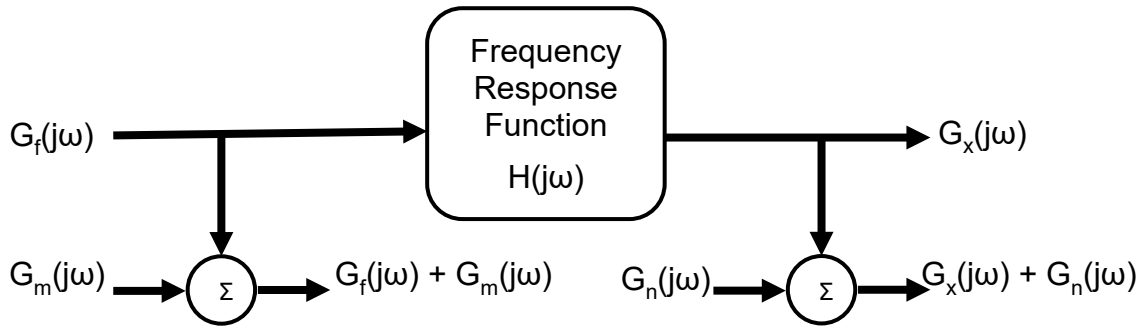

Figure 2.4 Bivariate frequency response function model including a force input (f), noise on the input (m), the response (x), and noise on the response (n).

In the figure above, *G* represents the single-sided complex linear spectrum of time domain signal using the Fourier transform. The input signal has subscript *f* and noise subscript *m*. The output signal has subscript *x* and noise subscript *n*. The independent variable ω has been omitted from the equations below.

The linear spectrum multiplied by its complex conjugate results in an autopower spectrum, and a linear spectrum multiplied by the complex conjugate of a different DOF results in the crosspower spectrum. These spectras are magnitude only and contain no phase information.

Autopower: $G_{xx} = G_x G_x^*$

Crosspower: $G_{xf} = G_x G_f^*$

The H1 estimator assumes the noise is only on the output (G_m). This estimation is biased low.

$$H1 = \frac{G_{fx}}{G_{ff} + G_{mm}}$$

The H2 estimator assumes the noise is only on the input (G_n). This estimation is biased high.

$$H2 = \frac{G_{xx} + G_{nn}}{G_{xf}}$$

The Hv estimator assumes the noise is on both the input (G_m) and output (G_n). This estimation solves the eigenvalue problem at each spectral line and is computationally expensive. The FRF is the eigenvector of the smallest eigenvalue.

$$\begin{bmatrix} G_{xx} & G_{xf} \\ G_{fx} & G_{ff} \end{bmatrix} \begin{Bmatrix} -1 \\ H \end{Bmatrix} = -\varepsilon \begin{bmatrix} G_{nn} & 0 \\ 0 & G_{mm} \end{bmatrix} \begin{Bmatrix} -1 \\ H \end{Bmatrix}$$

Coherence is a function that represents how linear the output is to the input. Coherence is less than or equal to 1, where 1 means perfect linear correlation and 0 means no correlation. Low coherence could indicate unmeasured inputs, no response, leakage, or system nonlinearities. Coherence drops at system anti-resonances but should be high at resonances.

$$\gamma^2 = \frac{G_{fx} G_{xf}}{(G_{ff} + G_{mm})(G_{xx} + G_{nn})}$$

Often, the measured inputs and responses are averaged to reduce uncorrelated artifacts and reduce signal variance.

2.6 Shock response spectrum

The shock response spectrum (SRS) is conceptually similar to the Fourier series, except it is a one-way calculation; a time domain shock response can be represented by peak responses of SDOF oscillators [9]. The SRS takes in acceleration time data at the base and displays it as a response at each logarithmically-spaced natural frequency. This is essentially filtering the time domain response at specified frequencies and recording the maximum response at that frequency.

2.6.1 Single degree of freedom model

For an acceleration time response of a shock event, each frequency's response is calculated. The acceleration time response is the input to the base of this model (y) (Figure 2.5). The acceleration of each SDOF system (x) is solved for.

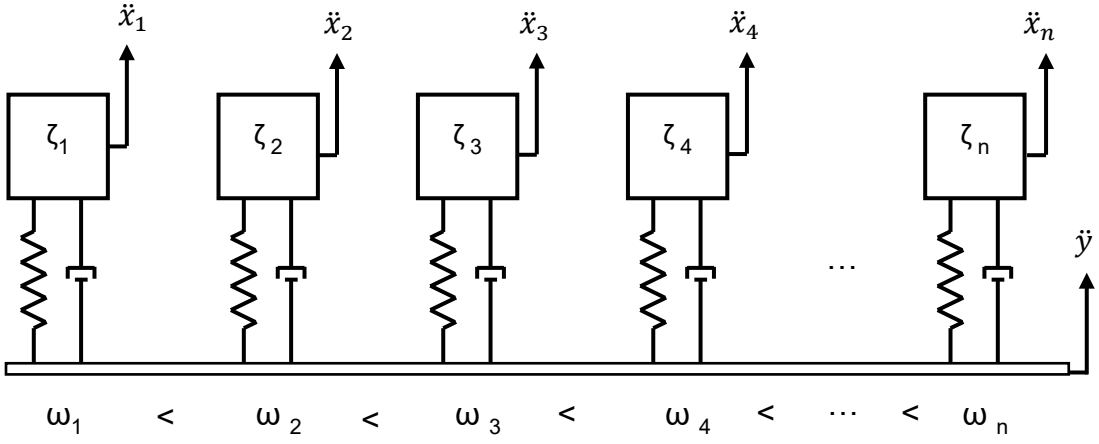

Figure 2.5. Single degree of freedom model used to develop the shock response spectrum equations using the base excitation (y) to calculate the response (x) of a set of logarithmically spaced single degree of freedom mass-spring-dampers, each with a different resonant frequency (ω) and generally the same damping ratio (ζ). Replicated from [10].

The equation of motion of the SDOF SRS model can be written as:

$$m\ddot{x}(t) + c(\dot{x}(t) - \dot{y}(t)) + k(x(t) - y(t)) = 0$$

Solving for the relative SDOF excitation:

$$z(t) = x(t) - y(t)$$

$$m\ddot{z}(t) + c\dot{z}(t) + kz(t) = -m\ddot{y}(t)$$

$$\ddot{z}(t) + \frac{c}{m}\dot{z}(t) + \frac{k}{m}z(t) = -\ddot{y}(t)$$

Simplifying in terms of natural frequency and damping:

$$\ddot{z}(t) + 2\zeta\omega_n\dot{z}(t) + {\omega_n}^2 z(t) = -\ddot{y}(t)$$

These equations can also be described in the LaPlace domain:

$$H(s) = \frac{X(s)_a}{Y(s)_a} = \frac{cs + k}{ms^2 + cs + k}$$

$$H(s) = \frac{X(s)_a}{Y(s)_a} = \frac{\frac{\omega_n s}{Q} + {\omega_n}^2}{s^2 + \frac{\omega_n s}{Q} + {\omega_n}^2}$$

The acceleration of each selected DOF (x) (1 through n) can be solved for using the DOF natural frequency (ω_n), damping ratio (ζ), and base excitation acceleration (y). A subscript of *a* means acceleration, *v* means velocity, and *x* means displacement. The above transfer function (response acceleration over base acceleration) is known as the maximum absolute acceleration SRS.

2.6.2 Implementation

The actual implementation of the SRS is through a second-order infinite impulse response filter. In the digital filter coefficients, *z* represents the independent variable of the Z transform. A complete list of filter coefficients for different SRS calculation methods can be found in standard ISO 18431-4 [11] [12, 13].

Continuous: $H(s) = \frac{-{\omega_n}^2 - 2\zeta\omega_n s}{s^2 + 2\zeta\omega_n s + {\omega_n}^2}$

Discrete: $H(z) = \frac{\beta_0 + \beta_1 z^{-1} + \beta_2 z^{-2}}{1 + \alpha_1 z^{-1} + \alpha_2 z^{-2}}$

A method to approximate these filter coefficients was developed by David Smallwood and is referred to as the Ramp Invariant Method. This allows the filter coefficients to be recursively calculated in the time domain.

For a maximax SRS curve, the filter coefficients are as follows (in ISO 18431-4):

$$\beta_0 = 1 - \frac{e^{-A}\sin(B)}{B}$$

$$\beta_1 = 2e^{-A}\frac{\sin(B)}{B - \cos(B)}$$

$$\beta_2 = e^{-2A} - \frac{e^{-A}\sin(B)}{B}$$

$$\alpha_1 = -2e^{-A}\cos(B)$$

$$\alpha_1 = e^{-2A}$$

Where:

$$A = \frac{\omega_n}{2QF_s}$$

$$B = \frac{\omega_n}{f_s}\sqrt{1 - \frac{1}{4Q^2}}$$

$$Q = \frac{\sqrt{km}}{c} = \frac{1}{2\zeta}$$

These filter coefficients change when the type of SRS calculation changes (maximax, pseudo-velocity, etc) because of the SDOF model equation of motion changes. The subscript denotes what data form to use (*a* for acceleration, *v* for velocity, and *x* for displacement).

The transfer functions in the LaPlace domain for other calculations are as follows:

Relative Velocity: $H(s) = \frac{X(s)_v - Y(s)_v}{Y(s)_a} = \frac{-ms}{ms^2+cs+k}$

Relative Displacement: $H(s) = \frac{X(s)_x - Y(s)_x}{Y(s)_a} = \frac{-m}{ms^2+cs+k}$

Pseudo Velocity: $H(s) = \frac{X(s)_x - Y(s)_x}{Y(s)_a}\omega_n = \frac{-m\omega_n}{ms^2+cs+k}$

Equivalent Static Acceleration: $H(s) = \frac{X(s)_x - Y(s)_x}{Y(s)_a}{\omega_n}^2 = \frac{-m{\omega_n}^2}{ms^2+cs+k}$

These other forms of the shock response spectrum can be found in chapter 3.2. This thesis uses Smallwood's original MATLAB code to implement the Ramp Invariant Method for *maximax* SRS calculations.

3 Literature

This chapter first describes a brief history of shock and shock testing methods. Then, more context is provided for the shock response spectrum. The topic shifts to pyroshock and resonant plate tests, shock data acquisition, and multi-axis shock tests. General issues with laboratory tests are covered and are applicable to both vibration and shock testing. The chapter concludes with substructuring terminology, issues, and solutions, especially focused on experimental frequency based substructuring.

3.1 Shock events and history

Pyroshock is a high-frequency, high-amplitude vibration event that often results in severe damage to electrical components. These events are prominent in live ordnance detonation, drop impacts or migration between stages in rocket flight. Pyroshock testing and quantification started as an interest in earthquake frequency content and damage potential. Maurice Biot, in his 1932 Ph.D. thesis, used undamped SDOF oscillators to quantify earthquake events and investigate damage potential to structures [14]. This concept was used to create the reed gauge, which is a physical implementation of Biot's SDOF oscillator model. Each reed is tuned to vibrate at a specific frequency. During a transient shock event, the reeds vibrate at their natural frequency and trace the amplitude on wax paper. This method decomposes the shock event into its individual frequency contributions [15]. Reed gages were often used on naval ships to quantify shock events [16]. This theory is still used to decompose and analyze shock events.

These events are simulated using three main shock profiles in the laboratory; classic shocks, oscillatory shocks, and complex shocks. There are five common classic shocks: haversine, half-sine, trapezoidal, initial-peak saw-tooth, and terminal-peak saw-tooth pulse [17]. Each of these pulses can be tuned by altering the amplitude and duration. Though these shocks appear different in the time domain, they produce similar shock responses. Classic shock pulses have a net velocity change.

Oscillatory shocks can be described by a decaying sinusoid with positive and negative transient events. These pulses have a low (often zero) net velocity change. Complex shocks can be described as a sum of two or more classic or oscillatory shock events. These complex shock pulses are like what the test component experiences in the service environment.

There are two parts to a shock event: the primary, and residual regions. The primary region of a shock event contains only information from the time history *during* the shock event. The residual region shows the response *after* the excitation has ended but the component is still responding [9].

Pyroshock events are a subset of shock events that produce high-frequency and high-stress with low-velocity change. Pyroshock events can be divided into near-, mid-, and far-field categories. Each division has acceleration and frequency limits defined by standards (Table 3.1). Often, far- and mid-field pyroshock events can be simulated by mechanical shock pulses. Near-field pyroshock events are replicated with live ordnance explosive events.

Table 3.1. Classification of Pyroshock Amplitude and Frequency Requirements

Standard	Region	Acceleration Amplitude (G)	Frequency Range (Hz)
NASA-STD-7003 A [18]	Far-field	< 1,000	< 10,000
	Mid-field	1,000 – 5,000	10,000 – 100,000
	Near-field	> 5,000	> 100,000
MIL-STD-810G Method 517 [19]	Far-field	< 1,000	< 3,000
	Mid-field	1,000 – 10,000	3,000 – 10,000
	Near-field	> 10,000	> 10,000

3.2 Shock response spectrum

The SRS is a calculation that allows comparison between two different shock events in terms of amplitude and frequency content. The SRS is calculated by using a model based upon Biot's Ph.D. thesis and the implementation of the reed gauge. The shock acceleration time history is applied to the base of this model (Y) and a response is calculated for each SDOF oscillator (X) at its natural frequency [10]. Formulas for the SRS calculations are found in chapter 2.6.

The absolute maximum, maximum positive, and maximum negative acceleration shock responses can be calculated. Theoretically, in a pure oscillatory shock response, the maximum positive and negative response curves are identical or meet a certain separation tolerance. Comparing the positive and negative spectras can be a good way to check laboratory shock tests for discrepancies. The maximum absolute response spectrum (*maximax*) contains both the primary and residual shock events and is defined in terms of the peak responses as a function of the systems natural frequency [9]. Figure 3.1 shows a sample shock in the time domain and as a maximax SRS with tolerance bands.

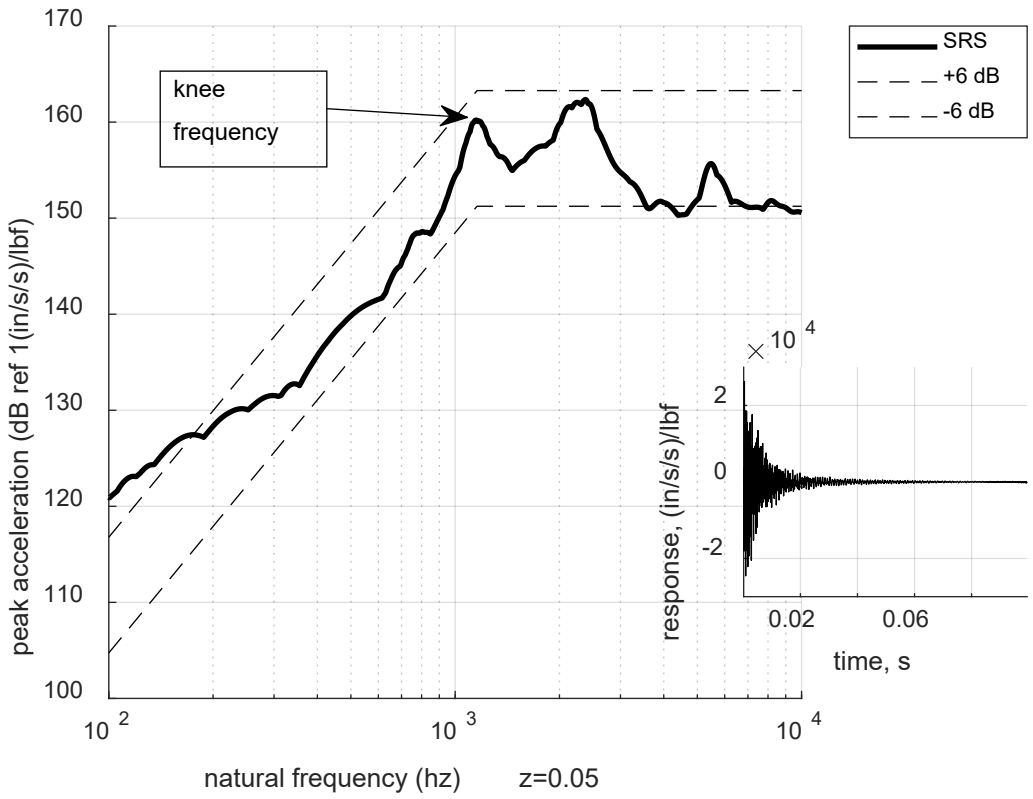

Figure 3.1 Sample shock represented in the time domain and shock response spectrum, calculated using a damping ratio of 5%, displayed with +/- 6 dB tolerance bands and an initial slope of 12 dB/octave. Replicated from [20] using experimental data collected for this thesis.

Each SRS plot follows a constant slope at the low frequencies up to the knee frequency. Depending on the type of shock event, this slope can be anywhere between 6 dB/octave (constant velocity) to 18 dB/octave. The first peak of the SRS is the knee frequency; all shock events have a knee frequency even if it's not evident in the SRS. The knee frequency is a property of the test environment, so laboratory fixtures are created to match field environment knee frequencies. The first bending mode of a resonant plate/bar/beam, and the drum mode of a circular plate, is the knee frequency on the SRS. The general SRS calculation parameters are a frequency resolution of at least 1/6th octave (1/12th maximum)

and a damping value of 5% (Q=10) [18]. This damping value can be altered to match estimated structure damping.

The shock response spectrum is a non-unique calculation, meaning that very different time histories can produce the same SRS. Even though the same SRS is produced, this does not mean the shocks are equally damaging. Other metrics are often used in conjunction with the SRS to quantify shock severity, such as modal velocity, pseudo-velocity (often plotted on tripartite paper), and band-limited temporal moments. Both modal velocity and pseudo-velocity are proportional to modal stress [21], which can be used as a damage metric and relate the shock event to strain energy. When pseudo-velocity is plotted on tripartite paper, it offers a condensed relationship between acceleration, velocity, displacement, and frequency. The first three to four temporal moments of the time domain shock pulse can be used to completely describe a shock event and are often used to reconstruct the shock for laboratory tests [22].

There are some advantages to the non-uniqueness of the SRS. Since a variety of shock events can produce the same SRS, this means different test methods can be used to meet the same qualifying SRS. The SRS is used to create a test specification from a shock event in the service environment. First, acceleration is recorded at the base of a component to capture the dynamics in the service environment. Then, an SRS is calculated from that service environment data (Figure 3.2). Tolerance bands are set around the service environment SRS and are now considered the laboratory test tolerances. Next, a shock test fixture is designed to meet the knee frequency and amplitude described by the tolerance bands. When the laboratory test is performed, the SRS must fall within the specified tolerance bands.

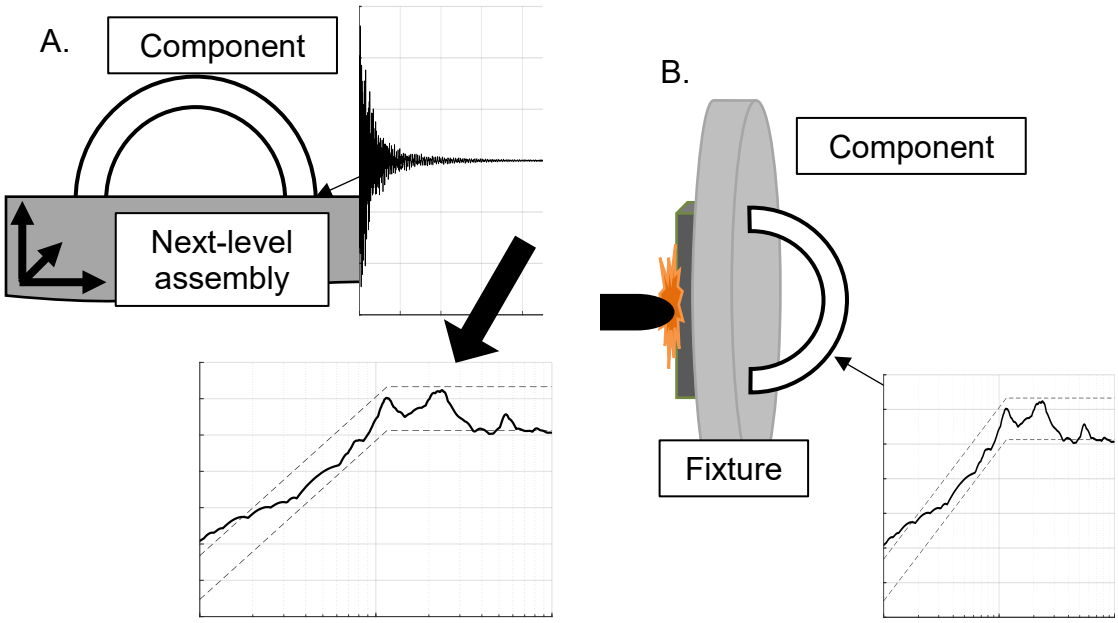

Figure 3.2 A, how service environment acceleration data is used to set laboratory test shock response spectrum tolerance bands, and B, how the test fixture is used to test the component and produce a shock response spectrum that falls within those tolerance bands

3.3 Pyroshock data acquisition

Pyroshock events occur over a short period of time (on the scale of milliseconds) and contain high frequencies and accelerations. Depending on the type of pyroshock (near-, mid-, or far-field), the required range of frequency and acceleration values change. There are many recommended practice documents for recording pyroshock data, but the most common and comprehensive is the MIL-STD-810G method 517. This standard outlines the basic requirements for proper shock test setup, instrumentation, acquisition, and SRS calculation.

In summary, the acquisition system needs to exhibit a high sample rate, large dynamic range, high signal-to-noise ratio (SNR), meet anti-alias filter (AAF) roll-off and attenuation requirements, and have a high slew rate. Most of these requirements can be determined directly from the specifications, excluding the slew rate. As it turns out, many different acquisition systems do not meet all these requirements simultaneously, but still, claim to

accurately collect pyroshock data. This often has to do with how the manufacturer's specifications are listed and how the acquisition system works [23].

Most modern acquisition systems have a sigma-delta (ΣΔ) analog to digital converter, which internally oversamples at a rate much higher than the specifications state. The analog signal first passes through an analog anti-aliasing filter (usually second-order) and has a cutoff frequency that reflects the high internal sample rate of the ADC. The alias-free analog signal goes into the ADC, where a single bit is used to detect changes in the input, digitally reconstructing the analog signal. The digitized waveform goes through a digital low pass filter with a cutoff frequency that reflects the user-defined sample frequency. Since the ADC oversampled the waveform, the digital alias-free signal is decimated to reflect the user-defined sample rate [8] (Figure 3.3).

Figure 3.3 Process of a sigma-delta data acquisition system recording an analog signal and storing a digitized signal.

The signal must pass through two low pass filters (LPFs) to protect the signal against aliasing for the two defined sample rates. The result is an alias-free bandwidth unless out-of-band energy folds back into the bandwidth of interest. This is a common occurrence in pyroshock data acquisition and is not always detected by the users. Anomalies caused by out-of-band energy can saturate the DAQ slew rate, causing clipping of the signal, which presents as zero-shift in acceleration or velocity data. To mitigate these concerns, a fast sample rate and overhead bins that prevent high-frequency content from contaminating the in-band data [24].

One way to see if pyroshock data has been contaminated by high-energy content is to look at the slew rate saturation of the acquisition system. Slew rate is the fastest rate of voltage change that can be detected by the acquisition system. The requirement listed in MIL-STD-

810G Method 517 states that the minimum slew rate value must be one-half full-scale voltage range in one microsecond. For example, a 20V peak-to-peak acquisition system must have a minimum slew rate of 10V/us. Manufacturer's specifications don't often include slew rate. If they do, it is the slew rate for the ADC chip, not the acquisition system. There is no standard calculation procedure for DAQ slew rate, but there are a few recommended methods. Bateman [25] uses a high-frequency sine wave to test the slew rate. Smith [24] uses a sine sweep across a large frequency range and identifies a "problem frequency" and calculates slew rate via the gain-bandwidth product (V*ω). Another method uses a low-frequency high-amplitude square wave.

$$V\_out = V * sin(\omega t)$$

$$Slew\ rate = {}^{dV_{out}}/_{dt} = V\omega * cos(\omega t)$$

The gain-bandwidth product is a constant, which means as frequency increases, available gain decreases. Slew rate saturation occurs when high-frequency high-amplitude signals exceed the gain-bandwidth product of the signal conditioner [26]. These slew rate calculations, combined with a slow sine sweep (100 Hz – 2 MHz) can reveal how well the DAQ attenuates high frequencies without contaminating the pyroshock data within the bandwidth of interest.

3.4 Pyroshock test methods

Shock test requirements are determined from service environment data and represented as a shock response spectrum. This becomes the laboratory test that a component is required to pass within a certain tolerance [5]. Different methods of laboratory shock testing are available based upon what dynamics the component experiences in the service environment. Pyroshock environments are difficult to replicate because the service environment can be destructive to sensors and acquisition equipment. For this reason, the pyroshock laboratory tests are not completely representative of the service environment, however, do offer safe data acquisition and are repeatable.

The common laboratory shock tests use shock machines, electrodynamic shakers, and resonant fixtures. Shock machines, originally developed and used by the Navy, replicate low-frequency shock environments and are not suitable for pyroshock testing [27]. Some electrodynamic shaker tests are limited by the force and acceleration capabilities of the shaker and may not be suitable for pyroshock tests.

Near-field pyroshock tests require pyrotechnic excitation (live ordinance), while mid- and far-field pyroshock test requirements can be met with mechanical excitation, like a metal-on-metal impact. Both excitation techniques commonly use a resonant fixture to test the component. A resonant fixture can be a plate, bar, or beam (Figure 3.4). The test component is mounted on one side of the fixture, while the excitation method impacts the other side (either live ordinance, air gun projectile, or drop hammer). This impact excites the first dominant mode of the resonant fixture, which is designed to be at the required SRS knee frequency [28].

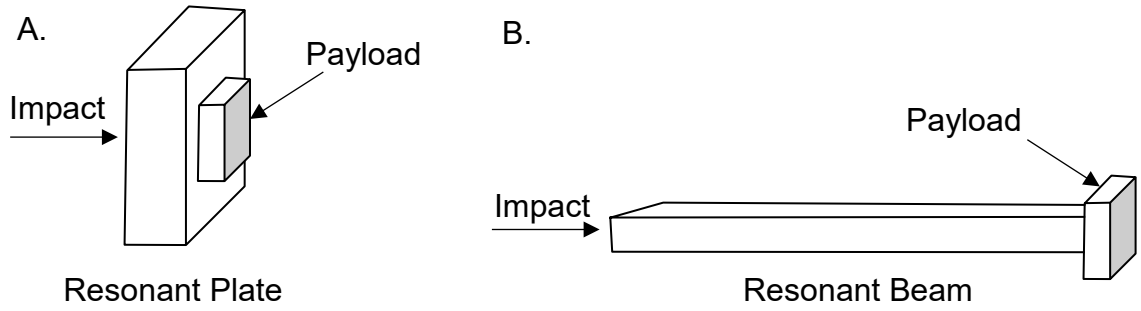

Figure 3.4 *A*, schematic of a resonant plate shock test and *B*, a resonant beam shock test. Replicated from [20].

The pyroshock test parameters can be tuned to meet different SRS requirements. A Mechanical Impulse PyroShock (MIPS) simulator is a resonant fixture assembly that allows repeatable alteration of test parameters such as impact material, location, mass, and response location. A MIPS simulator reflects “trial and error” methods in pyroshock testing. Different combinations are used to tune the component SRS to meet the

requirements. This process is well-documented, so the tests are repeatable once the test parameters have been determined.

The resonant fixtures are used in a similar way as the MIPS simulator: either the fixture is tuned to meet test requirements, or a new fixture is fabricated. The dynamics and test methods are the same, except the resonant plate is hung free-free while the MIPS simulator is set into a frame.

3.5 Resonant plate hardware and tests

The basic resonant plate design has not changed much since its first appearance in the mid-1980s. The traditional resonant plate is square or rectangular, is suspended using bungee cords or rope, and is impacted along the component mounting axis. Sandia National Laboratory used this resonant plate arrangement in 1986 [15] and is still in use [16].

The required knee frequency of the qualification SRS directly correlates to the first bending mode of the resonant plate. For example, if a component qualification SRS needed a knee frequency at 1500 Hz, the resonant plate material and dimensions would be selected to align the first bending mode to 1500 Hz. Note, that this is only for in-axis resonant plate testing! Low-frequency responses are controlled by the rigid body modes, the first bending mode controls the knee frequency peak, and a number of other modes participate in the plateau of the SRS [29]. The knee frequency of a square plate is the first bending mode, while the knee frequency of a circular plate is the first drum mode.

Michigan Technological University's original round plate design was the product of a Senior Capstone Design engineering team in December 2016. Their project, funded by Honeywell, was the start of MTU's resonant plate research. This resonant plate design was used in William Larsen's Master's thesis [30] and will continue to be used in this thesis. The round plate design was selected for its modal symmetry and minimal off-axis contribution when the payload is mounted at the center of the plate (Figure 3.5) [17]. There is no prior record of a round plate being used before this.

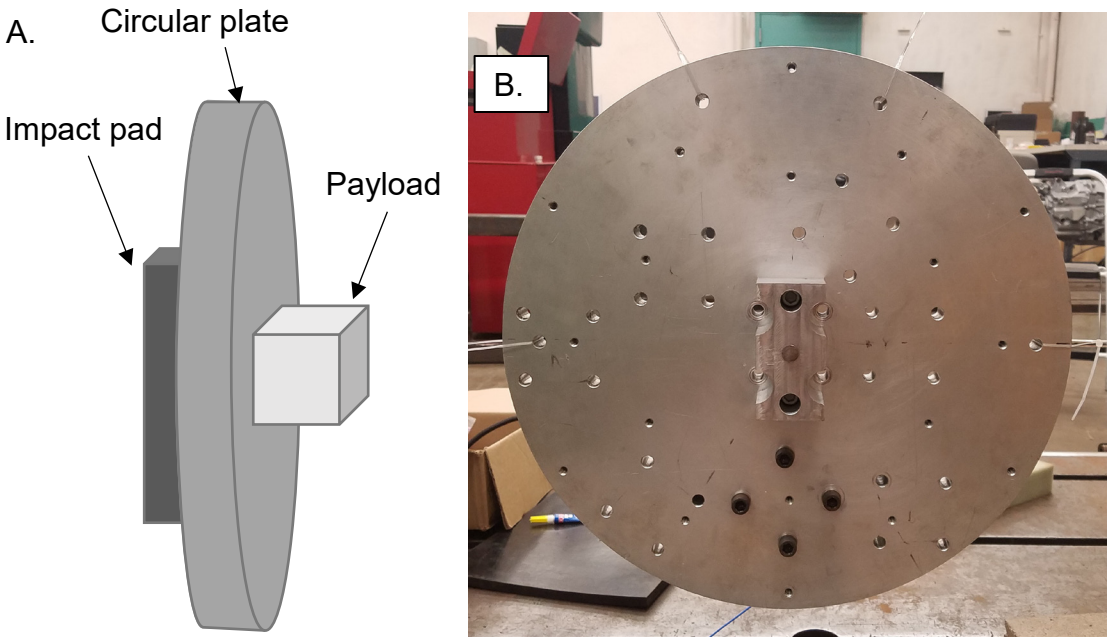

Figure 3.5 A, schematic of Michigan Tech's resonant plate assembly, and B, photo of the actual resonant plate assembly viewing the impact pad.

It is known that the first three modes' participation determines the shock response spectrum knee frequency [15]. However, there are few references using this information to "tune" the resulting SRS. In most pyroshock test cases, the optimal fixture location is determined through trial and error. With the increase in data storage and acquisition capabilities, full-scale modal tests are being performed on these resonant plate designs.

Aizawa and Avitable [18] used modal information from models to determine how each mode contributes to the shock response spectrum at different locations. Mass loading is investigated and used to further tune the required SRS. The relationship between modes and SRS is investigated in two ways: FRFs are superimposed on the resulting SRS, and new SRSs are derived from the modal information. This is performed for both model and test results. Although this method was performed on a resonant beam, it shows that information in the time, frequency, and modal domains can be used to tune a pyroshock resonant fixture test.

The resonant fixtures themselves can be altered to match the knee frequency in the required SRS. Mass can be added to nodes and ends on a resonant bar to shift the first longitudinal mode frequency. The fixed-fixed ends on a resonant beam can be moved to adjust the beam length and shift the first bending mode. This can be done in addition to altering test parameters in conjunction with MIPS simulators.

At Sandia National Laboratory, Spletzer, et al [31], investigated parameters of a resonant plate that can be used to tune the response SRS. Modifications were made to the newly-fabricated square plate analytically and experimentally. By adding damping material and clamps to the plate, the in-axis SRS was tuned to fit the required specification.

Los Alamos National Laboratory [32] performed similar experiments on a large shock plate. Both experimentally and analytically, the modal properties of the plate were investigated. Parameters were adjusted, such as boundary conditions (free-free, clamped), mass loading, and response location to tune the response SRS. The largest source for discrepancies was the damping estimates between the model and test.

3.6 Recent research on multi-axis pyroshock testing

Currently, the previous pyroshock test methods only account for one component axis at a time. To complete a multi-axis shock test, the component must be removed and re-oriented on the fixture for each required axis [14]. Not only is this method time consuming, but unmeasured off-axis responses exist within each single-axis test.

The response of a structure is a linear combination of all individual modes (chapter 2.3). For each combination of input and response locations, a new combination of modes is required to describe the motion. By expressing the acceleration response as a function of mode shapes, the modal contribution can be applied to multi-axis shock response spectrum calculations. Larsen, et al [29] used a finite element model of Michigan Tech's circular resonant plate to investigate the modal contribution of the off-axis response SRS. The in-axis response required only 5 modes to shape the entire SRS (knee frequency and initial

slope). The off-axis response required a larger number of modes, and different modes, to completely describe the SRS. Therefore, off-axis responses have different modes contributing to the shape of the SRS and the knee frequency.

Ferri and Hopkins [33] at Sandia National Laboratory used an air gun, projectile, and resonant structure to perform a series of multi-axis shock tests. The resonant structure was rectangular shaped with the impact location acting towards the edge of the structure. This excitation location creates off-axis moments, therefore creating an off-axis response. The four response locations were selected 90 degrees from each other, at random.

Hopkins and Sisemore [34] at Sandia National Laboratory analytically created a multi-axis shock test environment and experimentally verified the findings. They tested a square plate with three response locations (center and offset in each positive orthogonal direction) and two impact locations (center and off-center). The impact locations were determined by simulation. Calibration of the experimental setup (air gun pressure, projectile material, programming material) took much longer than for a single-axis test. It was noted that experimental multi-axis shock tests may require a higher impact force than single-axis tests. There was no description of how or why these three response locations were selected.

A critical observation in experimental multi-axis shock tests is that the criteria for evaluating shock data may have to change. One comment is that all three orthogonal axes might be in-phase, experiencing a higher shock, or out-of-phase, acting independently of one another. Using the single-axis evaluation criteria on a multi-axis test can be used for accepting multi-axis tests, but this must be investigated further before actual multi-axis tests are implemented for qualification.

There is currently no record of optimizing a multi-axis resonant plate test using modal contribution and fixture tuning. This work attempts to fill that gap by focusing on optimization via frequency based substructuring.

3.7 Dynamic testing limitations

An issue with laboratory testing is that the dynamics created in the laboratory do not match the dynamics in the service environment (Figure 3.6). Attempts to answer the question of "how do we make these environments match?" have been made for years and are still being investigated. Previously, the focus was on matching impedance between laboratory test and service environment by implementing a very stiff fixture. Now, with access to more modeling and testing capabilities, the discrepancies between the test and environment, and the interaction between the test fixture and component are being investigated in more detail. Different methods are being used to analyze fixture-component dynamics and determine how to equate the test and environment.

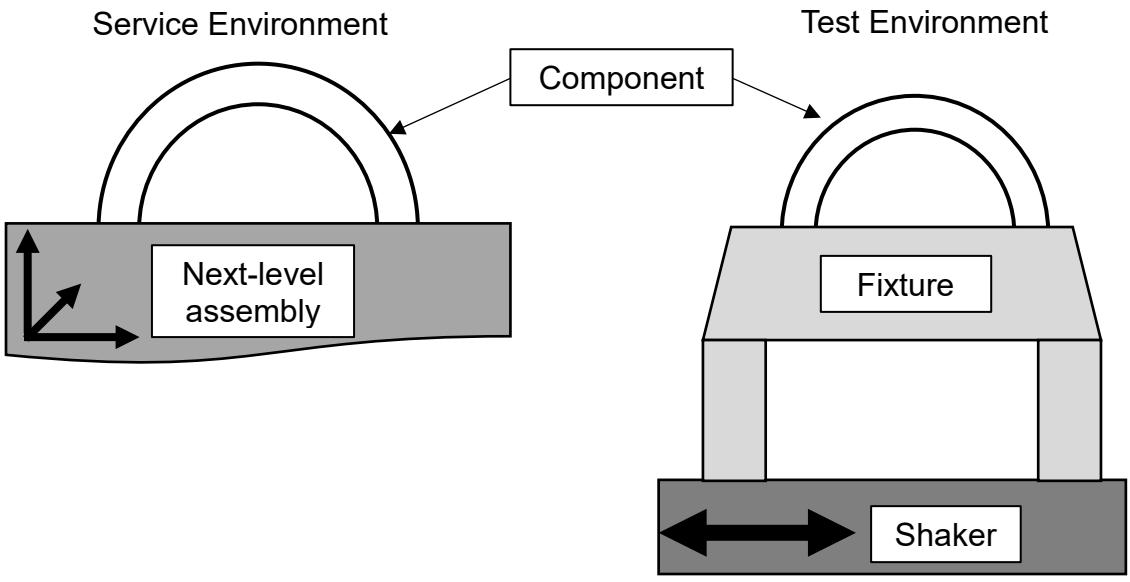

Figure 3.6 Schematic showing a component in the service environment attached to the next-level assembly, and the component in the test environment attached to a fixture on a shaker.

An overtest occurs when the dynamics in the lab exceed the service environment specifications. The opposite is known as an undertest. Overtesting is expensive and may fail devices that would otherwise survive the service environment. Undertests are dangerous and may result in a device passing that may otherwise fail in the service

environment. Over/undertesting is quantified by measuring the impedance of the lab test and comparing it to the service environment.

There are multiple test methods that attempt to correct this impedance mismatch and risk of over/under testing. However, there are physical limitations in the test hardware as to the maximum force that can be put into the test component. The method of infinite impedance testing attempts to match the acceleration profile of the service environment, regardless of the required force. This method also makes assumptions that neglect the component-fixture dynamics in the test environment [23]; the component-fixture assembly, theoretically, has infinite mass.

This mismatch can be addressed by multiple techniques that change the test input, such as force-limited vibration (FLV), dual-external control, force-acceleration product, and impedance-match multi-axis testing (IMMAT). FLV testing alters the test input impedance to reduce component response at fixture resonance, creating a "dynamic absorber effect" [24]. Dual-external control follows the input test envelopes for both acceleration and forces simultaneously, ensuring the test inputs never exceed both envelopes. Force-acceleration product method follows the envelope of the product of force and acceleration, where the level of peak force and acceleration are controlled at specific frequencies [23].

IMMAT better represents the proper service environment by using an array of small shakers implemented with multiple-input multiple-output (MIMO) control. The impedance of the service environment is considered in the test envelope, which, similar to dual-external control, ensures that the component response does not exceed the envelope. All directions are tested simultaneously. IMMAT is most often used in small modal tests but can be scaled to larger tests [25].

Another option is to use a shaker capable of testing more than one DOF at a time. Large 6-DOF shakers offer to control the translation and rotation input into the component. However, these shakers are limited in frequency and displacement capabilities [35]. These

methods are not appropriate for pyroshock testing because electrodynamic shakers do not meet the input frequency and amplitude requirements for an acceptable pyroshock test.

A development in understanding this interaction is through the use of substructuring. Since the mechanical impedance changes between different levels of assembly of the component test environment, the forces seen by the test component are not the same [36]. The input to the test environment can be altered to match the response of the component in the service environment, taking the component-fixture dynamics into account by decoupling the response. There are different substructuring methods and domains which can uncouple the response of the component and fixture.

Modal substructuring can be used to separate the modes of the test fixture and the component [37]. By comparing the component modal response in the service environment, to the component modal response in the laboratory, it can be decided if the test fixture imparts comparable strain in the laboratory. Furthermore, modal substructuring and decomposition can be used during the fixture design process to ensure comparable component modes between the service and laboratory tests. Modal truncation is a concern when utilizing modal substructuring. By projecting the laboratory test mode shapes onto the service environment mode shapes, a metric can describe how well the dynamics align at each independent DOF [38].

Another compensation method, as demonstrated by Reyes [39], uses frequency based substructuring to account for the fixture-component dynamics. This method aims to reduce testing inconsistencies across different fixtures and facilities. Frequency based substructuring methodology is used to relate two different test fixtures from the uncoupled fixture and component FRFs. The result is a spectrum of the fixture that causes the same component response. An IFFT is performed on this spectrum and used as an acceleration input into the fixture, creating the same component response among two different fixtures.

There are other methods that can be applied to the boundary condition problem, such as modal projection and transfer path analysis. Modal projection matching is not a

substructuring technique, but a mapping technique to relate the component response in the laboratory and service environment in the modal domain [40]. The process is based upon component mode synthesis (CMS) and modal superposition, creating a modal "recipe" contained in a single mapping matrix. This mapping matrix is used to figure out which fixture modes have to be excited, and how much, to match the component modal response. Component-based transfer path analysis (TPA) can derive equivalent forces at the assembly interface, and other locations where it may not be possible to measure force, through the subcomponent dynamics [35]. These equivalent forces are independent of the fixture dynamics and can be used during the fixture design phase to check the component response.

The discrepancies between laboratory test and service environment vibration tests also appear in shock testing. A prevalent issue with shock testing is that the specifications require a test to fall within a tolerance band on the shock response spectrum. The SRS is a one-way calculation, which means different tests can produce the same SRS, meaning different component dynamics can still qualify as a "pass". The question of "are these test dynamics the same" must also be asked of current shock test methods.

3.8 Frequency based substructuring

Frequency based substructuring (FBS) is a method that uses dynamics (FRFs) from individual subsystems to calculate fully-assembled dynamics. This eliminates the need for performing full-structure modal tests to obtain the necessary full structure dynamics. This method is often used in the automotive industry because it is difficult, costly, and time-consuming to perform modal analysis tests on a full vehicle. The vehicle's assembled structure dynamics can be obtained by performing modal tests on the subassemblies and performing FBS to create full system dynamics. Other applications of FBS are used during the design and assembly process. Periodically through the design process, full system dynamics are analyzed for potential problems *before* the design is finalized, especially in modular systems [41]. FBS can also be used for troubleshooting vibration issues and

investigating new solutions [42], like adding tuned mass-dampers to move a resonant frequency out of operating range.

There are different methods of implementing FBS, but all perform the same basic FRF-coupling process [43]. Frequency based substructuring has two methods to meet the basic EOM constraints. These constraints are the compatibility constraint (the DOFs being attached have the same displacement) and the force equilibrium constraint (interface forces are equal and opposite). The first method is called primal assembly and explicitly creates a new DOF set to eliminate the calculation of the interface forces. This is how finite element models are assembled [4]. The second method is called dual assembly and sets the interface forces equal to LaGrange multipliers. This method keeps all DOFs, meaning that some of them are redundant. However, this method can be rearranged to use measured FRFs without inverting the entire global impedance matrix. This method is ideal for working with experimental FRFs. This second method is known as LaGrange-Multiplier FBS.

The main difference between traditional and LM-FBS is the notation. Traditional FBS explicitly assembles together subsystems, which can be helpful at seeing what dynamics are contributing to the assembly dynamics. It is also easy to change the interface dynamics, for example, by adding a spring to the kernel. LM-FBS uses Boolean matrices to keep track of which DOFs to pair together. Though this is great for iteration, it's more difficult to see what's contributing to the kernel. This thesis uses LM-FBS and the full formulation is available in Appendix A.

There are many inherent issues that come with the use of experimental data and the calculation process in FBS. These errors include propagation of measurement noise, matrix inversion, lack of including the rotational degrees of freedom, measurement truncation, and the inability to collect measurements at the interface locations [4].

In the calculation process, a matrix of measurement FRFs must be inverted. If this matrix is poorly conditioned or has excessive noise, small errors will expand and have catastrophic

consequences. Great care must be taken to reduce measurement noise and ensure well-conditioned matrices [44]. Often, singular-value decomposition is used to clean up the measured FRFs and artificially provide a well-conditioned matrix. Another "cleanup" method includes, but is not limited to, using synthesized FRFs from modal parameters [44].

To implement FBS experimentally, measurements must be collected at the interface DOFs. This is not always possible. A method called virtual point transformation uses a model of the component and modal data to extrapolate the component dynamics at the interface DOF. Higher-quality interface measurements can be collected using a laser Doppler vibrometer (LDV), which offers precise, non-contact measurements. Using an LDV with virtual point transformation yields very accurate assembly dynamics [45], especially at high and low frequencies.

Other modal expansion and coupling methods, such as SEREP or static and dynamic compensations, can be used to achieve well-conditioned FRFs at the interface DOFs [46]. Since there are no accurate ways to measure the rotational behavior of a test structure, expansion methods can also be used to estimate their responses [47]. However, the effects of modal truncation in both models and measurements must be considered if any of these methods are used.

The Transmission Simulator (TS) method is another tool to aid in the collection accurate interface DOF FRFs, experimentally and analytically. A transmission simulator is a simple structure that attaches to the subsystem interface DOFs. Measurements are made on the subsystem + TS assembly, and just the TS. The dynamics of the TS are subtracted from the subsystem + TS dynamics (Figure 3.7). The implementation of a TS addresses issues that elimination of rotary DOFs has on experimental FBS. It also allows more accurate mode shape estimation at the interface DOFs and faster data collection for a large number of interface DOFs [48]. This method is also used to perform FBS on subsystems across experimental and analytical data. A TS can also be used in the modal domain for component mode synthesis [49].

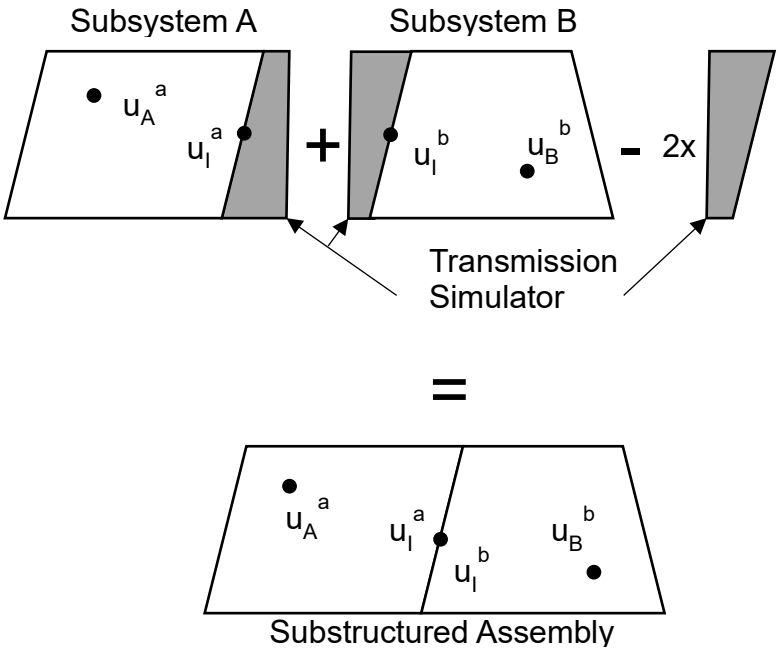

Figure 3.7 Schematic of how a transmission simulator is used in frequency based substructuring.

4 Analytical model

This chapter introduces the initial assumptions made for the model and tests. Then the finite element model, properties, and notation used for investigation of the LaGrange multiplier frequency based substructuring (Figure 4.1) calculations are discussed. Next is the notation of the finite element model and interface dynamics. Following is the discussion and investigation of determining the interface dynamics to include in the calculations. The chapter concludes by calculating the necessary frequency response functions for the iterative optimization scheme.

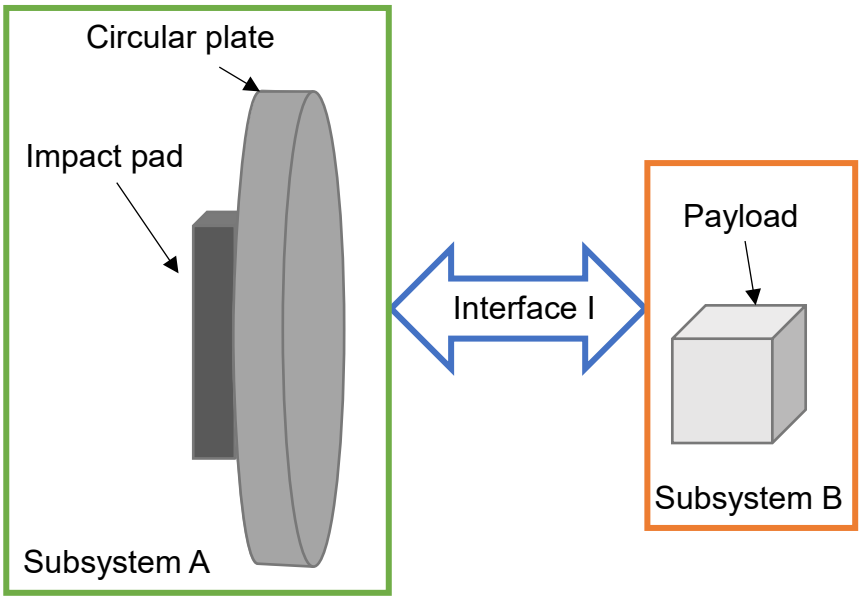

Figure 4.1 Schematic and components of Michigan Tech's resonant plate as defined for frequency based substructuring assembly

4.1 MATLAB simulation and assumptions

Analytical data was created in MATLAB before using experimental data. This way, the error propagation through the FBS calculations could be investigated and compared to a known solution. First, a simple mass-spring-damper system with one interface was investigated. Then, more DOFs and interface points were added. It was discovered that the condition number of the FBS kernel (BHB^T) increased at system resonances, aligning with

the results Voormeeren [50], et al, achieved. Even though the condition number increased, the substructured results matched the analytical truth data. However, when rotary DOFs were introduced to the problem but eliminated from FBS calculations, it was not possible to exactly match the truth data - even with Guyan reduction. After working through simple lumped-parameter models, assumptions were made about the data collection and calculation process for the project:

1. *Measurement noise is low*
2. *Ignoring rotary DOFS won't have a profound impact on FBS results*
3. *Modal truncation won't have a profound impact on FBS results*

These assumptions will be revisited in chapters 6.4 and 7.2.

4.2 HyperMesh finite element model

The resonant plate finite element model was initially developed by Will Larsen for his thesis. This model was created in HyperMesh Desktop 2017. Boundary conditions within the model replicate those in the laboratory – the circular plate is suspended by four loose springs at the top. The FEM consisted of three separate components and the support springs. The impact pad and payload (Figure 4.2) were modeled as solid aluminum with tet-10 elements, while the plate (Figure 4.3) was modeled as an aluminum shell using quad elements. Table 4.1 has more detail on the FEM properties.

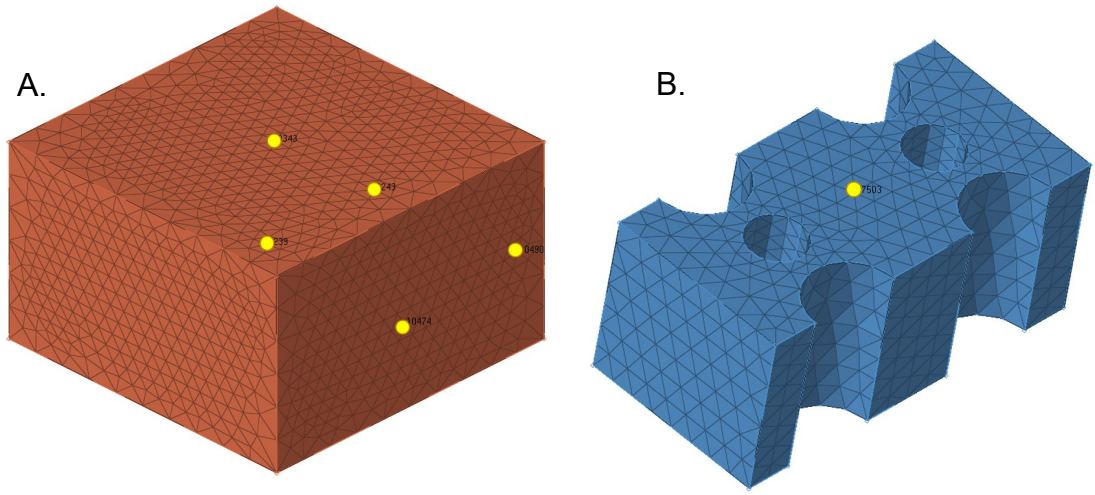

Figure 4.2 *A*, Payload finite element model component with five response nodes, and *B*, impact pad finite element model component with one input node.

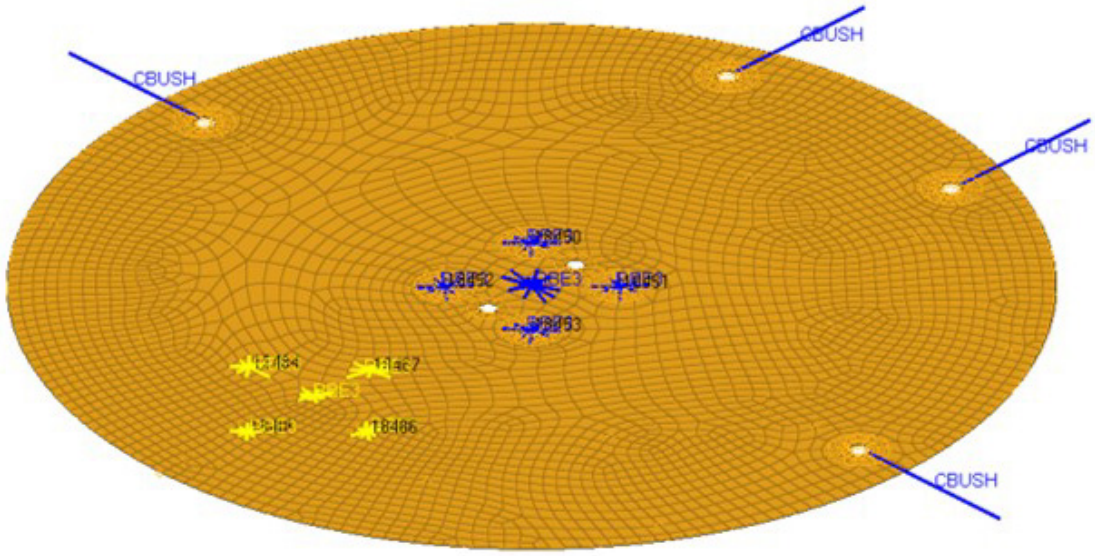

Figure 4.3 Circular plate finite element component with support springs and a subset of two interface node groups.

Table 4.1 Resonant plate HyperMesh finite element model properties.

Component	Card Image	Number of Elements	Property Card Image	Properties
Impact pad	CTETRA	5291	PSOLID	n/a
Plate	CQUAD4	3726	PSHELL	T = 1.125 in
Payload	CTETRA	41683	PSOLID	n/a
Springs	CBUSH	4	PBUSH	K1,2,3 = 200 lbf/in K4 = 100 lbf/in K5,6 = 0 lbf/in

The model has two contact surfaces; one between the plate and impact pad, and a second between the plate and payload. Each contact surface area was tuned to match the test case where the parts were bolted together (Figure 4.4). The contact surface card image was set to CONTACT with type FREEZE. The contact area on the plate consists of 3514 elements, the payload has 1156 elements, and the impact pad has 310 elements. If the impact pad or payload move, the closest contact surface pairing is automatically solved for.

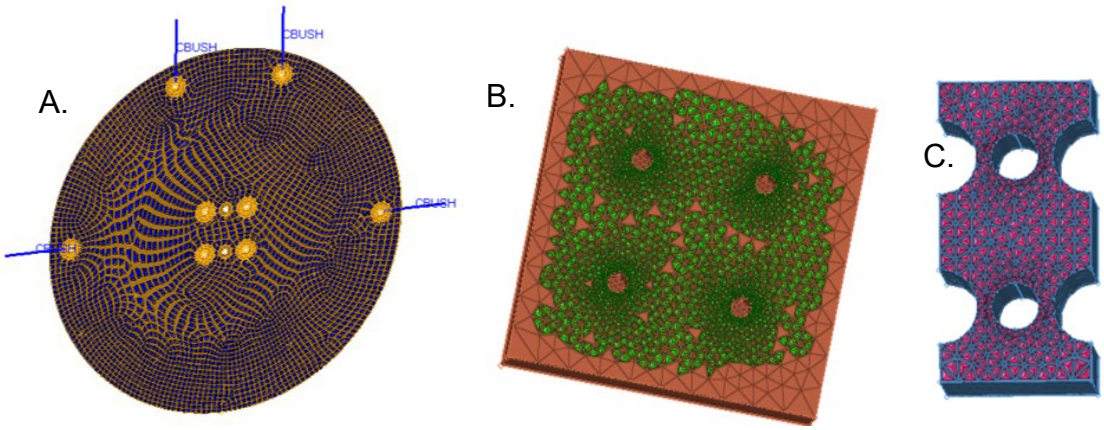

Figure 4.4 *A*, Contact surface on the circular plate finite element model, and *B*, contact surface patch on the payload finite element model, correlated with test data, and *C*, contact surface on the impact pad finite element model.

A second set of constraints were created to mimic the constraints that occur during LM-FBS calculations (Figure 4.5, Figure 4.6). Instead of using contact surfaces, which are much stiffer than the FBS results, direct rigid pairs of RBE2 elements tied together nodes that would be assembled in LM-FBS. These RBE2 elements were constrained in all 6 DOFs.

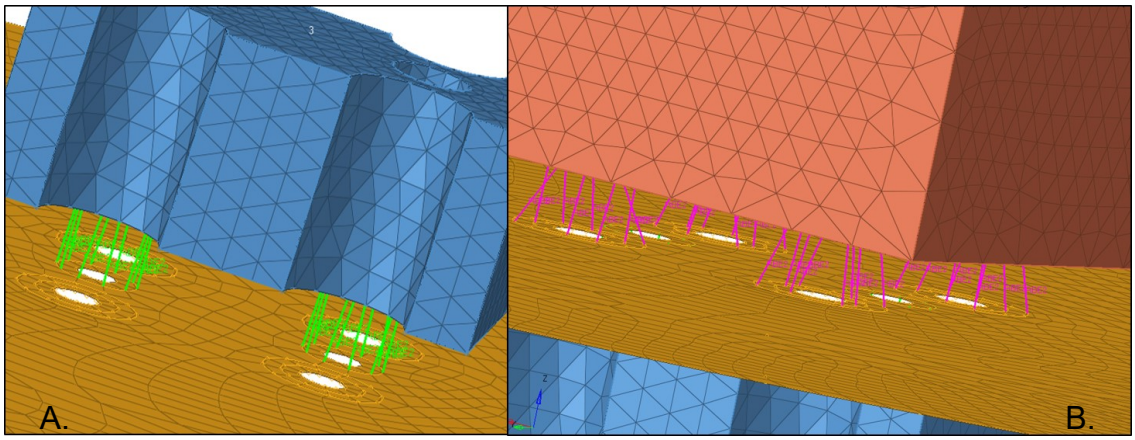

Figure 4.5 *A*, RBE2 elements connecting the impact pad to the circular plate to correlate with test data of circular plate + impact pad, and *B*, RBE2 elements connecting the payload to the circular plate to correlate with the mathematical assembly that occurs within the frequency based substructuring equations.

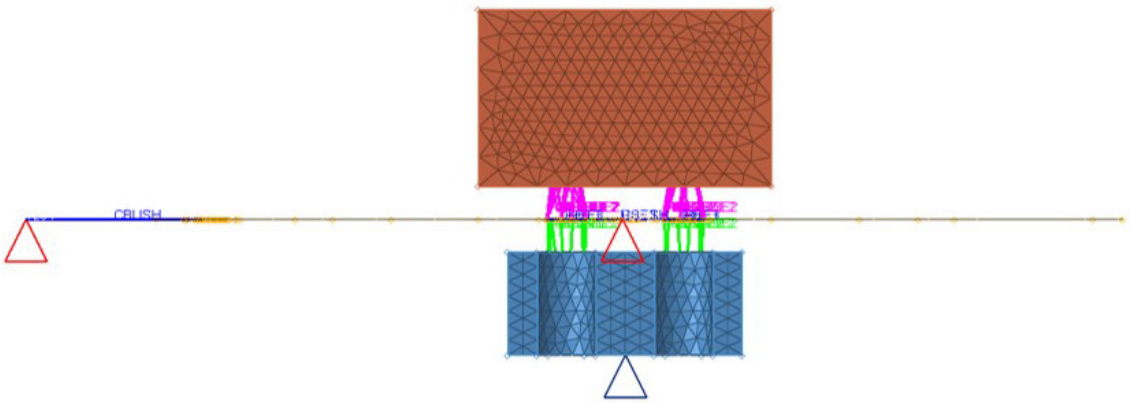

Figure 4.6 Full resonant plate finite element model assembly using the RBE2 elements between the circular plate and payload, and circular plate and impact pad.

Frequency response functions were collected from the full assembly (both RBE2 and contact surface conditions), the payload, and the circular plate + impact pad. The interface nodes between the plate and payload will be discussed further in chapter 4.4.

The FRFs were collected using a unit impulse frequency response function solver that used modal calculations. The frequency range was set from 100 Hz to 10 kHz. The eigenvalue solver method was set to *Lanczos*. A constant damping ratio of 0.5% was added to the entire model. OptiStruct was selected as the solver. The relationship between each DOF had to be solved for, meaning a full matrix must be filled. Each DOF was assigned as an input and output in the solver.

The desired input location on the resonant plate is at the center of the impact pad, in-axis (+Z). The selected response locations on the payload consist of five nodes, in all three orthogonal directions – three on the front face and two on the side. Practically, the payload response nodes can be selected to be anywhere. This subset was selected to reduce the complexity of the optimization. Figure 4.7 shows a schematic of LM-FBS on the resonant plate. Figure 4.8, Figure 4.9 shows the location of the desired input and response nodes used in the model and tests, however, all nodes were assigned as an input and output to fill the FRF matrix.

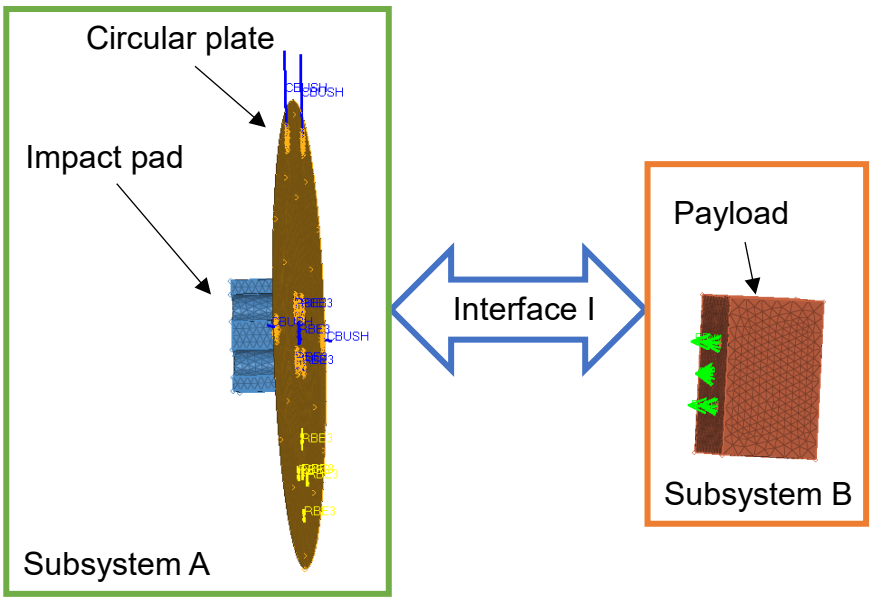

Figure 4.7 Schematic of subsystems and components of the resonant plate finite element model in the application of frequency based substructuring

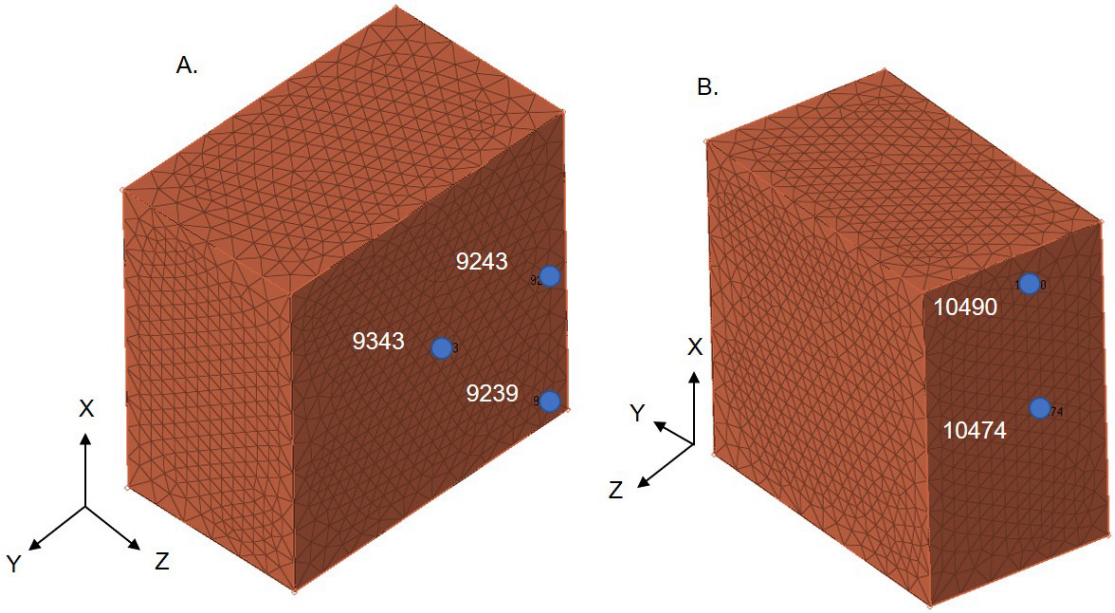

Figure 4.8 *A*, payload finite element model response nodes on the in-axis face, and *B*, payload finite element model response nodes on the off-axis face.

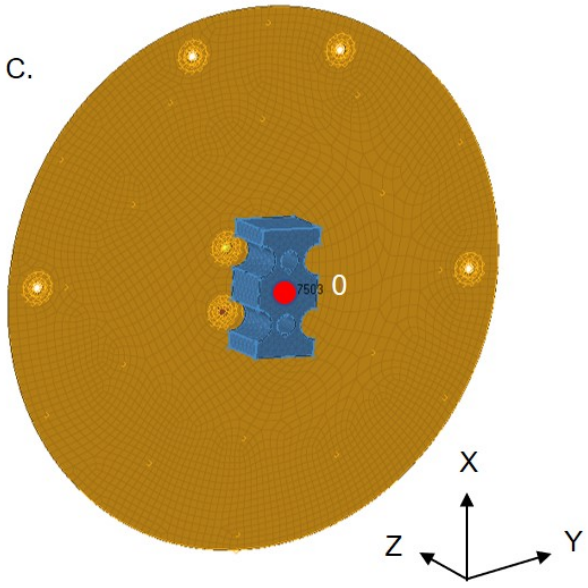

Figure 4.9 Circular plate + impact pad finite element model subsystem input node.

Below are figures comparing the FEM and physical plate assembly from the view of the impact pad (Figure 4.10).

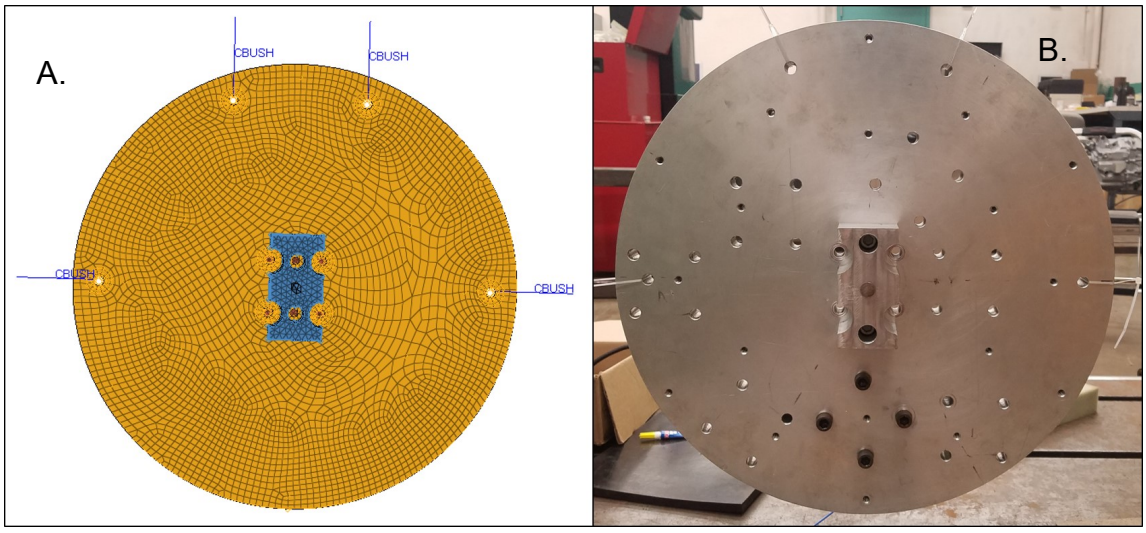

Figure 4.10 *A*, circular plate and impact pad finite element model, and *B*, circular plate and impact pad physical assembly.

4.3 Notation

There are four main groups of DOFs: the external DOFs on subsystem A (plate), the interface DOFs on subsystem A, the interface DOFs on subsystem B (payload), and the external DOFs on subsystem B (Figure 4.11). The substructured assembly contains all the DOFs present in the subsystems, meaning the interface DOFs are redundant calculations (Figure 4.12). The matrix of assembly FRFs is reduced so only the external DOFs are saved. Since the FEM of the payload is used for all substructuring, the node names remain the same as within the model. Table 4.2 goes over the subsystem, label, nodes, and DOFs that are used in LM-FBS equations for each configuration.

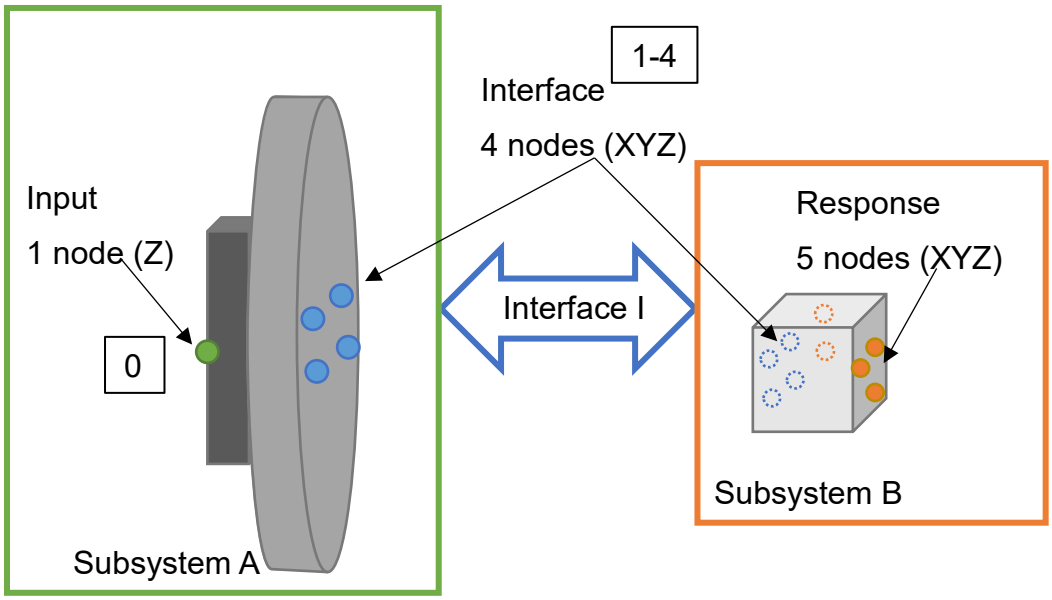

Figure 4.11 Resonant plate subsystems and nodes used in LM-FBS for any given configuration.

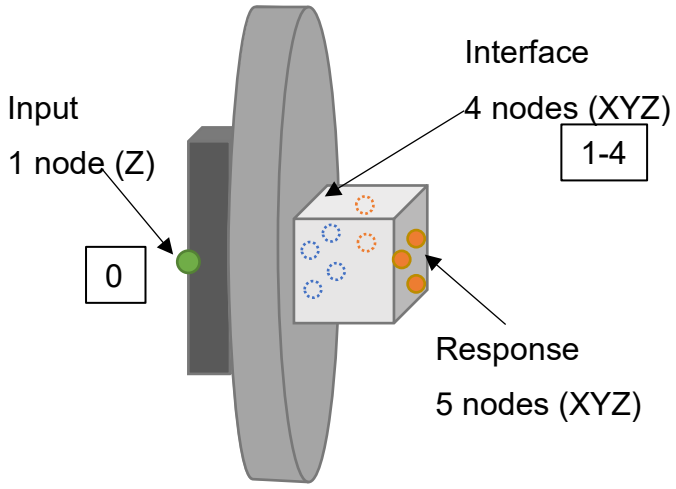

Figure 4.12 Resonant plate assembly and nodes produced from LM-FBS.

Table 4.2 Subsystems and their respective notation and matrix size for LaGrange Multiplier frequency based substructuring

Subsystem	Label	# of Nodes	DOFs per node	Names	Total DOFs
A (plate)	External	1	1	0:+Z	1
A (plate)	Internal	4	3	1:+X, … 4:+Z	12
B (payload)	Internal	4	3	1:+X, … 4:+Z	12
B (payload)	External	5	3	*Figure 4.8*	15
Assembly	External	1	1	0:+Z	1
		5	3	*Figure 4.8*	15

All LM-FBS calculations were performed in MATLAB R2018a. The FRFs were assembled in a block-diagonal matrix H. MATLAB's matrix computation ability was used

to solve 3-dimensional matrices (size *n* x *n* x *m*), where *n* corresponds to the total number of interface and response degrees of freedom and *m* corresponds to the number of spectral lines in the frequency response function measurements.

In the case of a single configuration, subsystem A has a 3D matrix *13 x 13 x 991* and subsystem B has *27 x 27 x 991*, for a full assembly of *40 x 40 x 991* that is reduced to *16 x 16 x 991*. These are the sizes of the model FRF matrices used for optimization. The test matrices have the same dimensions but have 8192 frequency lines instead of 991.

The impact pad is referred to as node 0. The interface nodes on both the plate and payload are referred to as nodes one through 4, where DOFs sharing the same label are paired together during LM-FBS. Notice that the plate and payload interface numbering are mirror images of each other (Figure 4.13) – this keeps the coordinate system the same between both subsystems. The payload response nodes are referred to by their FEM labels: 9243, 9343, 9239, 10474, and 10490 (Figure 4.8).

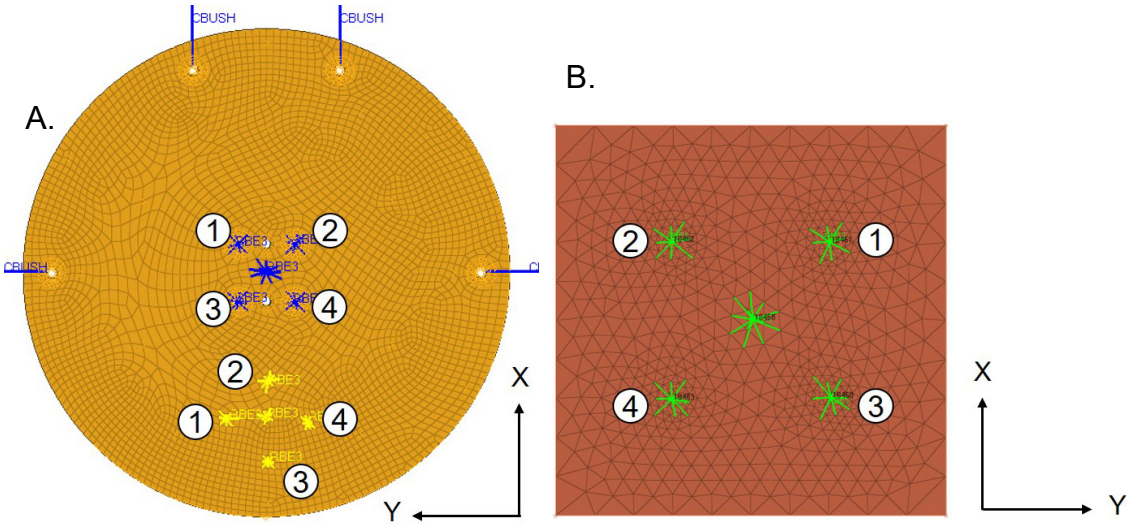

Figure 4.13 *A*, circular plate interface node orientation for 0-degree center configuration and 45-degree bottom configuration, and *B*, payload interface node labeling and orientation.

To invert the kernel, MATLAB's backslash command was used (x = A\B). This command solves a system of linear equations (Ax = B) and changes the computation algorithm

depending on the properties of the matrix. In this case, the matrix is square and is solved by LU factorization. The backslash command produces the same results as the pseudoinverse command (*pinv*) without any specified singular value decomposition tolerance.

4.4 Determining the interface dynamics

A small subset of possible payload locations was selected to identify the necessary interface conditions between the plate and payload to accurately reflect the assembly (truth). These positions were at the center, bottom, left, and corner of the plate with the payload at an orientation of 0 degrees and 45 degrees. A variety of interface conditions were solved for and compared to the truth assembly (contact surface FEM). These interface conditions explored how many nodes to pair, how to pair the nodes (direct or RBE3), and which directions (XYZ) to pair.

The focus of this thesis is to implement LM-FBS as a method of determining an appropriate assembly configuration for a multi-axis resonant plate shock test. That being said, the interface comparisons were done in the SRS domain, as opposed to the time, modal, or frequency domain. The finite element model is inherently stiffer than the actual assembly, so the focus was not on exactly matching modes but making sure the FBS knee frequency was at a similar amplitude to the truth data.

Using only one direction (Z) to capture the interface dynamics led to a poor off-axis response in the assembly. Directly pairing nodes can successfully define off-axis response, but many node pairs are required. Including a high number of node pairs (16, 32) with the three-axis response (XYZ) results in a high running and processing time (70 minutes). Figure 4.14 (below) demonstrates four different interface conditions – four or RBE3 groups using one (Z) or all (XYZ) DOFs. This is for response node 9243 of the corner configurations in the +X direction.

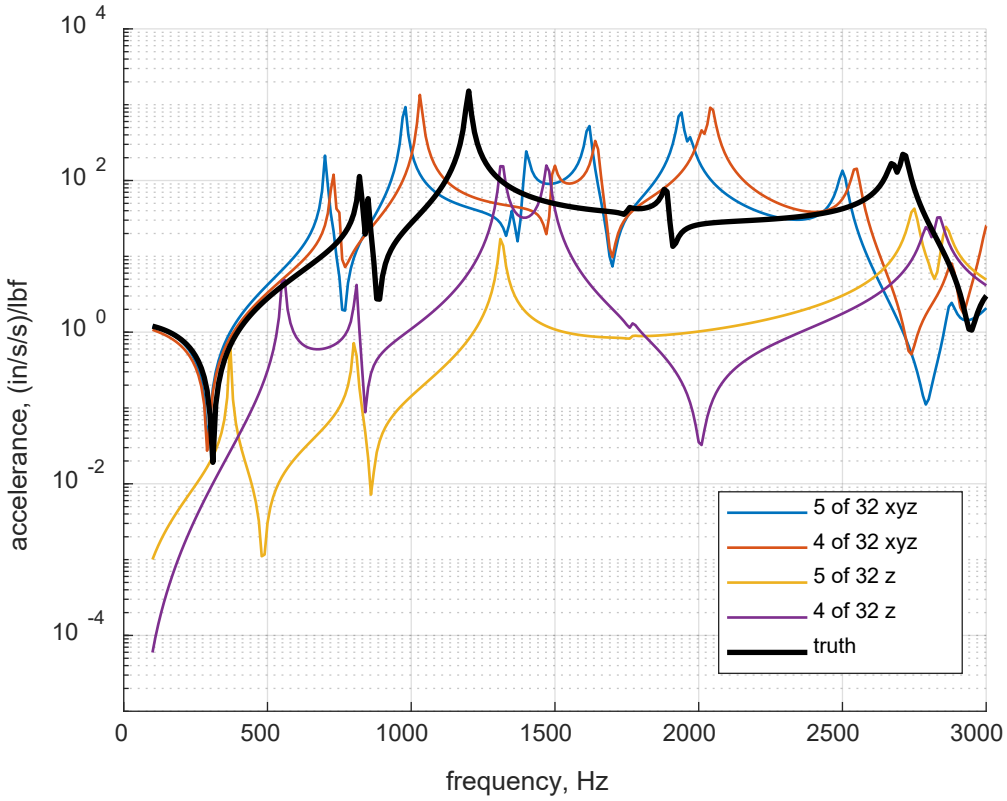

Figure 4.14 Multiple interface conditions for corner configuration, node 9243 +X, comparing using 4- or 5- sets of RBE3 groupings of 32 nodes, and comparing using only in-axis dynamics (z) or all-axis dynamics (xyz) in LM-FBS.

The selected interface method consisted of four RBE3 sets, one around each payload bolt hole (Figure 4.15). Approximately eight nodes per bolt hole were constrained together. All three translation DOFS of these nodes are necessary for constraining and transferring off-axis dynamics from the plate to the payload. This configuration is not an accurate representation of the contact surface on the truth assembly and was compared to the RBE2 truth assembly. The four-node RBE3 was selected for its simplicity, fast run time, and similarities to the laboratory testing environment.

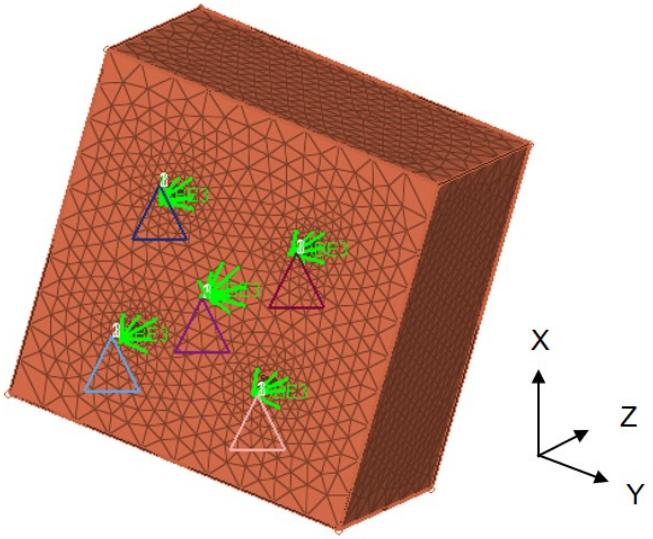

Figure 4.15 Five RBE3 elements on the interface nodes of the payload. Note that only four are used in the final interface decision (the four bolt holes, excluding the patch in the center).

4.5 Preparation for optimization

Due to the symmetrical mode shapes of the resonant plate (Appendix B), a small slice of 1/8 of the plate was identified as possible interface locations. A total of 22 locations were selected for optimization – 11 with the payload in its' original position and 11 with the payload rotated 45 degrees (Figure 4.16). The payload FRFs were collected twice, one for each payload rotation. Theoretically, a single set of payload FRFs could be used for all possible configurations as long as the proper coordinate transformation was applied to match that of the resonant plate (Figure 4.17).

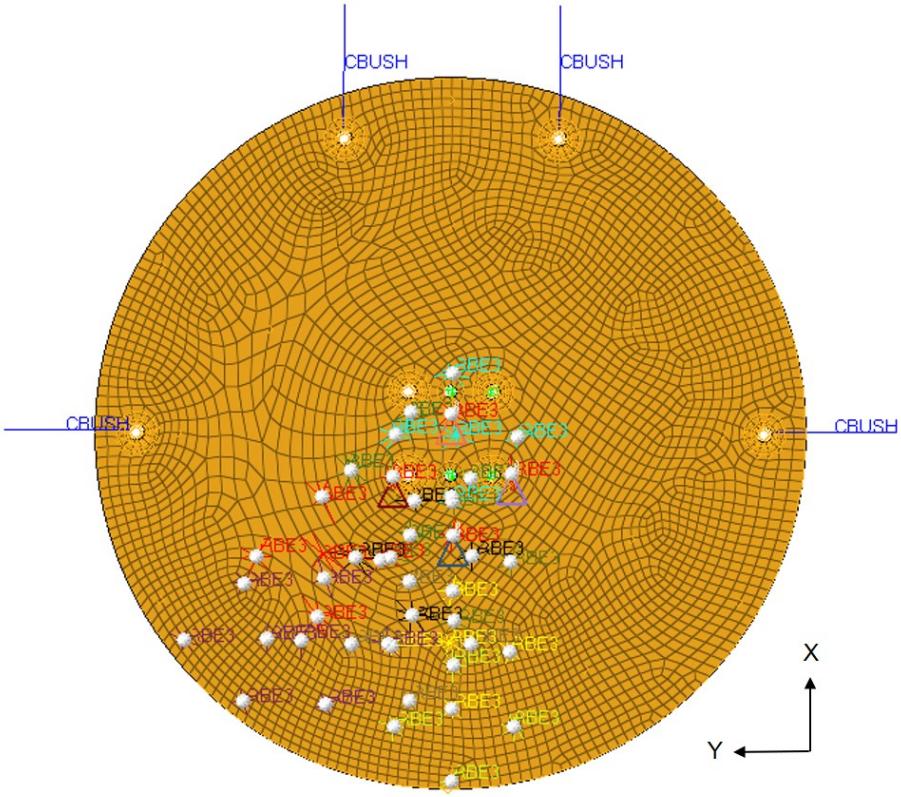

Figure 4.16 Circular plate finite element model with a subset of possible interface locations for the 45-degree oriented payload.

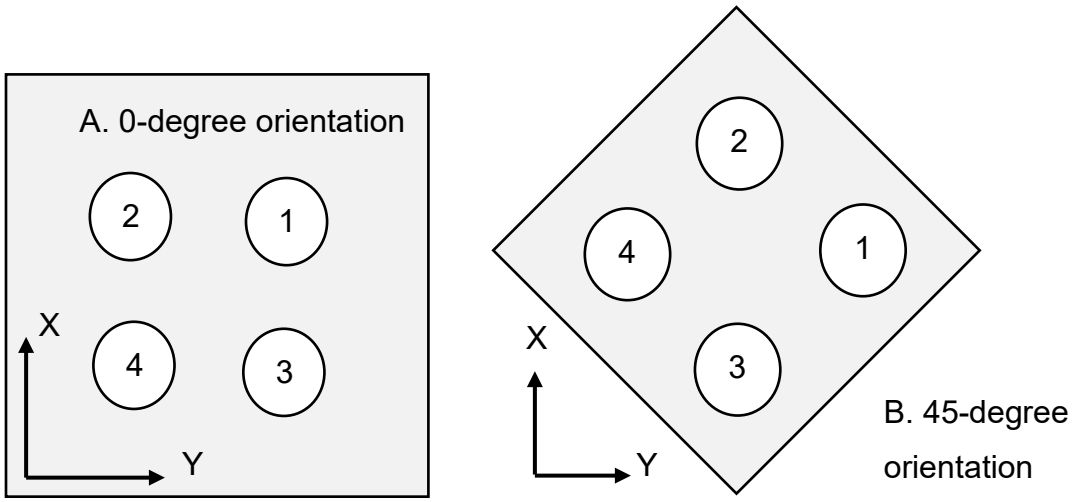

Figure 4.17 *A*, Payload interface location numbers for the 0-degree orientation and *B*, the 45-degree orientation.

Plate FRFs were collected using the RBE3 constraints at the four interface nodes and the center of the impact pad. The impact pad was constrained to the plate with rigid RBE2 elements to more accurately reflect the test data since the bolts were beginning to strip. Ideally, one giant matrix of all possible plate FRFs would be collected and used for optimization. Due to file size limitations, all 22 identified plate locations were considered and processed independently of one another. Each configuration has 5 response nodes, creating a total of 110 possible multi-axis shock test options.

5 Implementing LaGrange multiplier frequency based substructuring

This chapter first discusses how shock response spectras were calculated from the substructured assembly frequency response functions. Then the optimization method and objective functions are explained. The chapter concludes with a diagram of the optimization process and how this will be applied at test facilities.

5.1 Shock response spectrum calculation process

Time data is required to perform SRS calculations, and the result of LM-FBS is in the frequency domain. Several steps were taken to create shock response data out of the assembled system FRFs (Figure 5.1). First, an Inverse Fast Fourier Transform (IFFT) was performed on the assembled system FRFs. The result is a decaying sinusoid.

Second, the time response was convolved with a shock input impulse (Figure 5.2). This input was created based upon previous pyroshock test data (taken by Will Larsen). This step is necessary because the model FRFs are a result of supplying a unity impulse into the structure. This means that all frequencies are equally excited. Essentially, this convolution acts as a filter, modifying the contribution of all modes and replicating what is to be expected in a laboratory setting. It should be noted that the spectrum of the shock impulse has a first roll-off frequency around 1000 Hz and is not representative of all pyroshock input pulses.

Finally, the SRS is computed using David Smallwood's MATLAB code. A damping ratio of 5% (Q = 10) was used in the SRS calculations. Logarithmically spaced frequencies from 100 Hz to 10 kHz were used as the base natural frequency calculations for the SRS. The effective sample rate varied between test and model data; 6,000 S/s and 20,000 S/s, respectively.

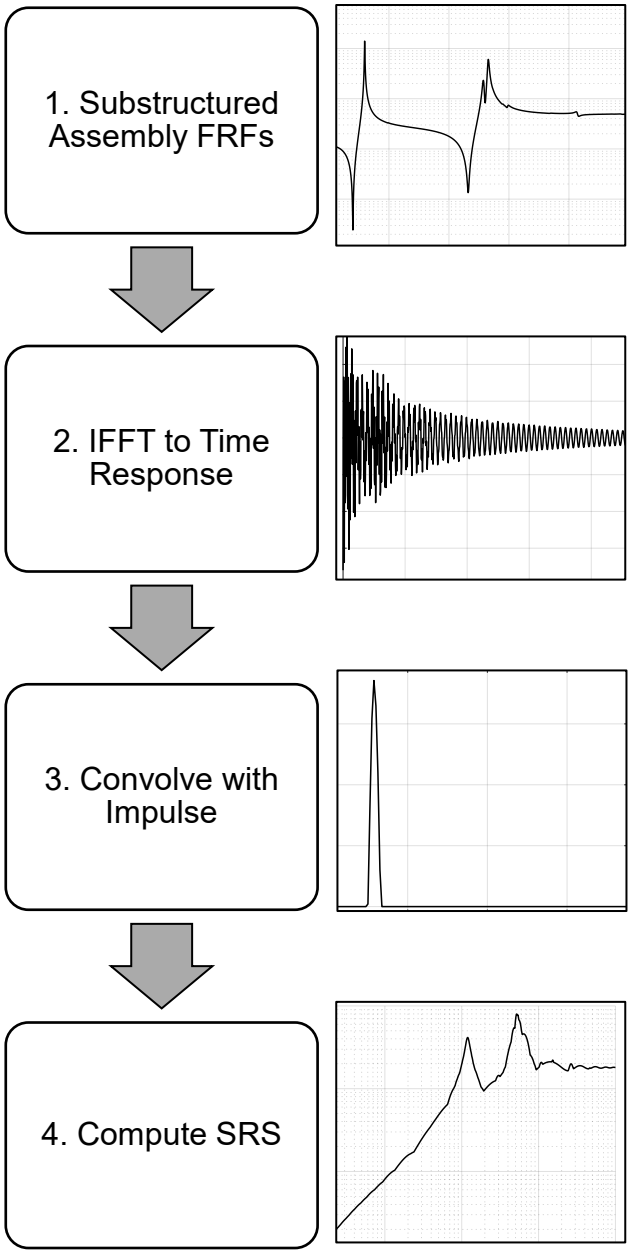

Figure 5.1 Computation process to calculate a shock response spectrum from a frequency response function as a result of LaGrange-Multiplier frequency based substructuring.

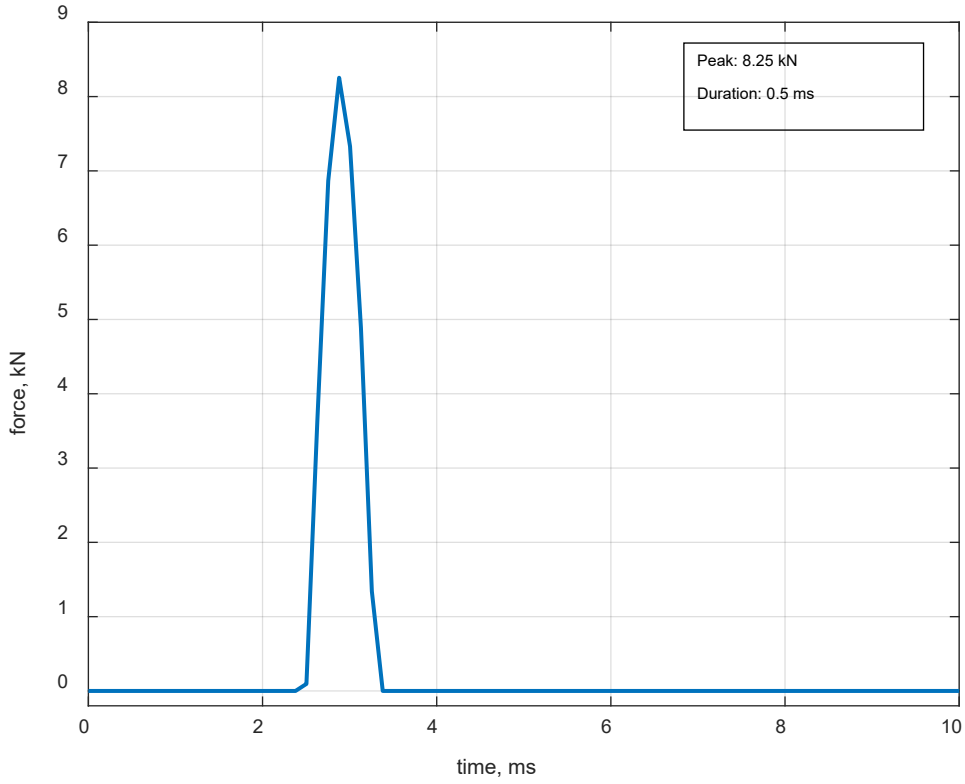

Figure 5.2 Shock pulse input to convolve with time domain assembly dynamics before shock response spectrum calculations, based off of previous shock tests.

Tolerance bands were placed around the generated shock spectrums. The starting slope of the tolerance bands is at 12 dB per octave, or two orders of magnitude per decade. The tolerance bands level off at the knee frequency. Since the actual specification tolerance bands were unavailable, these generated tolerance bands were fit to the in-axis (Z) SRS for each payload location and response node and adjusted as necessary to capture as much off-axis response as possible. Applicably, the process can be altered to allow a custom shock impulse and tolerance bands.

5.2 Optimization scheme

Using the in-axis (Z) SRS and fitted tolerance bands, several objective functions were calculated to determine how close the off-axis response lies to the in-axis response.

These objective functions discussed below, emphasize different parts of the SRS. The first objective function calculates the difference of the root mean square (RMS) average across the entire spectrum. This puts emphasis on the average amplitude difference. The second calculates the sum of the square of the residuals, similar to a least squares fit. This emphasizes the "line of best fit" difference. The third calculates the absolute difference, in decibels. Calculation methods two and three were repeated for a range of frequencies surrounding the knee frequency, capturing the *little dinker mode* below the knee frequency and the third bending mode about the knee frequency (700 – 2000 Hz).

1. Minimize RMS difference

$$minimize\ |RMS(X) - RMS(Z)| + |RMS(Y) - RMS(Z)|$$

$$RMS(x) = \sqrt{\frac{1}{m}\sum_{k=1}^{m} {x_k}^2}$$

2. Minimize the square root of the square of the sum of the residuals

$$minimize\ RSS(X, Z) + RSS(Y, Z)$$

$$RSS(x, y) = \sqrt{\frac{1}{m}\sum_{k=1}^{m} (x_k - y_k)^2}$$

3. Minimize absolute difference at knee frequency f

$$minimize\ \lceil X_f - Z_f \rceil + \lceil Y_f - Z_f \rceil$$

Even though the optimization scheme produced a configuration that minimized most of the objective functions, Engineering Judgement* was used to select the final configuration. As the payload moves outward radially, different modes contribute to the knee frequency and subsequent peaks surrounding the knee frequency. At the edge of the plate (where the calculated optimal configuration is), there is high participation from modes surrounding the knee frequency, bringing parts of the SRS beyond the tolerance bands. A new optimal location was selected to be right above the calculated optimal location (chapter 7.1).

** Engineering Judgement is something that is cultivated over time, requiring years of experience and exercise. My Engineering Judgement is still developing but is often provoked during group discussions and with guidance from my committee members, advisor, and primary investor. Thank you for your contributions to my academic and life-long growth and development.*

5.3 Application process flowchart

Below is a flowchart of the collection, substructure assembly, and optimization approach (Figure 5.3). Theoretically, this approach can be applied to any number of subsystems. In the case of the resonant plate assembly, the plate FRFs would be collected upon design and fabrication, either experimentally or analytically. A full matrix of every input and interface DOF is necessary for optimization. This part would be the most time consuming to set up but can be used repeatedly for any number of test components. The payload (or any test object) FRFs would be collected at the interface and response DOFs. Again, this can be done analytically or experimentally.

Parameters would be defined for the optimization scheme, such as frequency range, sample rate, tolerance bands (if applicable), shock impulse duration/amplitude, objective function range, or damping ratio for SRS calculations. LM-FBS would be performed using these parameters, iteratively, on the plate and payload FRFs. Once the iterations are complete, a list of configurations that minimize the objective functions is produced.

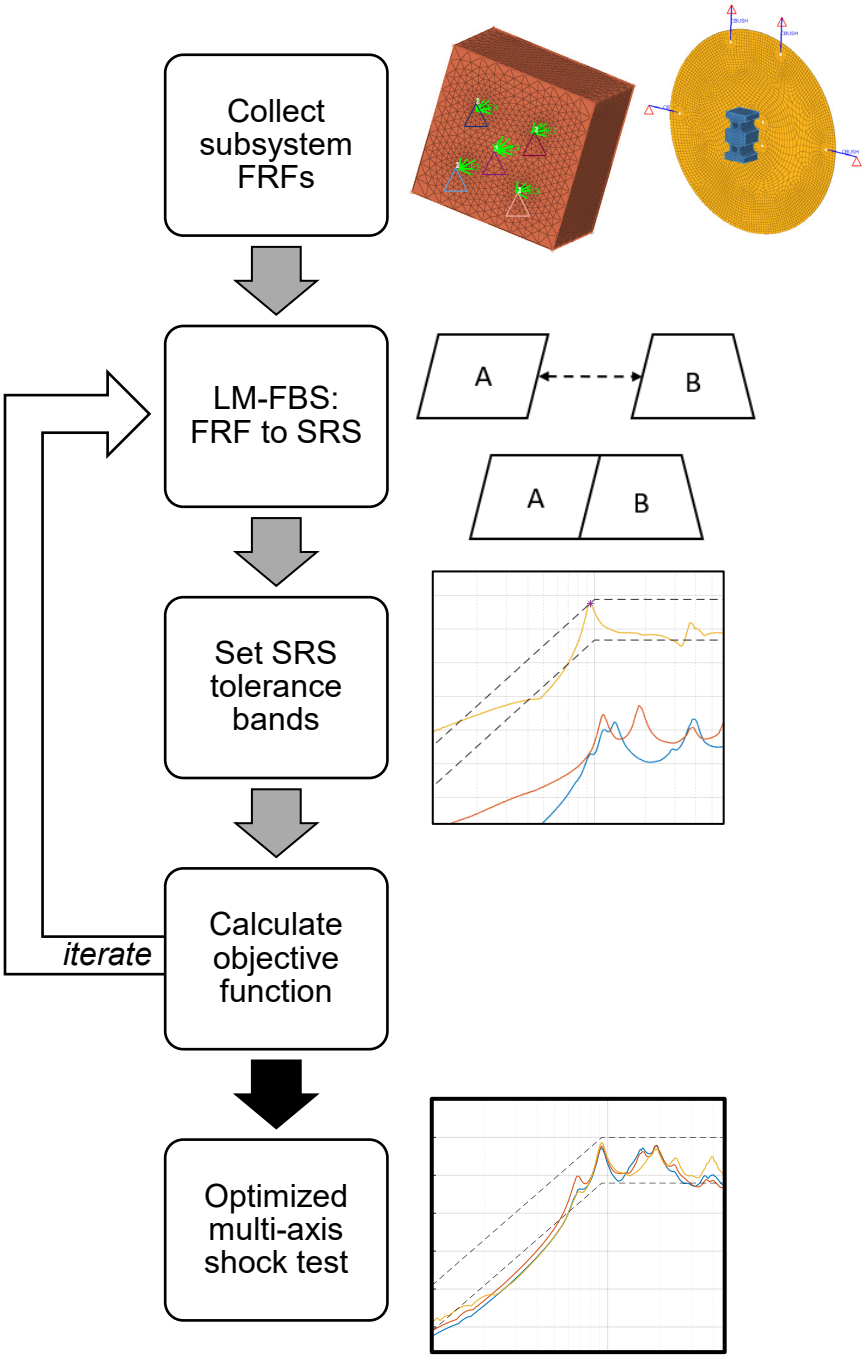

Figure 5.3 Optimization Process Diagram

6 Experimental model

Experimental data was collected and used to verify the correlation between the test and model, compare optimal assembly FRFs, and see how well experimental FBS corresponds to analytical FBS (Figure 6.1 Schematic of resonant plate hardware and payload model subsystems for experimental frequency based substructuring.*Figure 6.1). The resonant plate hardware and test setup are discussed, followed by initial experimental data and assumption assessment.*

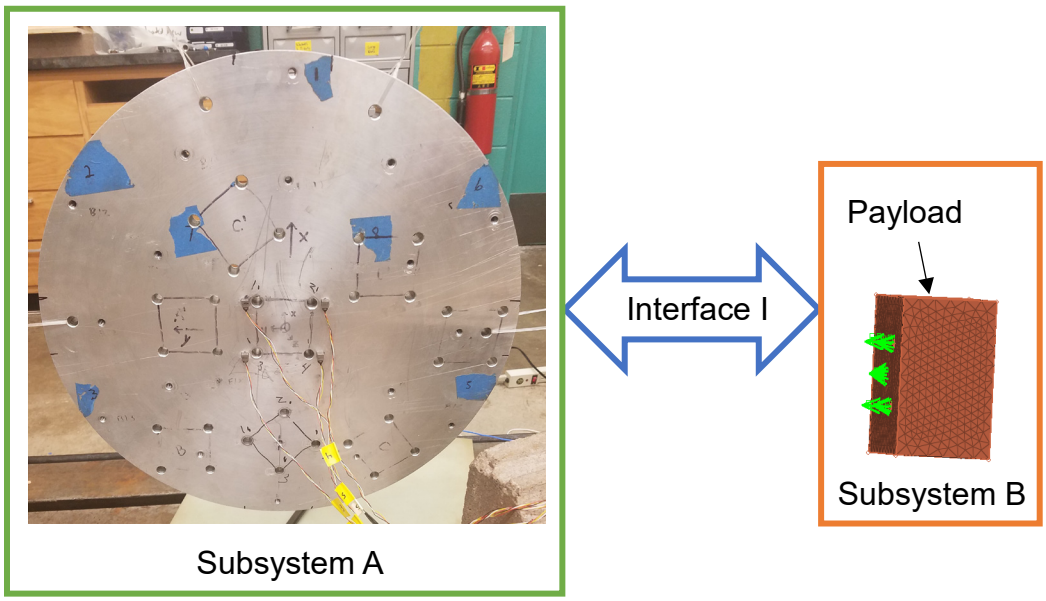

Figure 6.1 Schematic of resonant plate hardware and payload model subsystems for experimental frequency based substructuring.

6.1 Hardware

A physical resonant plate, made for single-axis mid-field pyroshock tests, was used for validation. The disassembled plate consists of two components: the impact pad + the circular plate (subsystem A), and the payload (subsystem B). The impact pad is made of aluminum and has rough dimensions of 4” x 2” x 1.5”. The impact pad connects to the circular plate with two 5/16”-24 bolts. The circular plate is made from 6061 T6 Aluminum

with a 17-inch diameter and a thickness of 1.125 inches. The circular plate has multiple sets of four through holes (3/8” diameter) for mounting the payload with 3/8”-24 bolts. The payload is made of aluminum with dimensions of 5” x 5” x 3. This round resonant plate was the product of a senior capstone design team at Michigan Technological University, completing a project sponsored by Honeywell.

The payload is a large block of aluminum, which has only a few modes in the frequency range of interest (Figure 6.2). Simulating free-free boundary conditions in the laboratory is not perfect and can contaminate data. In this case, the payload test FRFs had artifacts that were assumed to be dynamics of the fishing line and frame used for suspension. The payload FRFs used in the final test LM-FBS calculations were taken from the finite element model.

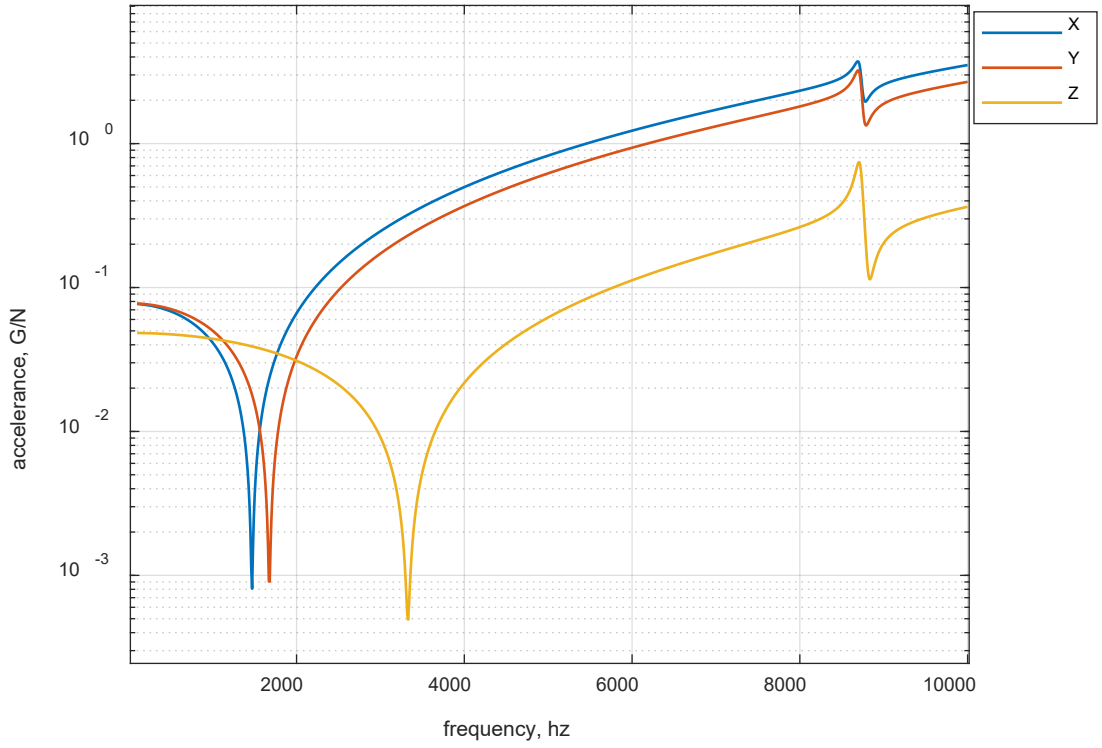

Figure 6.2 Drive point frequency response functions from the finite element model of payload at interface location 1.

6.2 Setup

Each component was suspended by fishing line to simulate free-free boundary conditions without contaminating the low frequencies. An array of measurement points was selected on the plate corresponding to the desired interface and response degrees of freedom. For the subsystem component tests, four small triaxial accelerometers were attached to the plate using epoxy. Another accelerometer was attached to the impact pad, near the excitation location, using epoxy. For the full assembly tests, only one accelerometer was glued to the payload at the predetermined response node. Table 6.1 contains information about the transducers used in these tests.

Table 6.1 Equipment list, make, model, and sensitivities used for collecting frequency response functions on the circular plate assembly for experimental frequency based substructuring

Equipment	Make	Model	Nominal Sensitivity
Impact Hammer	PCB	086C04	1.1 mV/N
Triaxial Accelerometer	PCB	356A15	5 mV/G
Triaxial Accelerometer	PCB	356A13	100 mV/G

Data were collected using a Siemens LMS SCADAS III outfitted with PQFA cards. Data collection was performed in Siemens LMS Test.Lab 17 Impact Testing module. In order to input substantial energy into the high frequencies, the impact hammer was outfitted with a metal tip (084B03) and added mass (084A08, 75 grams) both which were provided with the hammer. All transducers were calibrated with a portable vibration calibrator (TMS 9110D). The impact hammer was calibrated with a previously calibrated accelerometer (PCB 356A13) and a gravimetric calibration system (TMS 9961005A). Frequency response functions were calculated using the H1 estimation method. Table 6.2 contains the data acquisition parameters between the model and test setups.

Table 6.2. Data acquisition parameters used for collection of circular plate assembly frequency response functions, and equivalent analytical data acquisition parameters used in the finite element model

	Experimental	Analytical
Bandwidth	6,400 Hz	10,000 Hz
Spectral Lines	8,192	990
Frequency Resolution	0.7813 Hz	10 Hz
Window	Force-exponential (input 0.36%, response 25%)	n/a
Linear Averages	5	n/a

Impact tests were performed on the plate + impact pad to obtain the interface dynamics, and the full assembly (plate + impact pad + payload). These tests were performed in three configurations: the original center assembly (Figure 6.3), the optimal assembly from the optimization scheme (corner) (Figure 6.4), and a third arbitrary assembly (bottom) (Figure 6.5). To obtain the full interface matrix necessary for LM-FBS, input and response had to be recorded at each location. The plate test had a total of 13 input DOFs and 13 response DOFs (5 nodes). The assembly test had only one input DOF and three response DOFs (one node).

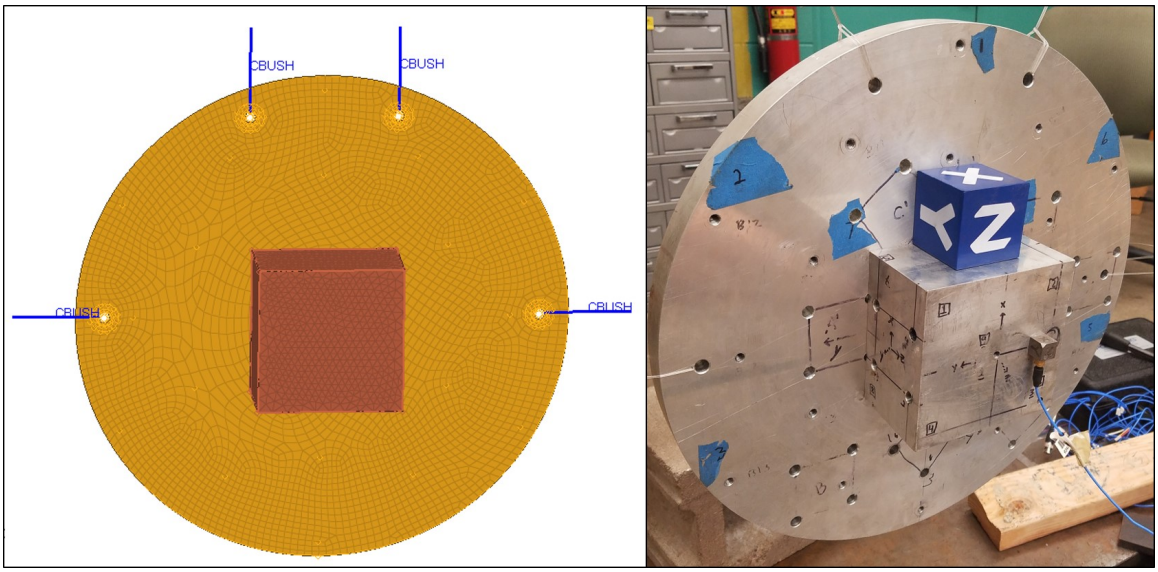

Figure 6.3 Center configuration assembly finite element model and physical test.

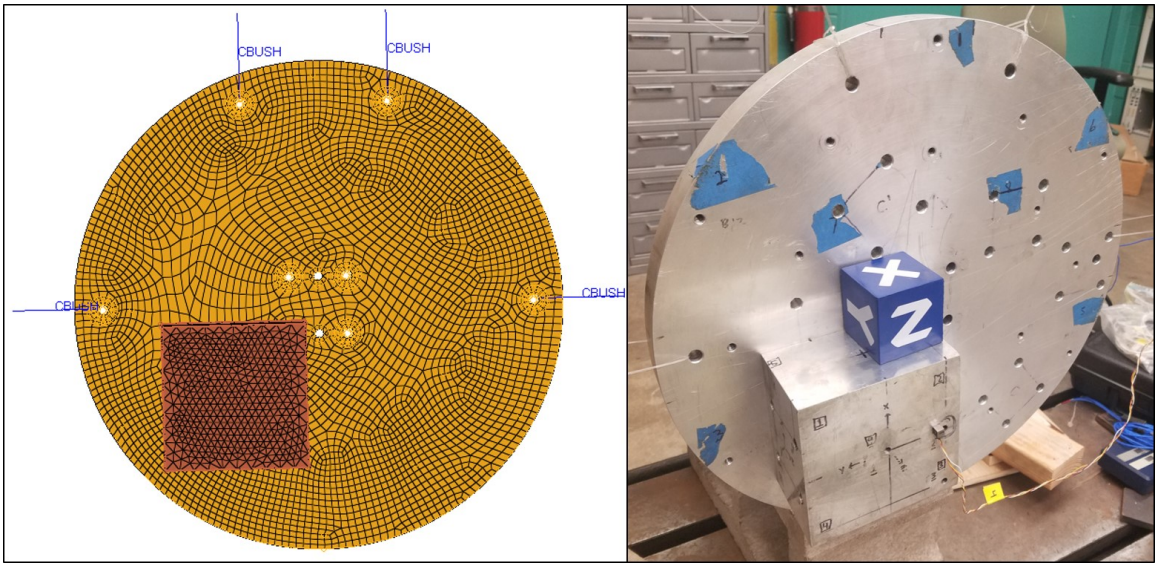

Figure 6.4 Optimal corner configuration assembly finite element model and physical test.

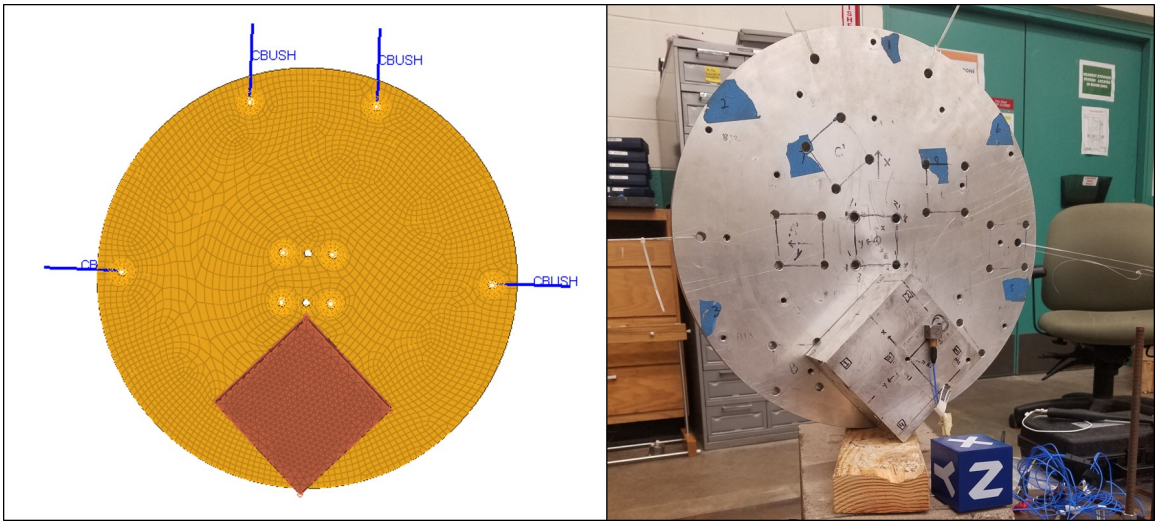

Figure 6.5 Bottom configuration assembly finite element model and physical test.

Assembly tests were also performed on the plate + impact pad and payload using lock washers in between the payload and plate (Figure 6.6). This configuration replicates the RBE2 direct node pairs in the model assembly and FBS interface calculations.

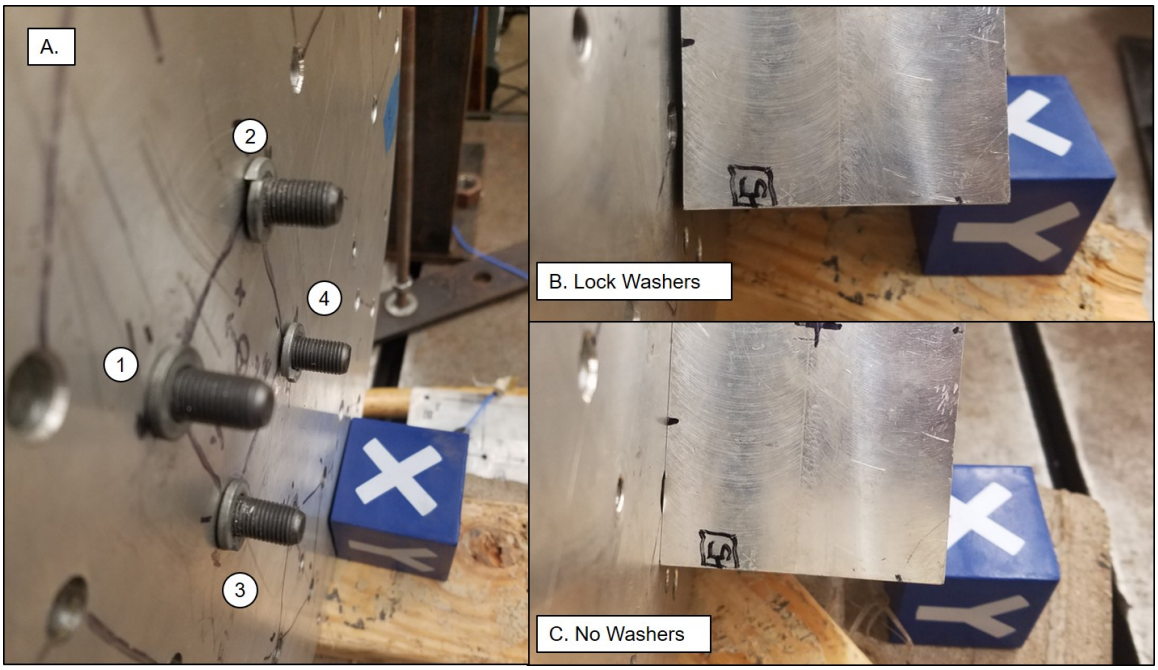

Figure 6.6 *A*, Center configuration showing the circular plate + impact pad bolts and lock washers before installing the payload, and *B*, the resonant plate test assembly with the lock washers

installed, and *C*, the resonant plate test assembly without the lock washers installed, how the resonant plate is normally assembled.

Drive point measurements (in-axis, +Z) were made on the other side of the plate from the accelerometer location. The off-axis measurements were made by impacting the side of the plate in the center along the axis of the accelerometer.

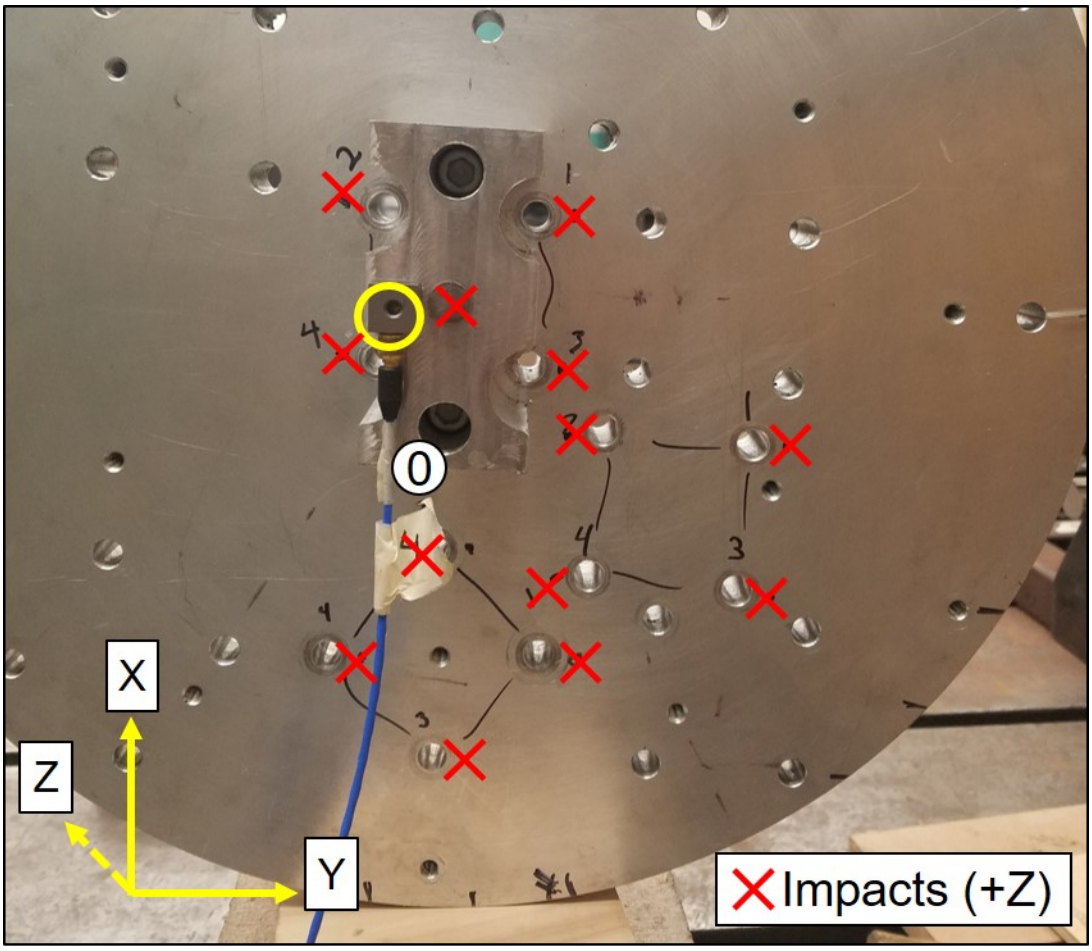

Figure 6.7 Accelerometer placement near the impact pad input node and all in-axis impact hammer locations.

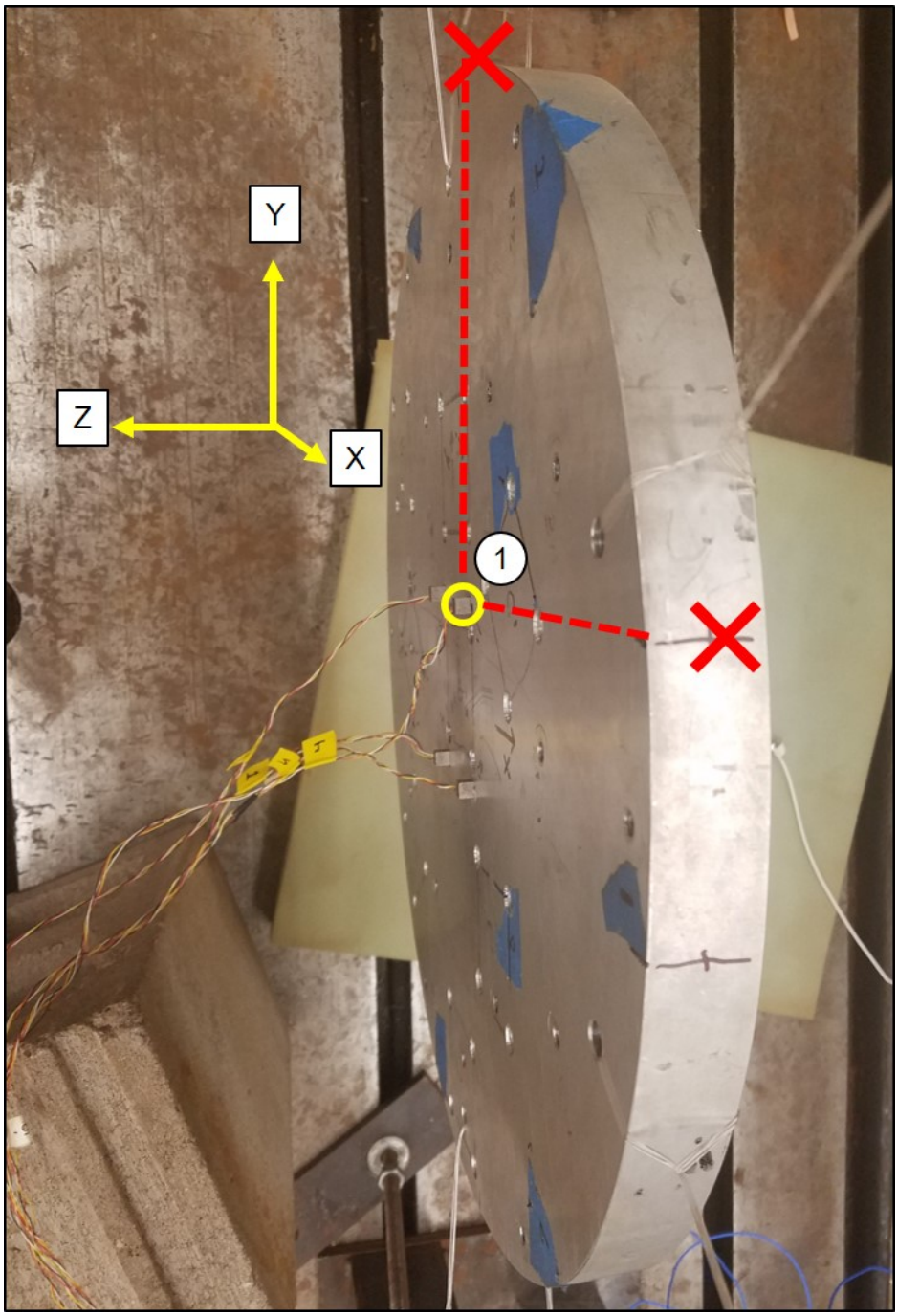

Figure 6.8 Example of off-axis impacts at interface location 1 on the center configuration.

Figures below show the accelerometer locations for the plate subsystem tests on the center configuration (Figure 6.9), corner configuration (Figure 6.10), and bottom configuration (Figure 6.11).

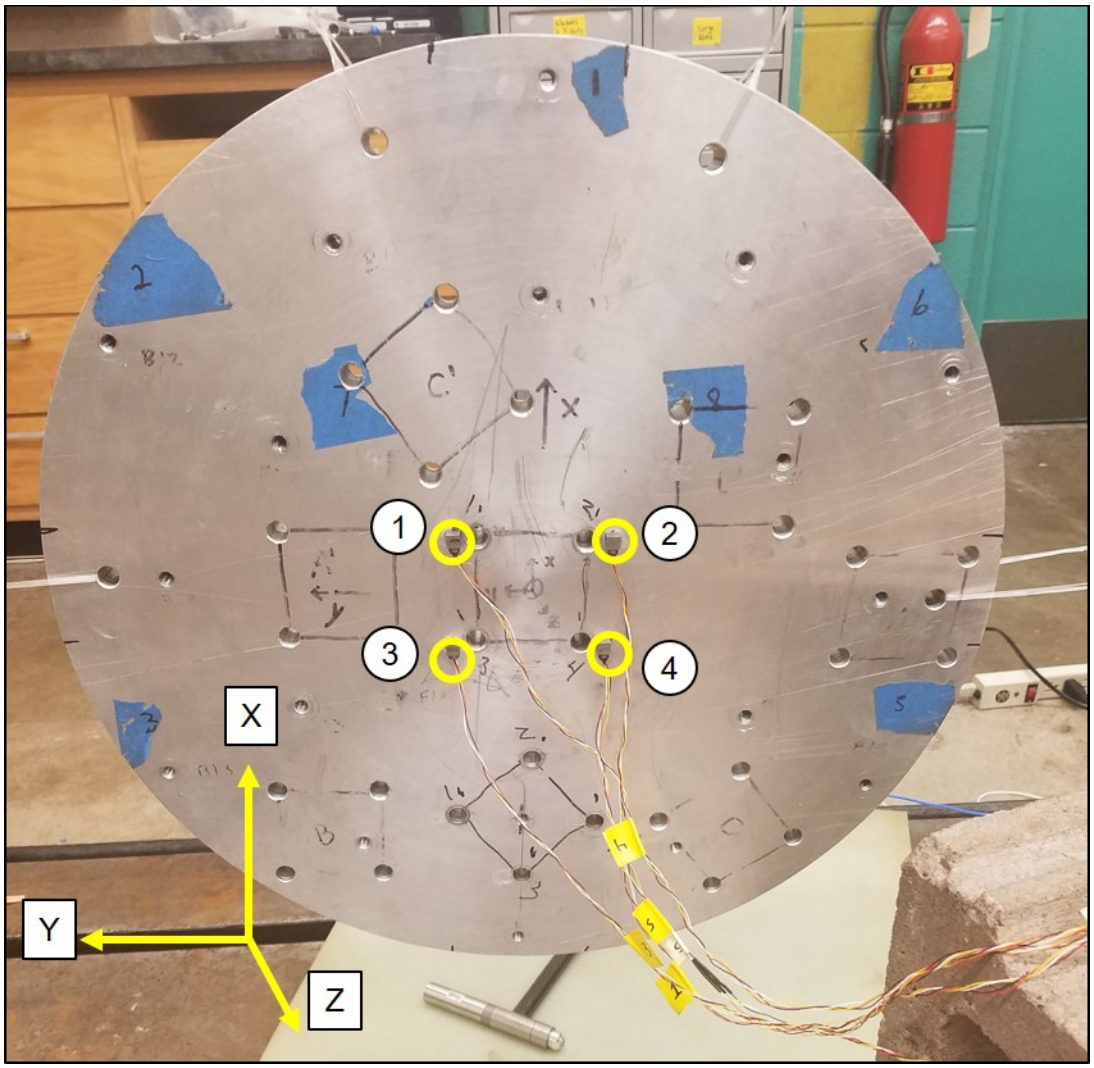

Figure 6.9 Accelerometer placement near interface bolt holes in the center configuration circular plate + impact pad test setup.

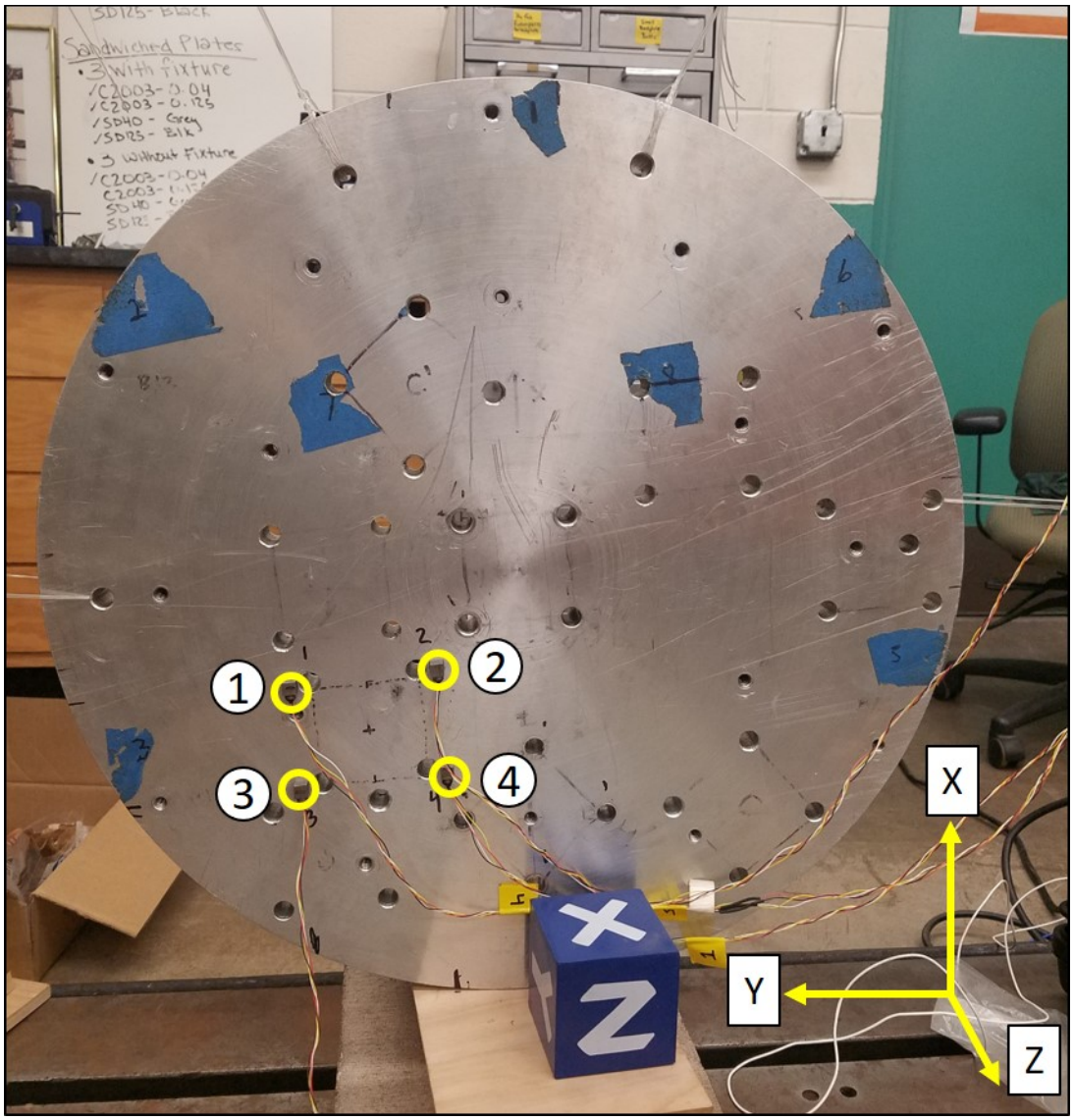

Figure 6.10 Accelerometer placement near interface bolt holes in the corner configuration circular plate + impact pad test setup.

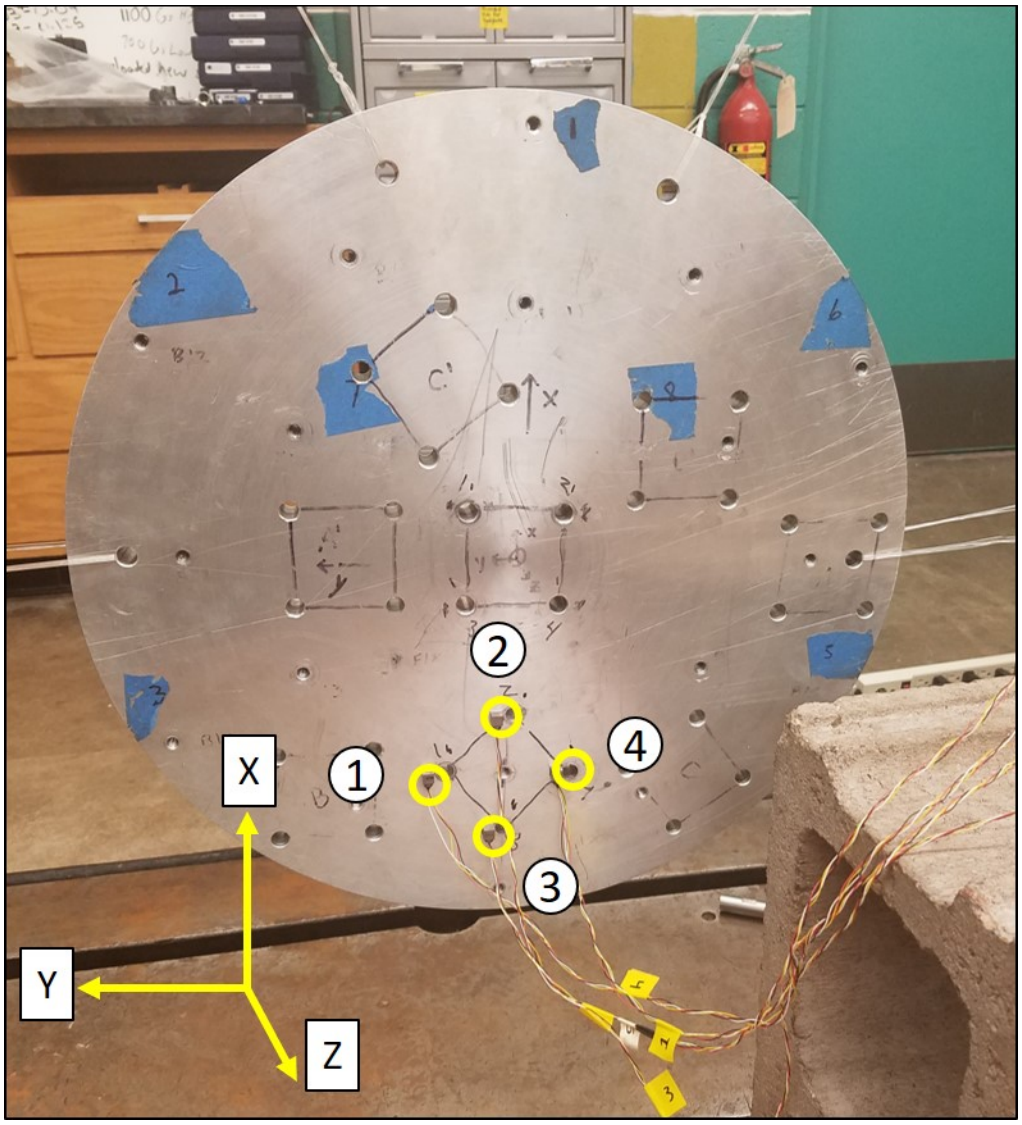

Figure 6.11 Accelerometer placement near interface bolt holes in the bottom configuration circular plate + impact pad test setup.

6.3 Initial experimental data

The impact hammer, equipped with the metal tip and extra mass, was able to excite out to 3,000 Hz within a 6 dB decrease of the input autopower (Figure 6.12). This is an acceptable range to excite the first few modes that contribute to the knee frequency of the resonant plate. Reciprocity holds well across the in-axis (+Z) inputs and responses, while there is

more noise in the off-axis inputs and responses (Figure 6.13). The in-axis drive point measurements have clean phase, while the off-axis drive point measurements frequency cross zero (Figure 6.14). In-axis coherence is higher than off-axis, but all axes have high coherence at resonances, particularly at the knee frequency (Figure 6.15).

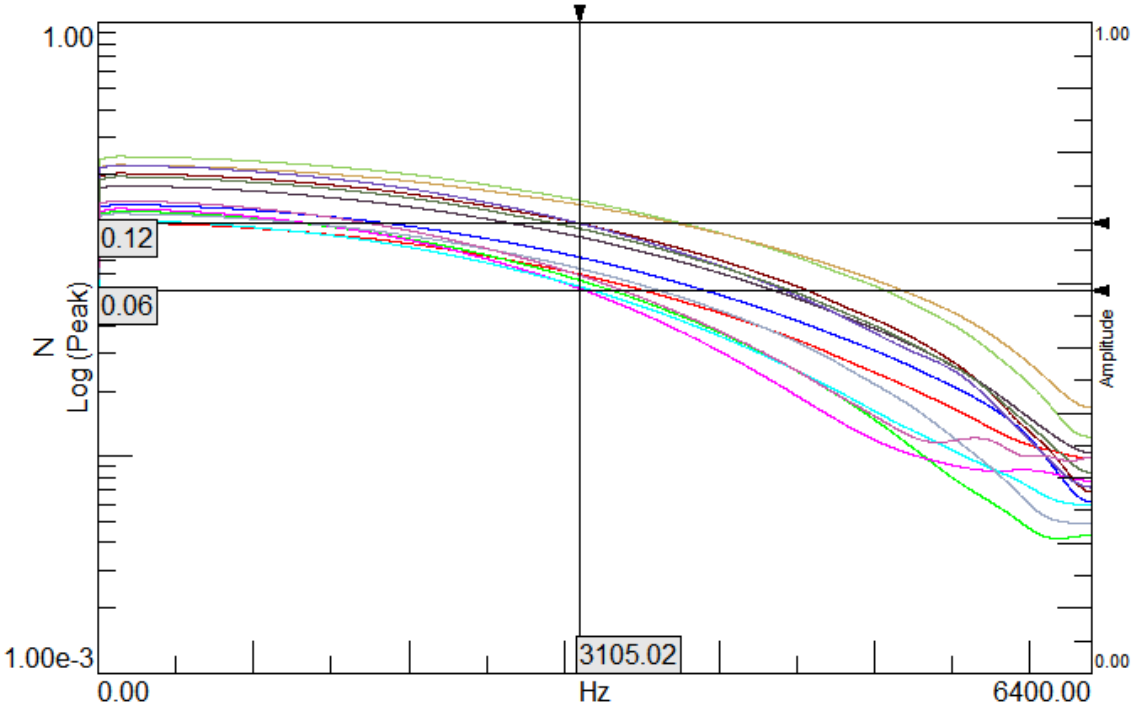

Figure 6.12 Input autopower from the impact hammer of all 13 impact locations on the center configuration.

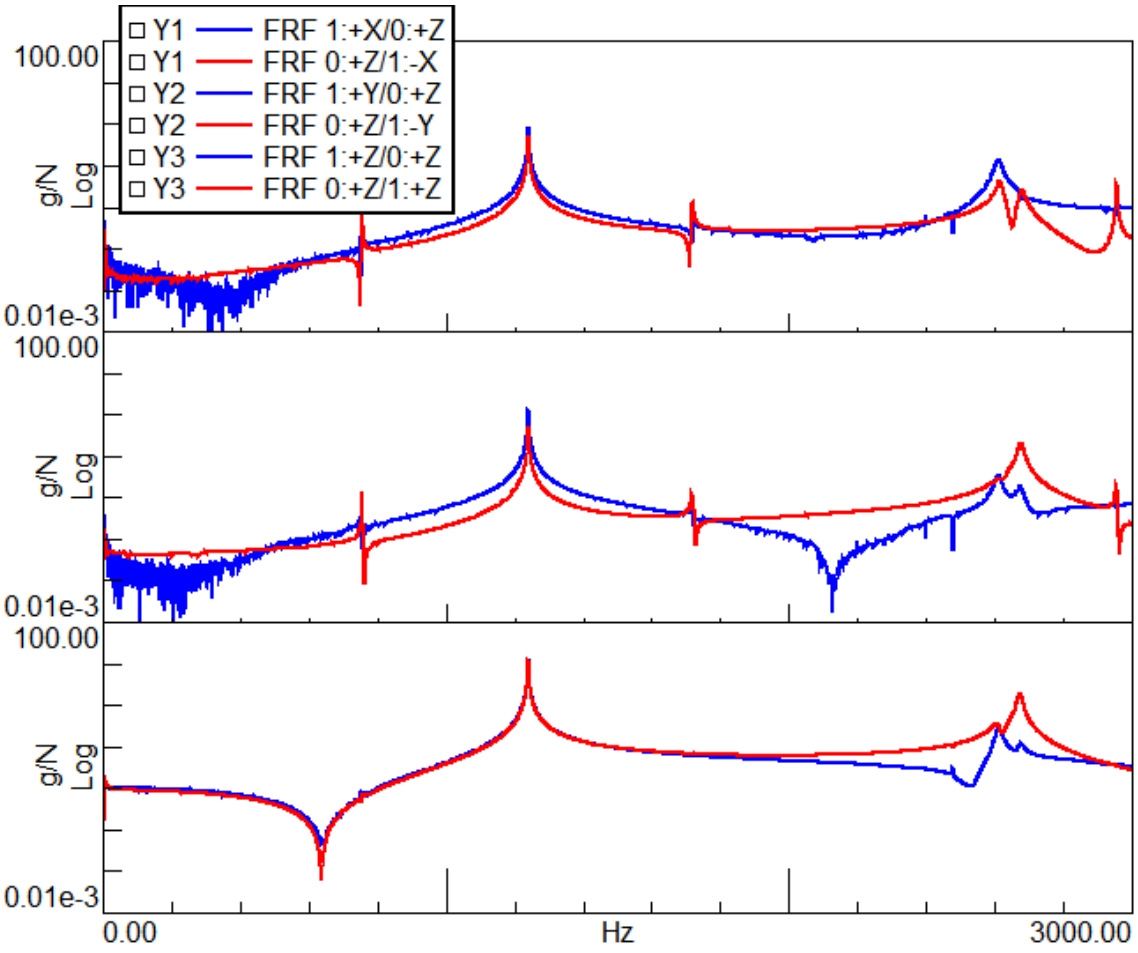

Figure 6.13 Reciprocity between the impact pad (0:+Z) and the center configuration interface location 1 in all three orthogonal directions (+XYZ).

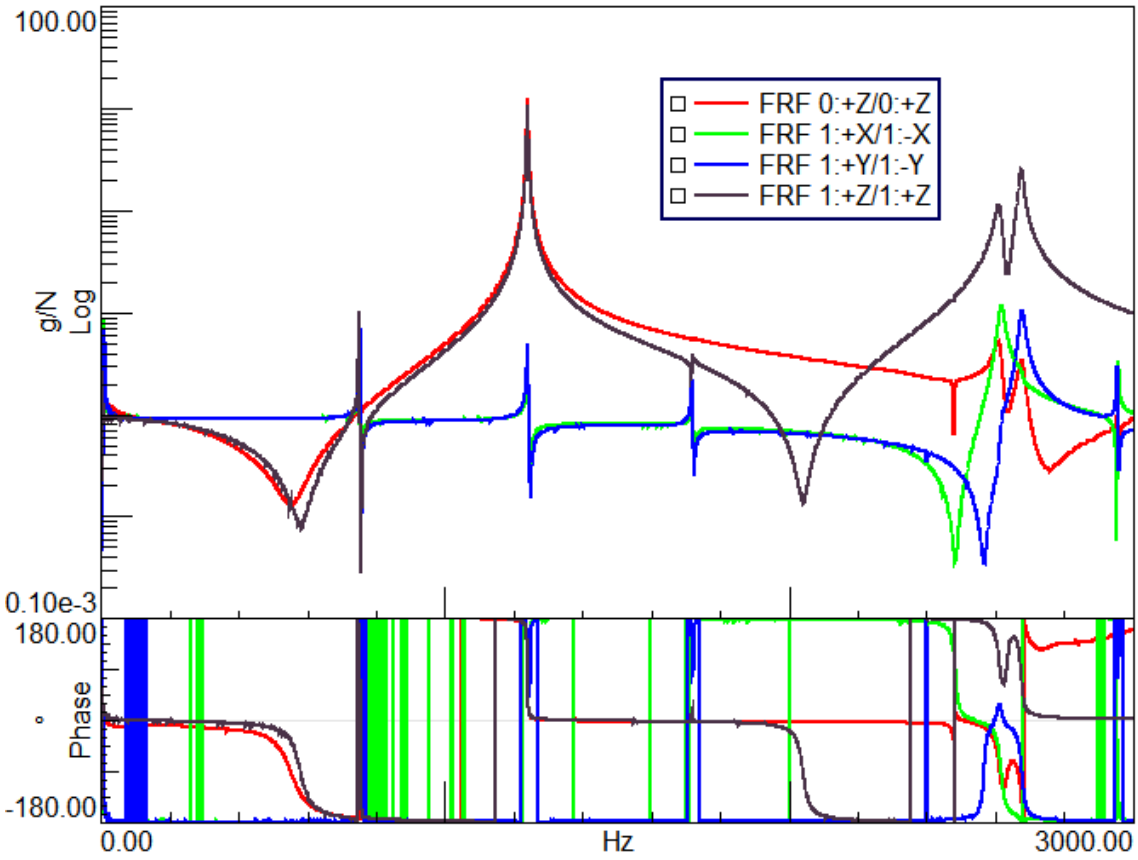

Figure 6.14 Drive point FRFs and phase of the impact pad (0:+Z) and the center configuration interface location 1, in all three orthogonal directions (+XYZ).

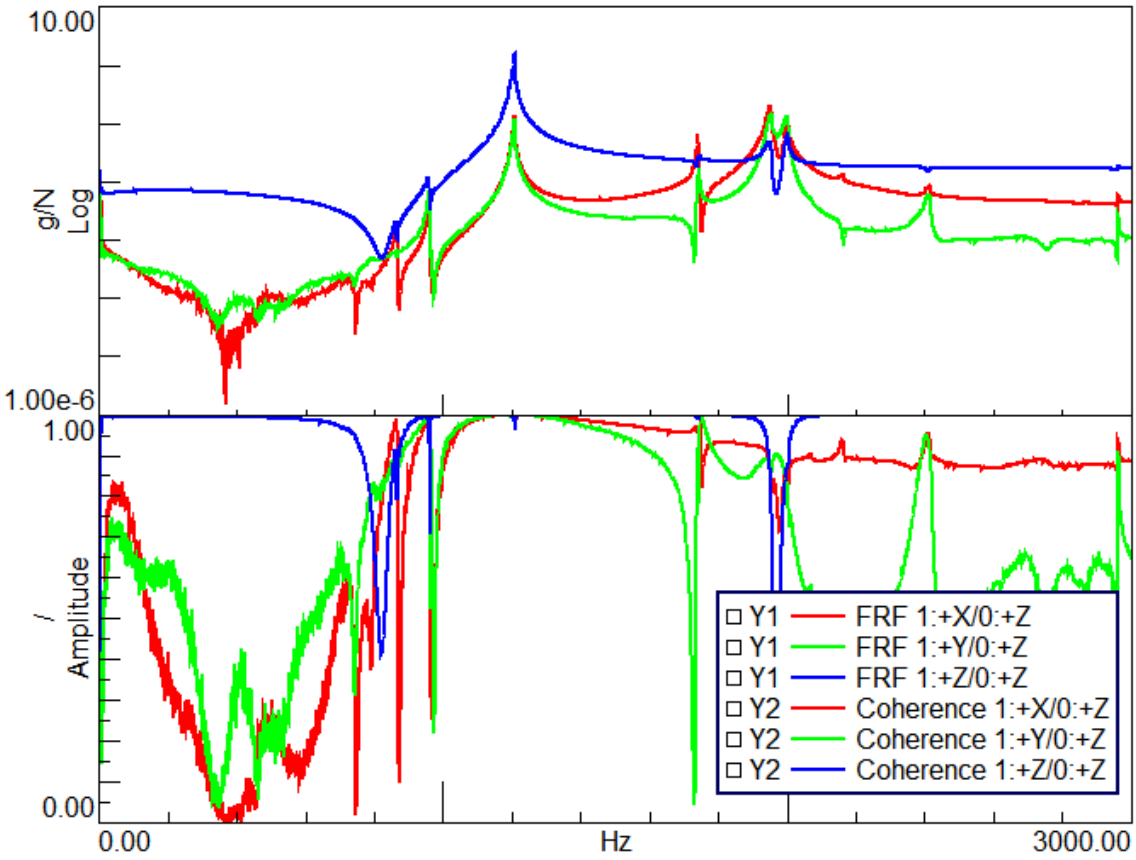

Figure 6.15 FRFs and coherence of the center configuration assembly, with the input at the impact pad node (0:+Z) and the response at the payload node 9243 (1:+XYZ), assembly without washers.

6.4 Assessment of assumptions

Though the FEM was correlated to match test data, it is inherently stiff. Initially, the FEM damping was assumed to be 1% across all frequencies. After comparing to the test data, the damping ratio was lowered to 0.5%. Curve fitting was done on a small set of test data using LMS Test.Lab's PolymaxPlus algorithms. Test data damping estimates varied between 0.1% and 0.8% at resonances.

There are inherent errors that come with experimental data collection. The first is that the impact consistency and direction are not perfect. Although great care was taken to reject sloppy impacts, impacting in the orthogonal directions on the edge of a round plate was

proven to be very difficult. The experiment boundary conditions also had potential to contaminate test data – the fishing line used to suspend the plate relaxed over time, and eventually snapped during a test. Those were changed out multiple times during testing. The plate was suspended from a large metal frame, which is known to contaminate data at high frequencies. This is the reason why model FRFs were used for the payload instead of test FRFs. The experimental data focused on dynamics around the knee frequency, while the model FRFs were computed out to 10 kHz without contamination.

There is a considerable difference in off-axis dynamics between the model and test data. Figure 6.17 (below) shows the drive point FRFs from interface location 3 on the plate, for both the test and model. The off-axis (X&Y) test data has resonances corresponding to the in-axis resonances (+Z). However, the off-axis model data has one resonance in the frequency range up to 3000 Hz. Figure 6.17 shows the FRFs of the plate interface location 1 with the input being in-axis location 1 (+Z) and all three orthogonal responses (+XYZ). This shows that transverse sensitivity exists in the non-drive point measurements. However, the difference in the drive point measurements can be attributed to imperfect orthogonal impacts and off-axis modal excitation and is further discussed in chapter 7.2.

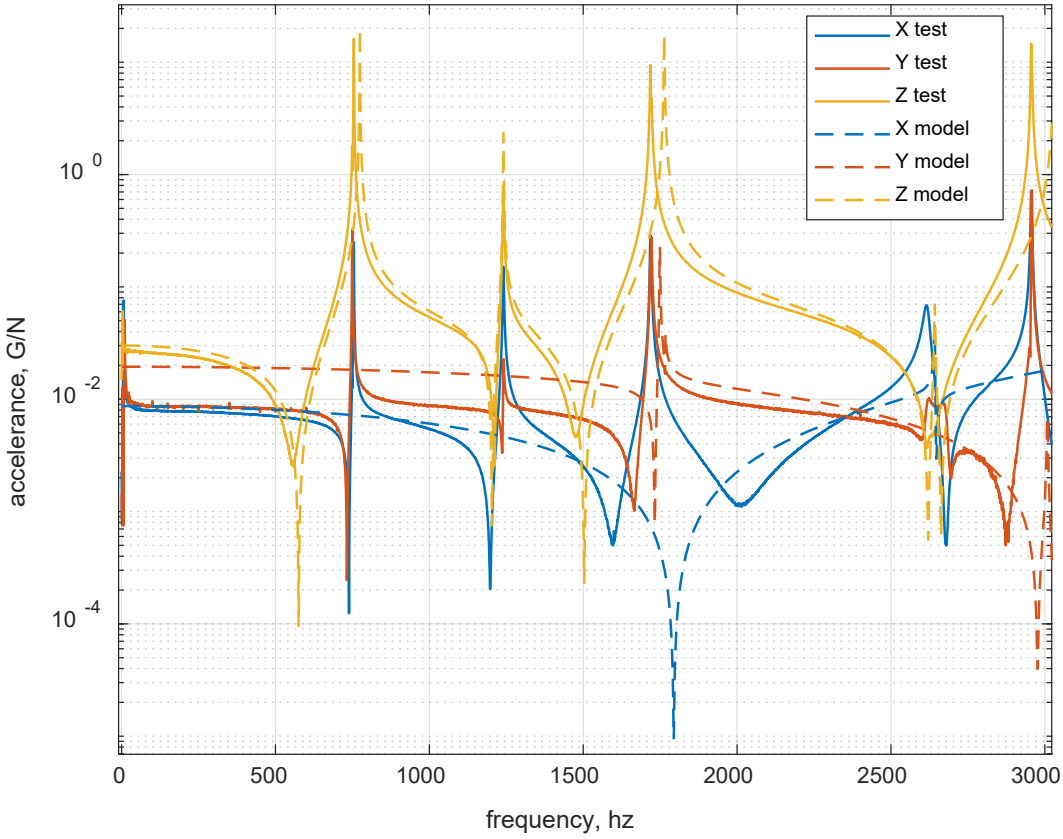

Figure 6.16 Comparison between test and model drive point FRFs on the center configuration circular plate at interface location 3.

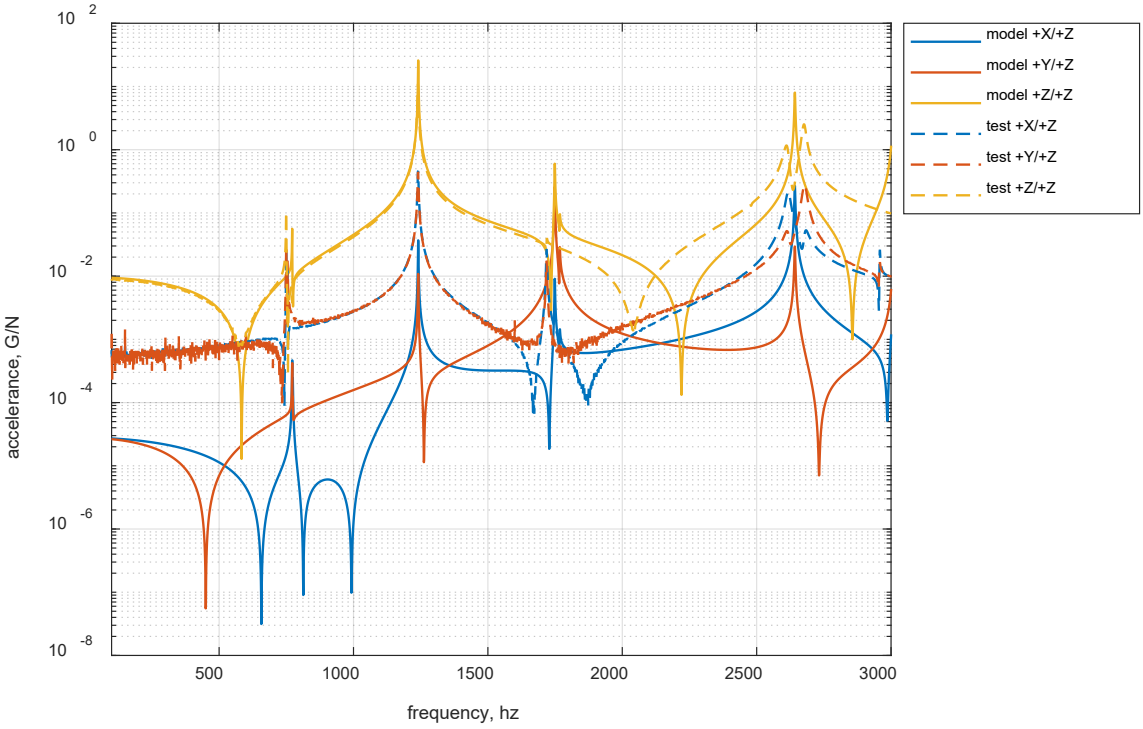

Figure 6.17 Comparison between test and model FRFs all response axes with an in-axis input on the center configuration circular plate at interface location 1.

Even when using FRFs obtained from a model, the condition number of the kernel rose to high values (Figure 6.18). This is always a concern for experimental data, where measurement noise and leakage can distort the FRFs, causing the condition number of the inverted kernel to increase. A large condition number allows small errors to get considerably large, possibly contaminating the data. The condition number between the model and test followed the same pattern – the condition number increases at and around system resonances. There are some discrepancies at the low frequencies that can be attributed to the measurement noise of the test data.

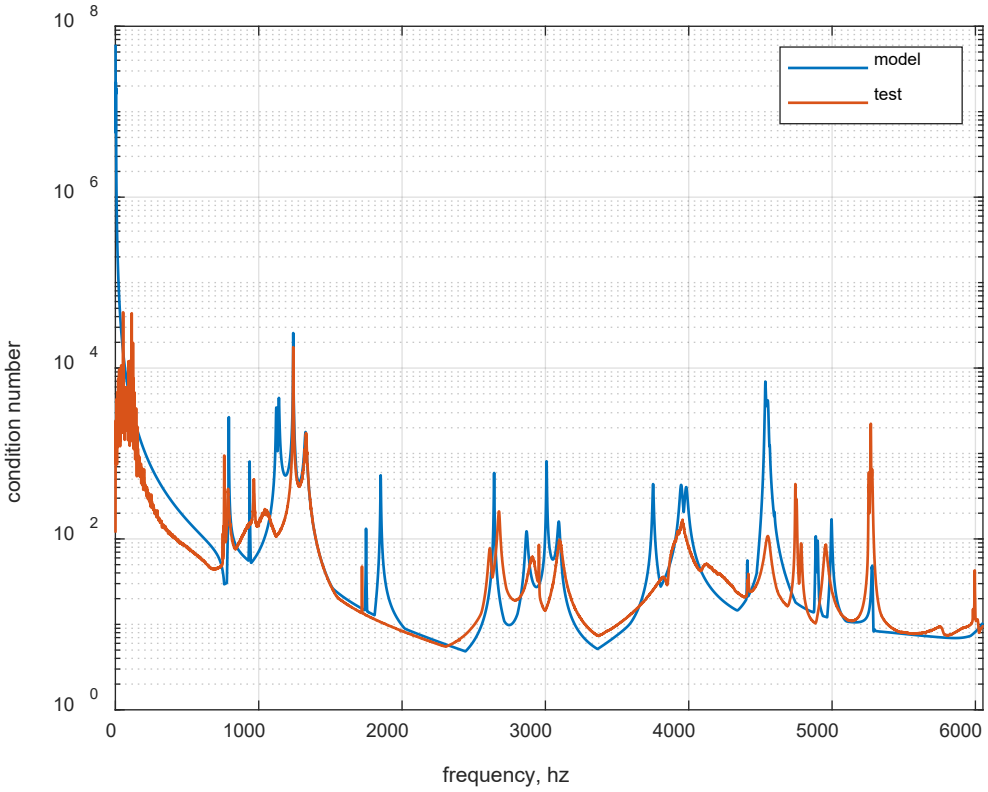

Figure 6.18 Condition number of the kernel matrix between test and model data in the center configuration.

7 Results

This chapter first discusses the optimal configuration, the objective functions, and modal participation. Then, the knee frequencies of the three configurations (Table 7.1) are compared, addressing discrepancies and re-evaluating the original assumptions. The chapter concludes with a graphical comparison between test and model results of all configurations, showing correlation and verifying the optimization output.

Table 7.1 The three configurations analyzed for results and validation discussions with payload position, orientation, and response node.

Configuration Name	Payload Position (X,Y) inches	Payload Rotation degrees	Response Node
Center	(0,0)	0	9243
Bottom	(-5,0)	45	9243
Corner	(-3,3)	0	9243

7.1 Optimal configuration

Using 22 possible configurations and four objective functions, the optimal assembly for the 0-degree oriented payload was the far corner (X = -3in, Y = 3in) and for the 45-degree oriented case was the far corner (X = -5in, Y = 5in). Due to the location of the interface nodes required for assembly, it was not possible to move the 0-degree oriented payload to the far corner (X = -5 in, Y = 5 in). Both oriented payloads reported response **node 9243** as the optimal node. Figure 7.1 shows how SRSs change across different response nodes on the 45-degree oriented payload at position (-5,5).

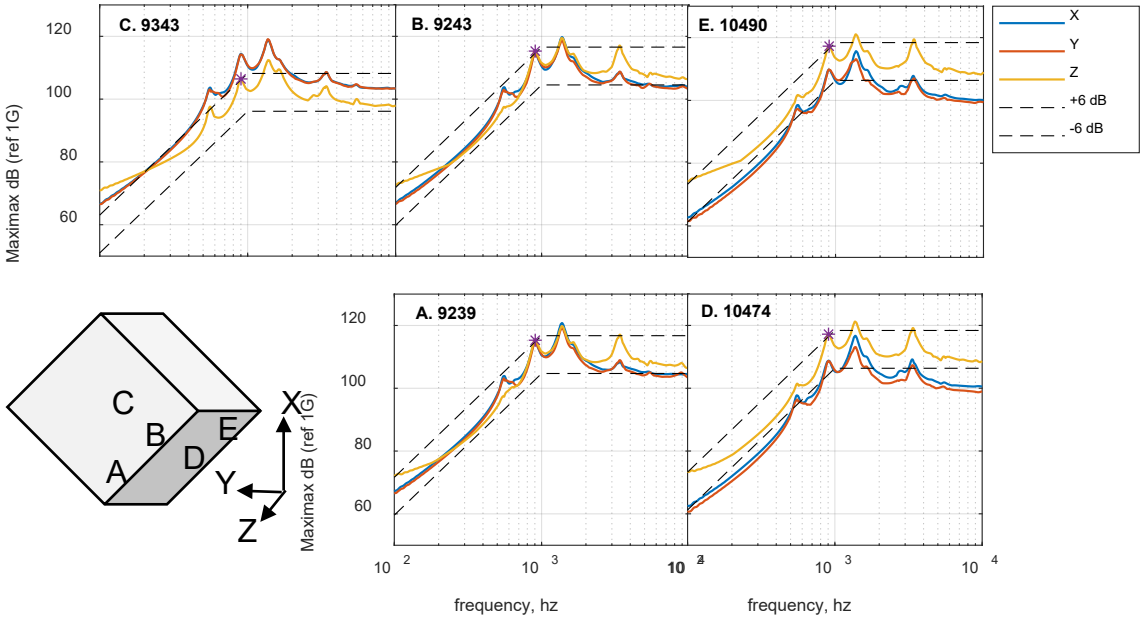

Figure 7.1 How the shock response spectrum changes across the five response node locations, data from the corner configuration (-5,5) and the payload in the 45-degree orientation.

Looking at how the SRSs change with distance from the center of the plate shows that certain modes, when excited, can add unwanted amplitudes to the SRS. As the payload moves outward from the center of the plate, the modes directly surrounding the knee frequency increase in amplitude. This is especially evident when comparing the 45-degree oriented payload with response node 9243 at locations (-5,5) and (-3,3) (Figure 7.2).

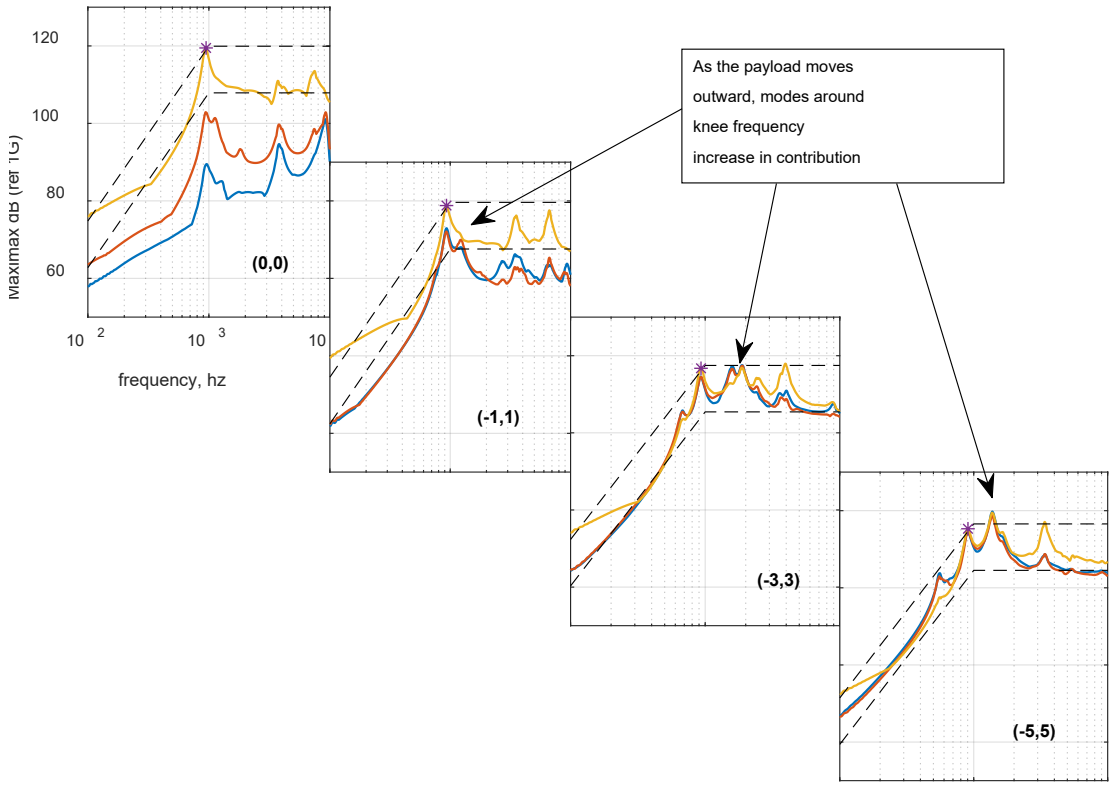

Figure 7.2 As the payload moves outward from the center of the plate, the modes around the knee frequency increase in contribution, data from 45-degree oriented payload response node 9243.

By looking at the SRSs in the figure above, it is clear that the (-3,3) location has amplitudes that remain within the tolerance band more than the (-5,5) location, despite the (-5,5) location minimizing the objective functions. The optimal location is selected as the **corner (-3,3)** for this reason.

The objective function results for the optimal node and location were compared between the two payload orientations (Figure 7.3, Table 7.2). The optimal payload orientation is the **0-degree oriented payload** because the differences between in-axis and off-axis responses are less than the 45-degree oriented across all objective functions, except the least squares range.

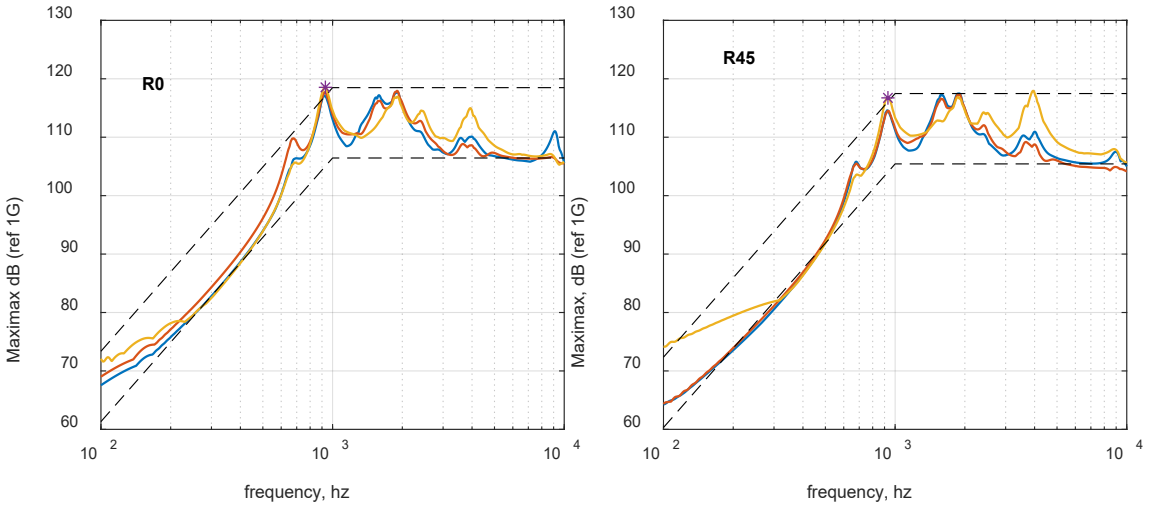

Figure 7.3 Comparison between 0-degree and 45-degree oriented payload SRS for the optimal payload location (-3,3) and response node (9243).

Table 7.2 Objective function results for both 0-degree and 45-degree oriented payloads at the optimal payload location (-3,3) and response node (9243).

Method	**R = 0**	**R = 45**
1. RMS	0.97178	2.0582
2. LS	135.472	264.3644
2. LS Range	55.3797	55.3149
3. dB @ Knee	2.6053	4.4837
3. dB Range	2.845	3.0531

From the 22 locations and orientations, and five response nodes selected as possible payload responses, the configuration that minimizes the objective functions is:

- Location: **(-3, 3)**
- Orientation: **0-degree**
- Response Node: **9243**

Figure 7.4 shows the optimal configuration SRS calculated from model LM-FBS. All three response axes remain within the +/- 6 dB tolerance bands from 600 Hz to 3000 Hz.

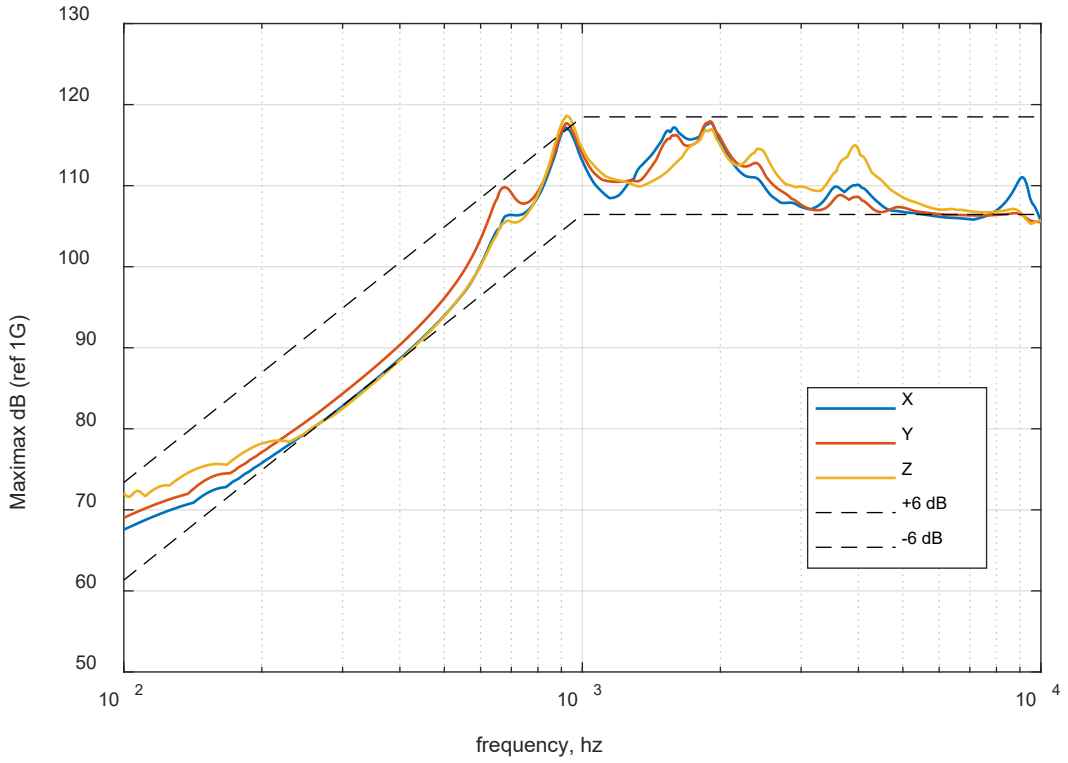

Figure 7.4 SRS of the optimal configuration from model data.

7.2 Comparisons and discussion

It was expected that the knee frequencies between the test and model, truth and FBS data would not align. Again, the focus on this thesis is on SRS amplitude, not knee frequency. However, it is important that the dynamics are comparable between all possible methods. This section will discuss the results in terms of knee frequencies and SRSs. Additional

plots and comparisons (including FRFs) can be found in Appendix C. Table 7.3 compares the knee frequencies between the three configurations (center, bottom, and corner) across the three assembly methods (FBS, RBE2/washers, and CS/no washers) for each test and model.

Table 7.3. Comparison of Knee Frequencies (Hz) Between FBS and Truth Assemblies.

Configuration	Method	FBS	Adjusted Assembly	Truth Assembly
Center	Model	936	966	1177
	Test	965	950	1209
Bottom	Model	873	922	1103
	Test	921	962	1132
Corner	Model	920	970	1190
	Test	860	924	1057

There is both frequency and amplitude agreement between the FBS and RBE2 assembly results. The truth data is stiffer than the FBS/RBE2 assemblies, although it is expected that the FBS data would converge to the truth data if a higher number of interface locations were selected. This was investigated during the initial interface condition modeling. There is an agreement in both frequency and amplitude between the model and tests at each stage of assembly (FBS, RBE2, and CS), though the experimental FBS is slightly higher in frequency.

The only source of difference between model and test FBS results are the plate FRFs. As discussed in the reassessment of assumptions, the off-axis test interface FRFs contain more dynamics than the model. The accelerometers used to collect the plate FRFs have a

transverse sensitivity of ≤5%. It is also difficult to impact perfectly along one axis without exciting the other axes. Theoretically, the off-axis response should be zero (like the model), but the impacts are causing off-axis excitation, and the accelerometers are recording it. This off-axis excitation is a combination of imperfect orthogonal impacts and not impacting at an off-axis modal node, exciting the off-axis modes. When referring back to the plate drive point FRFs (Figure 6.17) and transverse FRFs (Figure 6.17), the test data off-axis peaks align with the in-axis peaks, but the amplitudes are about two orders of magnitude lower, correlating to the ≤5% transverse sensitivity specification.

The kernel within LM-FBS calculations is the sum of each drive point interface measurement between the plate and payload FRFs. Within the model kernel, the plate FRFs dominate the sum of the in-axis measurements, while the payload FRFs dominate the sum of the off-axis measurements. Within the test kernel, the plate FRFs dominate the sum of all measurements. Figure 7.5 shows the kernel breakdown for the center configuration between test and model for the sum of plate drive point 1X and payload drive point 3Y. This shows the discrepancies in off-axis kernels between model and test. Note that the kernel is referred to the FRFs before inversion. Figure 7.6 shows the kernel breakdown for the center configuration between test and model for the sum of plate drive point 1Z and payload drive point 3Z, showing the agreement of the in-axis dynamics between model and test.

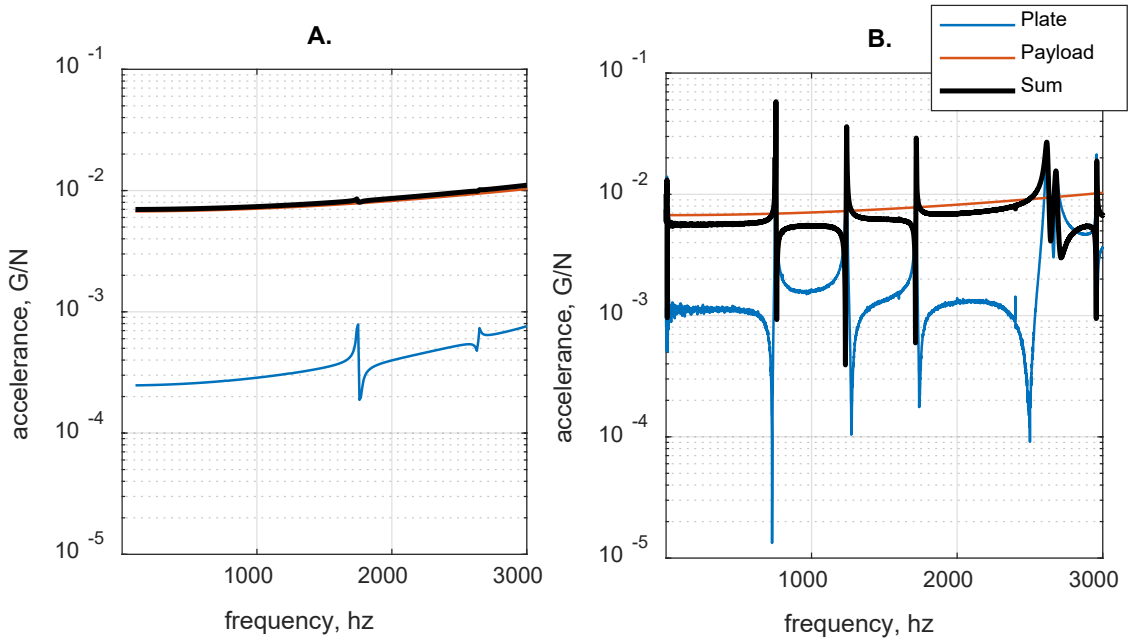

Figure 7.5 *A*, kernel components between plate interface 1:+X and payload interface 3:+Y of model LM-FBS in the center configuration, and *B*, kernel components between the same plate and payload interface nodes of test LM-FBS in the center configuration.

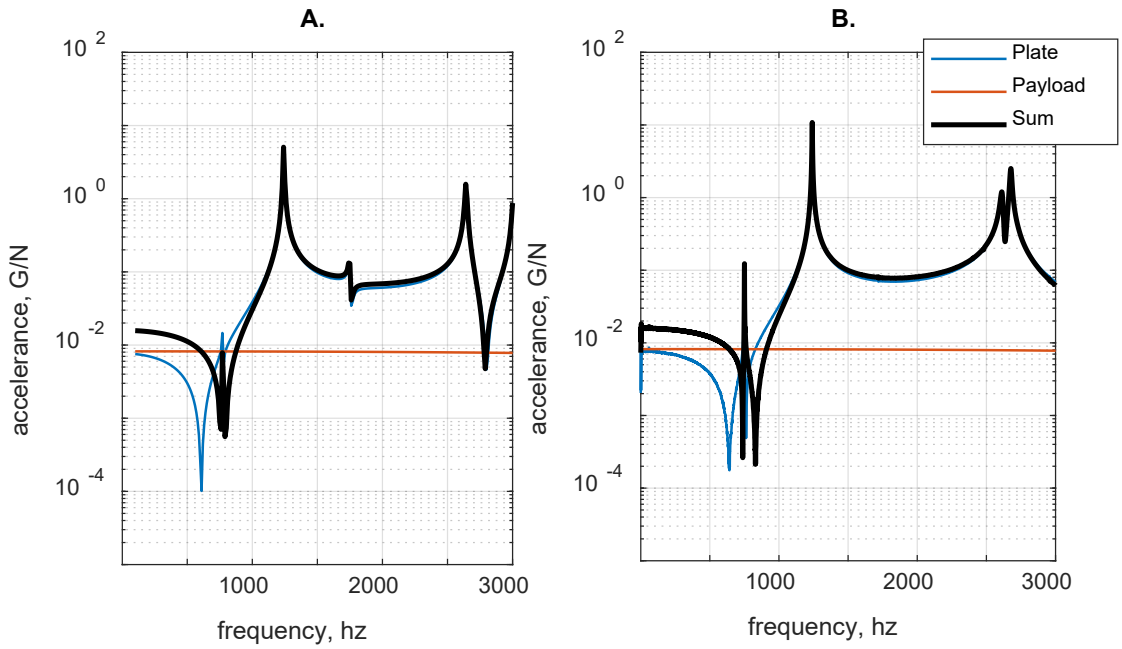

Figure 7.6. *A*, kernel components between plate interface 1:+Z and payload interface 4:+Z of model LM-FBS in the center configuration, and *B*, kernel components between the same plate and payload interface nodes of test LM-FBS in the center configuration.

Comparing all the model FRFs of the corner configuration, it can be observed that the RBE2 adjusted assembly well represents the FBS calculations. However, both are still lower in frequency than the truth assembly (Figure 7.7). The same can be said for all test FRFs of the corner configuration (Figure 7.8).

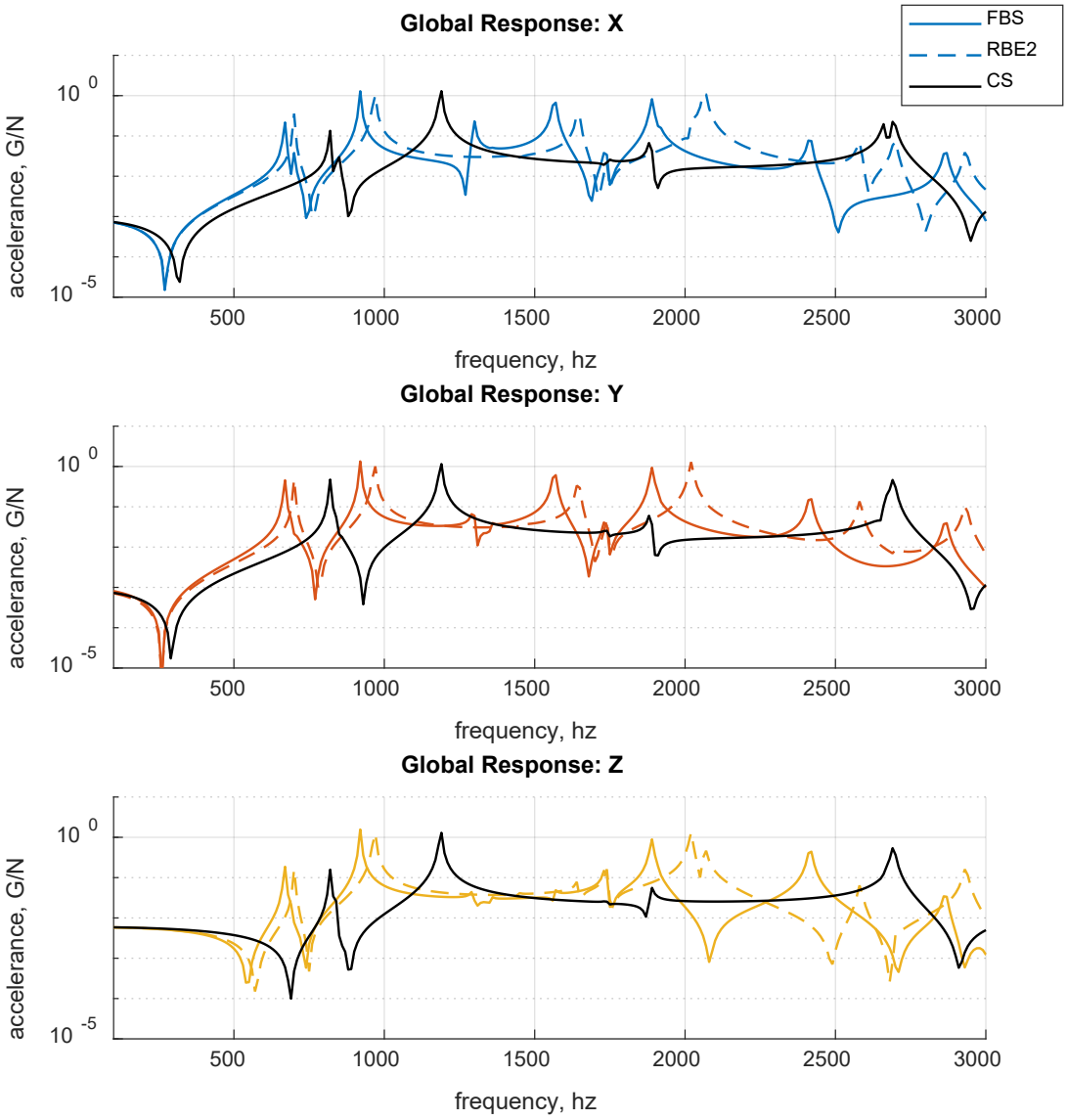

Figure 7.7 Model frequency response functions of the corner configuration comparing FBS, RBE2, and contact surface dynamics of the global input/response between all three axes.

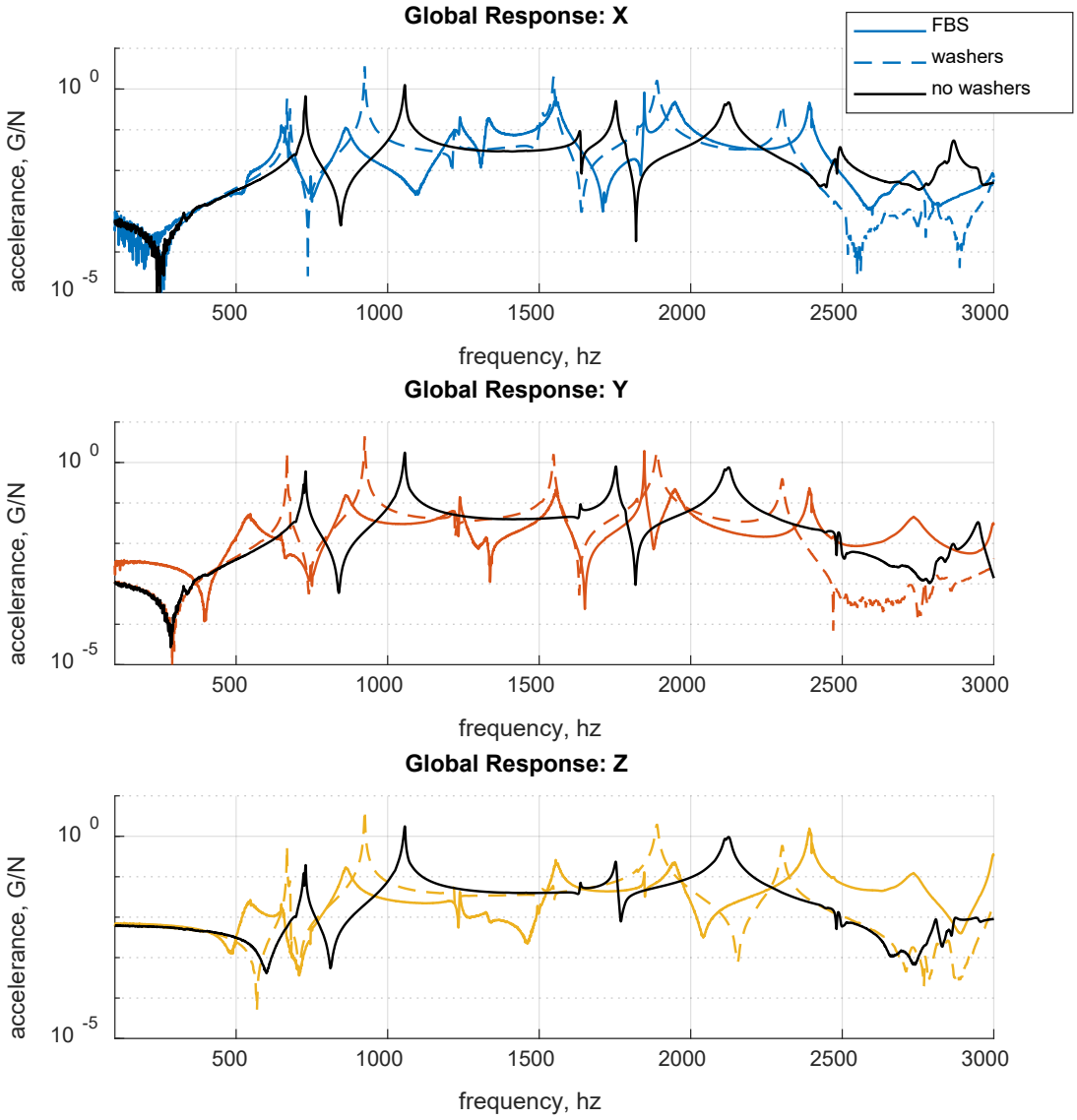

Figure 7.8 Test frequency response functions of the corner configuration comparing FBS, RBE2, and contact surface dynamics of the global input/response between all three axes.

The important observation to make is that the model FBS data can predict the test assembly. Figure 7.9 (below) shows that the model FBS and test adjusted assembly of the corner configuration are very close in amplitude and frequency, especially at the knee frequency.

Even though both model FBS and adjusted test are lower in frequency than the test truth assembly, the difference is coming from the interface dynamics.

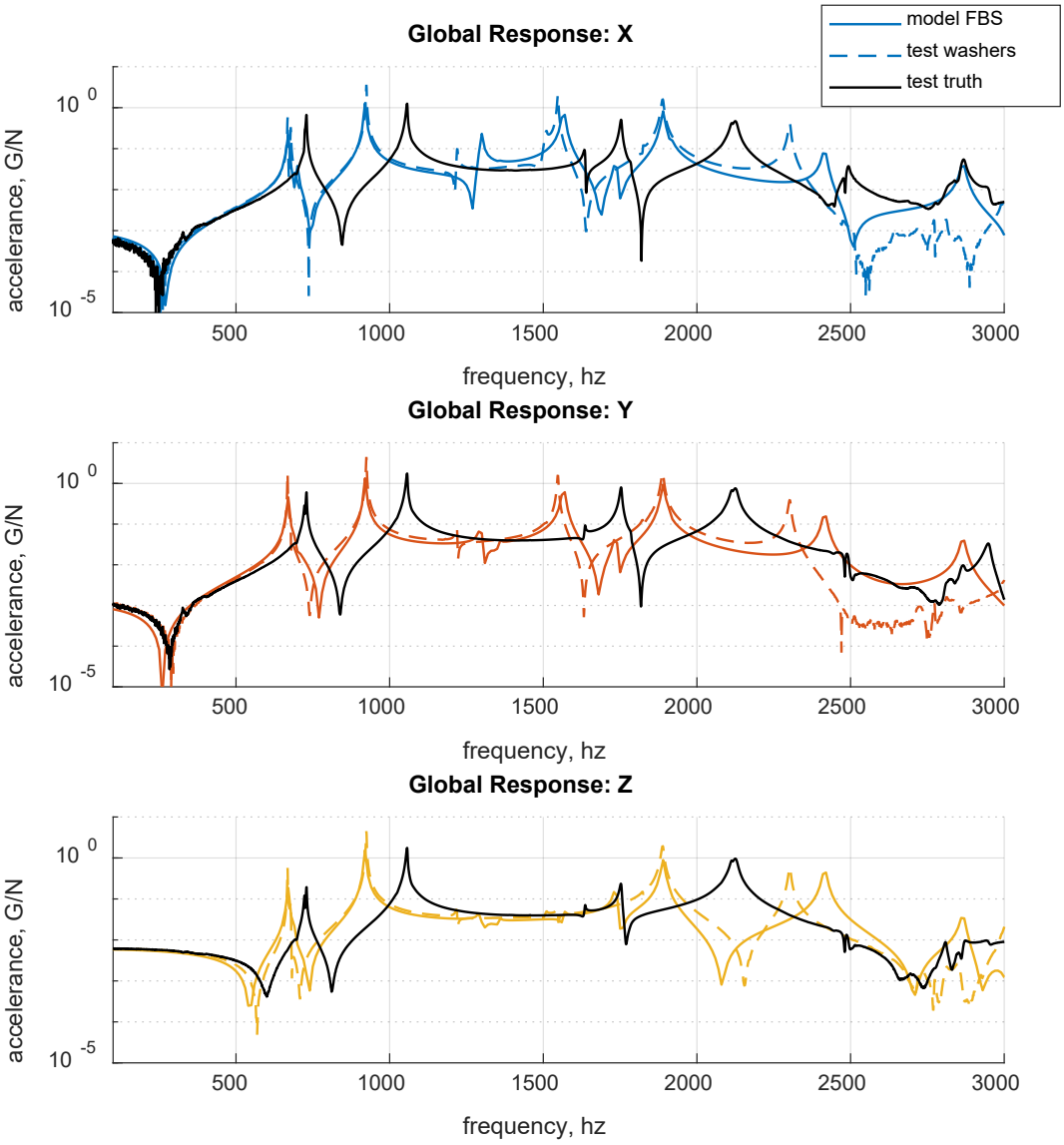

Figure 7.9 Corner configuration comparison of model FBS and test adjusted assembly to test truth assembly, separated by axes.

7.3 Validation of model and test results

The same comparisons between model FBS, test adjusted assembly, and test truth assembly are made below for the center (Figure 7.10) and bottom (Figure 7.11) configurations.

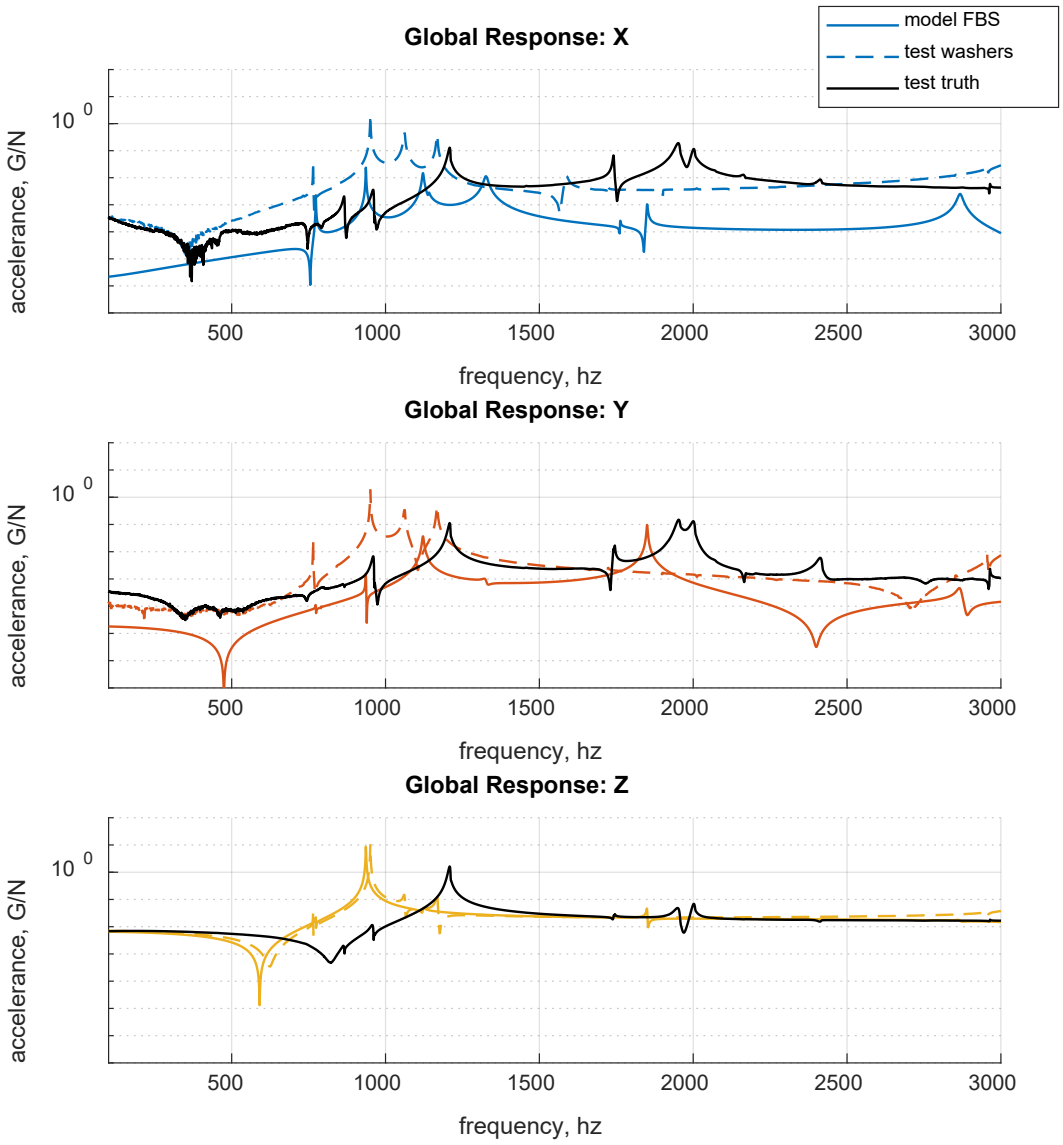

Figure 7.10 Center configuration comparison of model FBS and test adjusted assembly to test truth assembly, separated by axes.

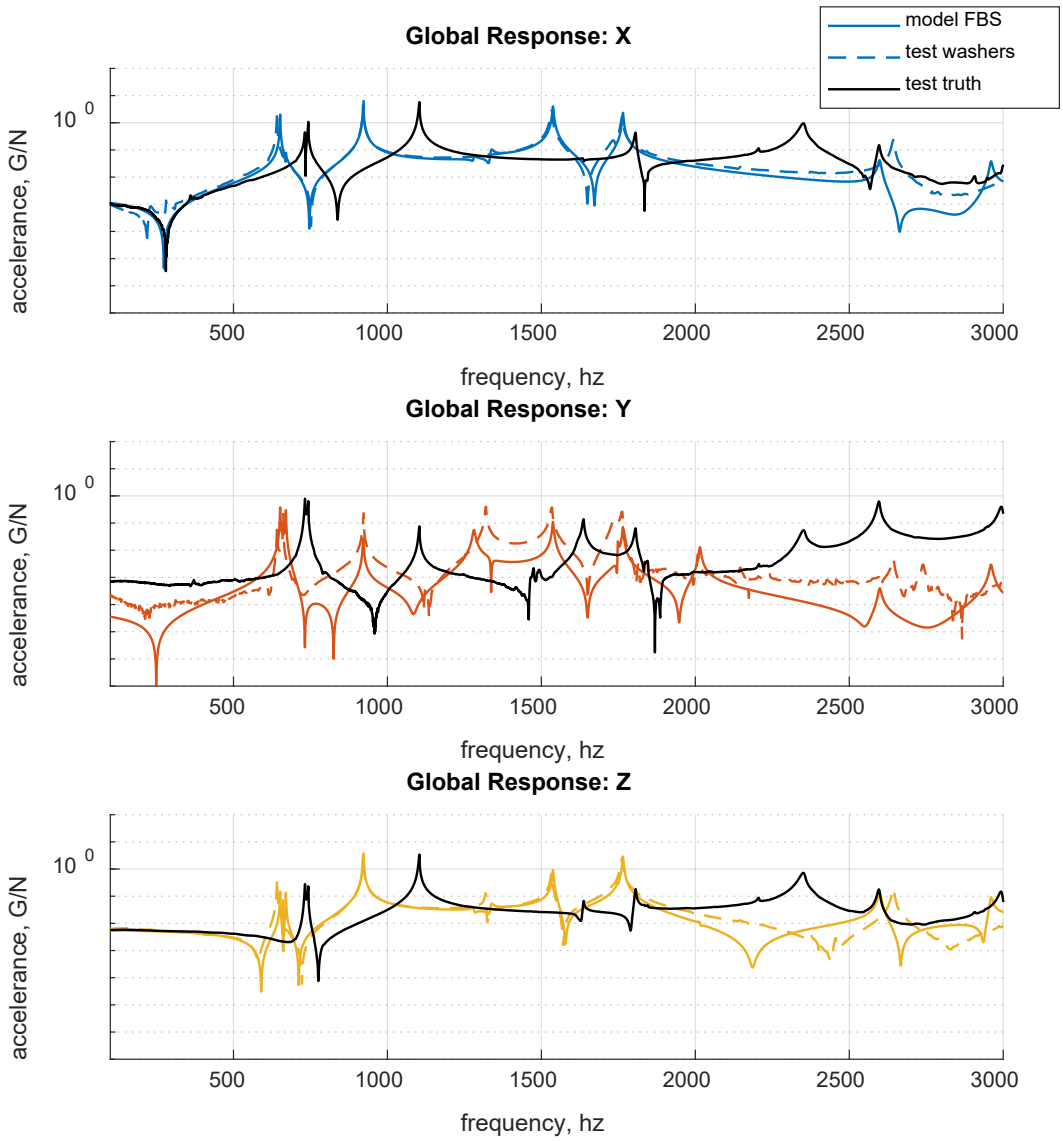

Figure 7.11 Bottom configuration comparison of model FBS and test adjusted assembly to test truth assembly, separated by axes.

The knee frequencies, amplitudes, and general dynamics were compared across model, test, FBS, and assemblies for all three configurations. Figures below focus on the FRF dynamics around the knee frequency (500 to 1500 Hz) for the center (Figure 7.12), bottom (Figure 7.13), and corner (Figure 7.14) configurations, respectively.

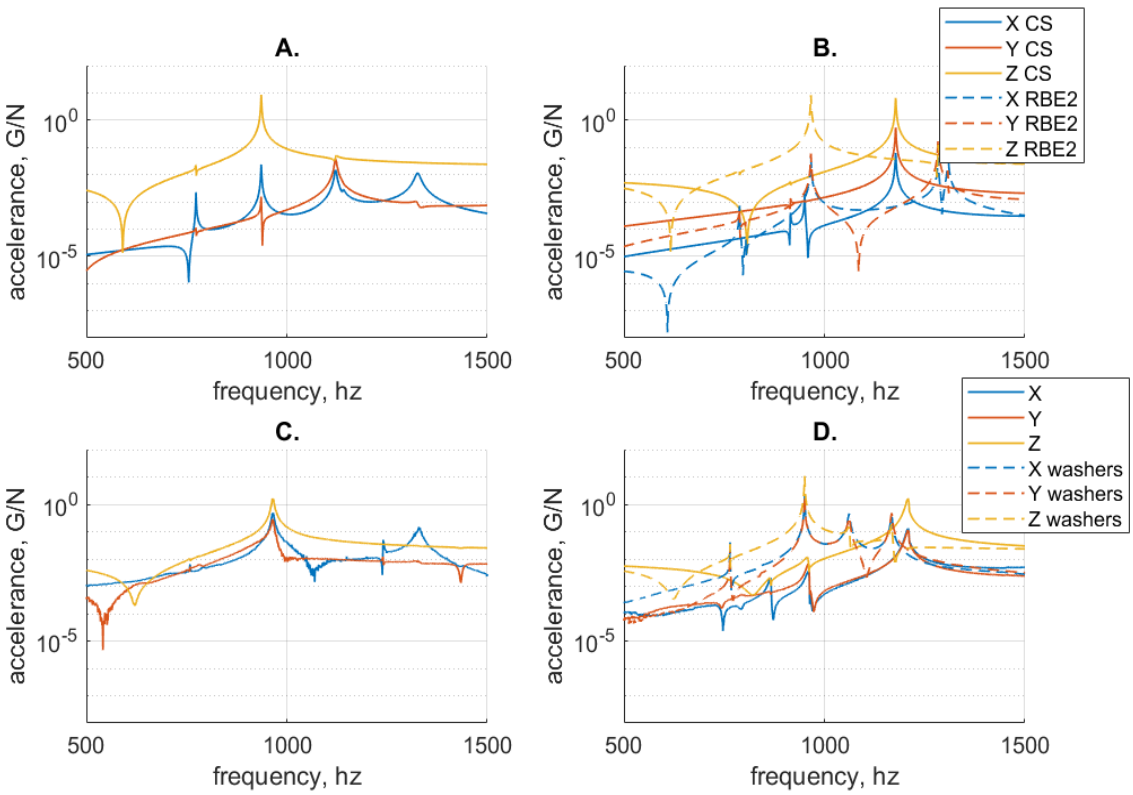

Figure 7.12 Center configuration comparison of FRFs around the knee frequency of the model FBS (A), model assemblies (B), test FBS (C), and test assemblies (D).

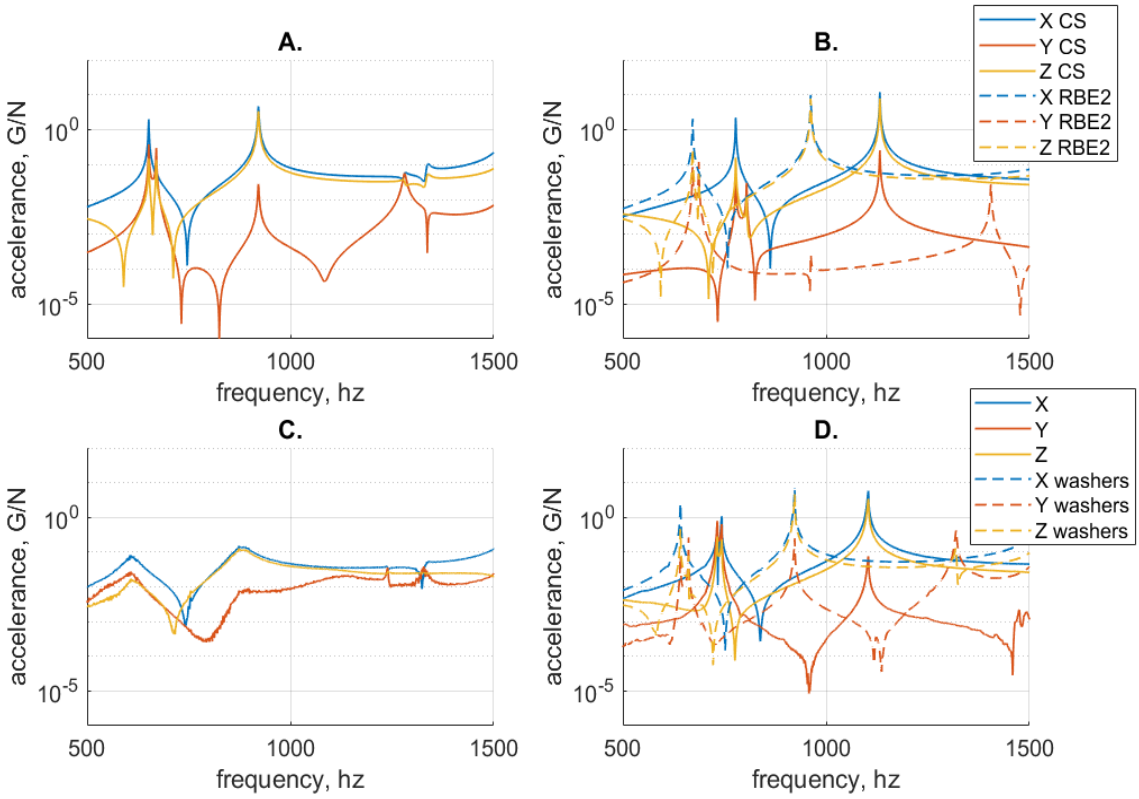

Figure 7.13 Bottom configuration comparison of FRFs around the knee frequency of the model FBS (A), model assemblies (B), test FBS (C), and test assemblies (D).

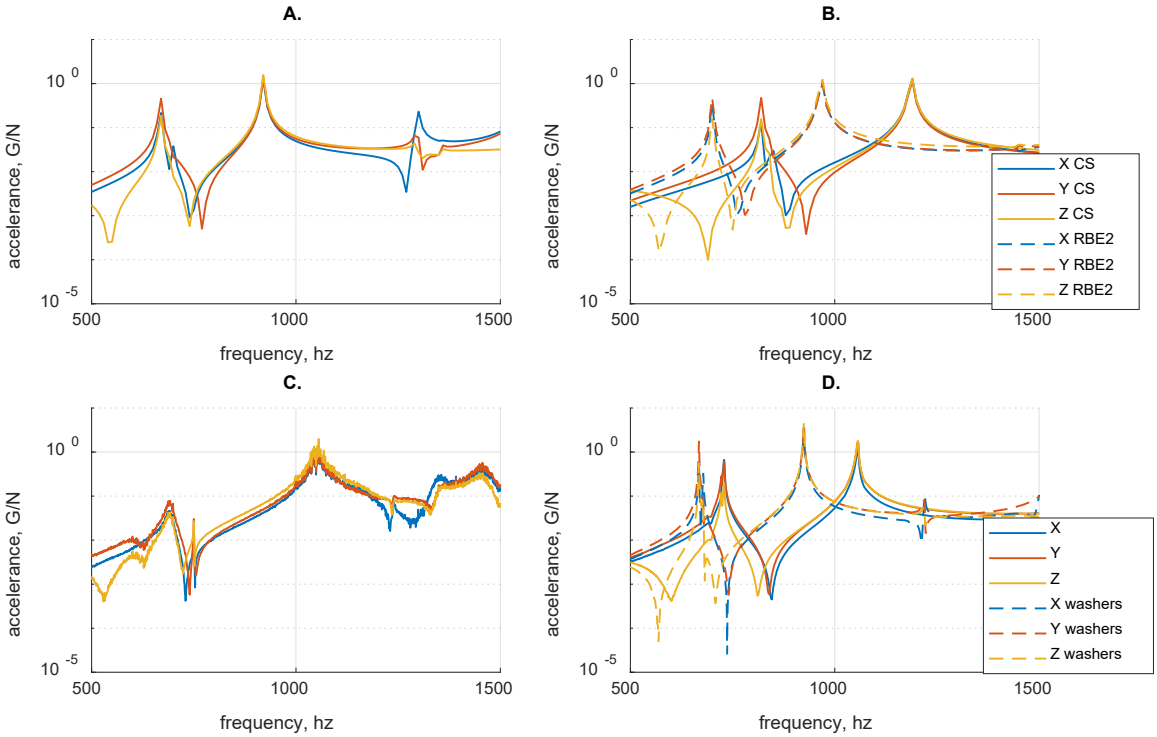

Figure 7.14 Corner configuration comparison of FRFs around the knee frequency of the model FBS (A), model assemblies (B), test FBS (C), and test assemblies (D).

8 Conclusions and recommendations

This chapter starts by discussing observations from the results and how this process can be practically implemented. Then, options to re-assess the assumptions and better correlate the frequency based substructuring method are covered. Next steps and general comments about shock and vibration are discussed. The chapter concludes with four key summary points.

8.1 Discussion

The general process of using LM-FBS iteratively to minimize an objective function can be applied to any assembly, especially modular assemblies or during the early design phases. Specifically, this process works well for optimizing multi-axis shock tests because of the flexibility to change the test object (payload) and adapt to different tests. Previously, multi-axis shock tests were performed through "guess and check" but iterating and satisfying an objective function takes all the "guessing" and "checking" out of finding the optimal assembly. This method can be tuned specifically to each test facility, where a "library" of resonant fixtures and shock impulses can be created, stored, and used for future tests. Adding another subsystem, such as a small mass or damping material, could add even more possibilities for a multi-axis shock test. Theoretically, a single resonant plate could be used for a variety of tests requiring different SRS tolerance requirements and knee frequencies.

It is recommended that this method be implemented using finite element model data. Experimental FBS has been proven to be quite difficult, especially in controlling and monitoring assumptions. The most time-consuming part of this method would be building the initial library of fixture FRFs and keeping track of the bookkeeping. However, this would only have to be done once for each resonant fixture. But first, the assumptions of this thesis should be re-assessed to bring the FBS results closer to the truth assembly. At some point, a real resonant plate shock test with a projectile should be performed to verify the optimization results. The optimization should be repeated while altering the impact location, orientation, and force.

Addressing and re-evaluating the assumptions that were initially decided for this thesis could improve the correlation between FBS and truth assemblies. The initial MATLAB investigations showed that including the rotary DOFs on a full 6-DOF problem is necessary for the FBS and truth assemblies to agree. This can be addressed within the FEM.

Increasing the number of interface nodes should bring the FBS and truth assemblies closer together. A more practical way to define a large number of the interface DOFs is through the use of a transmission simulator (section 3.8). The large number of interface DOFs can be measured through the transmission simulator, experimentally or analytically. This method can also help constrain the interface rotary DOFs and displacements of the experimental data for more accurate interface FRFs.

Though an optimal assembly was identified through SRS data, the dynamic differences between FBS and truth assemblies should be investigated further. Alluding back to the laboratory testing limitations (chapter 3.7), just because the SRSs are experiencing the same excitation across each axis doesn't mean the dynamics are the same. After effort is made to bring the FBS assembly closer to the truth assembly, the inherent differences between the two should be quantified different domains.

The end goal of the laboratory test is to inflict the same damage potential to a structure, which can be quantified in terms of forces, dynamics, responses, and stresses. Since this optimization was performed on SRSs, the question of "*are these dynamics the same?*" hasn't been answered. Some insight could be gained through comparing FRFs and mode shapes of modal substructuring and frequency based substructuring results. Other possible comparisons to investigate are equivalent forces at the interface DOFs, modal velocity, and stress. The optimization could be performed on FRFs or mode shapes, while still producing a valid multi-axis shock test configuration.

8.2 Summary

1. There are configurations of the resonant plate assembly that produce equal-magnitude in-axis and off-axis responses. These configurations can be found by optimizing the shock response spectrum through iterative LaGrange-Multiplier frequency based substructuring.
2. This process can be expanded to include more payload locations, rotations, and response nodes. Changing the impact location, magnitude, and direction, and adding mass or damping material to structurally modify the resonant plate can also be added into the iteration process for a fully tunable multi-axis resonant plate.
3. There is room for improvement within interface dynamics used for frequency based substructuring, either test or model, to closer correlate the substructured assembly to the truth assembly. Including rotary degrees of freedom in the model and using a transmission simulator on both the test and finite element model are two options.
4. It would be beneficial to compare these results in different domains and try different substructuring techniques, particularly looking at mode shapes and the use of modal substructuring.

9 Reference list

[1] R. J. Allemang, *Vibrations: Analytical and Experimental Modal Analysis*. Cincinnati, OH, 1994.

[2] P. Avitabile, *MODAL TESTING A PRACTITIONER'S GUIDE*. Hoboken, NJ: John Wiley & Sons Ltd, The Society for Experimental Mechanics, 2018, p. 524.

[3] W. Heylen, S. Lammens, and P. Sas, *Modal Analysis Theory and Testing*. Belgium.

[4] D. deKlerk, D. J. Rixen, and S. N. Voormeeren, "General Framework for Dynamic Substructuring: History, Review, and Classification of Techniques," *AIAA,* vol. 46, no. 5, May 2008 2008.

[5] M. V. van der Seijs, *Experimental Dynamic Substructuring*. 2016.

[6] B. Jetmundsen, R. L. Bielawa, and W. G. Flannelly, "Generalized Frequency Domain Substructure Synthesis," *American Helicopter Society,* vol. 33, no. 1, pp. 55-64, 1988.

[7] J. P. DeClerck, "MEEM5702: Analytical VibroAcoustics," ed, 2018.

[8] S. W. Smith, *Digital Signal Processing: A Practical Guide for Engineers and Scientists*. Burlington, MA: Newnes, 2003.

[9] S. Rubin and K. Ahlin, "Chapter 20 Shock Data Analysis," in *Harris' Shock and Vibration Handbook*, A. G. P. Piersol, Thomas L, Ed.: The McGraw-Hill Companies, Inc.

[10] T. Irvine, "AN INTRODUCTION TO THE SHOCK RESPONSE SPECTRUM," July 9, 2012 2012.

[11] D. O. Smallwood, "AN IMPROVED RECURSIVE FORMULA FOR CALCULATING SHOCK RESPONSE SPECTRA," in *VibrationData.com* vol. August 2001, ed: Tom Irvine, 2001.

[12] T. Irvine, "Derivation of the Filter Coefficients for the Ramp Invariant Method as Applied to Base Excitation of a Single-degree-of-Freedom System," May 17, 2018.

[13] J. Tuma and P. Koci, "CALCULATION OF SHOCK RESPONSE SPECTRUM," presented at the DYNAMICS OF MACHINES, Prague, 2009.

[14] M. Biot, "Transient Oscillations in Elastic Systems," Doctorate in Aeronautics Engineering and Applied Sciences PhD Dissertation, California Institute of Technology, 1932.

[15] H. C. Pusey, "An Historic View of Shock and Vibration," *Shock & Vibration,* no. Dynamic Testing Reference, p. 4, 2008.

[16] (1949). *654, Design of a Multifrequency Reed-Type Shock Gage with an Inertia-Operated Trigger*.

[17] C. Sisemore, "Shock Response Spectrum Primer," PowerPoint Presentation, 2018.

[18] *NASA-STD-7003A Pyroshock Test Criteria*, NASA-STD-7003A, 2011.

[19] *MIL-STD-810G chg.1: Environmental Engineering Considerations and Laboratory Tests*, 2014.

[20] J. Eriksson and M. Hansson, "Measuring and Analysis of Pyrotechnic Shock," Masters of Science in Mechanical Engineering, Applied Acoustics and Structural Mechanics, Chalmers University of Technology, Gothenburg, 1999.

[21] H. A. Gaberson and R. H. Chalmers, "MODAL VELOCITY AS A CRITERION OF SHOCK SEVERITY," *Shock & Vibration Bulletin,* vol. 40, 1969.

[22] J. S. Cap and D. O. Smallwood, "A Methodology for Defining Shock Tests Based on Shock Response Spectra and Temporal Moments," 1997.

[23] S. Smith, "Chapter 13: Shock and Vibration, Data Acquisition," in *Harris' Shock and Vibration Handbook*, A. G. Piersol and T. L. Paez, Eds.: The MicGraw-Hill Companies, Inc.

[24] S. Smith, "The Effect of Out-Of-Band Energy on the Measurement and Analysis of Pyroshock Data," 2009.

[25] V. Bateman, "The MIL-STD-810G, Change 1, Solution to the Aliasing Problem," *Sound and Vibration,* vol. 47, no. 3, pp. 4-5, 2013.

[26] V. Bateman, H. Himelblau, and R. Merritt, "Validation of Pyroshock Data," *Sound and Vibration,* vol. 46, no. 3, pp. 6-11,14, 2012.

[27] V. Bateman, "Chapter 27 Shock Testing Machines," in *Harris' Shock and Vibration Handbook*, A. G. Piersol and T. L. Paez, Eds.: The McGraw-Hill Companies, Inc.

[28] V. I. Bateman and N. T. Davie, "Chapter 28 Pyroshock Testing," in *Harris' Shock and Vibration Handbook*, A. G. Piersol and T. L. Paez, Eds.: The McGraw-Hill Companies, Inc.

[29] W. Larsen, J. R. Blough, J. DeClerck, V. Charles, D. Soine, and R. Jones, "Understanding Multi-Axis SRS Testing Results," presented at the International Modal Analysis Conference (IMAC), Orlando, FL, 2018.
[30] W. S. Larsen, "ANALYSIS OF THE SHOCK RESPONSE SPECTRUM AND RESONANT PLATE TESTING METHODS," Master of Science, Mechanical Engineering, Michigan Technological University, 2018.
[31] M. Spletzer and C. Sisemore, "DESIGN OF A RESONANT PLATE SHOCK FIXTURE TO ATTENUATE EXCESSIVE HIGH-FREQUENCY ENERGY INPUTS," 2017.
[32] R. Hsieh, R. M. Moore, S. Sroka, J. Lake, C. Stull, and P. Avitabile, "Analysis and Dynamic Characterization of a Resonant Plate for Shock Testing," in *International Modal Analysis Conference (IMAC)*, 2013, vol. 6: Society for Experimental Mechanics.
[33] B. A. Ferri and R. N. Hopkins, "A Method for Determining Impact Force for Single and Tri Axis Resonant Plate Shock Simulations," presented at the International Modal Analysis Conference (IMAC), Orlando, FL, 2019.
[34] R. Hopkins and C. Sisemore, "DESIGN OF A RESONANT PLATE SHOCK TEST FOR SIMULTANEOUS MULTI-AXIS EXCITATION," presented at the Shock and Vibration Exchange, Dallas, TX, 2019.
[35] J. M. Harvie and M. van der Seijs, "Application of Transfer Path Analysis Techniques to the Boundary Condition Challenge Problem," presented at the International Modal Analysis Conference, Orlando, FL, 2019.
[36] J. M. Harvie and R. Mayes, "Quantification of Dynamic Differences Between Boundary Conditions for Environment Specification Improvement," presented at the International Modal Analysis Conference (IMAC), Orlando, FL, 2018.
[37] J. M. Harvie, "Using Modal Substructuring to Improve Shock & Vibration Qualification," presented at the International Modal Analysis Conference (IMAC), Orlando, FL, 2018.
[38] T. F. Schoenherr, J. Rouse, and J. M. Harvie, "Quantification of Modal Truncation with Respect to a Test Fixture's Ability to Replicate a Structural Dynamic Environment," 2019.
[39] J. M. Reyes, P. Avitabile, R. Jones, and D. Soine, "Fixture Neutralization Method - Adjustment of Vibration Response to Account for Fixture-Test Article Dynamic Coupling Effects Using Measured Frequency Response Functions," 2019.
[40] B. Zwink, P. Avitabile, and D. G. Tipton, "Modal Projection Matching," presented at the International Modal Analysis Conference (IMAC), Orlando, FL, 2019.
[41] A. M. Steenhoek, M. W. van der Kooij, M. L. J. Verhees, D. D. van den Bosch, and J. M. Harvie, "Test-based modeling, source characterization and dynamic substructuring techniques applied on a modular industrial demonstrator," in *International Modal Analysis Conference (IMAC)*, Orlando, FL, 2019.
[42] J. Brunetti, W. D'Ambrogio, and A. Fregolent, "Dynamic Substructuring of Agricultural Tractors and Mounted, Semi-mounted and Trailed Machinery," in *International Modal Analysis Conference (IMAC)*, Orlando, FL, 2019.
[43] D. deKlerk, D. J. Rixen, and J. deJong, "The Frequency Based Substructuring (FBS) Method reformulated according to the Dual Domain Decomposition Method."
[44] D. Nicgorski and P. Avitabile, "Conditioning of FRF measurements for use with frequency based substructuring," *Mechanical Systems and Signal Processing,* vol. 24, pp. 340-351, 2010.
[45] F. Trainotti, T. F. C. Berninger, and D. J. Rixen, "USING LASER VIBROMETRY FOR PRECISE FRF MEASUREMENTS IN EXPERIMENTAL SUBSTRUCTURING," 2019.
[46] K. Wyckaert, P. Mas, and K. O. Xu, "THE VIRTUES OF STATIC AND DYNAMIC COMPENSATION FOR FRF BASED SUBSTRUCTURING."
[47] P. Avitabile, "TWENTY YEARS OF STRUCTURAL DYNAMIC MODIFICATION - A REVIEW," presented at the International Modal Analysis Conference (IMAC) XX, Los Angelos, CA, 2002.
[48] K. C. Konjerla, "FRF Based Experimental-Analytical Dynamic Substructuring using Transmission Simulator," Master's of Science, Engineering Mechanics, KTH Royal Institute of Technology, Stockholm, Sweden.

[49] R. L. Mayes, "A Modal Craig-Brampton Substructure for Experiments, Analysis, Control and Specifications," presented at the International Modal Analysis Conference (IMAC), Orlando, FL, 2018.
[50] S. N. Voormeeren, D. deKlerk, and D. J. Rixen, "Uncertainty quantification in experimental frequency based substructuring," *Mechanical Systems and Signal Processing,* vol. 24, pp. 106-118, 2010.

A LaGrange-multiplier frequency based substructuring derivation

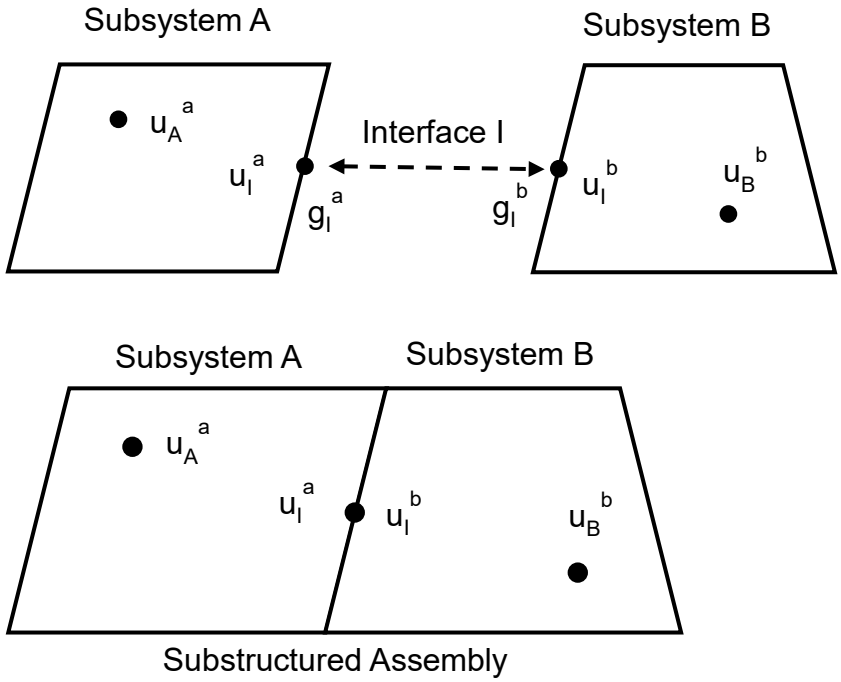

For this sample derivation, subsystem A and B each have one external and one interface DOF. These DOFs are represented as *u* and can be displacement, velocity, or acceleration. In the case of using measured FRFs from impact tests, *u* is acceleration, making the FRFs *accelerance*. These DOFs are arranged in block matrix form. Note that the relationship between every DOF on each subsystem is required for LM-FBS.

$$H^a = \begin{bmatrix} h_{AA} & h_{AI} \\ h_{IA} & h_{II} \end{bmatrix}$$

$$H^b = \begin{bmatrix} h_{BB} & h_{BI} \\ h_{IB} & h_{II} \end{bmatrix}$$

$$H = \begin{bmatrix} [H^a] & 0 \\ 0 & [H^b] \end{bmatrix}$$

Where *h* is the vector frequency response function between a single input and single output across all sampled frequencies, and H is the 3D matrix of all input and output DOFs across all sampled frequencies.

$$u^a = \begin{Bmatrix} u_A \\ u_I \end{Bmatrix}$$

$$u^b = \begin{Bmatrix} u_B \\ u_I \end{Bmatrix}$$

$$u = \begin{Bmatrix} u^a \\ u^b \end{Bmatrix}$$

Derived from the EOM, Z is inertance (or dynamic mass), the inverse of accelerance (represented as H).

$$H = \frac{u}{f} = Z^{-1}$$

The first condition that must be met, the *compatibility condition*, states that the interface DOFs have the same displacement/velocity/acceleration.

$$u_I^a = u_I^b$$

$$u_I^a - u_I^b = 0$$

$$Bu = 0$$

$$B = [0 \quad 1 \quad 0 \quad -1]$$

Because the interface acceleration of subsystem A is at global DOF 2, and the interface acceleration of subsystem B is at global DOF 4. The negative sign is added to either DOF to satisfy their equivalence. The signed Boolean matrix has as many rows as coupling pairs, and as many columns as total DOFs.

The second condition, the *force equilibrium condition*, states the interface forces, g, are equal and opposite.

$$g_I^a = -g_I^b$$

These interface forces are not explicitly solved for and are represented as LaGrange multipliers.

$$g_I^a = -g_I^b = \lambda$$

$$g = B^T\lambda$$

Combine the interface forces, g, and the external forces, f, into a single expression for force:

$$F = f + g = Zu + B^T\lambda$$

$$F = Zu + B^T\lambda$$

Both conditions can be met simultaneously by using LaGrange multipliers and the signed Boolean matrix. The top rows satisfy the force equilibrium condition and the bottom rows satisfy the compatibility condition.

$$\begin{bmatrix} Z & B^T \\ B & 0 \end{bmatrix} \begin{Bmatrix} u \\ \lambda \end{Bmatrix} = \begin{Bmatrix} F \\ 0 \end{Bmatrix}$$

These equations can be rearranged to get the final LM-FBS equation by first using the measured FRFs H instead of the inverse, Z:

$$Zu = F - B^T\lambda$$

$$u = H(F - B^T\lambda)$$

Substitute back into the compatibility condition:

$$Bu = B\big(H(F - B^T\lambda)\big) = 0$$

Solve for the LaGrange Multiplier:

$$BHB^T\lambda = BHF$$

$$\lambda = (BHB^T)^{-1}BHF$$

Substitute back into the combined conditions:

$$u = H(F - B^T(BHB^T)^{-1}BHF$$

Expand and simplify:

$$u = HF - HB^T(BHB^T)^{-1}BHF$$

$$u = F(H - HB^T(BHB^T)^{-1}BH)$$

$$\widehat{H} = \frac{u}{F}$$

$$\widehat{H} = H - HB^T(BHB^T)^{-1}BH$$

In this example, H is a 4x4 matrix and B is a 1x4 vector. In the general case, H will be the size of all subsystem DOFs (always square), and B will have a row for each interface and the same number of columns as H.

The resulting substructured FRFs, $\widetilde{H}$, will have the same number of DOFs as H. The number of redundant DOFs is equal to the number of interface DOFs. In this case, there are two DOFs that are equivalent (1 redundancy), global DOFs 2 & 4.

In the case of a single resonant plate configuration, subsystem A (circular plate + impact pad) has one external and 12 interface DOFs (4 nodes, 3 DOFs each). Subsystem B (payload) has 12 interface and 15 external DOFs (five nodes, 3 DOFs each). Subsystem A has 13 DOFs and subsystem B has 27 DOFs, making a total of 40 DOFs for the substructured assembly. The signed Boolean matrix is 12 x 40. This occurs over 990 frequency lines (100 Hz to 10 kHz in 10 Hz increments).

The actual implementation in MATLAB performs the LM-FBS calculations at each frequency line, pulling the required H values from a 3D matrix and storing the substructured assembly $\widetilde{H}$ values into a new 3D matrix.

B Resonant plate mode shapes

The mode shapes between 1 and 10,000 Hz were solved for the three configurations using HyperMesh Normal Modes process. The modal solver was selected as Lanczos. Below is a table of the first 20 modes for each configuration. This is **excluding the first 6 rigid body modes**. These calculations were done on the truth FEM with the contact surface. The circular geometry of the resonant plate produces repeated roots, revealed as pairs of modes that are similar in frequency and shape.

The third mode is the knee frequency. The shape of the SRS and whether or not it remains inside the +/- 6 dB tolerance bands depends on the participation of the modes surrounding the knee mode – modes 1, 2, 4, and 5. The mode shapes for the first five modes of each configuration are below.

Mode	Center	Bottom	Corner
1	915.22	777.65	819.01
2	950.77	804.43	844.90
3	1177.73	1132.10	1187.36
4	1790.15	1682.01	1741.03
5	1792.12	1865.33	1885.20
6	1901.58	2422.30	2662.12
7	1926.76	2705.03	2692.55
8	3035.69	3170.45	3107.84
9	3036.49	3217.17	3327.95
10	4531.44	4041.31	3906.55
11	4536.23	4493.96	4323.10
12	5101.59	4835.84	4816.87
13	5121.65	4886.20	4844.31
14	5279.53	4914.90	5036.78
15	5446.43	5121.26	5094.10
16	5455.69	5456.67	5462.22
17	5783.74	5601.30	5592.61
18	5858.34	5980.07	5808.89
19	5932.76	6136.70	6159.60
20	6008.57	6359.57	6372.67

B.1 Center configuration

Mode 1:

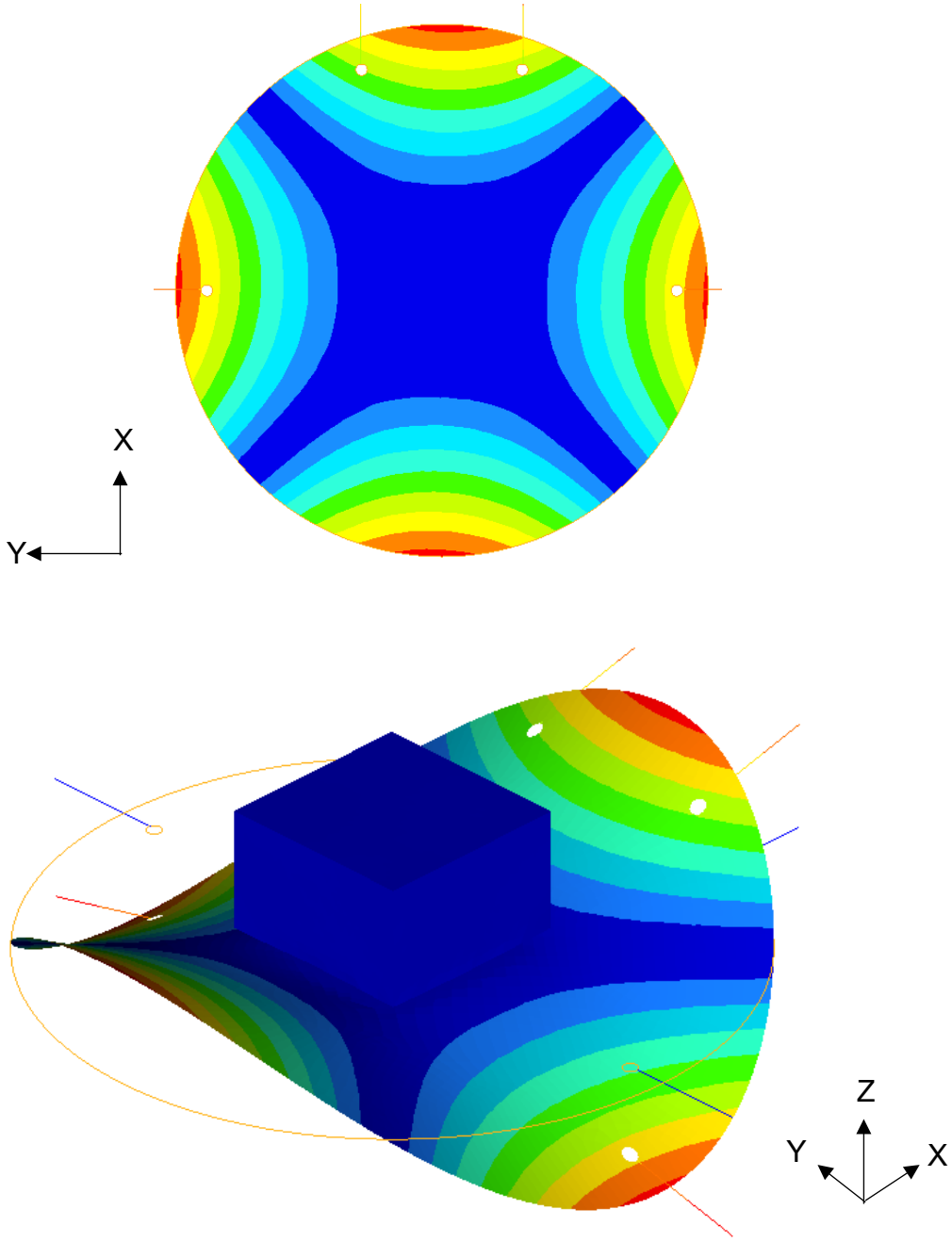

Mode 2:

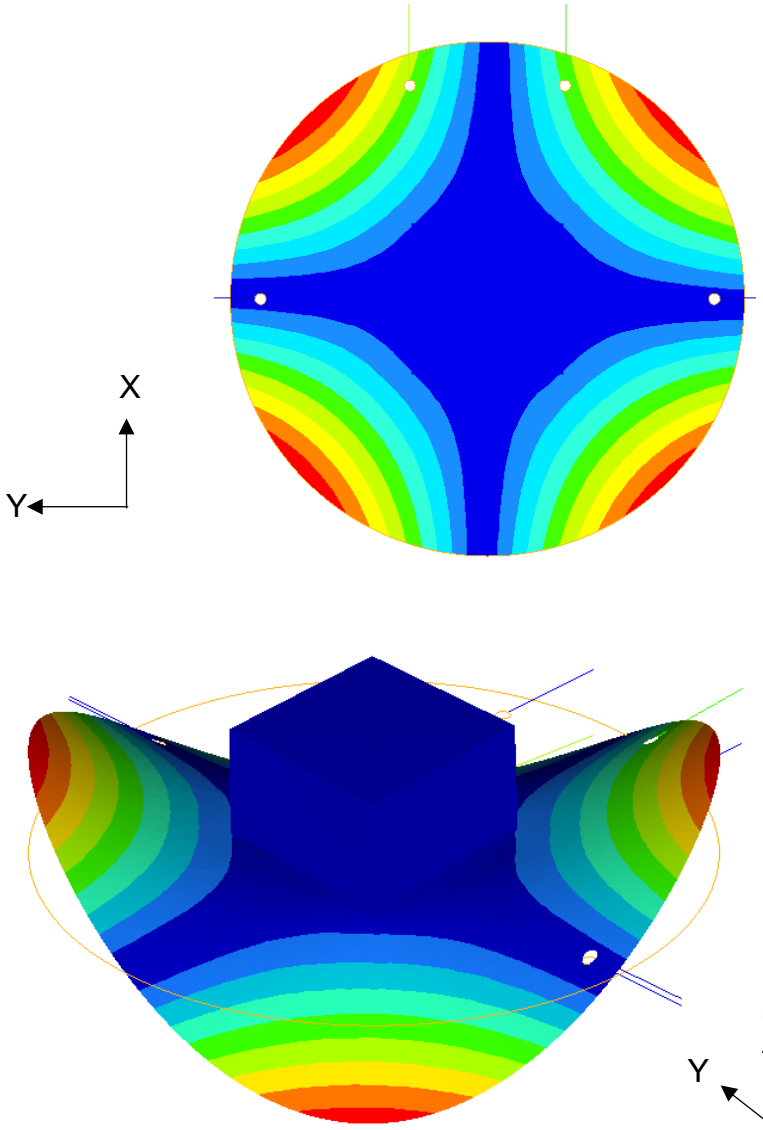

Mode 3:

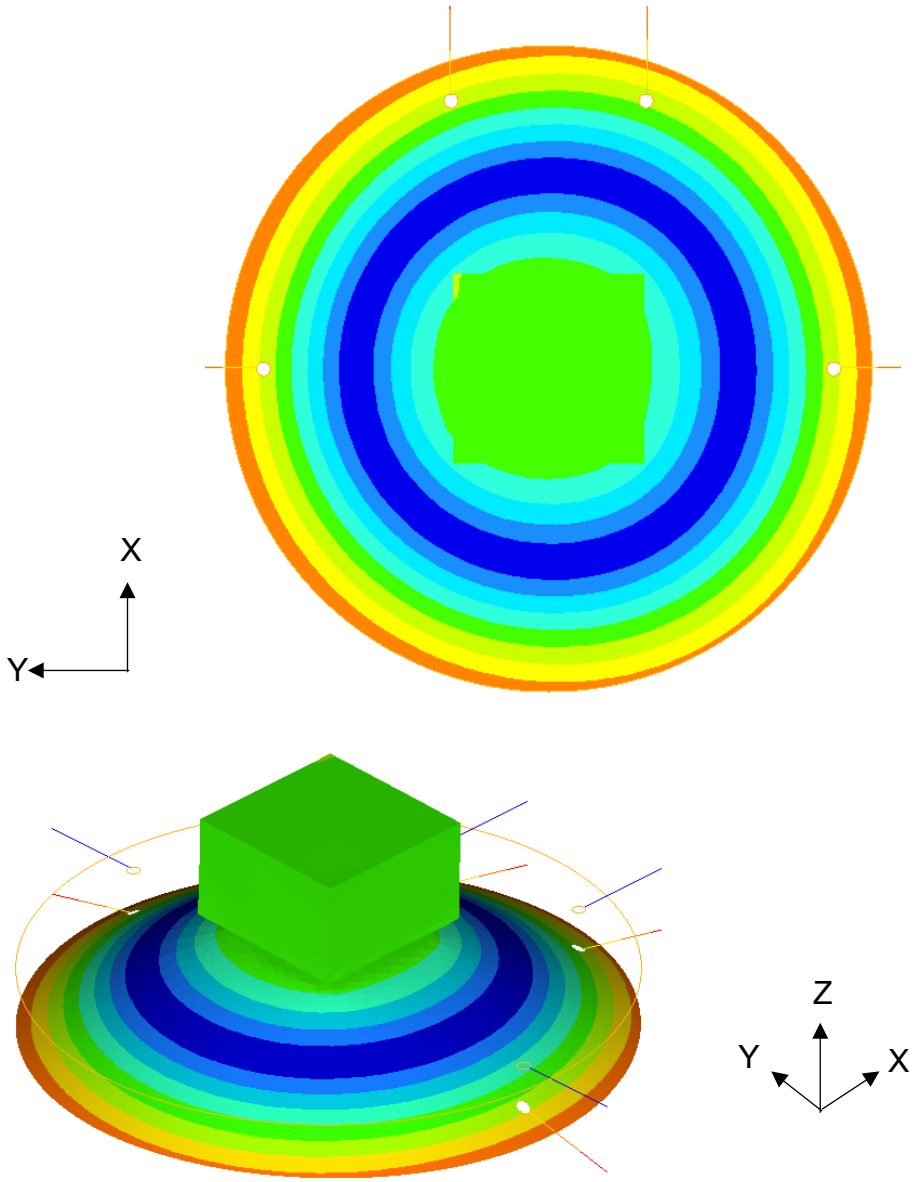

Mode 4:

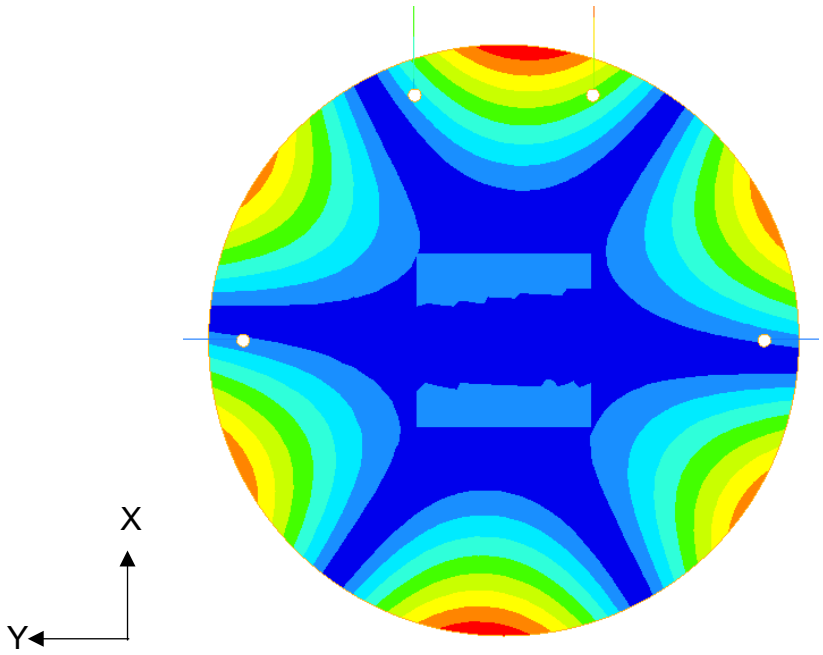

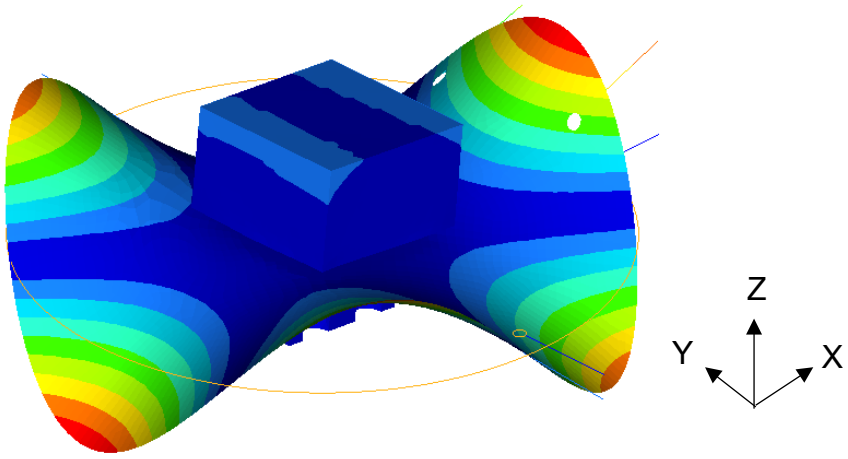

Mode 5:

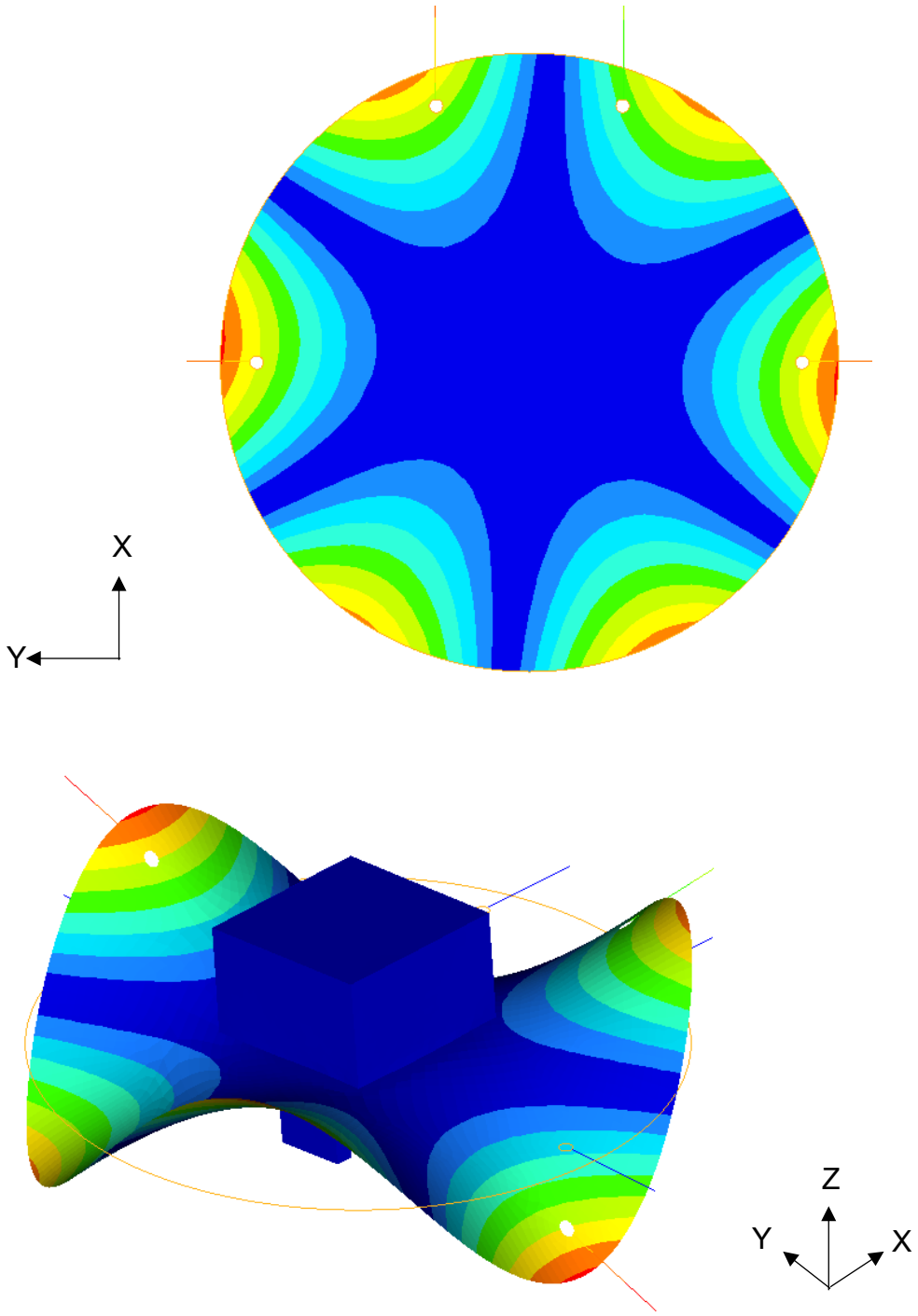

B.2 Bottom configuration

Mode 1:

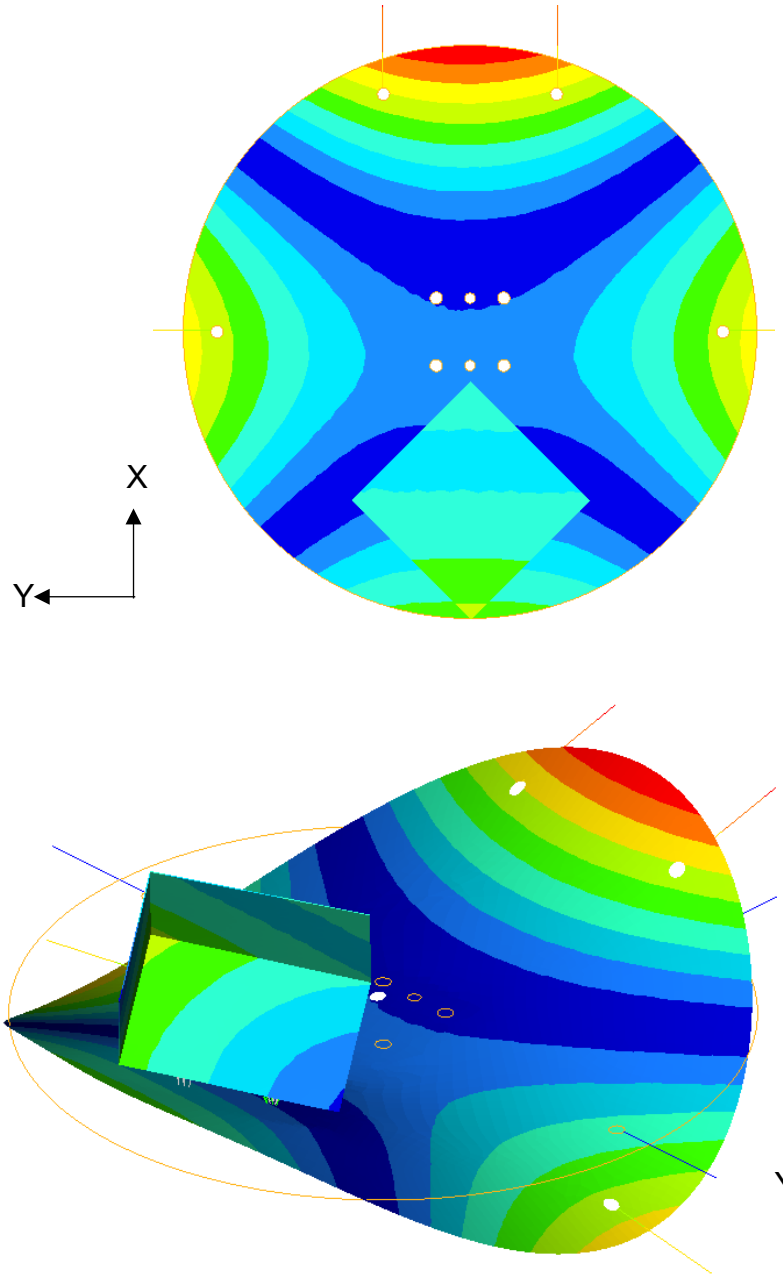

Mode 2:

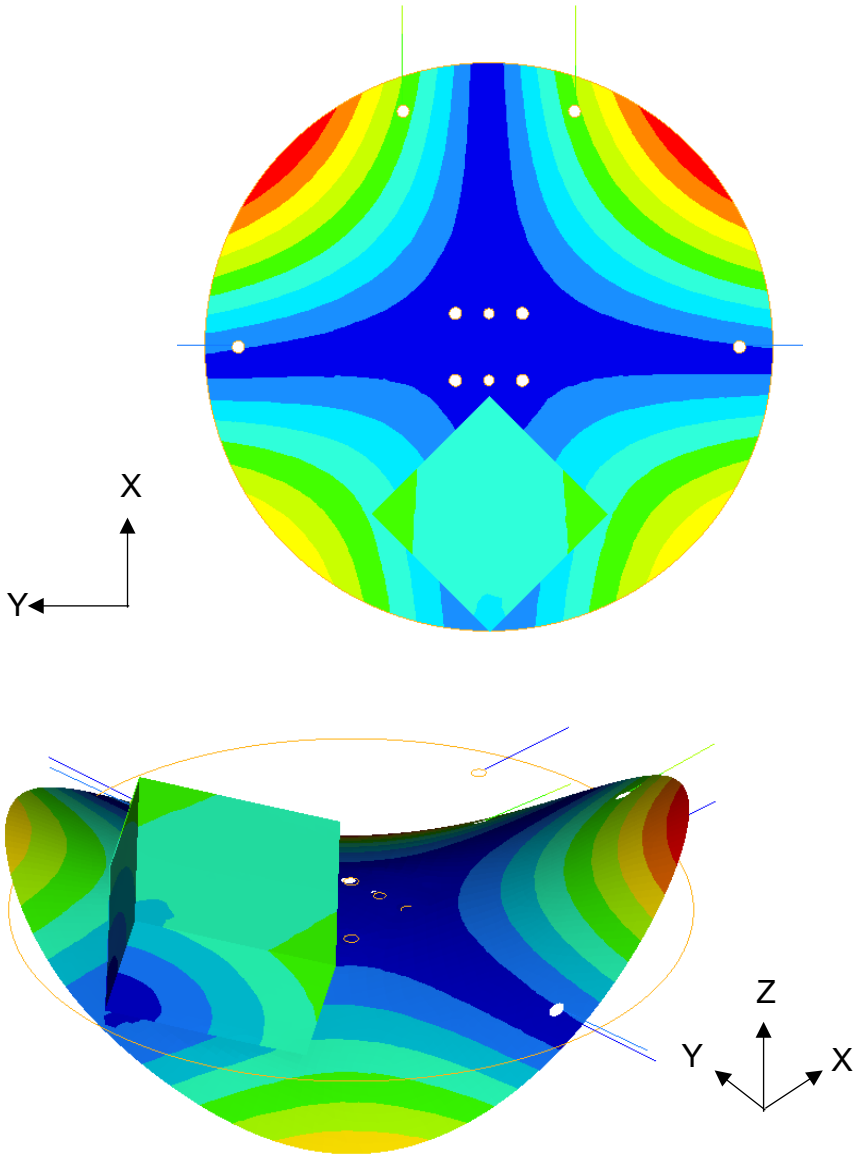

Mode 3:

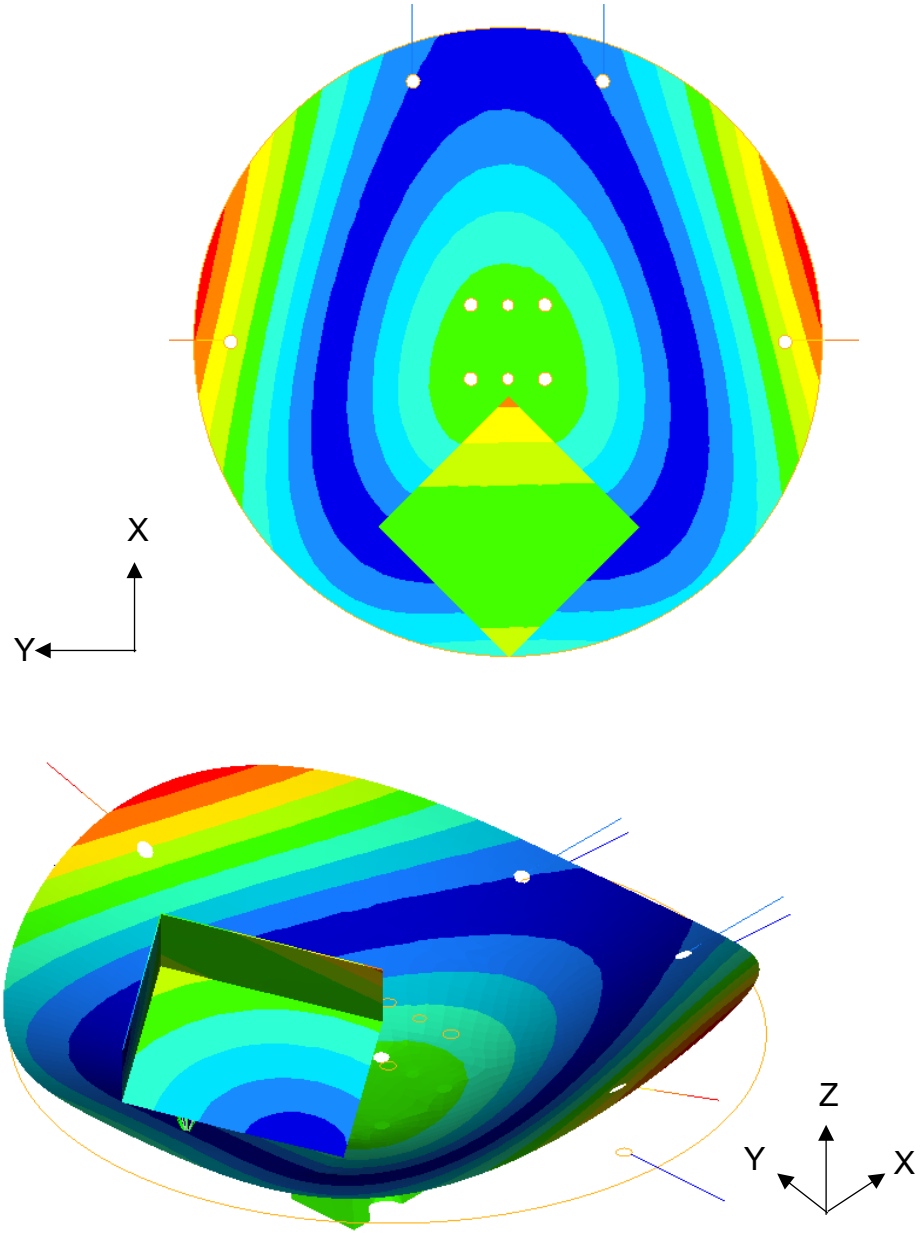

Mode 4:

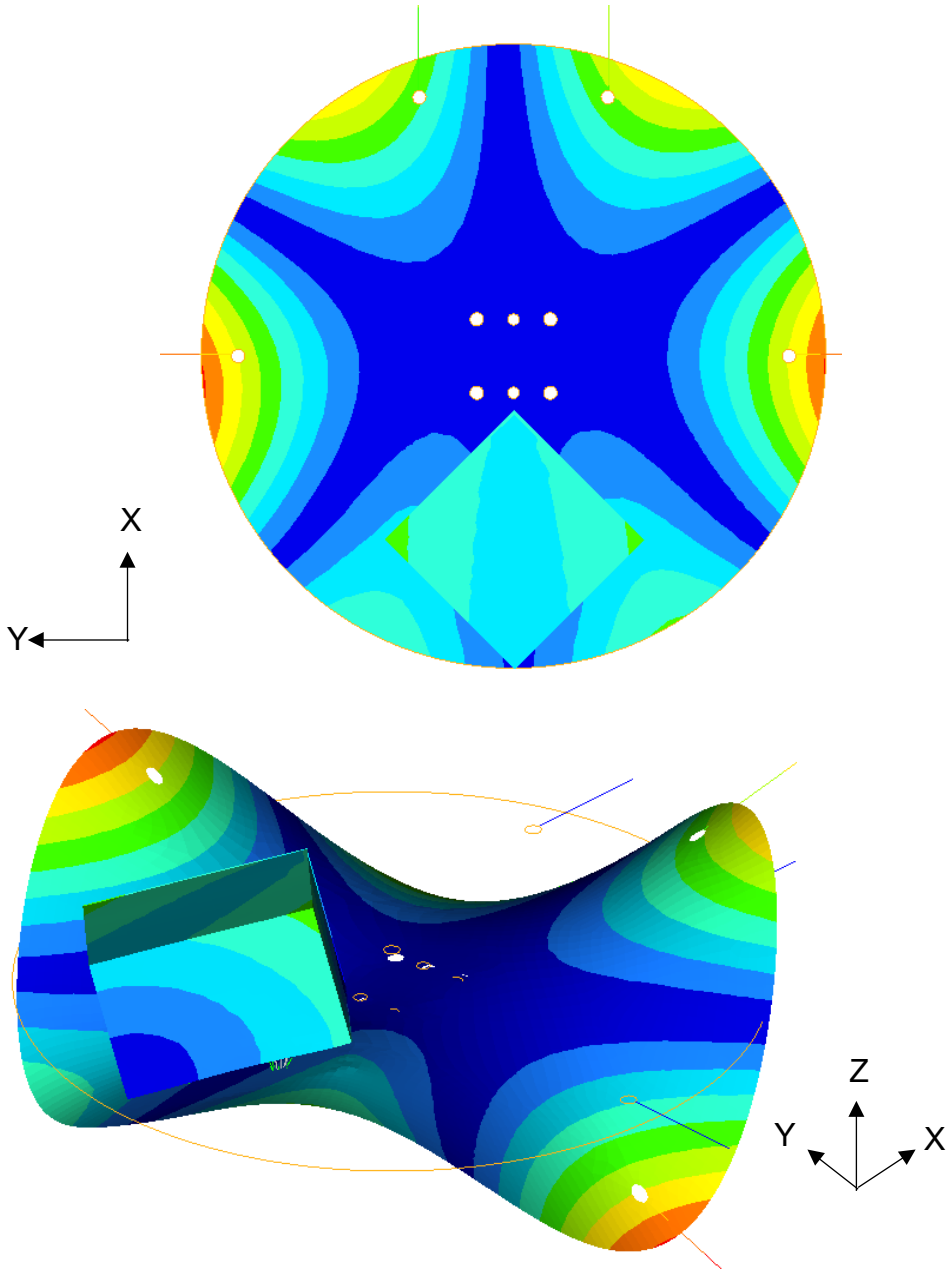

Mode 5:

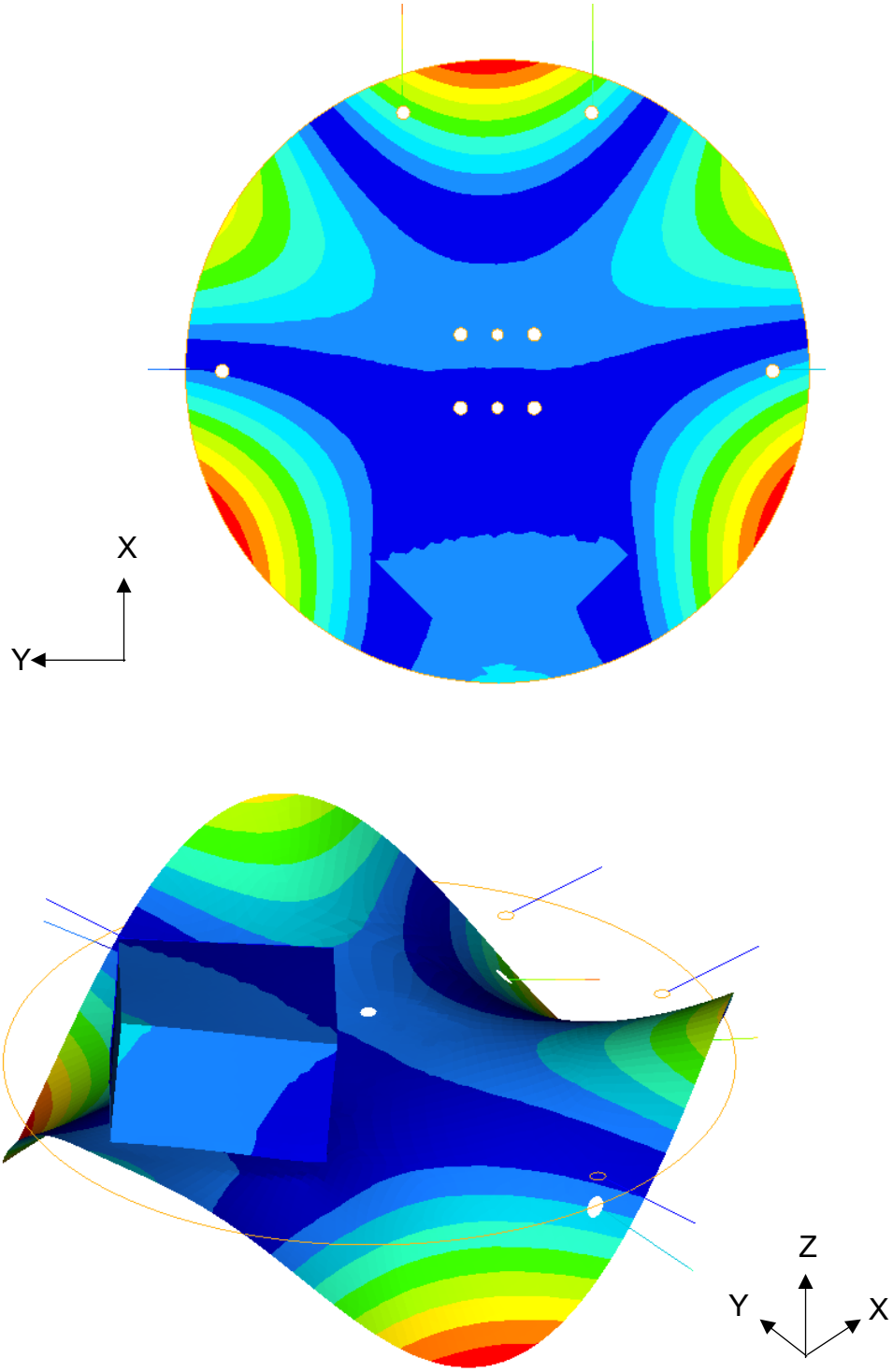

B.3 Corner (optimal) configuration

Mode 1:

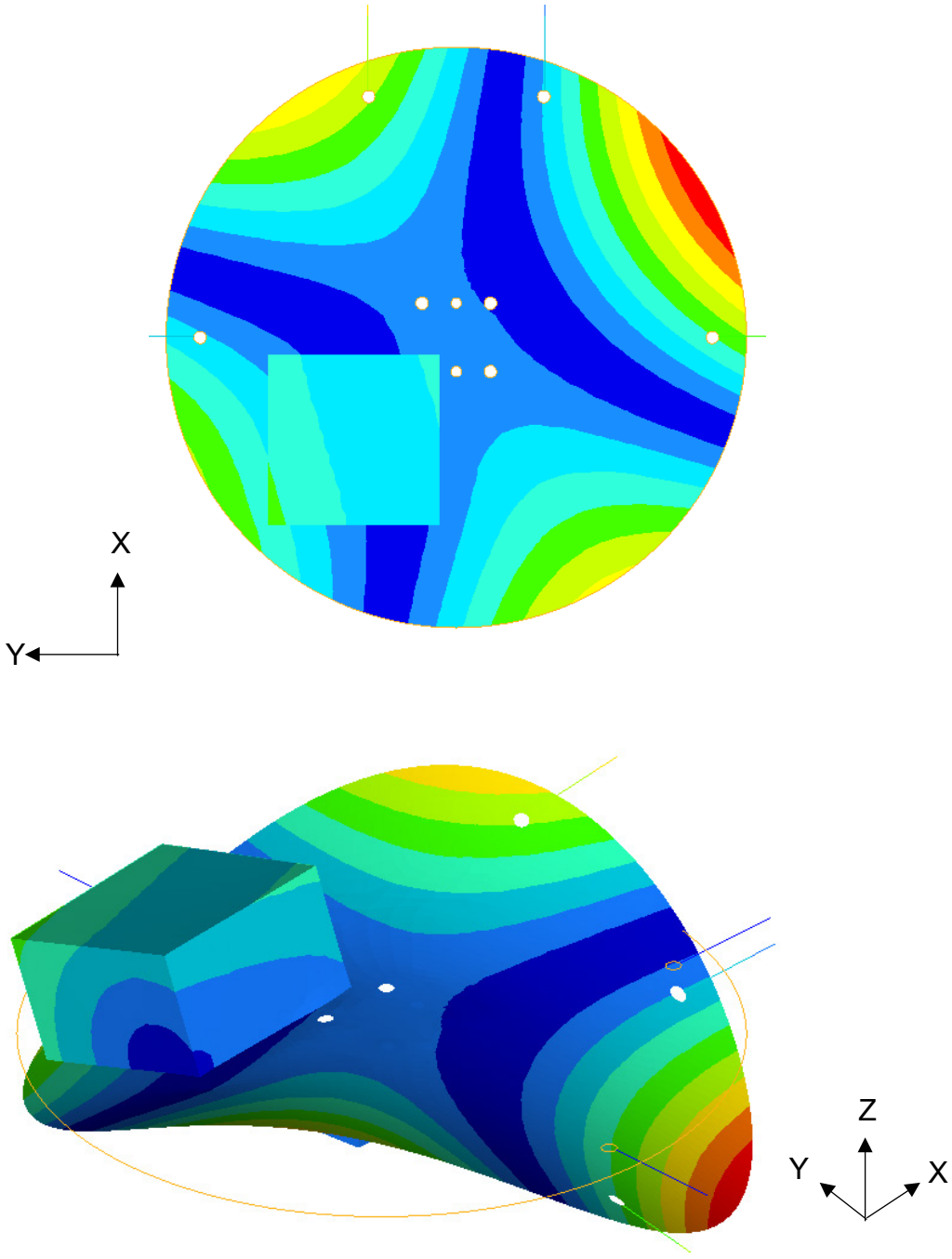

Mode 2:

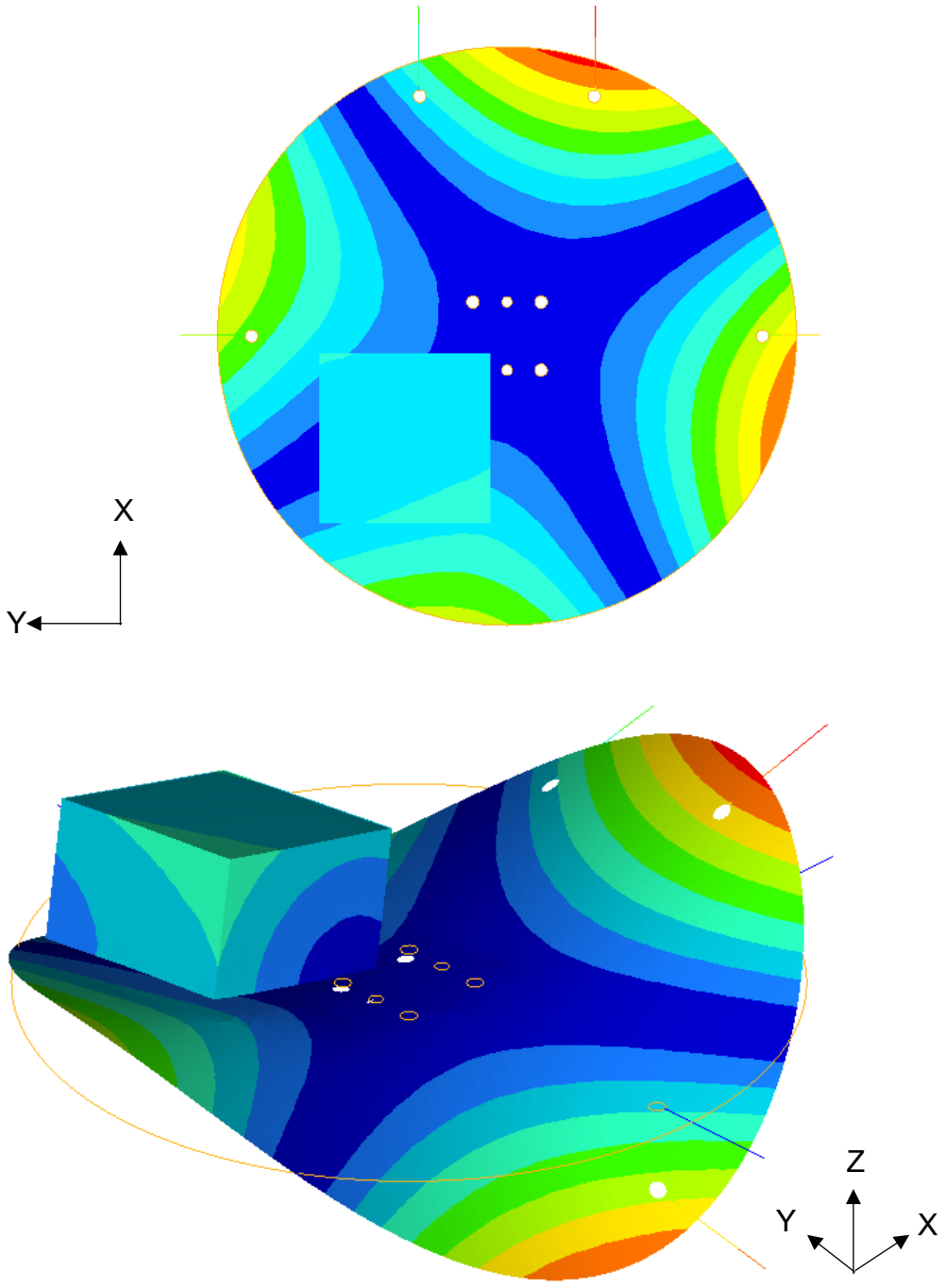

Mode 3:

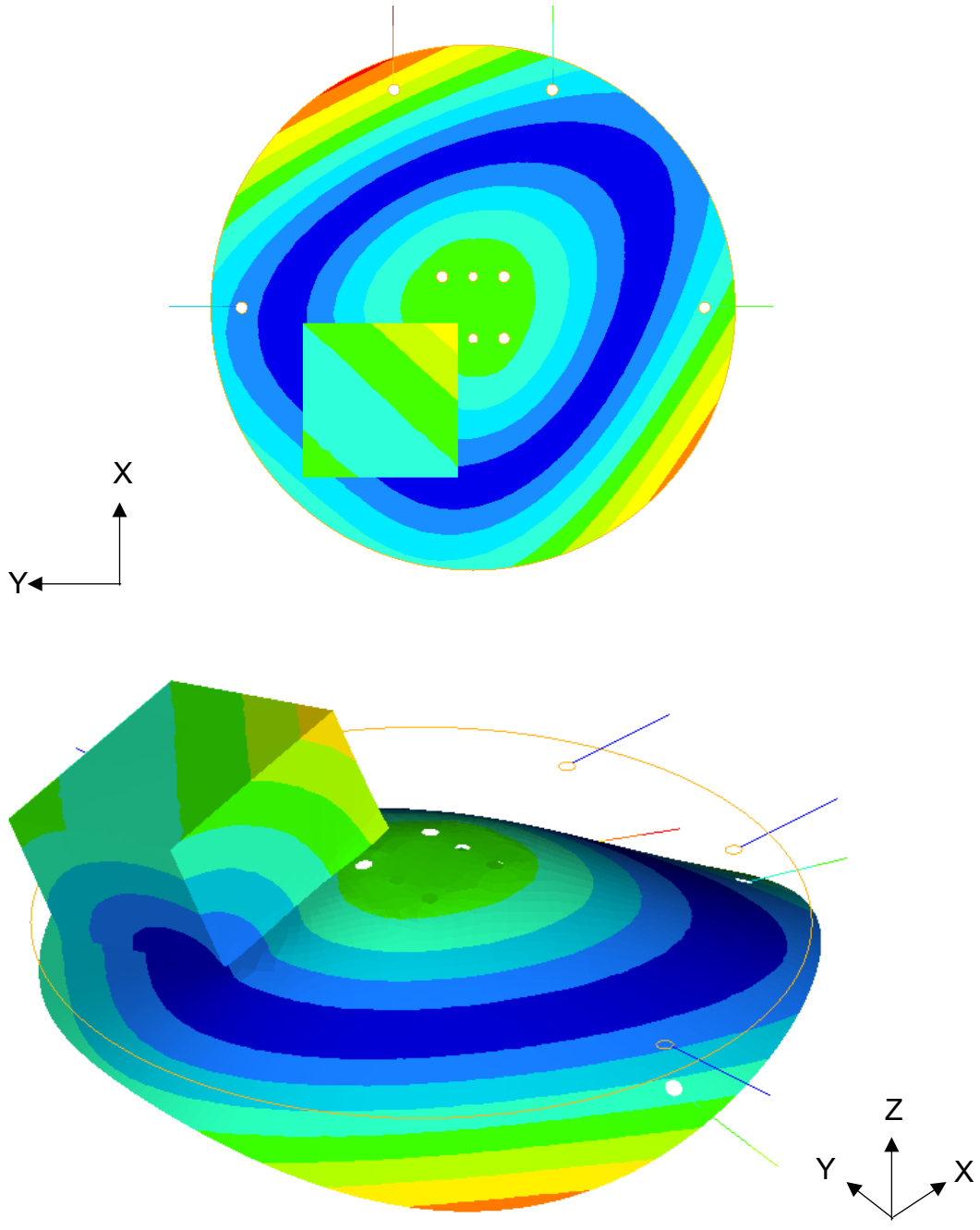

Mode 4:

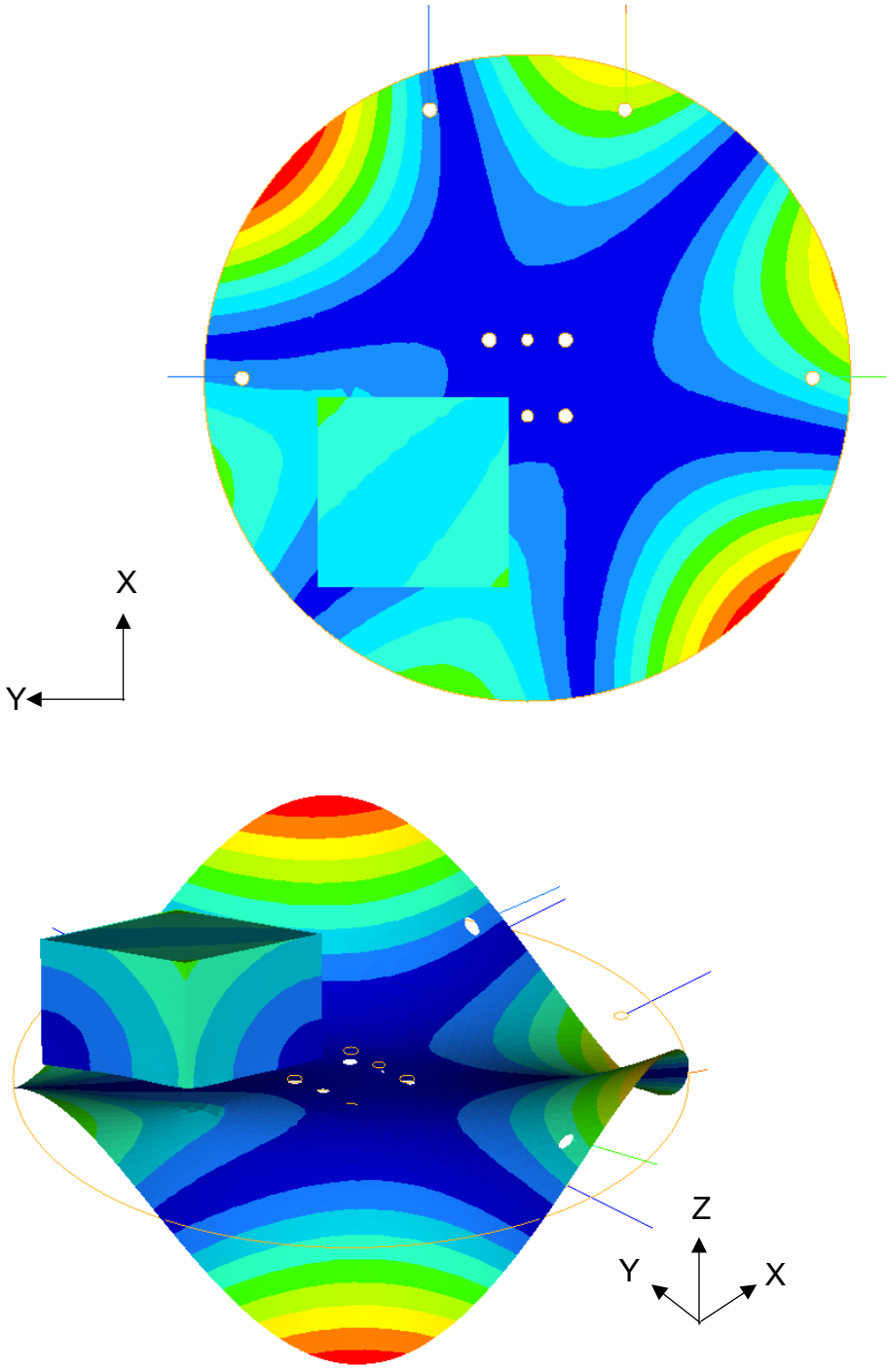

Mode 5:

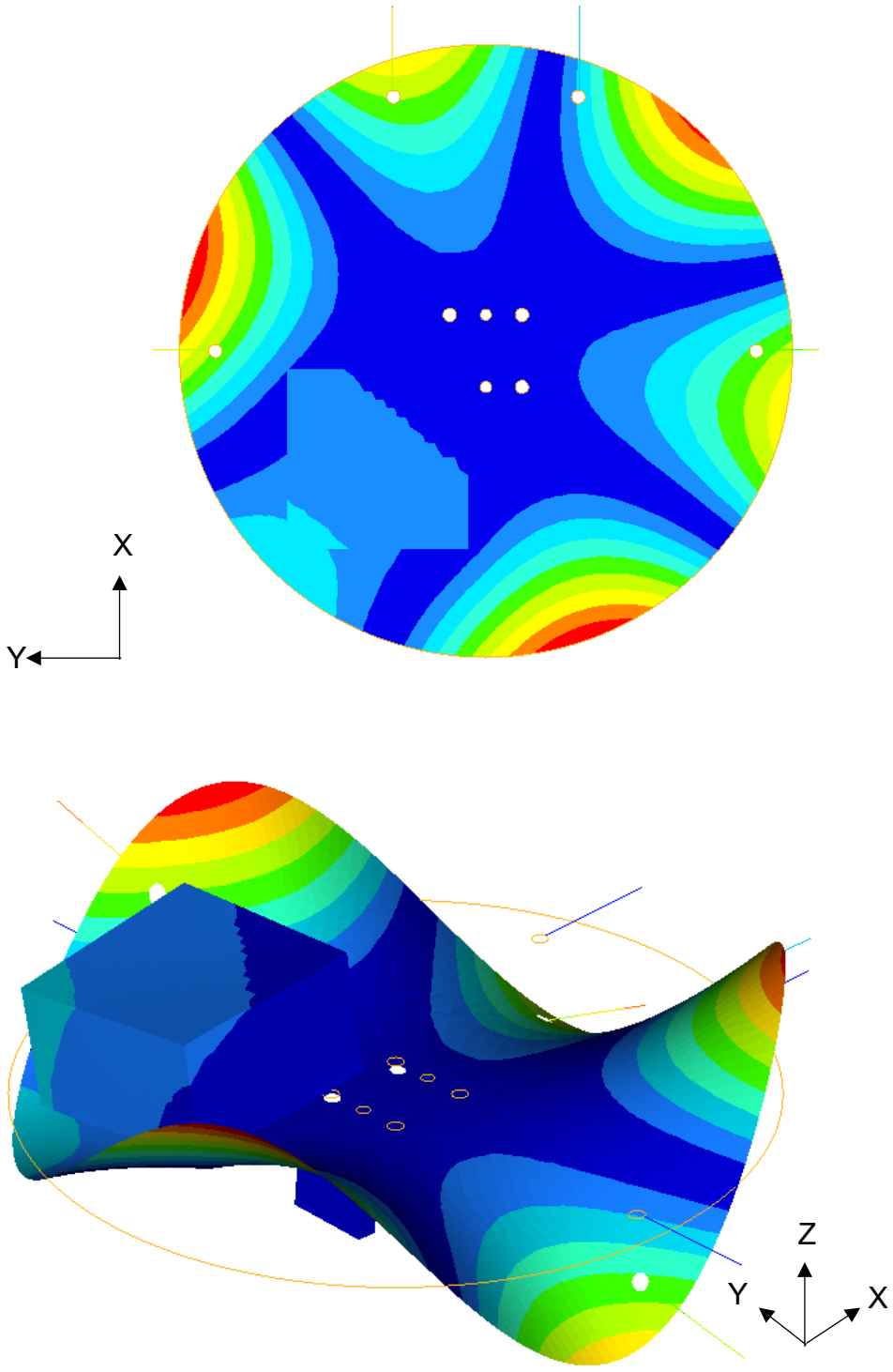

C Additional figures

Below is a compilation of extra figures that may be of interest. Each section is separated by configuration: center, bottom, and corner, respectively. Within each section, the order is as follows:

1. FBS
2. Truth assembly
3. Adjusted assembly to mimic FBS interface

This is repeated for both model and test conditions and reported first as FRFs then again as SRSs. Each plot has a title explaining what the configuration, condition, and assembly method is used.

C.1 Center configuration

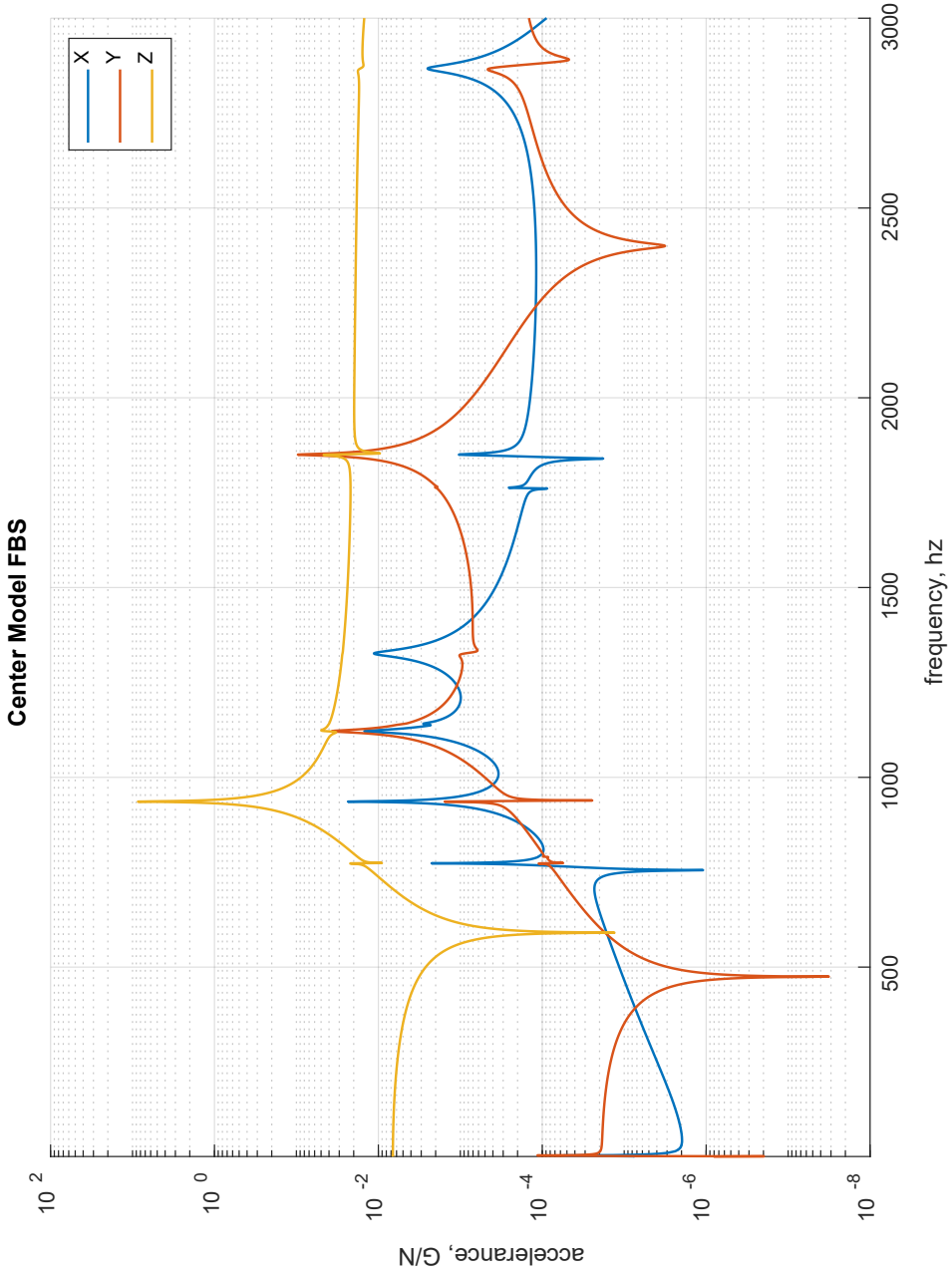

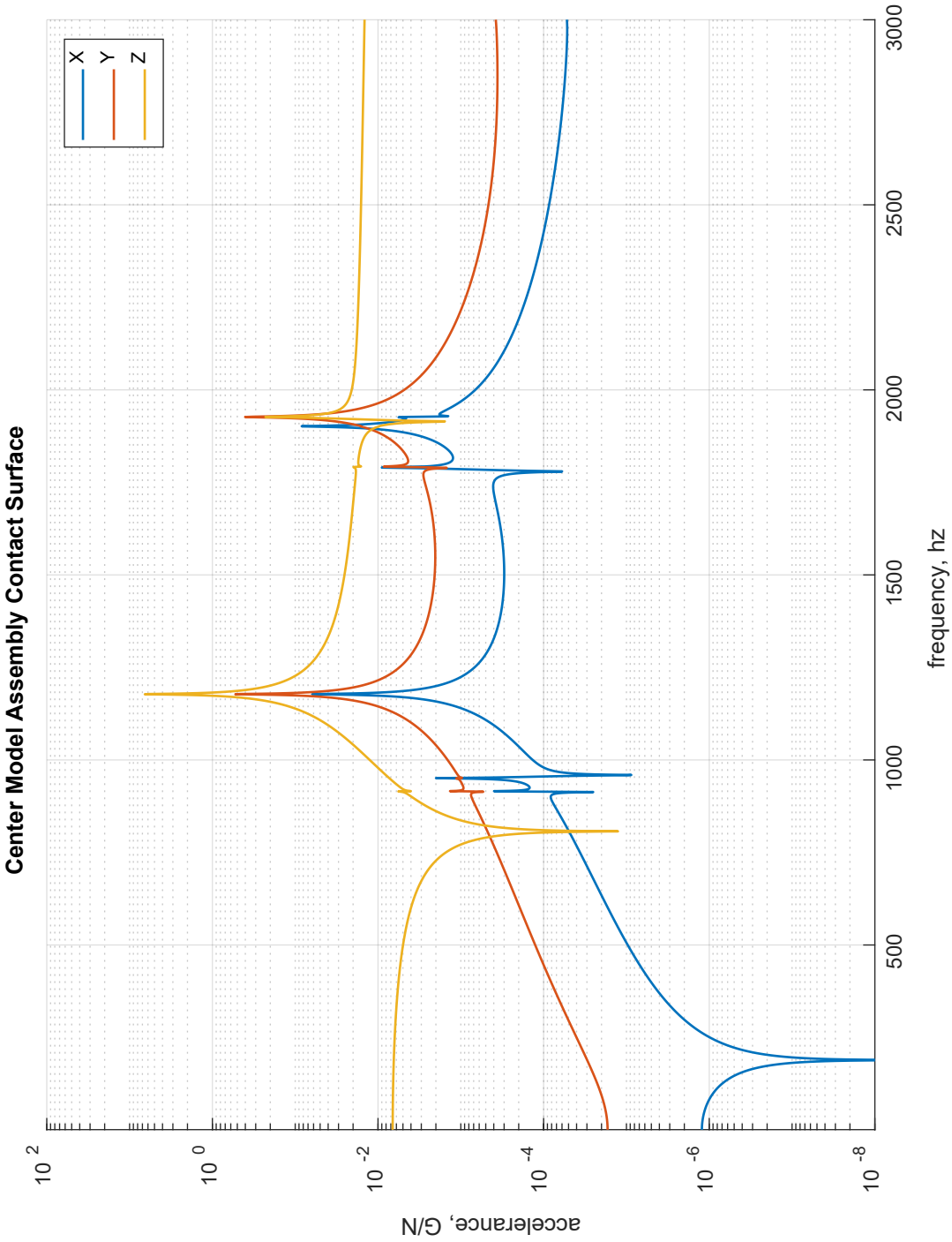
Center Model Assembly Contact Surface
X
Y
Z
acceleranse, G/N
frequency, hz
10 2
10 0
10 -2
10 -4
10 -6
10 -8
500
1000
1500
2000
2500
3000

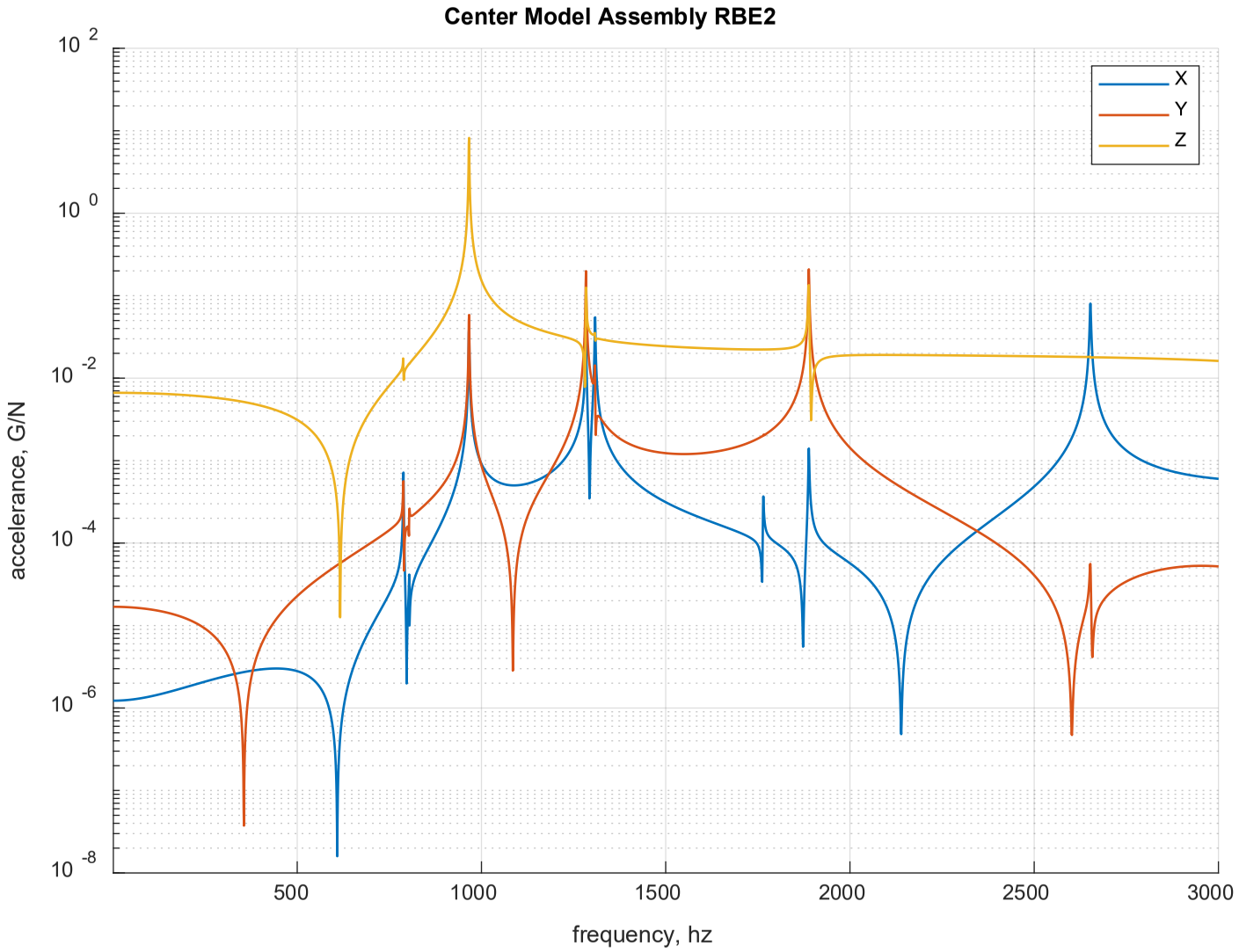
Center Model Assembly RBE2
X
Y
Z
accelerance, G/N
frequency, hz
10 2
10 0
10 -2
10 -4
10 -6
10 -8
500
1000
1500
2000
2500
3000

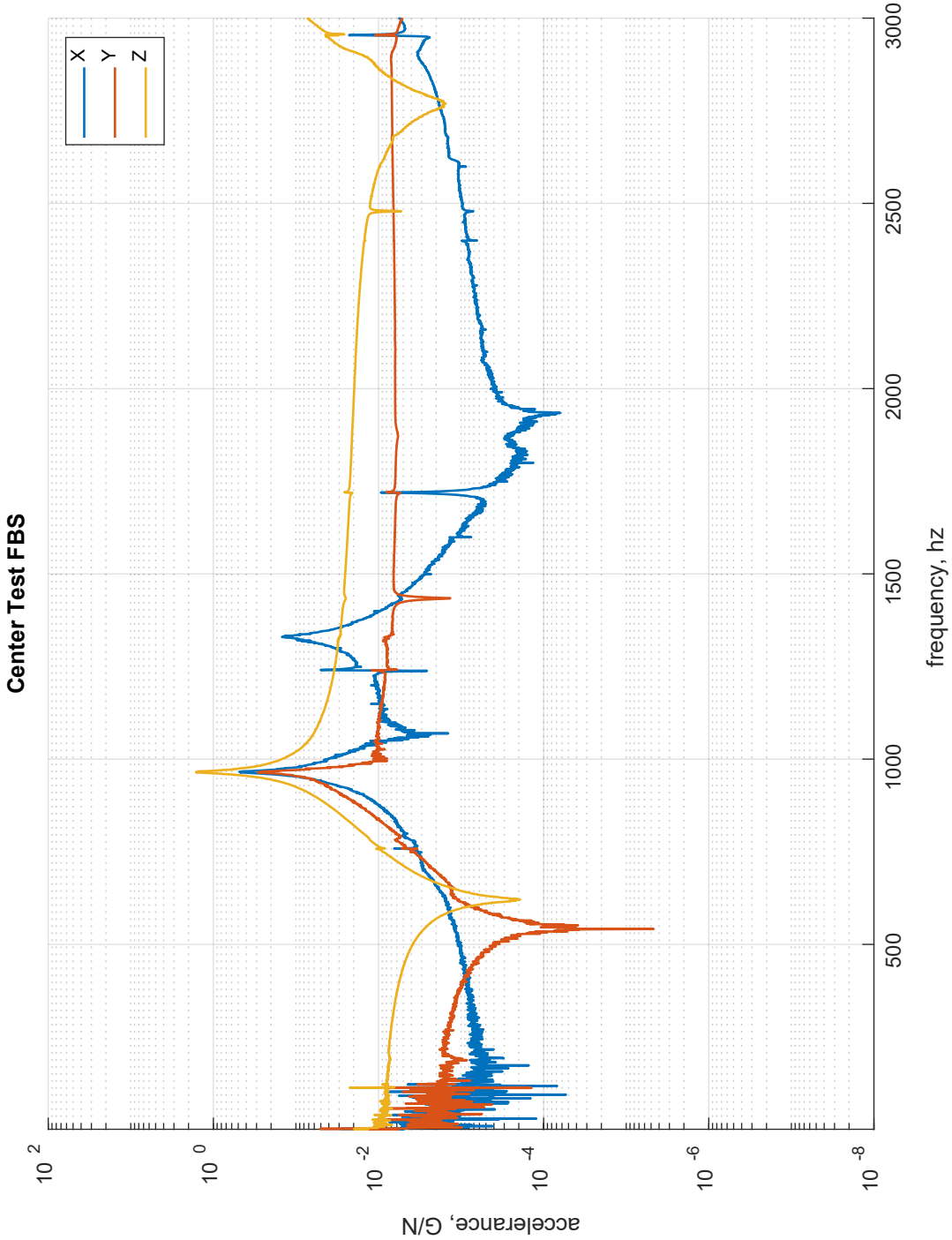
Center Test FBS
X
Y
Z
acceleranse, G/N
frequency, hz
10 2
10 0
10 -2
10 -4
10 -6
10 -8
500
1000
1500
2000
2500
3000

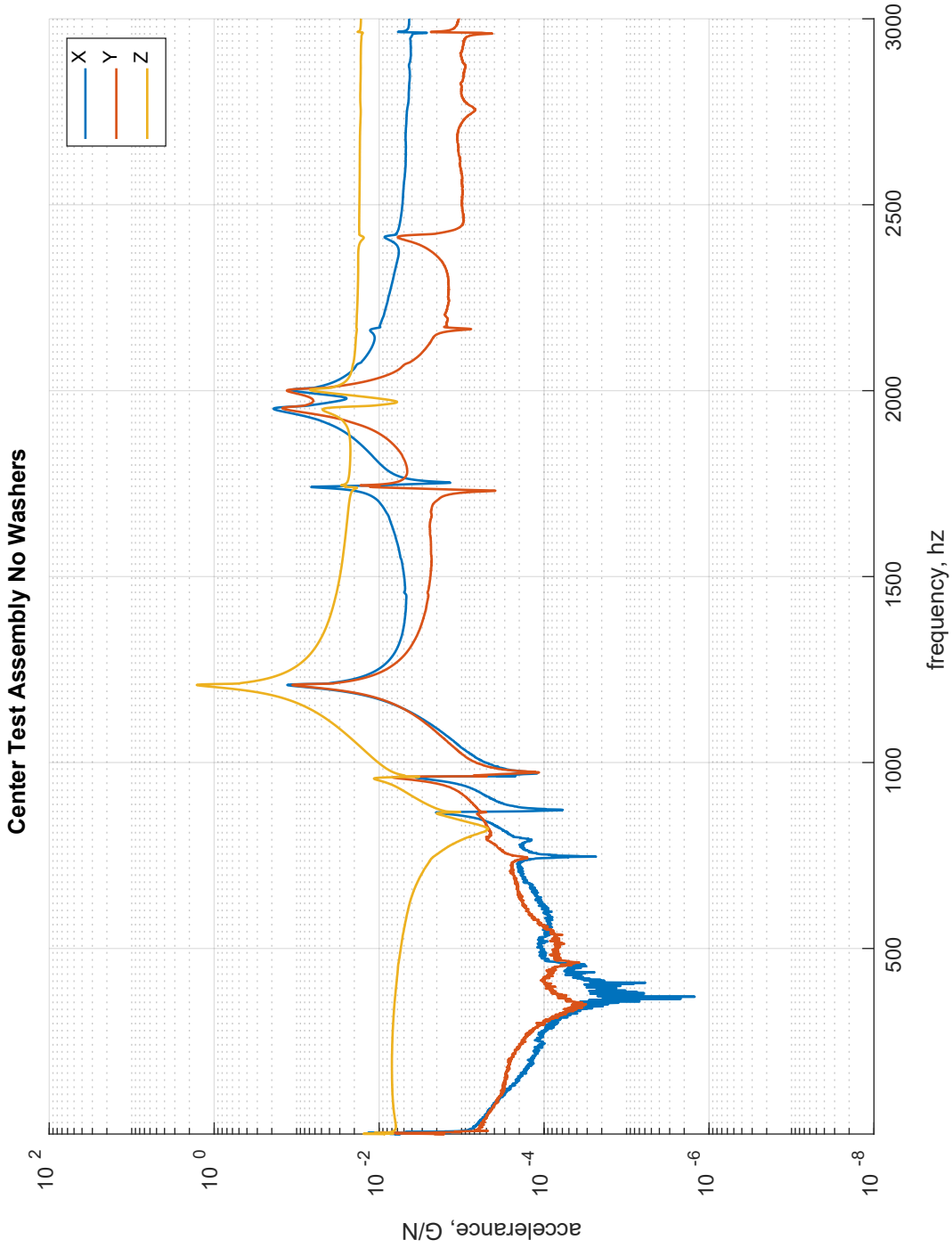
Center Test Assembly No Washers
X
Y
Z
acceleranee, G/N
frequency, hz
10 2
10 0
10 -2
10 -4
10 -6
10 -8
500
1000
1500
2000
2500
3000

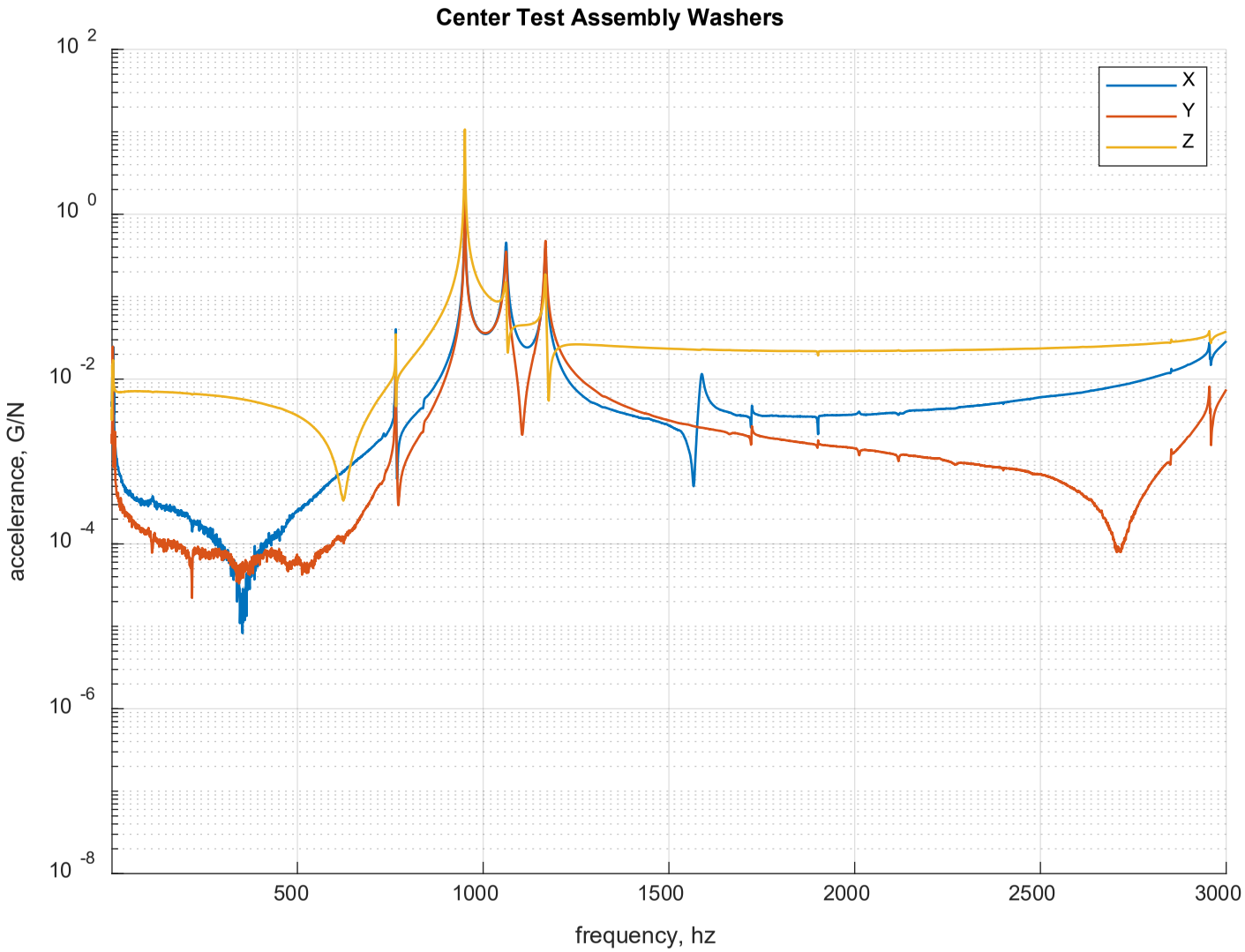
Center Test Assembly Washers
X
Y
Z
accelerance, G/N
frequency, hz
10 2
10 0
10 -2
10 -4
10 -6
10 -8
500
1000
1500
2000
2500
3000

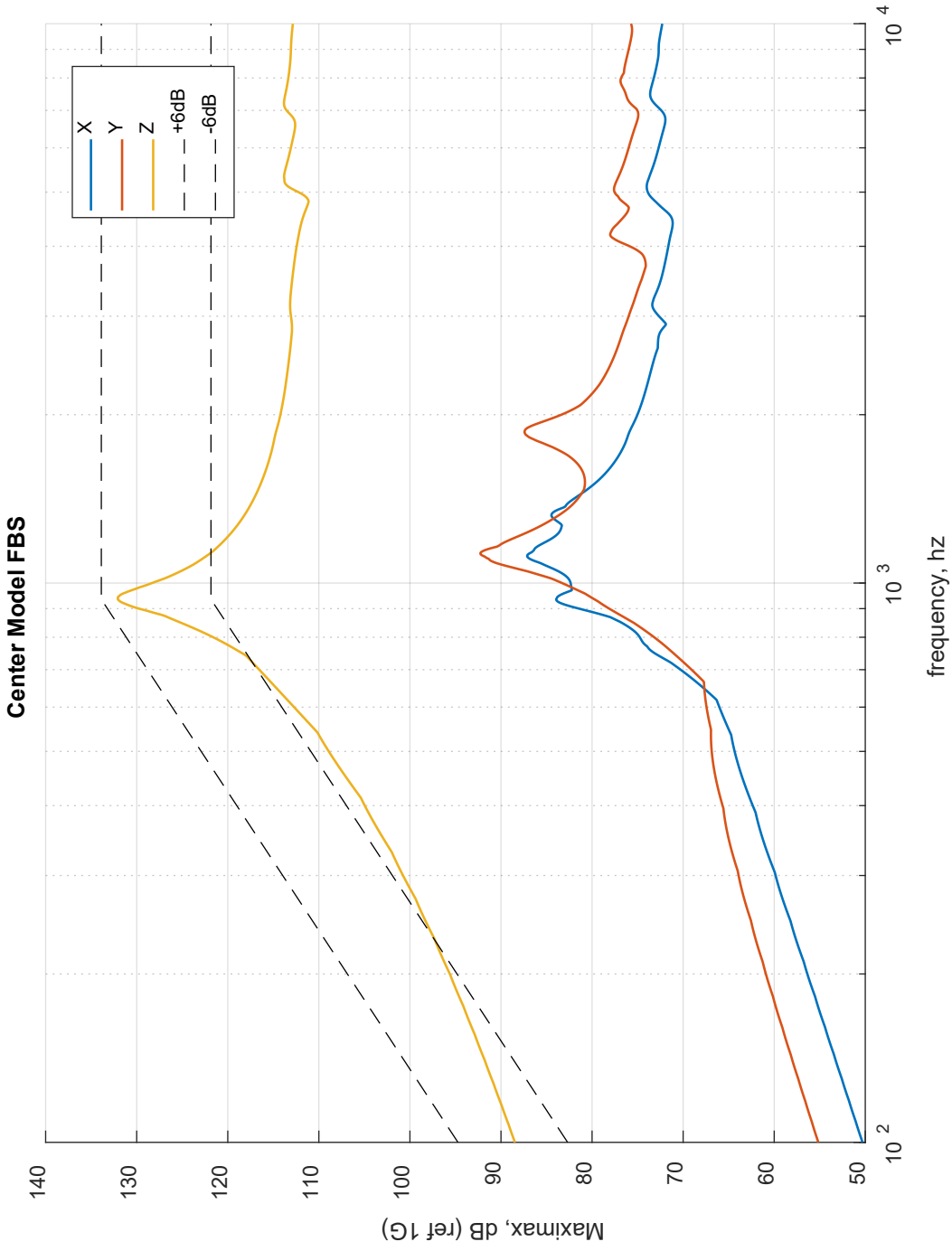
Center Model FBS
Maximax, dB (ref 1G)
frequency, hz
X
Y
Z
+6dB
-6dB
140
130
120
110
100
90
80
70
60
50
10 2
10 3
10 4

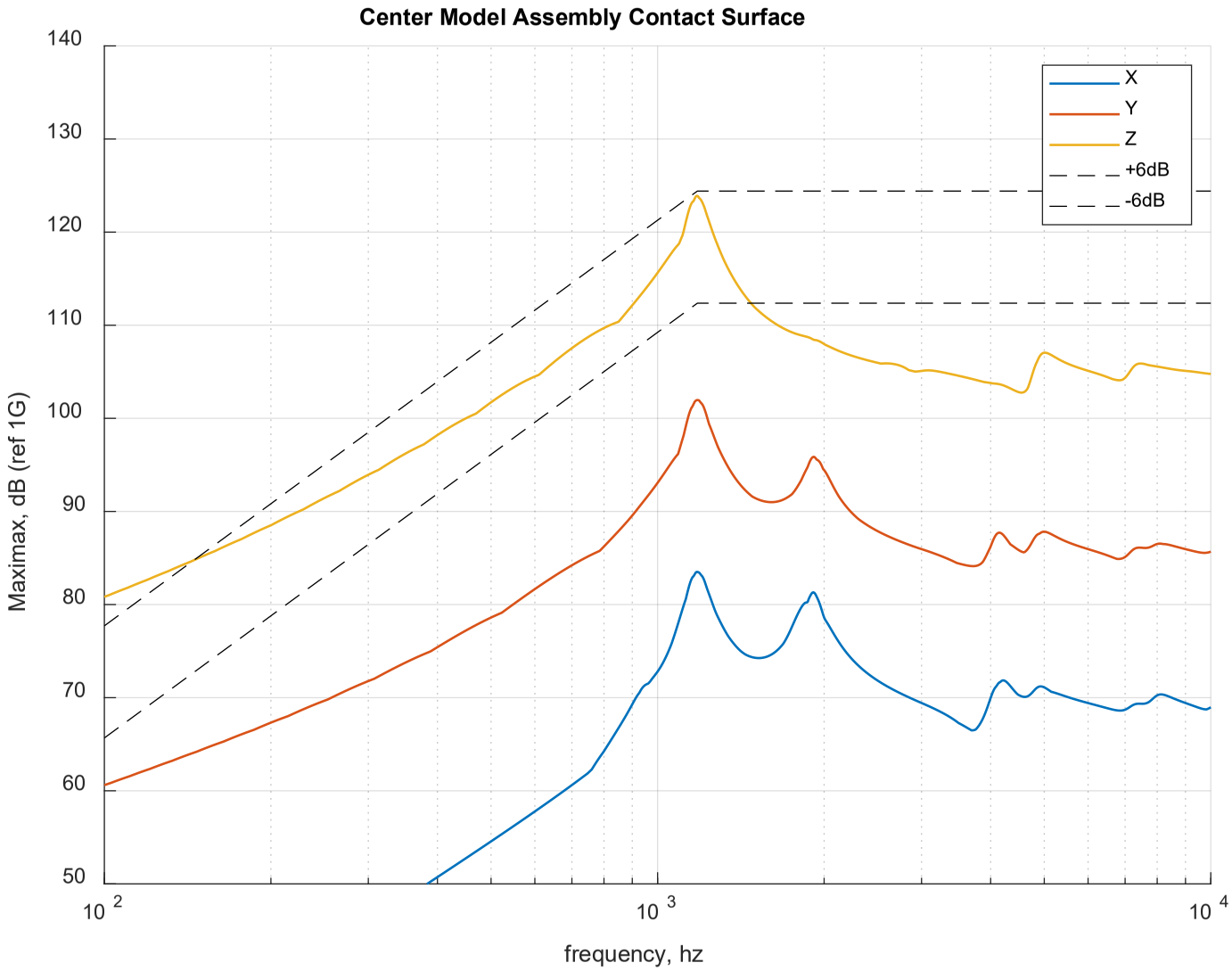
Center Model Assembly Contact Surface
Maximax, dB (ref 1G)
frequency, hz
X
Y
Z
+6dB
-6dB
140
130
120
110
100
90
80
70
60
50
10 2
10 3
10 4

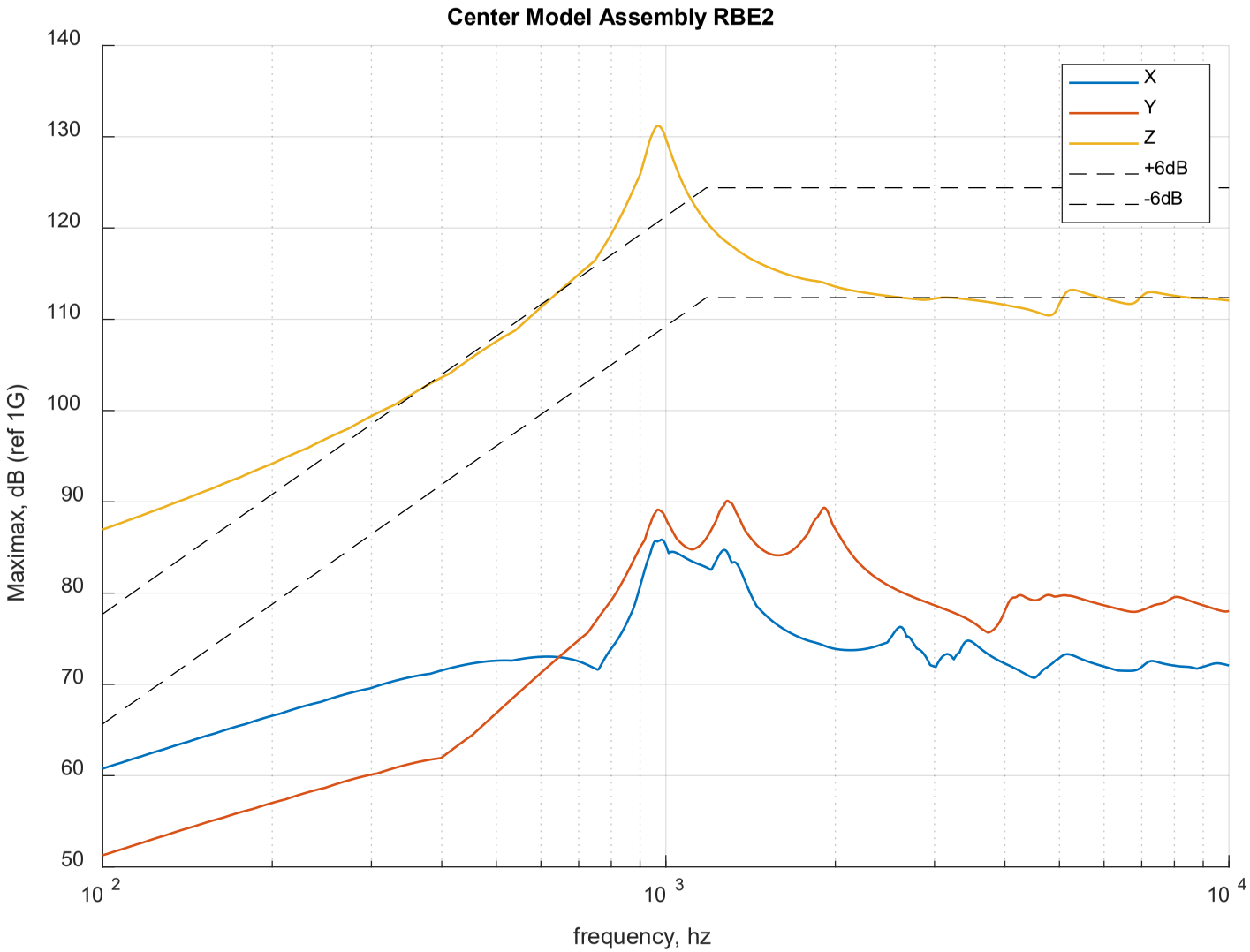
Center Model Assembly RBE2
140
130
120
110
100
90
80
70
60
50
Maximax, dB (ref 1G)
10 2
10 3
10 4
frequency, hz
X
Y
Z
+6dB
-6dB

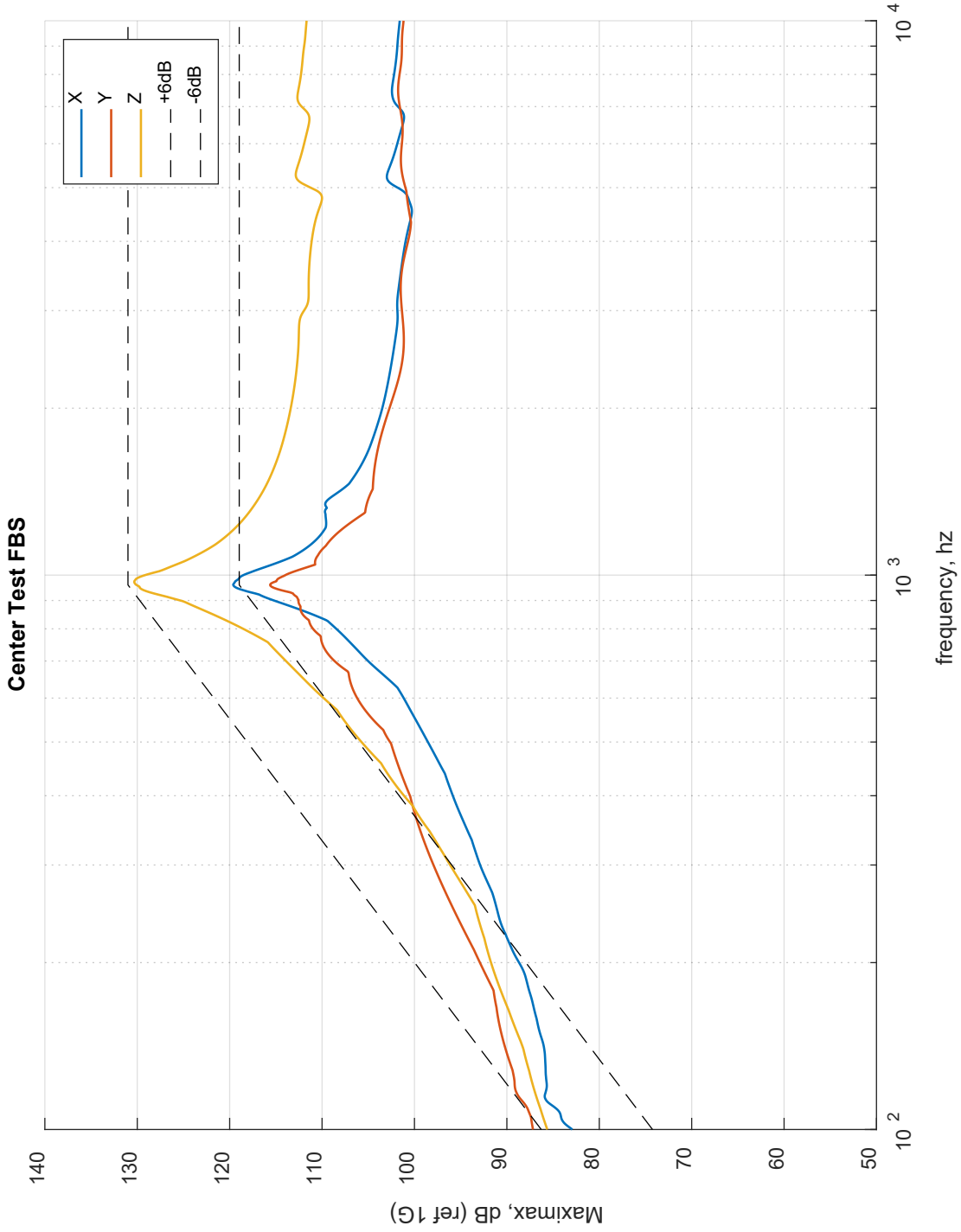
Center Test FBS
X
Y
Z
+6dB
-6dB
Maximax, dB (ref 1G)
frequency, hz
140
130
120
110
100
90
80
70
60
50
10 2
10 3
10 4

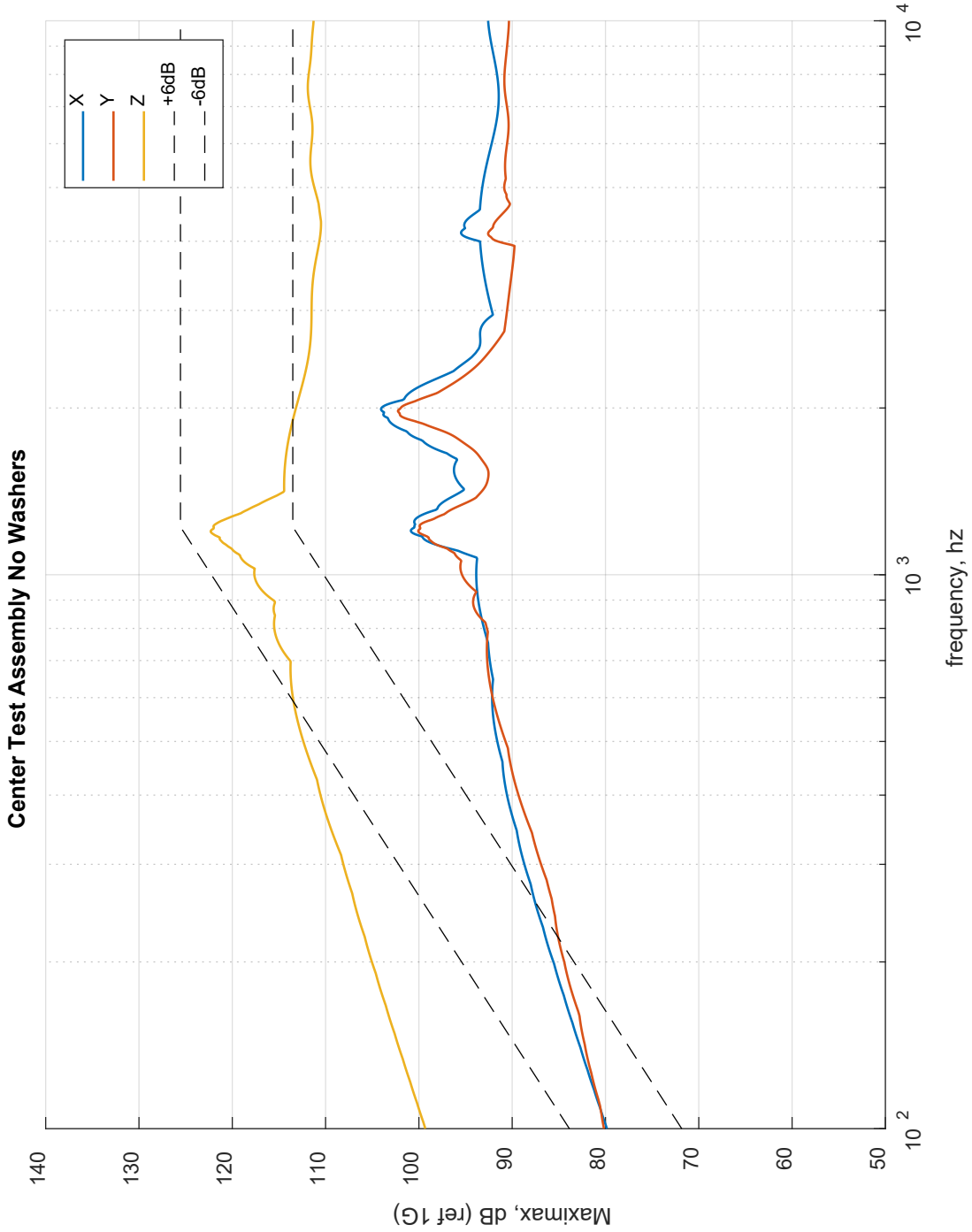
Center Test Assembly No Washers
X
Y
Z
+6dB
-6dB
Maximax, dB (ref 1G)
frequency, hz
140
130
120
110
100
90
80
70
60
50
10 2
10 3
10 4

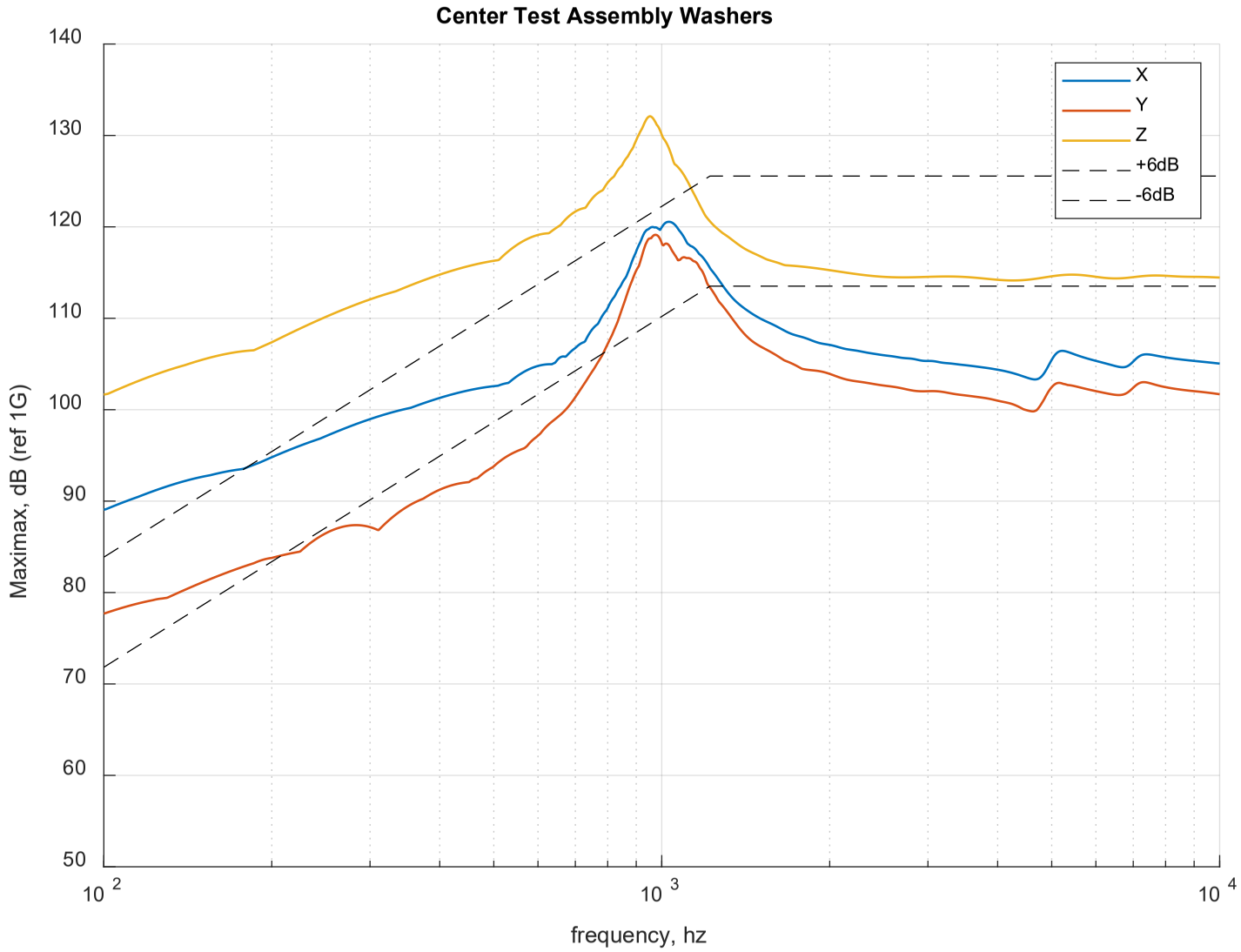
Center Test Assembly Washers
140
130
120
110
100
90
80
70
60
50
Maximax, dB (ref 1G)
10 2
10 3
10 4
frequency, hz
X
Y
Z
+6dB
-6dB

C.2 Bottom configuration

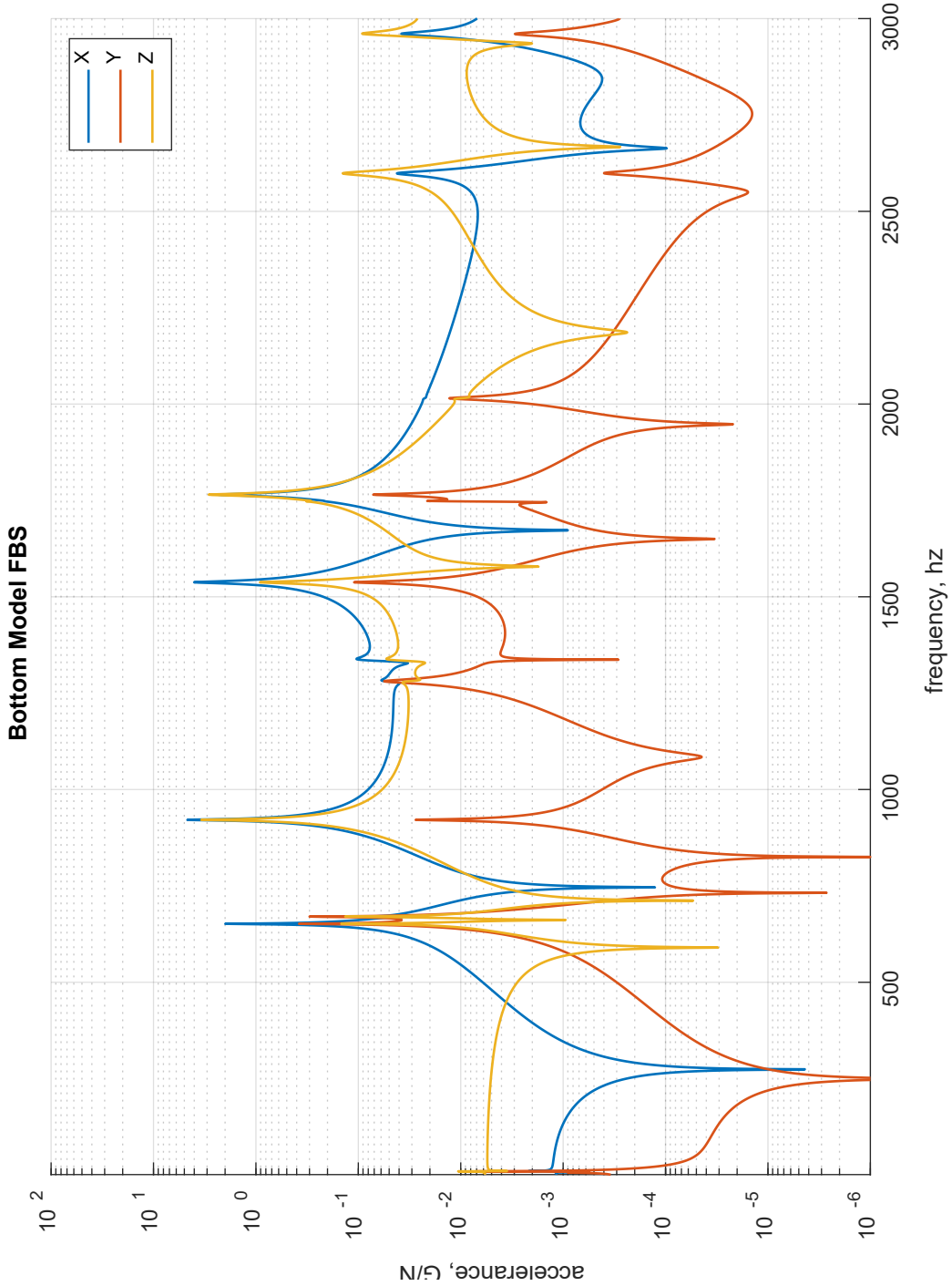

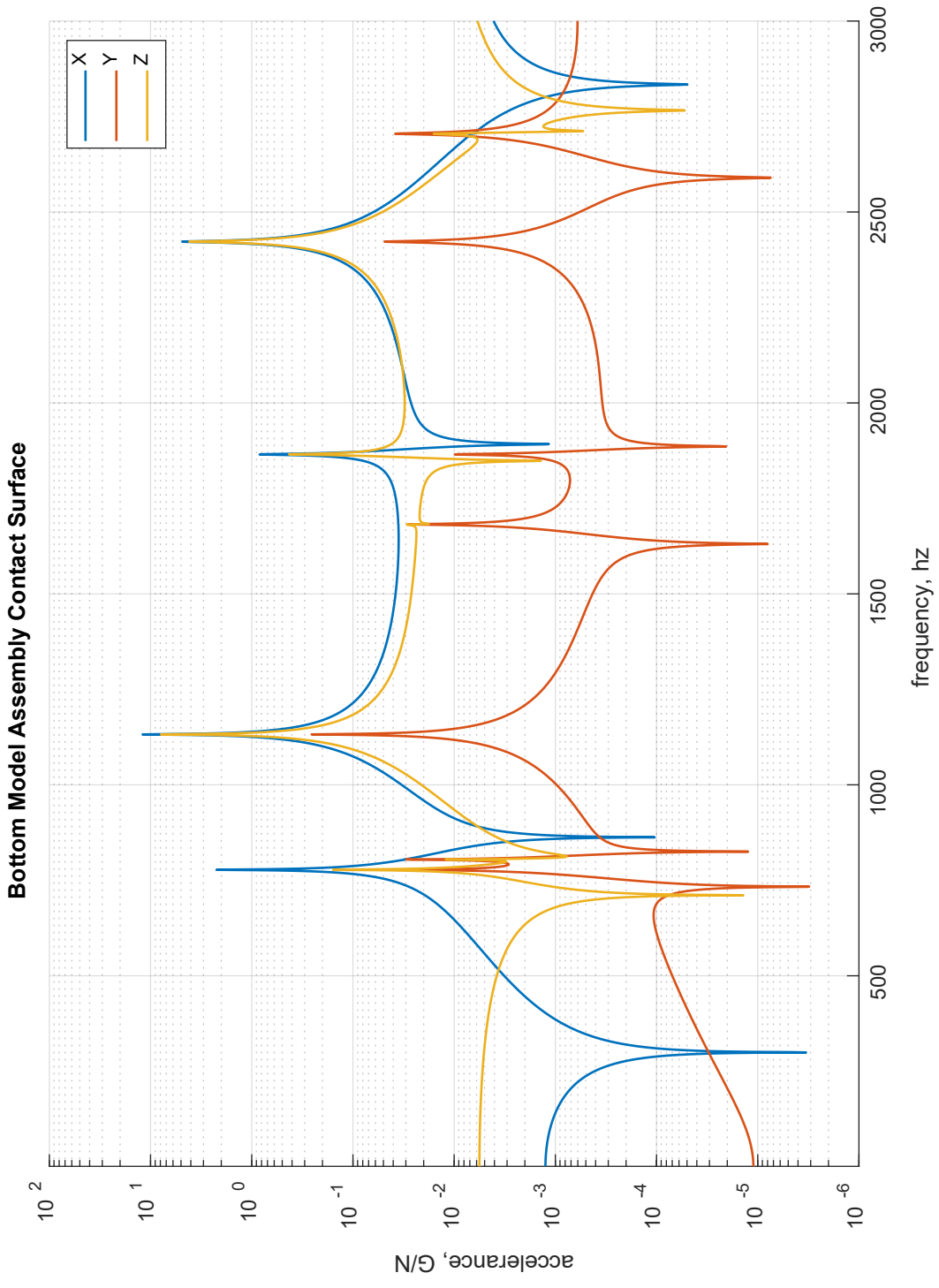
Bottom Model Assembly Contact Surface
X
Y
Z
acceleranee, G/N
frequency, hz
10 2
10 1
10 0
10 -1
10 -2
10 -3
10 -4
10 -5
10 -6
500
1000
1500
2000
2500
3000

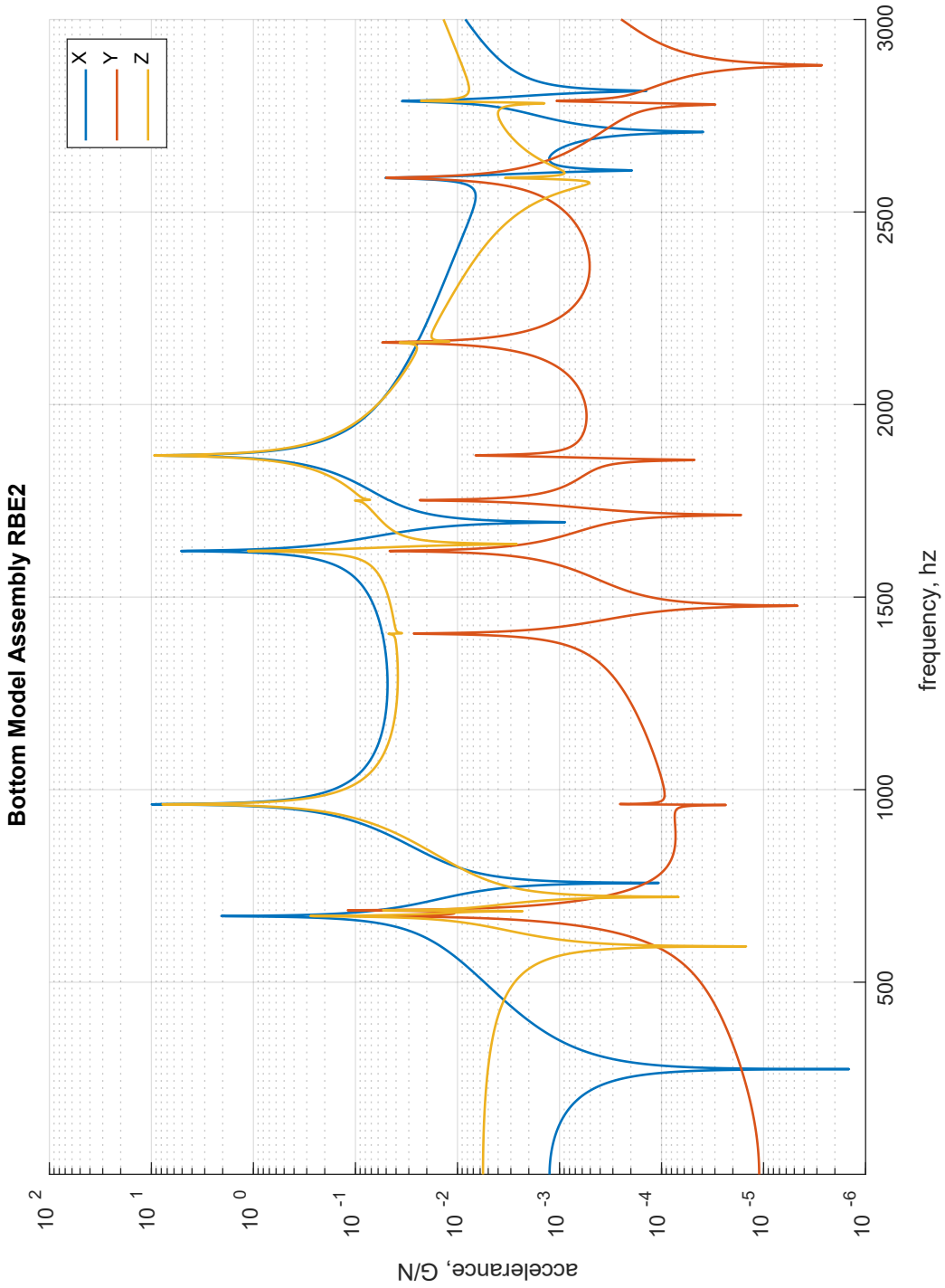
Bottom Model Assembly RBE2
X
Y
Z
acceleration, G/N
frequency, hz
10 2
10 1
10 0
10 -1
10 -2
10 -3
10 -4
10 -5
10 -6
500
1000
1500
2000
2500
3000

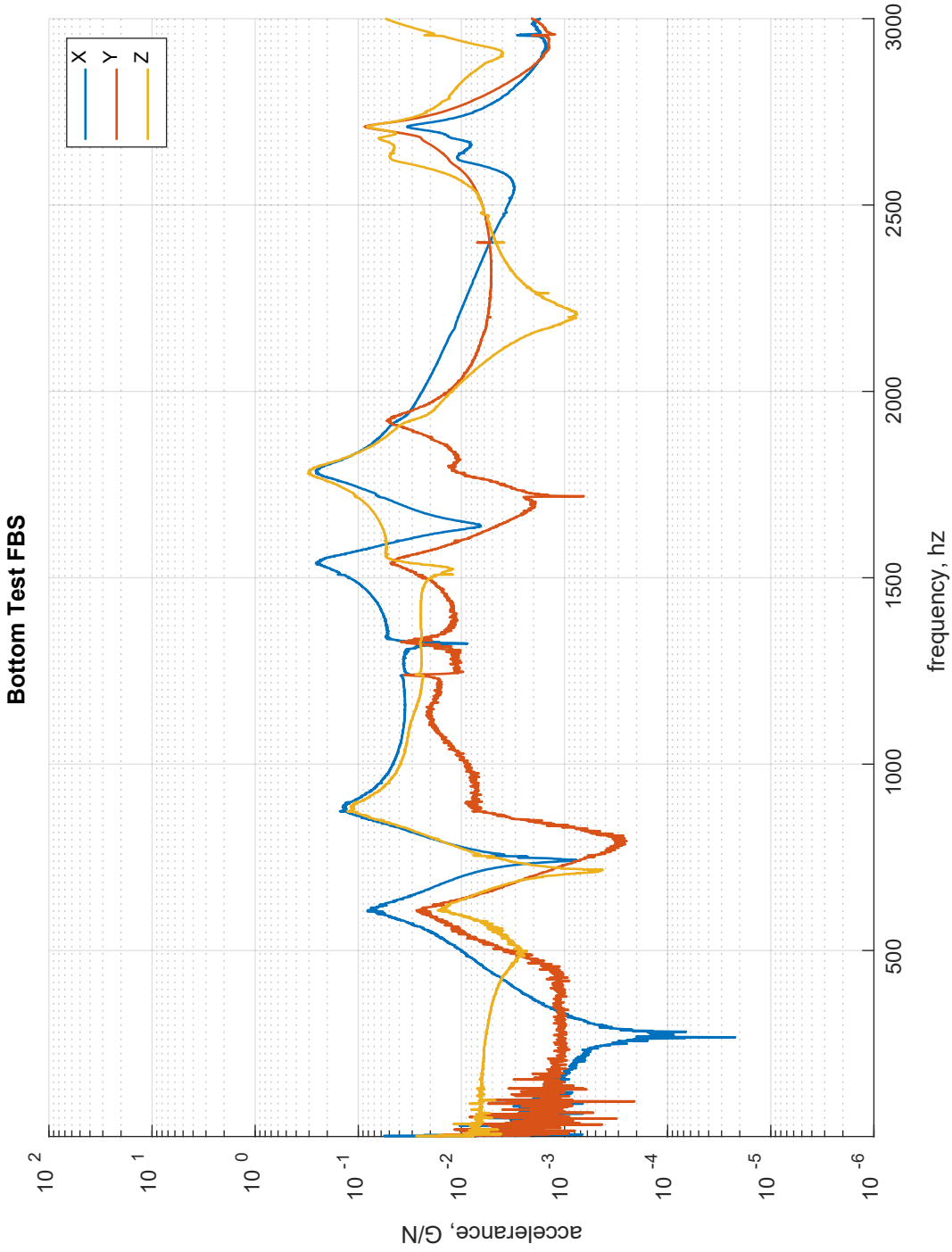
Bottom Test FBS
X
Y
Z
acceleranse, G/N
frequency, hz
10 2
10 1
10 0
10 -1
10 -2
10 -3
10 -4
10 -5
10 -6
500
1000
1500
2000
2500
3000

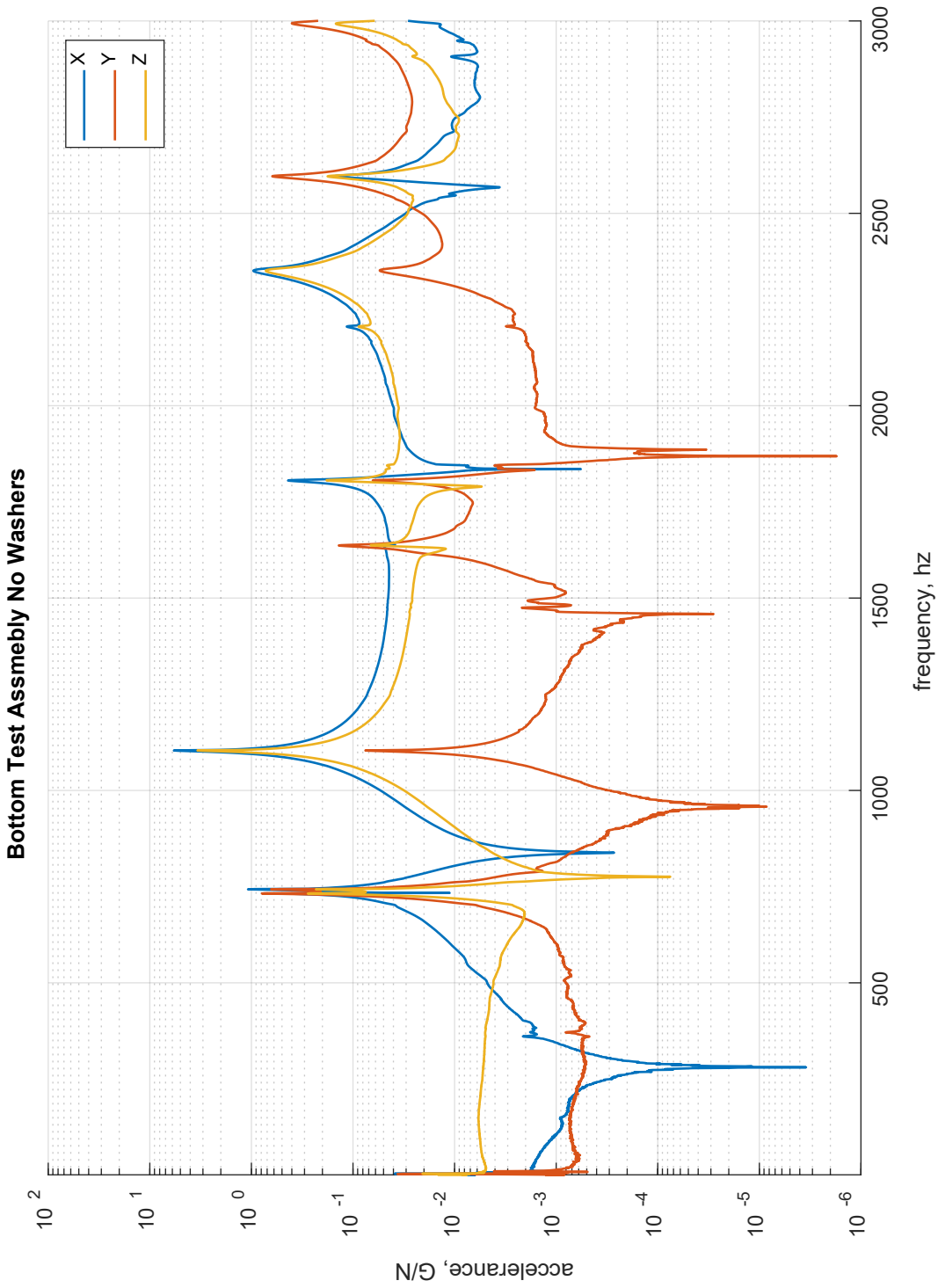
Bottom Test Assmebly No Washers
X
Y
Z
acceleranse, G/N
frequency, hz
10 2
10 1
10 0
10 -1
10 -2
10 -3
10 -4
10 -5
10 -6
500
1000
1500
2000
2500
3000

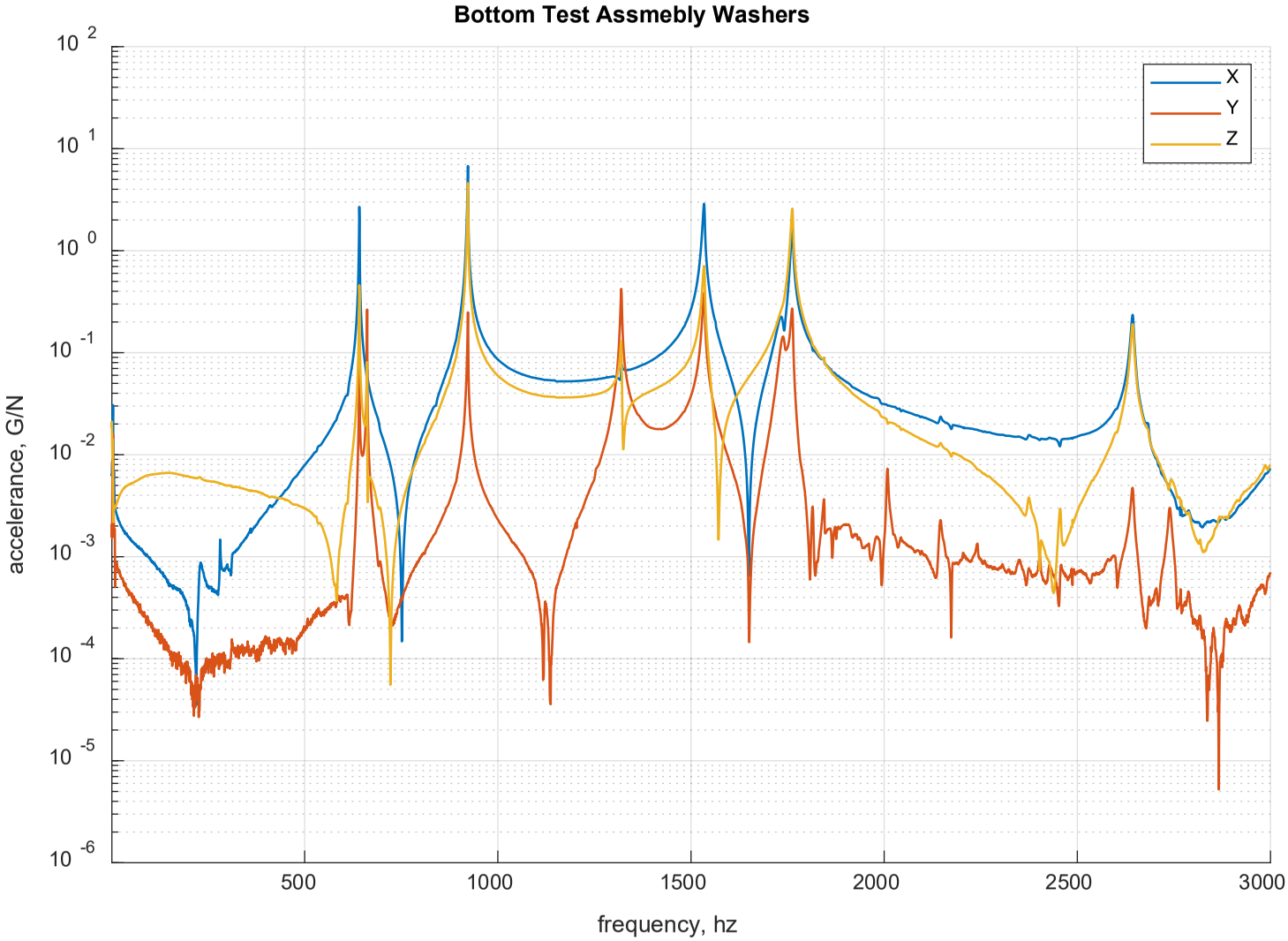
Bottom Test Assmebly Washers
X
Y
Z
accelerance, G/N
frequency, hz
10 2
10 1
10 0
10 -1
10 -2
10 -3
10 -4
10 -5
10 -6
500
1000
1500
2000
2500
3000

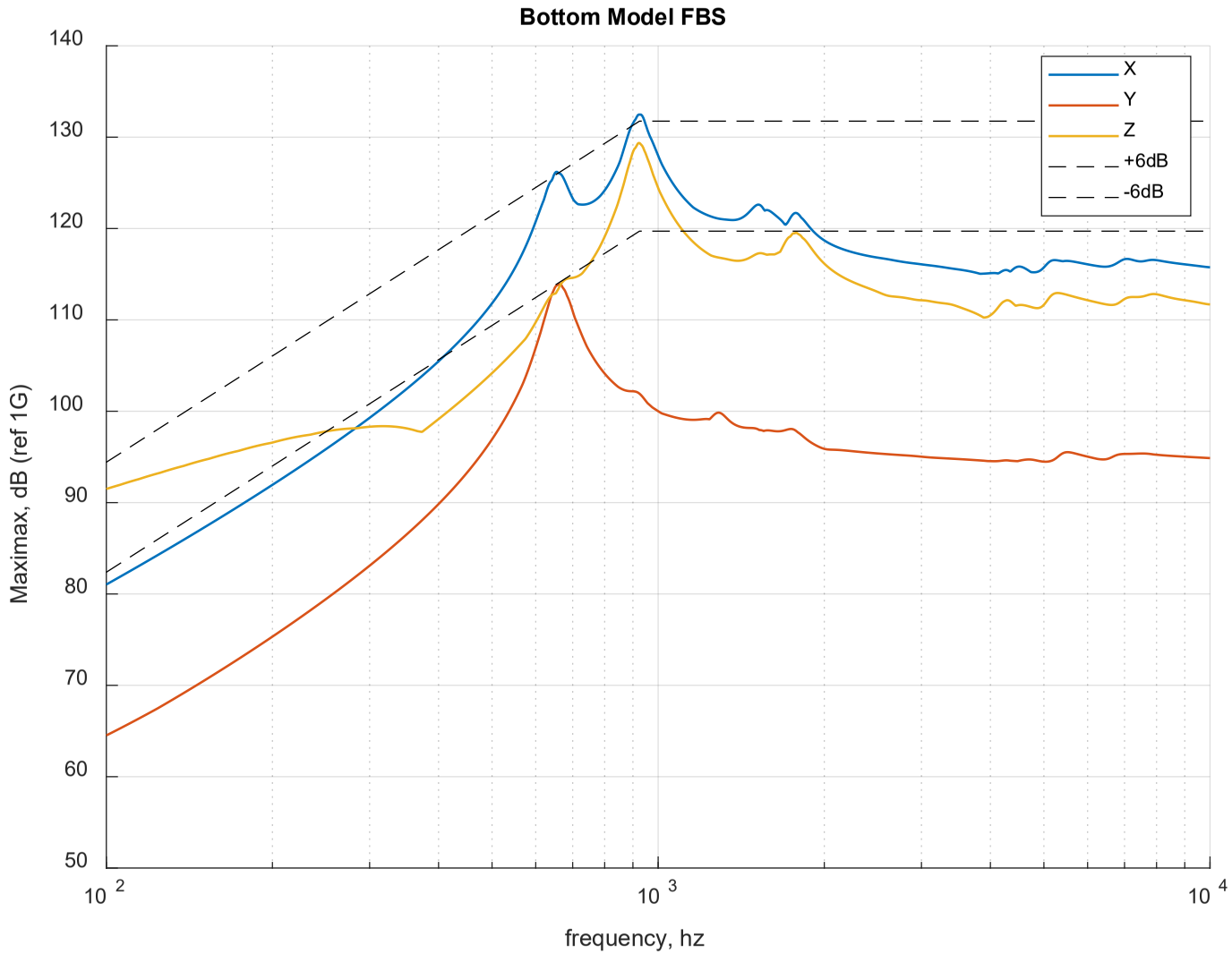
Bottom Model FBS
140
130
120
110
100
90
80
70
60
50
Maximax, dB (ref 1G)
10 2
10 3
10 4
frequency, hz
X
Y
Z
+6dB
-6dB

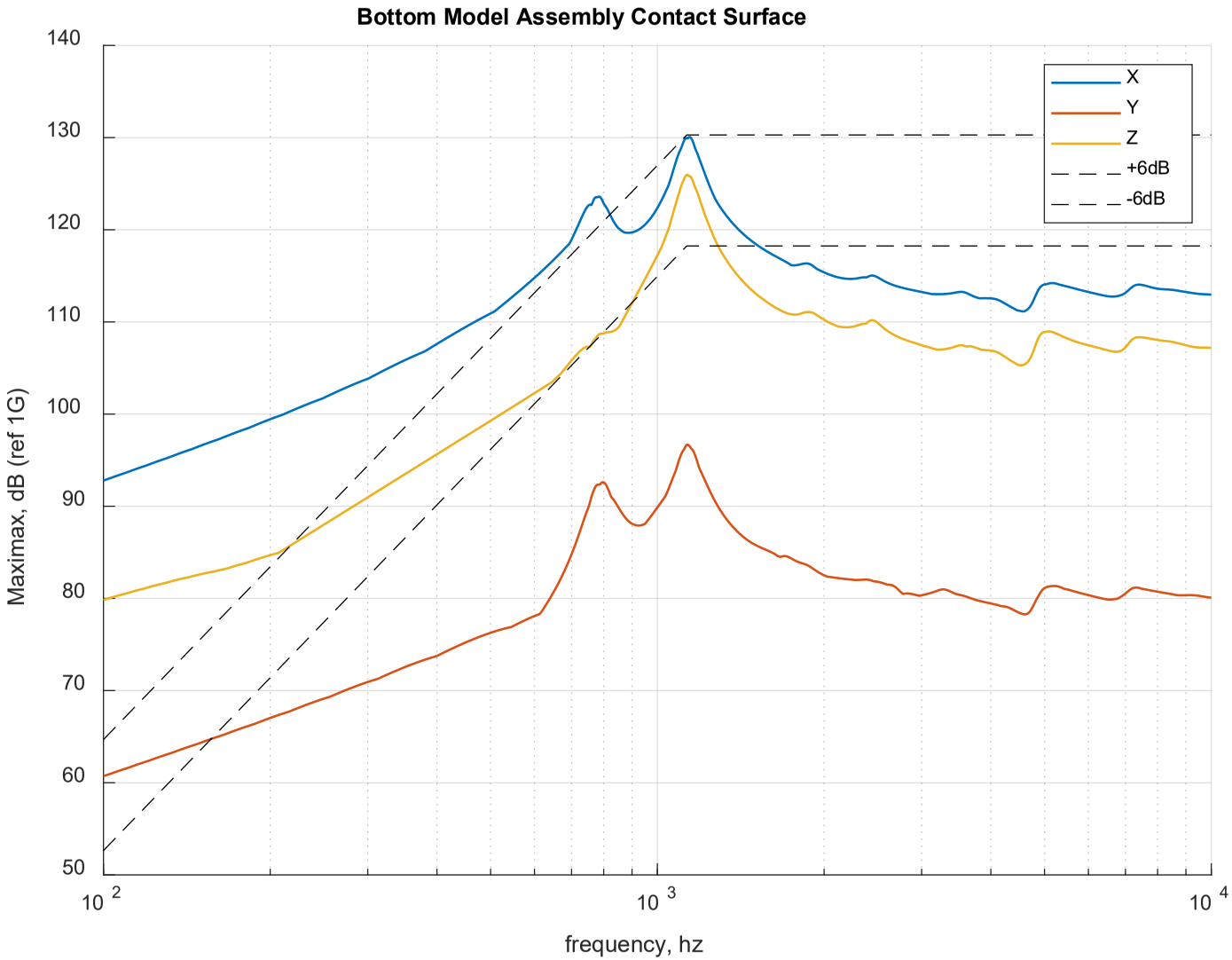
Bottom Model Assembly Contact Surface
140
130
120
110
100
90
80
70
60
50
Maximax, dB (ref 1G)
10 2
10 3
10 4
frequency, hz
X
Y
Z
+6dB
-6dB

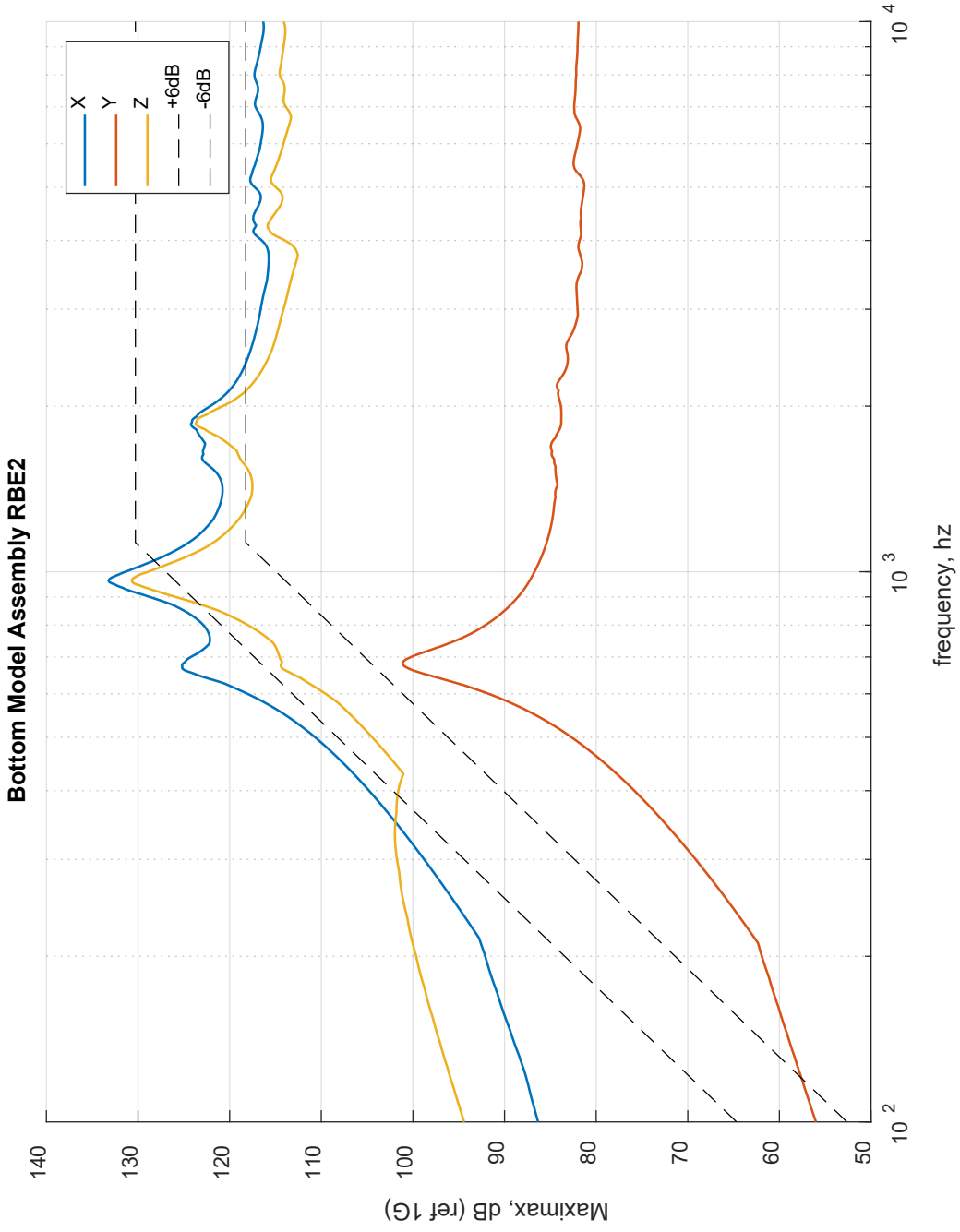
Bottom Model Assembly RBE2
Maximax, dB (ref 1G)
frequency, hz
X
Y
Z
+6dB
-6dB
140
130
120
110
100
90
80
70
60
50
10 2
10 3
10 4

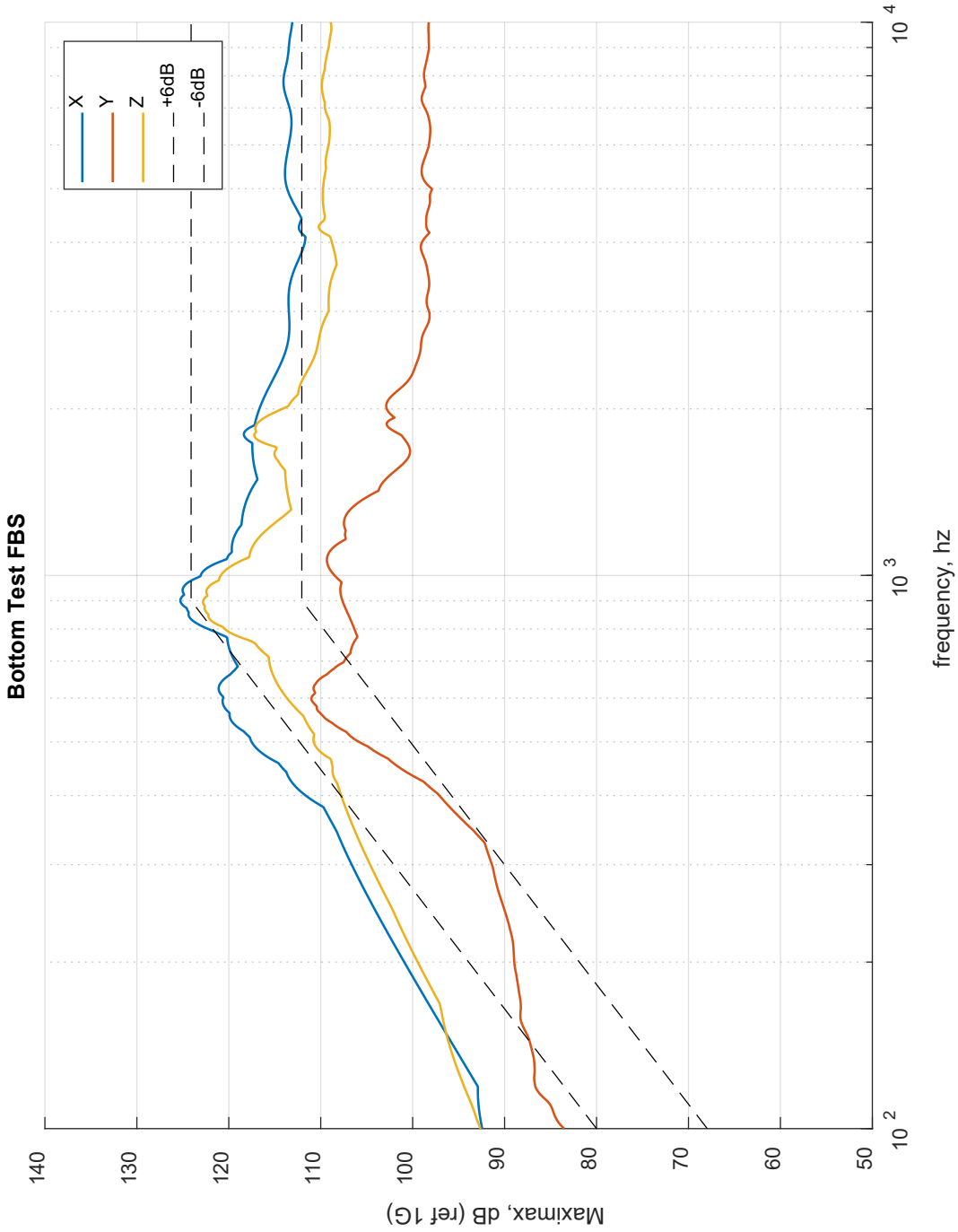
Bottom Test FBS
X
Y
Z
+6dB
-6dB
Maximax, dB (ref 1G)
140
130
120
110
100
90
80
70
60
50
10 2
10 3
10 4
frequency, hz

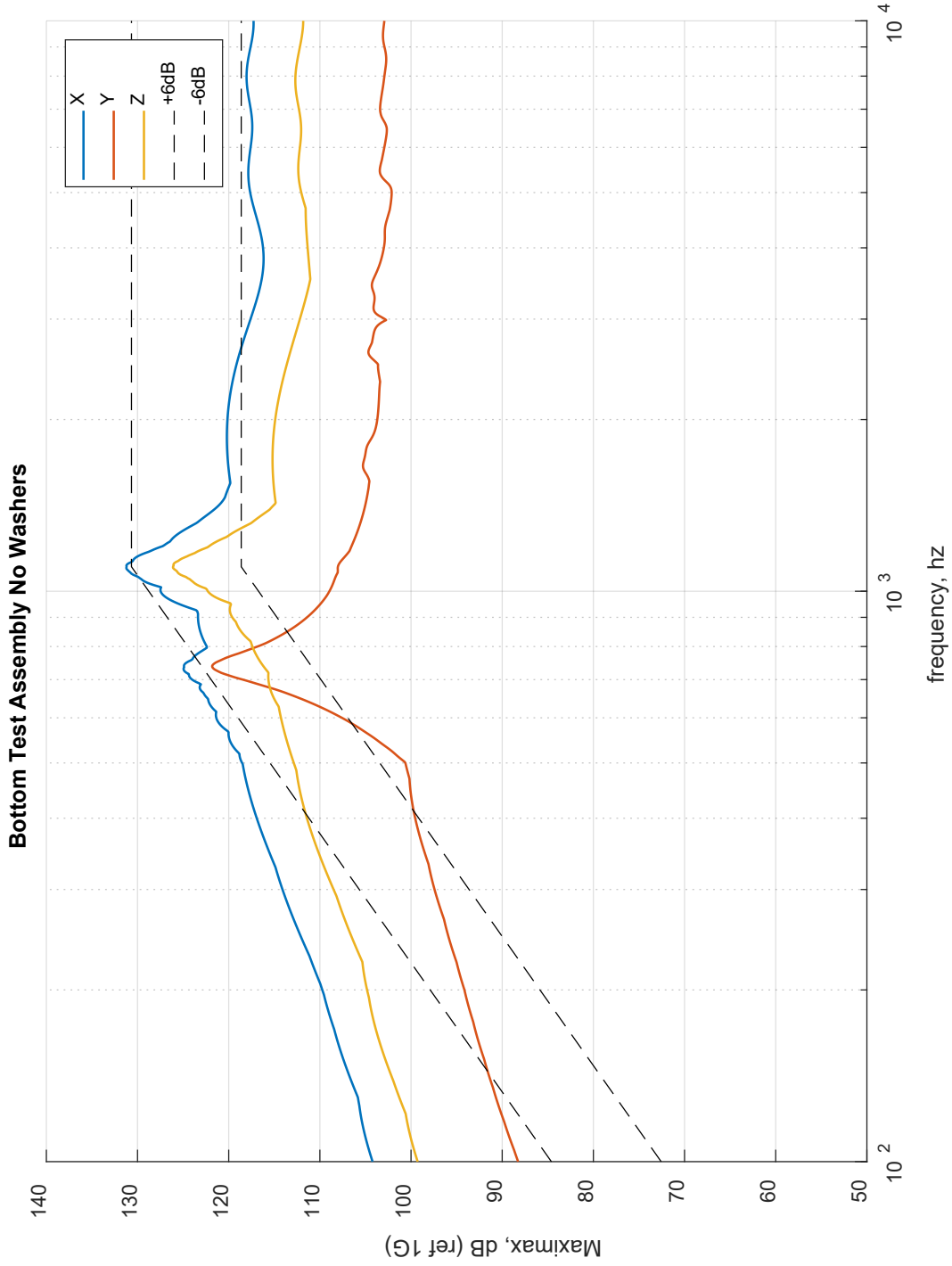
Bottom Test Assembly No Washers
X
Y
Z
+6dB
-6dB
Maximax, dB (ref 1G)
frequency, hz
140
130
120
110
100
90
80
70
60
50
10 2
10 3
10 4

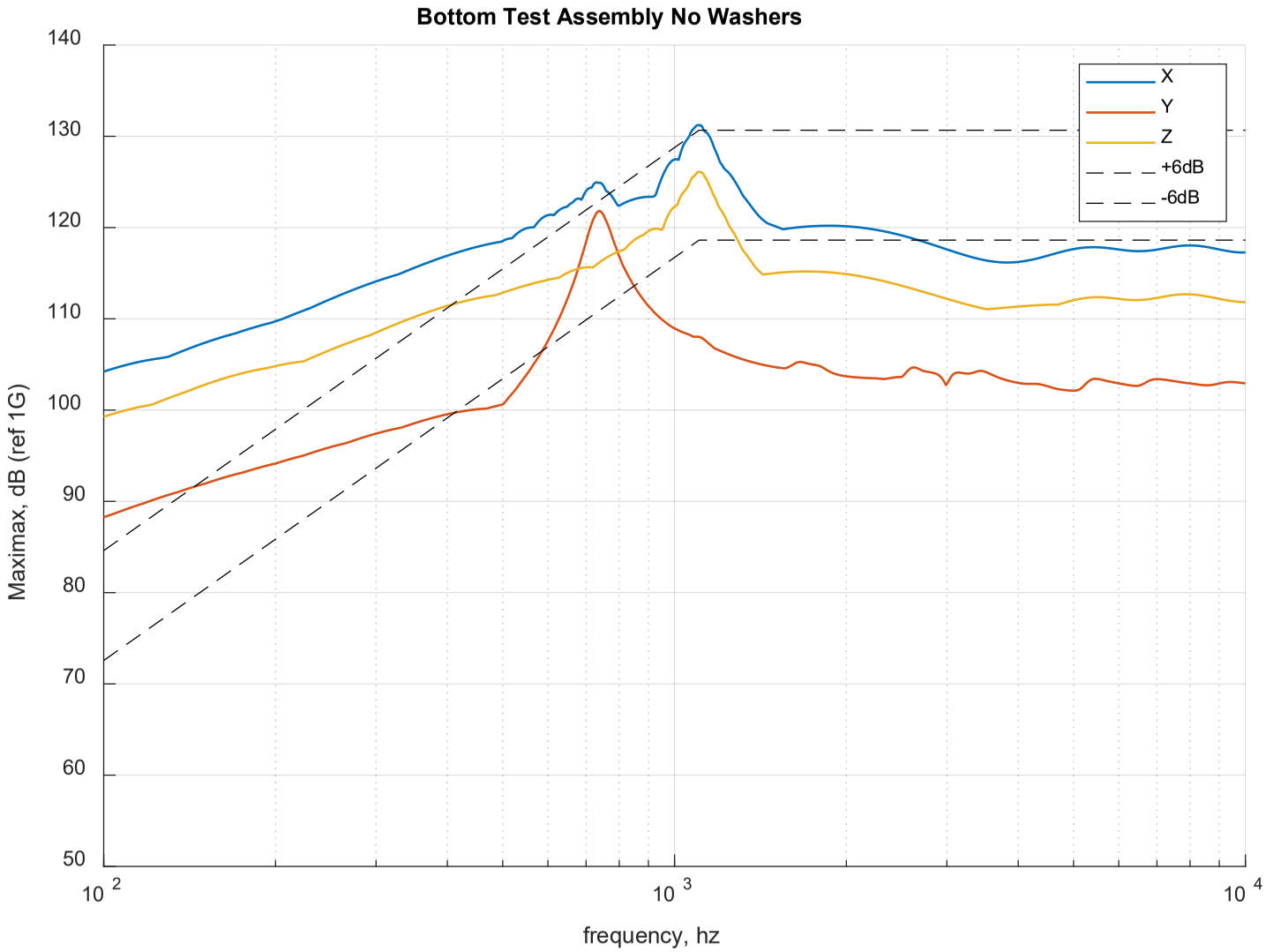
Bottom Test Assembly No Washers
140
130
120
110
100
90
80
70
60
50
Maximax, dB (ref 1G)
10 2
10 3
10 4
frequency, hz
X
Y
Z
+6dB
-6dB

C.3 Corner configuration (optimal)

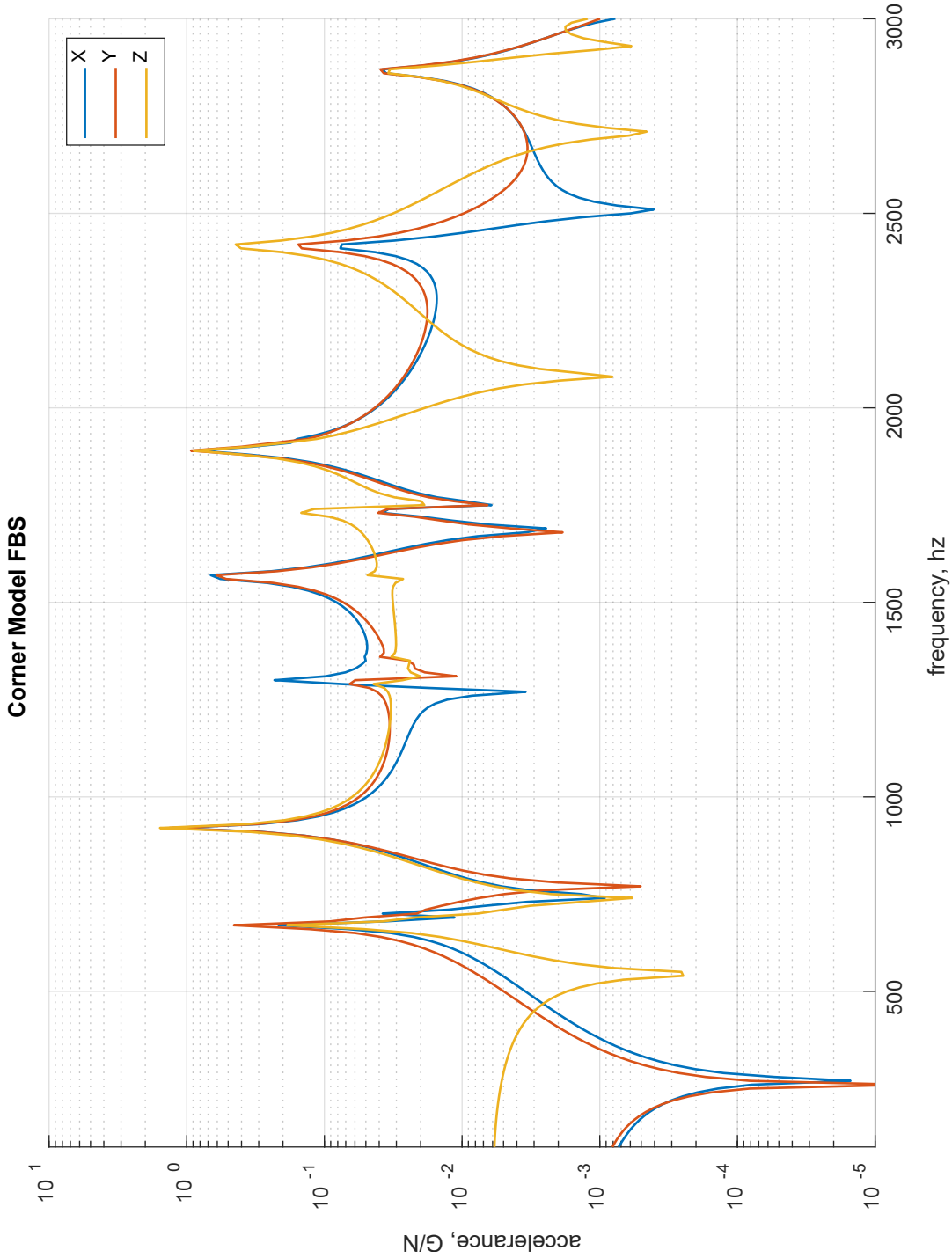

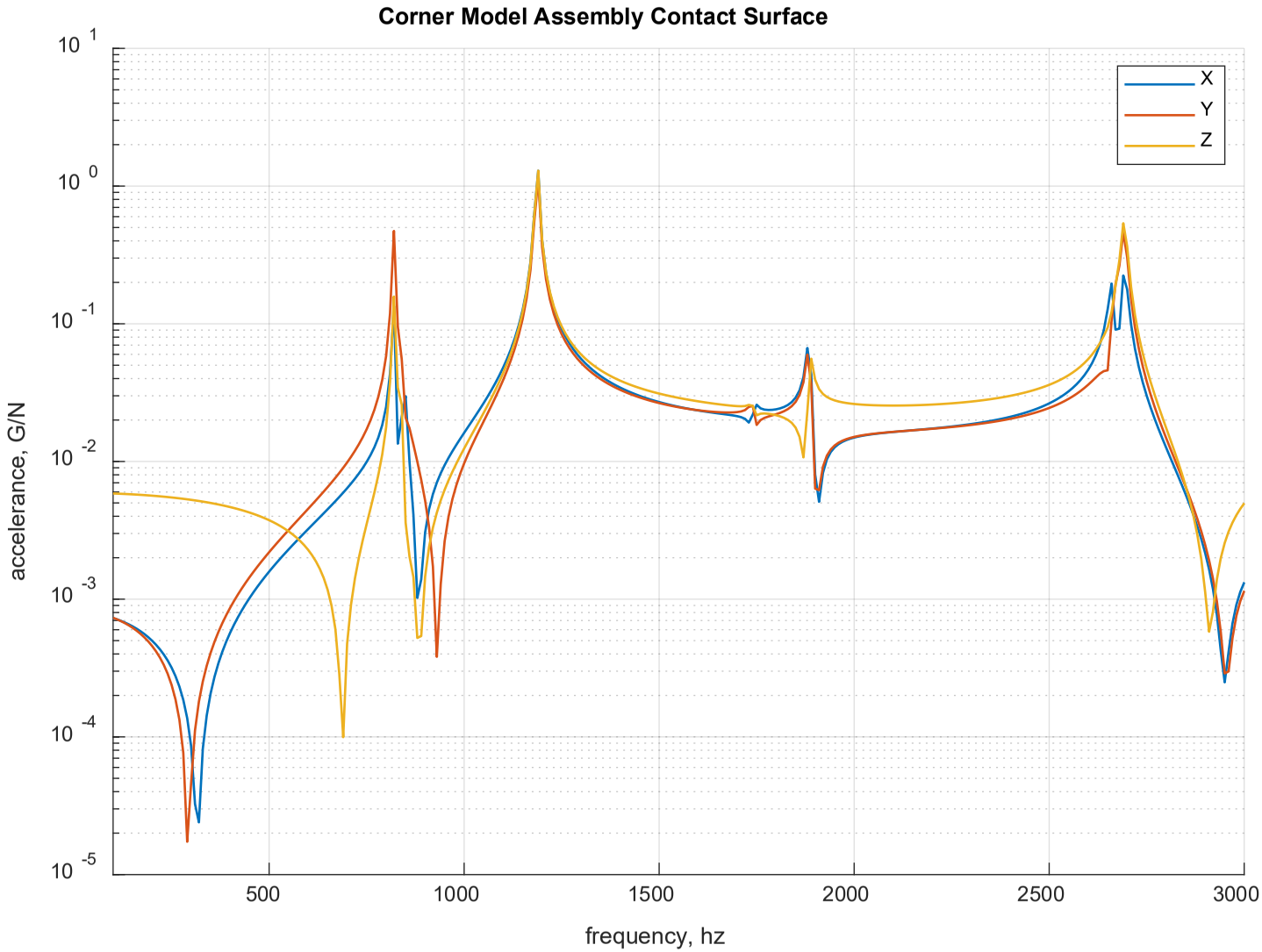
Corner Model Assembly Contact Surface
accelerance, G/N
frequency, hz
X
Y
Z
10 1
10 0
10 -1
10 -2
10 -3
10 -4
10 -5
500
1000
1500
2000
2500
3000

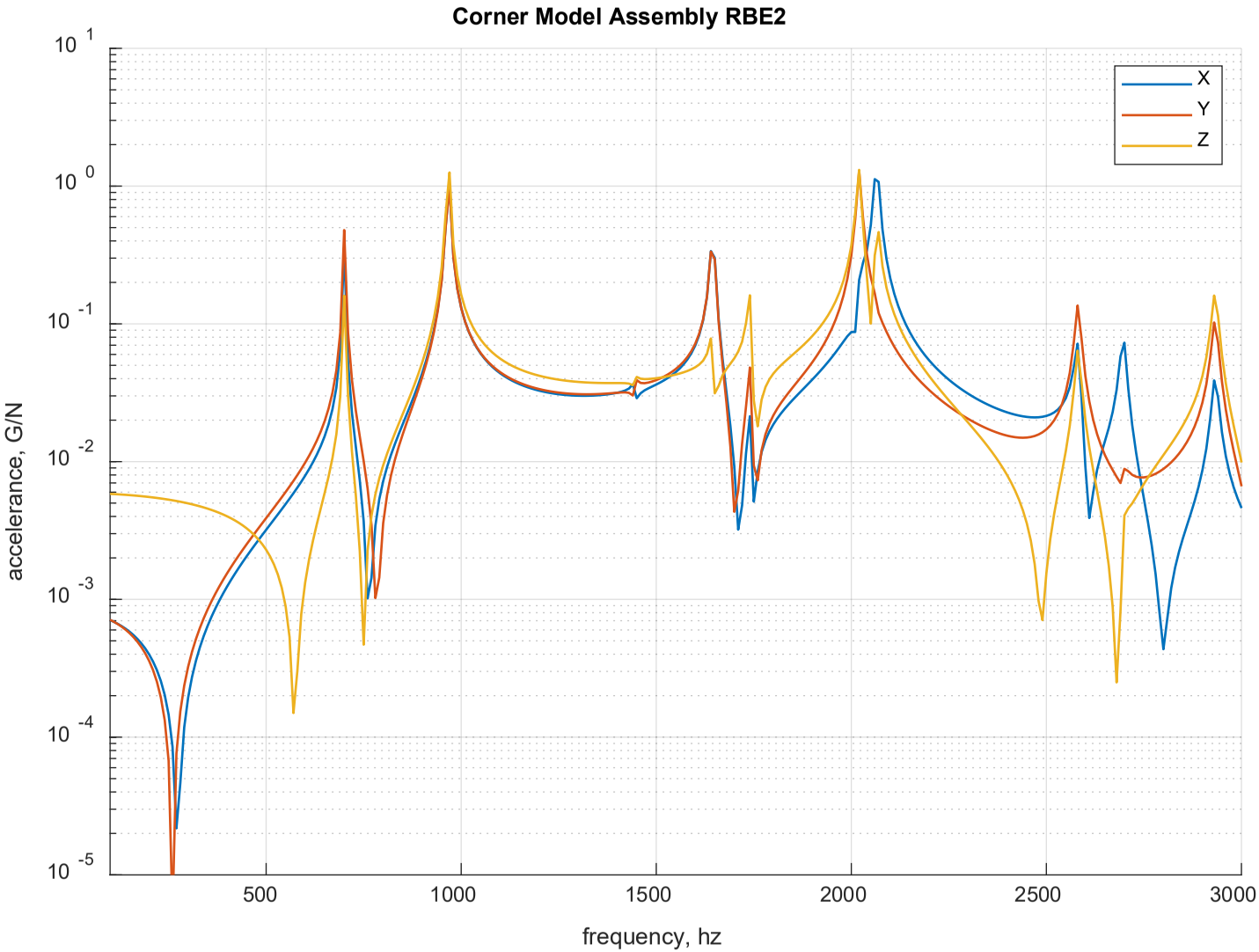
Corner Model Assembly RBE2
X
Y
Z
accelerance, G/N
frequency, hz
10 1
10 0
10 -1
10 -2
10 -3
10 -4
10 -5
500
1000
1500
2000
2500
3000

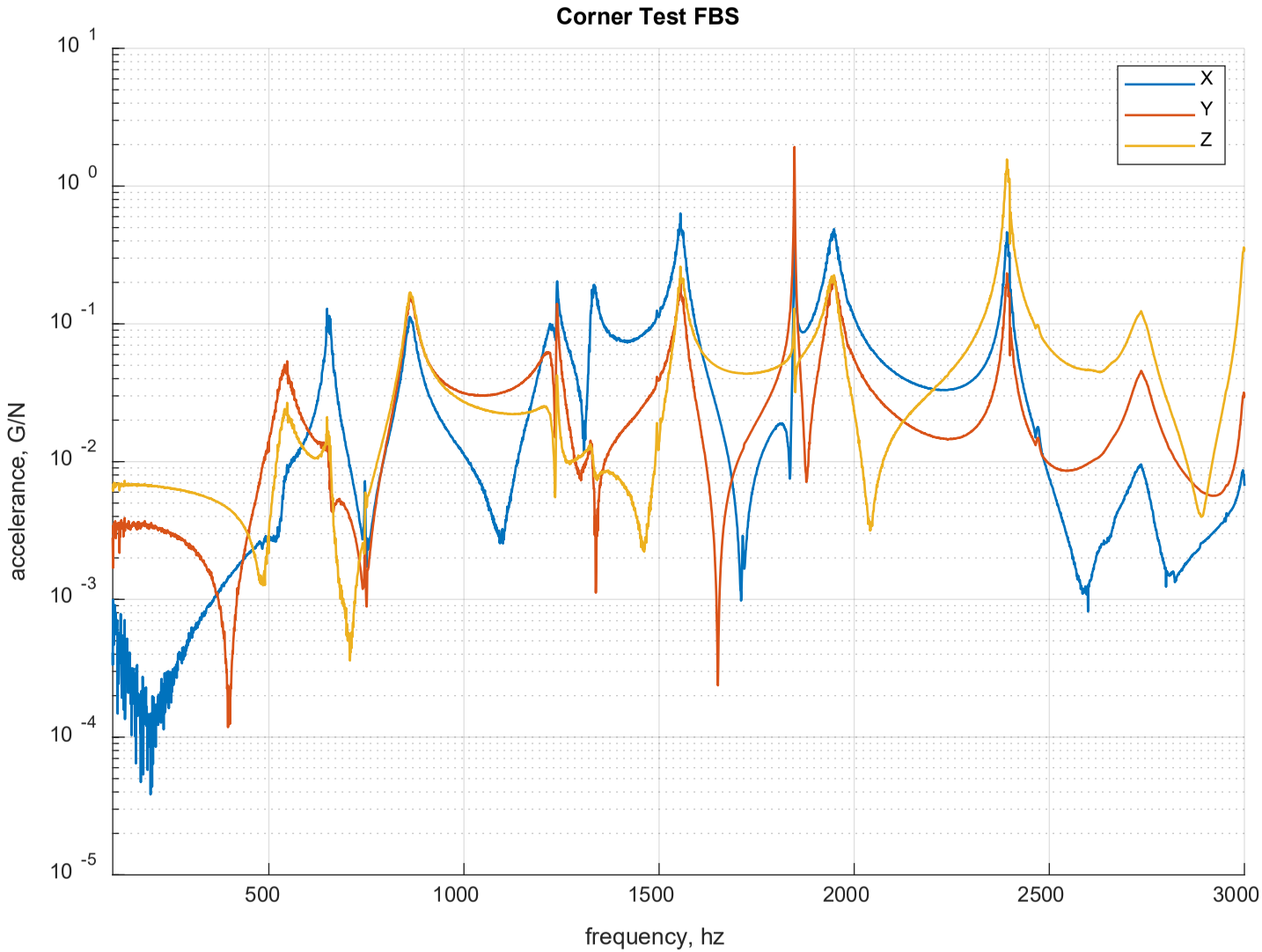
Corner Test FBS
X
Y
Z
accelerance, G/N
frequency, hz
10 1
10 0
10 -1
10 -2
10 -3
10 -4
10 -5
500
1000
1500
2000
2500
3000

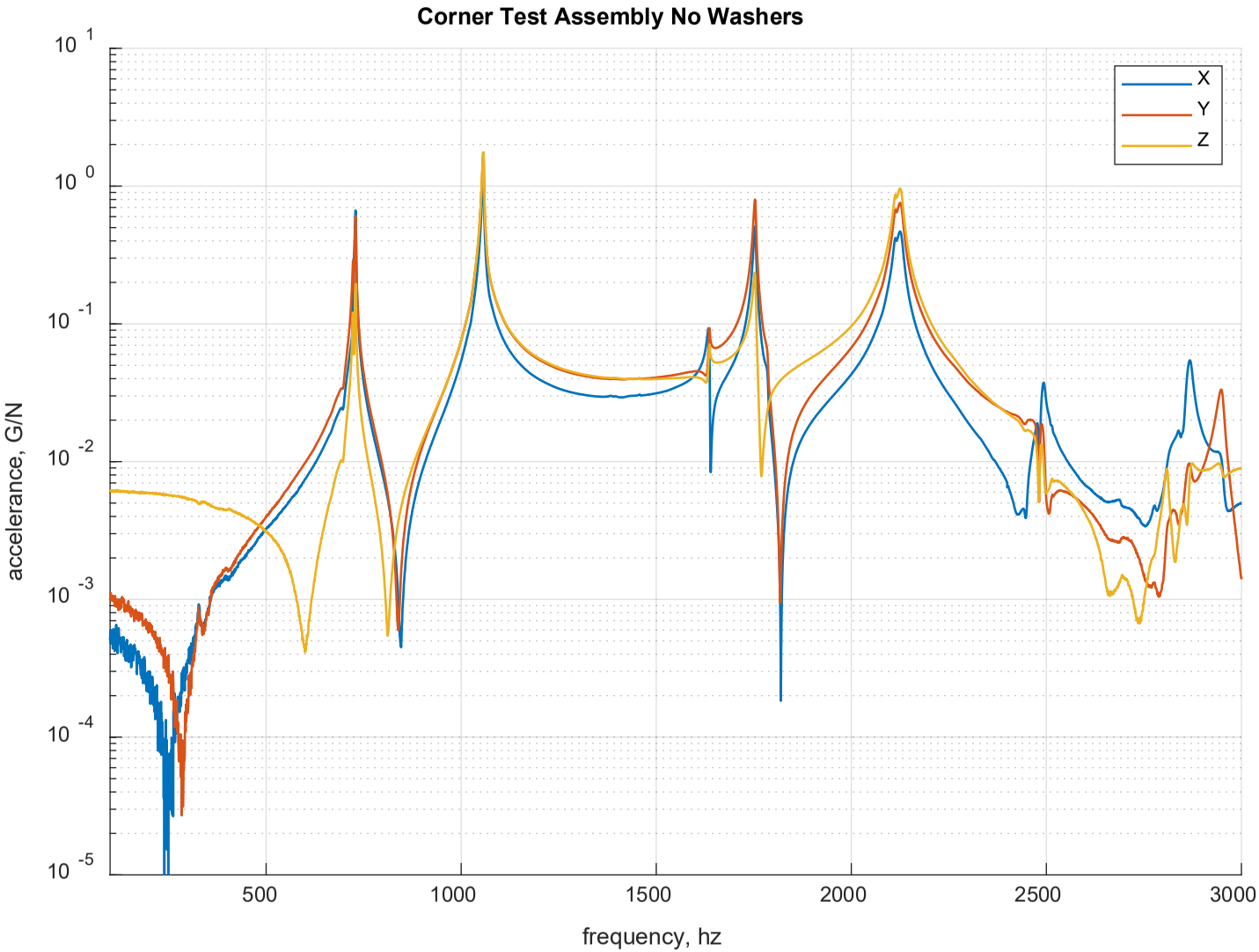
Corner Test Assembly No Washers
X
Y
Z
accelerance, G/N
frequency, hz
10 1
10 0
10 -1
10 -2
10 -3
10 -4
10 -5
500
1000
1500
2000
2500
3000

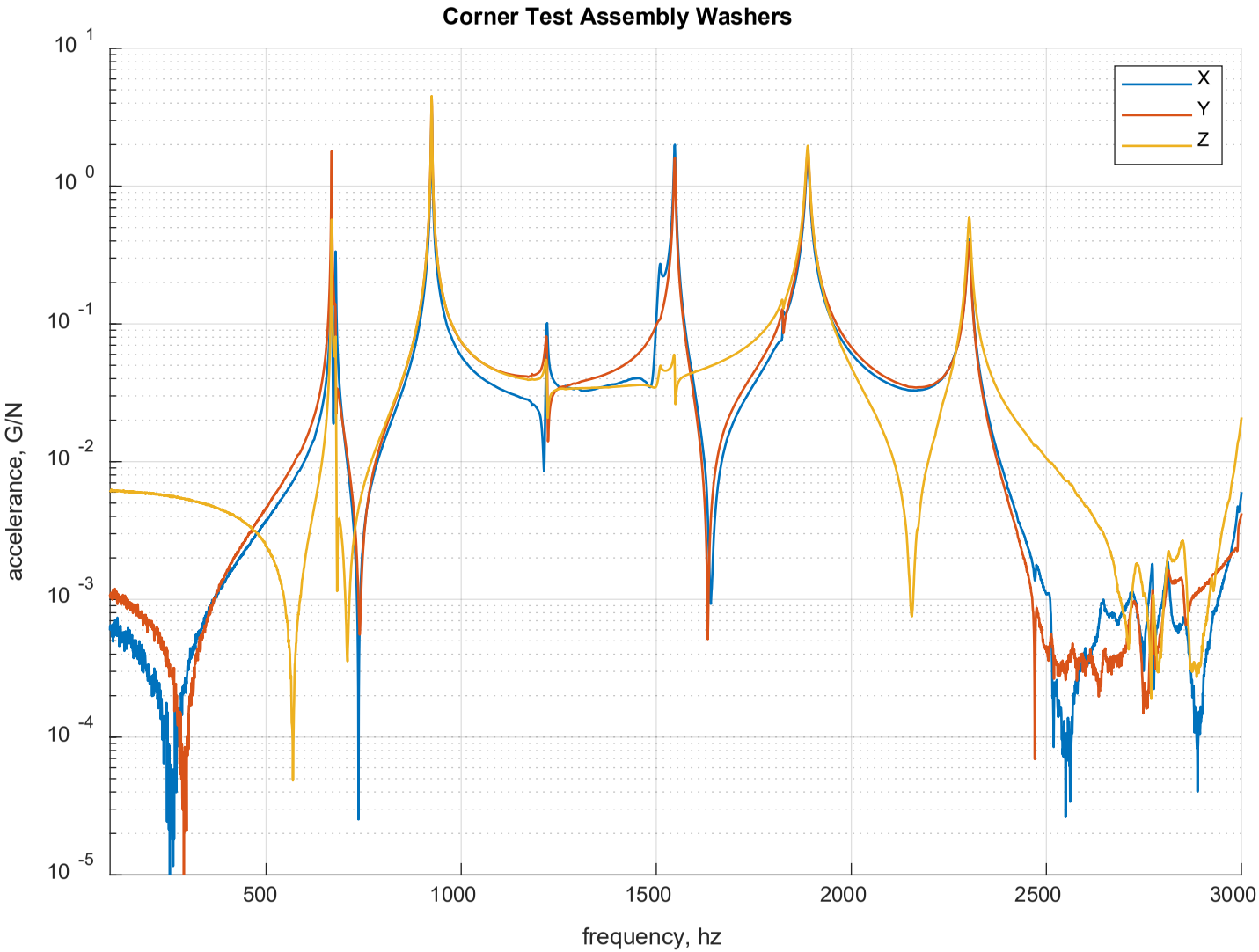
Corner Test Assembly Washers
X
Y
Z
accelerance, G/N
frequency, hz
10 1
10 0
10 -1
10 -2
10 -3
10 -4
10 -5
500
1000
1500
2000
2500
3000

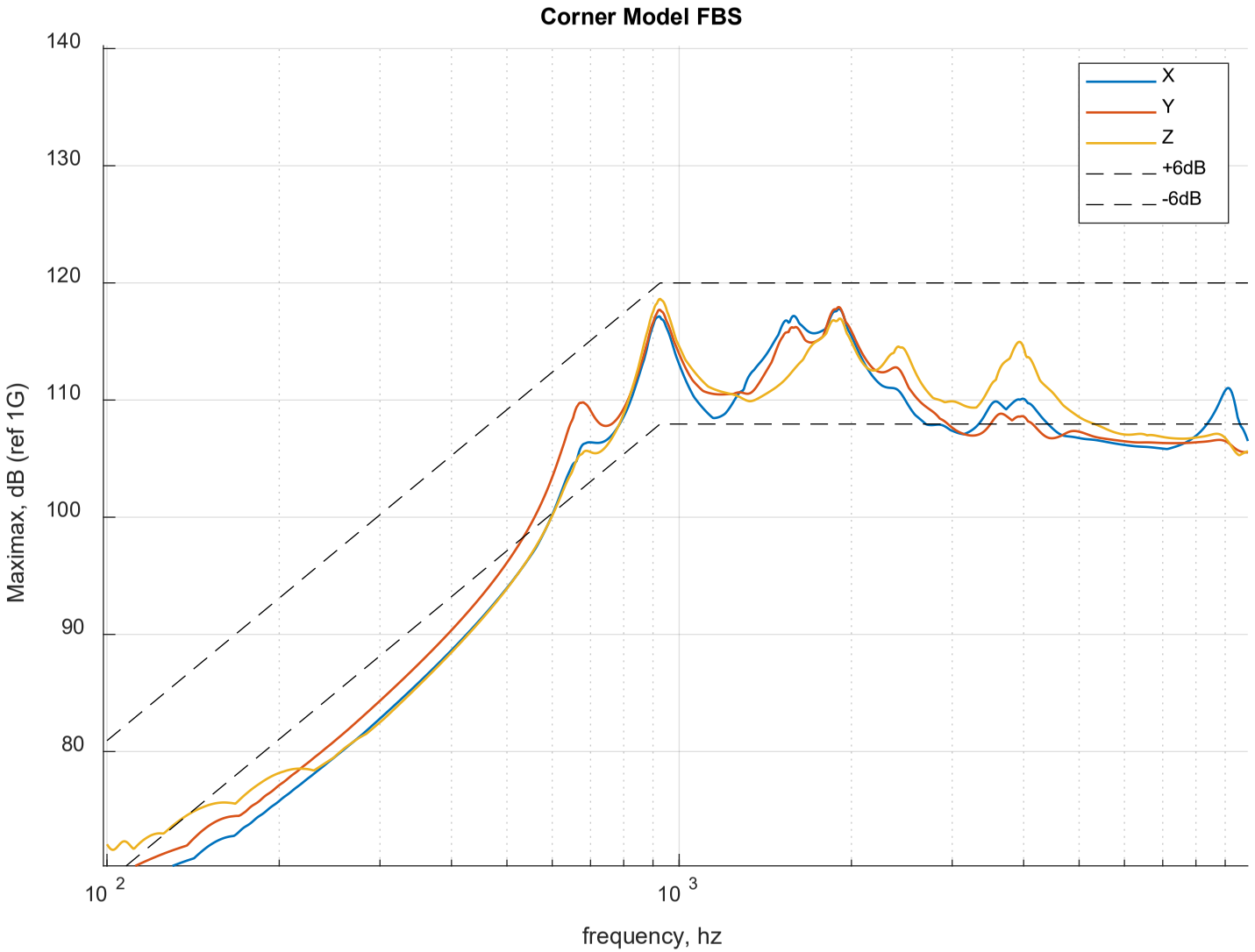
Corner Model FBS
140
130
120
110
100
90
80
Maximax, dB (ref 1G)
10 2
10 3
frequency, hz
X
Y
Z
+6dB
-6dB

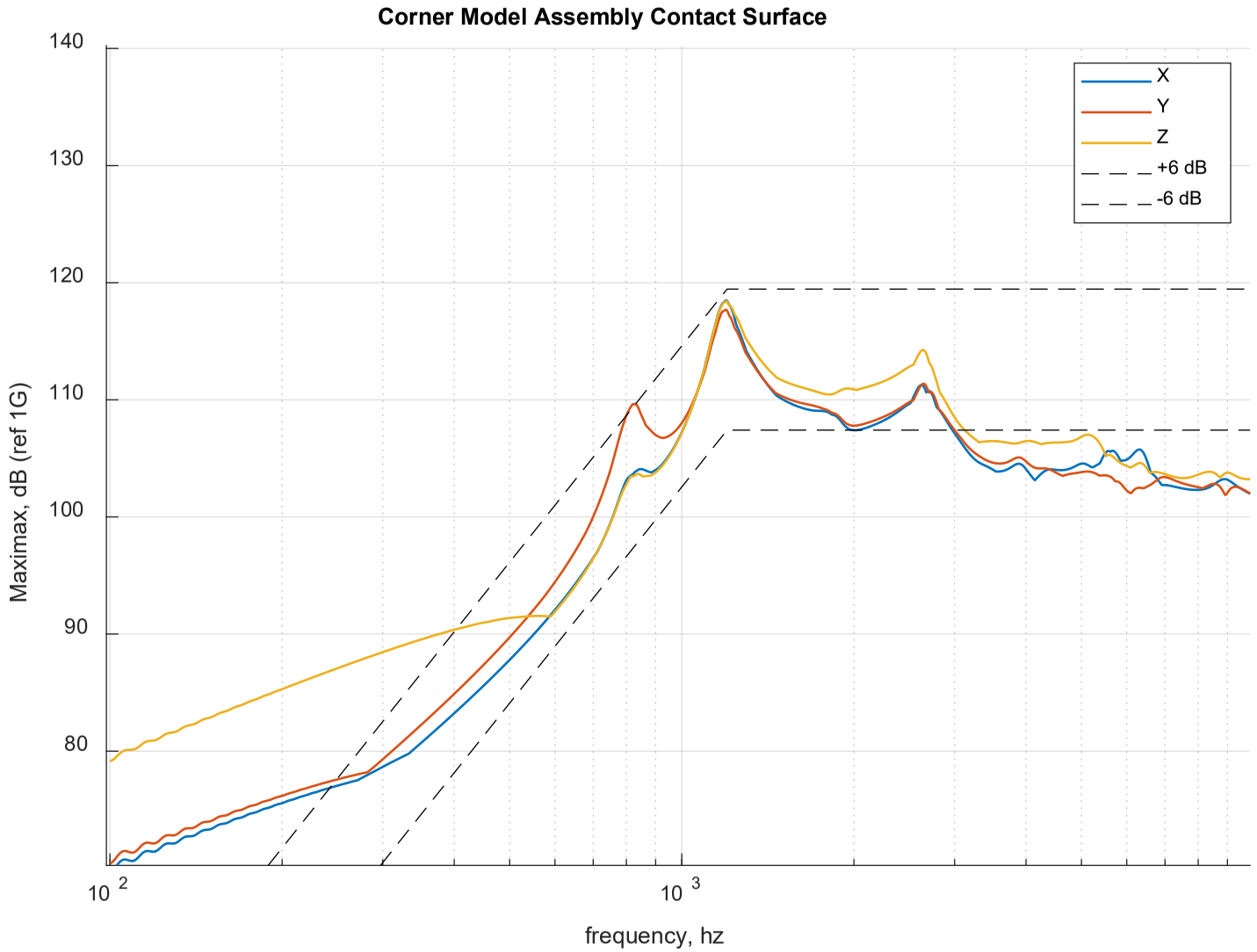
Corner Model Assembly Contact Surface
140
130
120
110
100
90
80
Maximax, dB (ref 1G)
10 2
10 3
frequency, hz
X
Y
Z
+6 dB
-6 dB

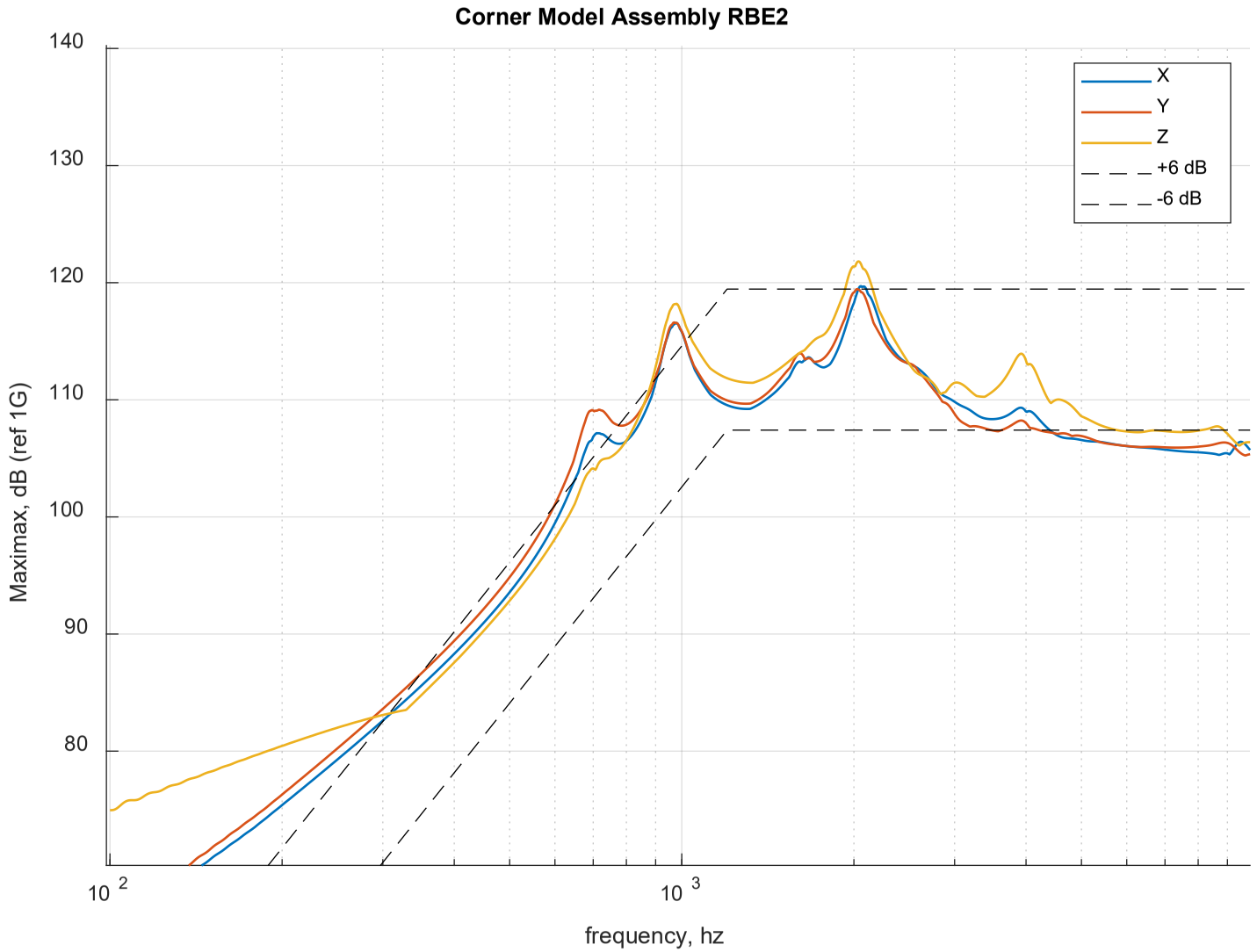
Corner Model Assembly RBE2
140
130
120
110
100
90
80
Maximax, dB (ref 1G)
10 2
10 3
frequency, hz
X
Y
Z
+6 dB
-6 dB

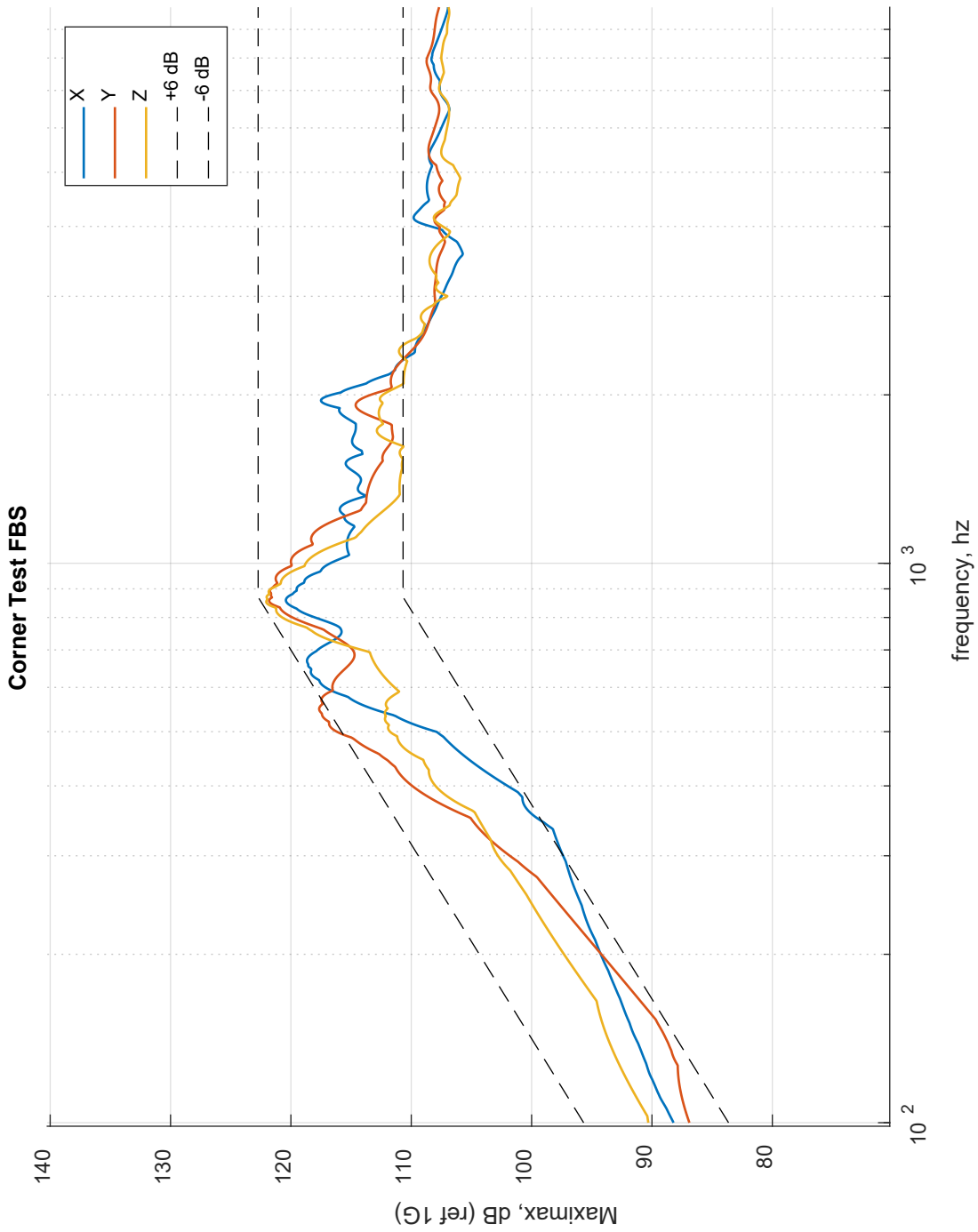
Corner Test FBS
X
Y
Z
+6 dB
-6 dB
Maximax, dB (ref 1G)
140
130
120
110
100
90
80
10 2
10 3
frequency, hz

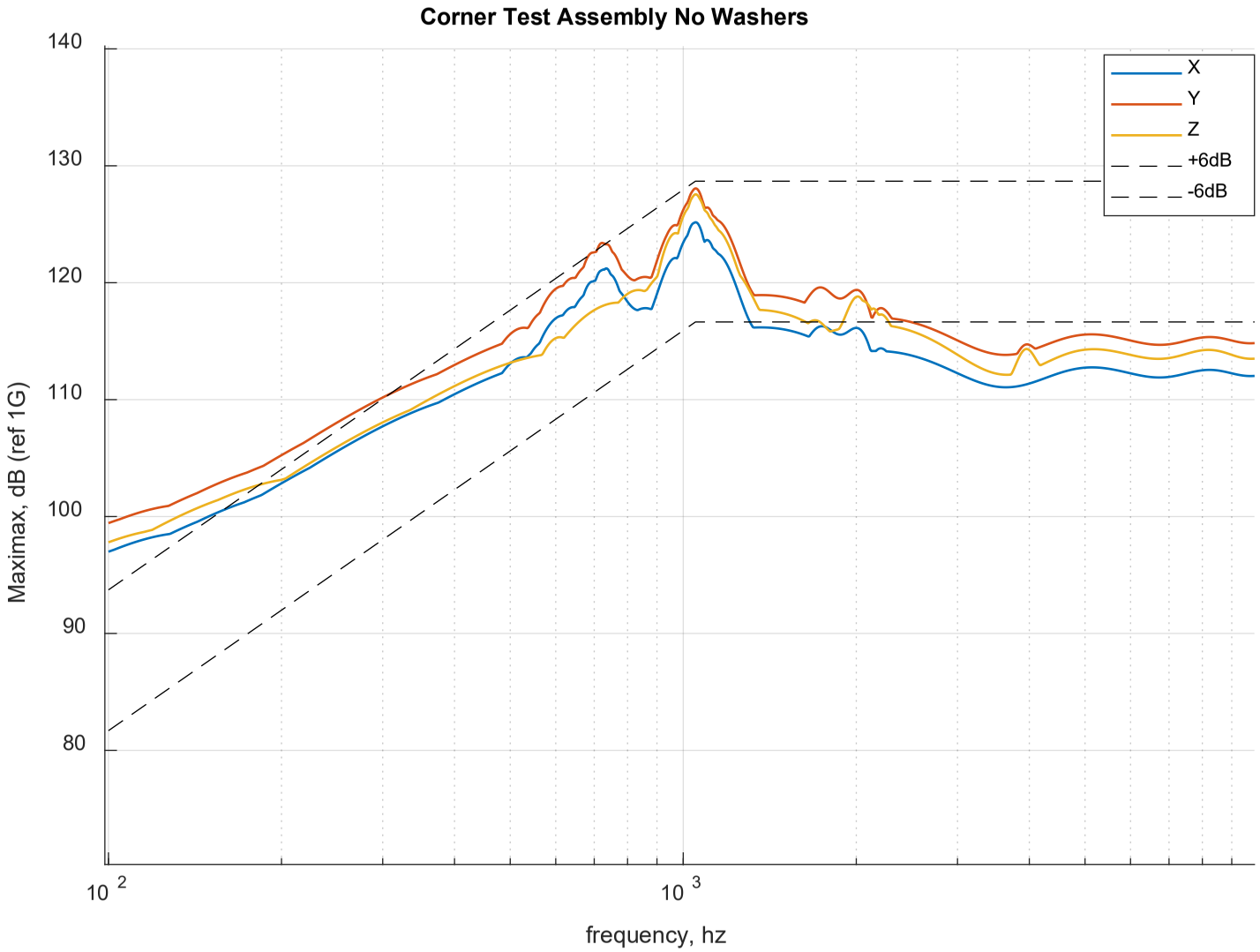
Corner Test Assembly No Washers
140
130
120
110
100
90
80
Maximax, dB (ref 1G)
10 2
10 3
frequency, hz
X
Y
Z
+6dB
-6dB

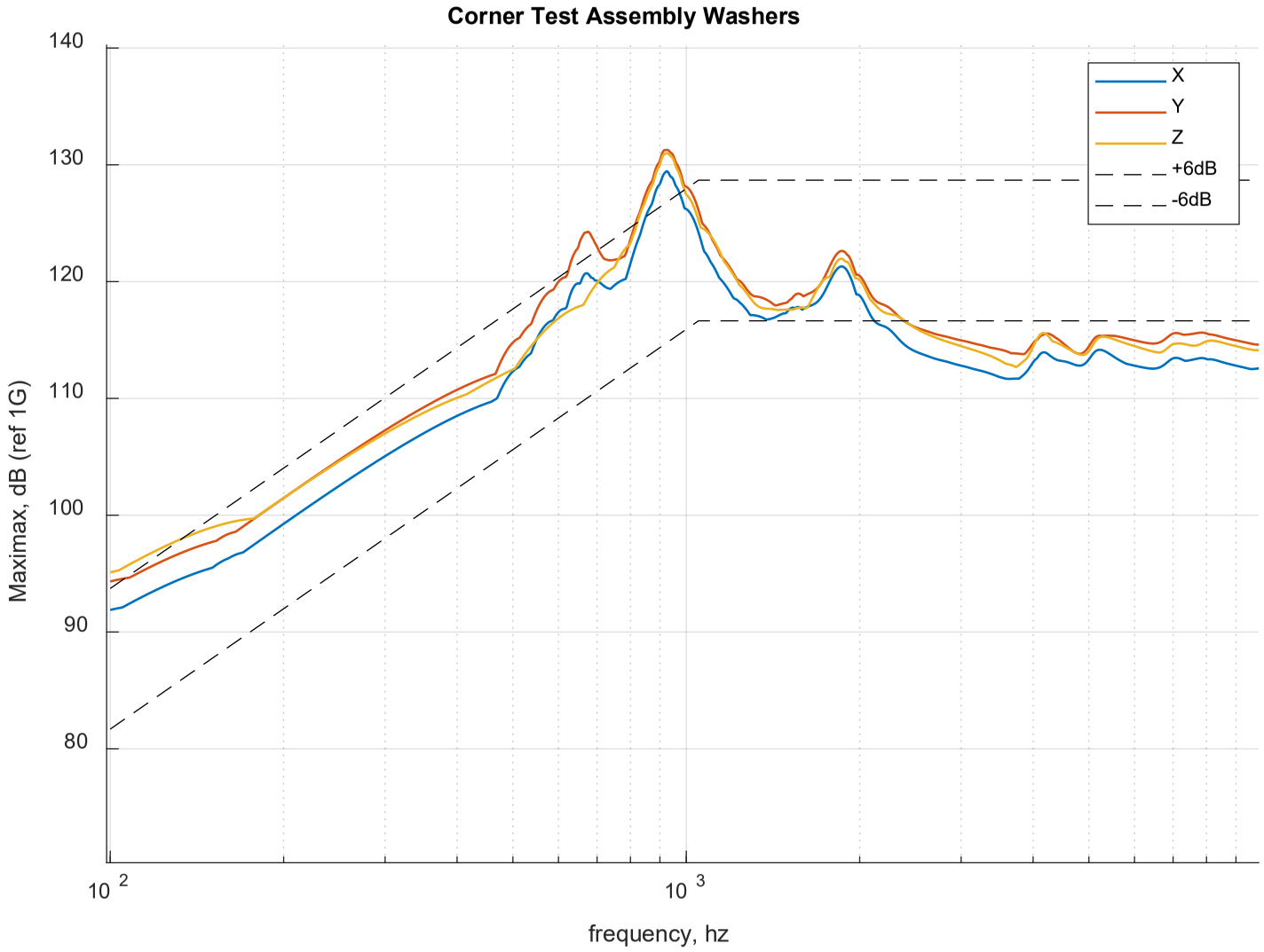
Corner Test Assembly Washers
140
130
120
110
100
90
80
Maximax, dB (ref 1G)
10 2
10 3
frequency, hz
X
Y
Z
+6dB
-6dB